geosciences

Special Issue Reprint

Advances in Thermo-Hydro-Mechanical Characterization and Modelling of Unsaturated Soils

Edited by
Laureano R. Hoyos and Dunja Perić

mdpi.com/journal/geosciences

MDPI

Advances in Thermo-Hydro-Mechanical Characterization and Modelling of Unsaturated Soils

Advances in Thermo-Hydro-Mechanical Characterization and Modelling of Unsaturated Soils

Guest Editors

Laureano R. Hoyos
Dunja Perić

MDPI

Basel • Beijing • Wuhan • Barcelona • Belgrade • Novi Sad • Cluj • Manchester

Guest Editors

Laureano R. Hoyos University of Texas at Arlington Arlington USA	Dunja Perić Kansas State University Manhattan USA

Editorial Office
MDPI AG
Grosspeteranlage 5
4052 Basel, Switzerland

This is a reprint of the Special Issue, published open access by the journal *Geosciences* (ISSN 2076-3263), freely accessible at: https://www.mdpi.com/journal/geosciences/special_issues/GZW9672Z0K.

For citation purposes, cite each article independently as indicated on the article page online and as indicated below:

Lastname, A.A.; Lastname, B.B. Article Title. *Journal Name* **Year**, *Volume Number*, Page Range.

ISBN 978-3-7258-2891-3 (Hbk)
ISBN 978-3-7258-2892-0 (PDF)
https://doi.org/10.3390/books978-3-7258-2892-0

Cover image courtesy of Dunja Perić

Contents

About the Editors

Laureano R. Hoyos

Dr. Laureano R. Hoyos currently serves as a Full Professor (tenured) in the Civil Engineering Department of the University of Texas at Arlington. He earned his Ph.D. degree from the Georgia Institute of Technology (1998) and subsequently became a licensed Professional Engineer in the State of Texas (2004). His research interests are in the areas of experimental and computational geomechanics, particularly applied to unsaturated and problematic soils. He has authored/co-authored numerous, fully refereed publications among book chapters, journal articles, and geotechnical special publications and has been invited to deliver several keynote, state-of-the-art, and plenary lectures on the subject. Dr. Hoyos is the recipient of the College of Engineering Teaching Excellence Award (2024), Lockheed Martin Aeronautics Excellence in Teaching Award (2014), Research Excellence Award (2009), Outstanding Civil Engineering Instructor Award (2005), and Outstanding Early Career Faculty Award (2003). He also served as Chair of the Technical Committee on Unsaturated Soils of the Geo-Institute of the American Society of Civil Engineers (ASCE), as well as Chair of the Organizing Committee of PanAm-UNSAT 2017: Second Pan American Conference on Unsaturated Soils, Dallas, Texas, Nov. 2017. He also represents the U.S.A. as a voting member on the Technical Committee TC106 on Unsaturated Soils of the International Society of Soil Mechanics and Geotechnical Engineering (ISSMGE).

Dunja Perić

Dr. Dunja Perić currently serves as a Full Professor (tenured) in the Department of Civil Engineering at Kansas State University. She earned her Ph.D. degree from the University of Colorado in Boulder. Her research interests are in the areas of experimental/computational geomechanics, particularly in the areas of strain localization and instabilities in pressure-sensitive materials, unsaturated soils, soil–structure interaction, and energy piles. Her research has been published in some of the most prestigious journals in mechanics, including the *International Journal of Plasticity*, *Computers and Geotechnics*, as well as *Cement and Concrete Research*. She has been involved in national and international research collaborations and has been named a Visiting Associate Professor by the University of Colorado in Boulder and a Visiting Fellow by the University of New South Wales, Sydney, Australia. Dr. Perić has served as an Associate Editor of the ASCE *Journal of Geotechnical and Geoenvironmental Engineering* and is currently an active member of the ASCE Geo-Institute Unsaturated Soils Committee. She has been listed several times in the "Who's Who Among America's Teachers" national roster and a recipient of the Kansas State University's "Making a Difference at Kansas State" Award, Outstanding University and Professional Service Award, Outstanding ASCE Advisor Award, Outstanding Teaching Award, and Outstanding Colleague Award.

Preface

In the last few decades, significant progress has been made in characterizing and modelling both the hydro-mechanical response and the thermo-hydro-mechanical behaviour of unsaturated soils, including the decisive refinements of experimental techniques and the recent developments of reasonably robust constitutive and computational models under static and dynamic loads. This Special Issue of *Geosciences*, sponsored by the Unsaturated Soils Committee of the Geo-Institute of the American Society of Civil Engineers (ASCE), brings together 11 papers documenting some of the most recent advances, made in the last few years, in the areas of hydro-mechanical and thermo-hydro-mechanical characterization and modelling of unsaturated soils, including crucial field applications. The contributions were subjected to a rigorous peer-review process and are primarily focused on the thermo-hydro-mechanical testing of unsaturated soils, including equipment, test protocols, and data interpretation, as well as the postulation of refined computational modelling frameworks based on thorough experimental evidence. The Special Issue is hence expected to be a high-value reference material for scholars and practitioners alike.

The first three contributions, addressing fundamentals, include novel laboratory setups to experimentally assess thermally induced moisture flows in silty sand, as well as the effect of cyclic freeze–thaw and wetting–drying on the water retention properties and hydraulic conductivity of tailings. The following four contributions, focused on modelling, include papers introducing a hyperelastic bounding surface plasticity model for unsaturated granular soils, as well as a THM meshfree paradigm for predicting shear banding and cracking in unsaturated porous media. Additional papers in this group address the thermo-hydro-mechanical-chemo effects on SWCC modelling, and the postulation of a stress-based model for interpreting s-wave velocity in unsaturated soils from in situ SCPT data. The last four contributions, related to field applications, include papers addressing the impact of a specific type of vegetation, as well as of climate change, on the stability of unsaturated and expansive soil slopes. Additional papers document a multi-physics approach to simulating frost heave mitigation in cold region pavements using wicking geotextiles, as well as the seismic response of pile foundations considering the soil suction changes induced by soil–atmospheric interactions.

The efforts of all authors and their peer reviewers, many of them from the Unsaturated Soils Committee of the Geo-Institute of the ASCE, as well as the dedication of the *Geosciences* publication staff in producing this Special Issue are gratefully acknowledged.

Laureano R. Hoyos and Dunja Perić
Guest Editors

geosciences

MDPI

Article

Thermally Induced Moisture Flow in a Silty Sand under a 1-D Thermal Gradient

Nice Kaneza [1,2], Aashish Pokhrel [2], Laureano R. Hoyos [2] and Xinbao Yu [2,*]

[1] WSP in the U.S., Indianapolis, IN 46204, USA; nice.kaneza@mavs.uta.edu
[2] Department of Civil Engineering, University of Texas, Arlington, TX 76019, USA; axp8401@mavs.uta.edu (A.P.); hoyos@uta.edu (L.R.H.)
* Correspondence: xinbao@uta.edu

Abstract: Thermally induced moisture flow in unsaturated soils involves complex coupled thermal–hydro processes with the moisture flow in both the vapor and liquid phases. The accurate measurement of the moisture flow in unsaturated sands remains a challenging task due to low moisture migration, the temperature effect on moisture sensors, and the gravity effect on moisture flow. This study aims to accurately measure transient moisture flow, heat transfer, and thermal conductivity in a silty sand with 35% non-plastic fines in a closed heat cell with a controlled 1-D temperature gradient. The heat cell consists of two temperature-controlled heat exchanger plates, heat flux sensors, moisture sensors, thermocouples, and thermal conductivity sensors. The soil moisture sensors were calibrated in the test soil at room temperature and then at elevated incremental temperatures. Soil samples compacted at various initial moisture contents were tested under a constant 1-D temperature gradient of 4 °C/cm. Soil moisture redistribution, temperature, and thermal conductivity profiles were determined from the test results. Transient temperature responses indicated that a lower initial moisture content led to a higher temperature drop after reaching the peak, or a more concaved temperature profile in a steady state due to enhanced moisture migration driven by the temperature gradients. Dry soils exhibited uniform thermal properties, while moist soils showed varying thermal conductivity profiles. A critical moisture content was identified when the maximum moisture migration occurred. Thermal conductivity in soils increased with the distance from the heat source due to thermally induced moisture migration. These findings provide valuable insights into coupled moisture–heat flow dynamics in unsaturated sands.

Keywords: thermally induced moisture flow; critical moisture content; coupled thermos–hydro processes; unsaturated sand

Citation: Kaneza, N.; Pokhrel, A.; Hoyos, L.R.; Yu, X. Thermally Induced Moisture Flow in a Silty Sand under a 1-D Thermal Gradient. *Geosciences* **2024**, *14*, 207. https://doi.org/10.3390/geosciences14080207

Academic Editors: Meng Lu and Jesus Martinez-Frias

Received: 26 June 2024
Revised: 24 July 2024
Accepted: 29 July 2024
Published: 2 August 2024

1. Introduction

Water in soils moves and redistributes under the influence of the temperature gradient [1–4]. The water redistribution in the soil induces the associated heat transfer and changes in soil thermal properties. Therefore, moisture flow in unsaturated soils under non-isothermal conditions is highly coupled with the heat transfer process. Coupled heat transfer and moisture flow in unsaturated soils are critical to the understanding of many thermal geotechnical structures, such as buried electrical cables [5–7], ground heat exchangers [8], energy piles [9], thermally active embankments [10], and heat storage in soils [11]. For example, buried electrical transmission cables generate heat, causing a rising temperature in the cable sheath, which leads to the migration of moisture away from the cable under the thermal gradient. The soil surrounding the cable dries out, and its thermal conductivity decreases remarkably. As a result, the cable temperature continues to rise, which may lead to cable failure and the thermal instability of the soil surrounding the cable [5,6]. In an energy pile, the moisture moves away from the pile during the heating operation and moves toward the pile during the cooling operation. The moisture flow causes thermal and mechanical changes in the soil near the pile and thus can affect the thermal performance of the energy pile, as well as its bearing capacity [12,13]. The study of thermally induced moisture movement is crucial for effectively addressing these thermal geotechnical problems. This understanding can improve the design of more resilient infrastructures and energy systems that can better adapt to environmental thermal changes.

Thermally induced soil water movement in unsaturated soils is a complex process involving various components in both the vapor and liquid phases governed by different physical laws [5,6]. Soil vapor pressure increases with the increase in temperature. Water molecules in the vapor diffuse from a warmer region towards a lower temperature region in the direction of the decreasing temperature gradient. This vapor diffusion process is generally governed by Fick's first law of diffusion [1–3]. The vapor condenses to liquid water in the cooler temperature region and creates an additional difference in the soil moisture potential, contributing to the liquid moisture flow. The liquid moisture flow caused by the temperature gradient is more complex and is governed by several physical phenomena, such as thermo-self-diffusion, thermos-osmotic flow in fine-textured soil, and thermocapillary film flow [1]. The net liquid moisture flow is a combination of all the above liquid flow phenomena. The most dominant liquid moisture flow is the viscous capillary flow caused by a net differential in soil suction. The dynamic balance of the vapor and liquid water flow determines the net moisture movement in the soil, or whether it becomes dry or wet [1–3].

Thermally induced moisture migration in unsaturated soil is a complex process influenced by several factors, including temperature gradient, soil type, moisture content, and gravitational effects [1–4,14,15]. Bouyoucos [16] used a closed soil column to measure both heat flux and moisture for several soils at different moisture contents and temperature gradients. The researcher concluded that the thermally induced moisture flux was influenced by the laws of surface tension and the viscosity of water in the soil and were maximized at an optimum moisture content. This optimum moisture content was defined as at the point at which water transfer from warmer to colder parts is most efficient under a constant thermal gradient [16,17]. The findings are corroborated by various subsequent researchers [18–23]. They determined that the quantity of water migrating from warm to cool regions was mainly influenced by the initial moisture content and magnitude of the temperature gradients. Wang and Su [24] tested thermally induced moisture flow in loess soils and found that a higher gradient and a lower soil density cause more pronounced moisture migration. When the initial moisture content is close to dry or near saturation, the thermally induced moisture increase is small. However, maximum thermally induced moisture flow was observed in soils with a moderate initial moisture content. Hedayati-Dezfooli [25] also determined that the temperature gradient is the primary factor causing moisture migration. It was found that a significant moisture migration was observed at a temperature difference of roughly 65 °C between the top and bottom plates. Dang [26] observed that coarser soils could not hold pore water, and they experienced more significant moisture movements than did fine and medium soils. Faizal et al. [12] remarked that changes in volumetric water content continued to fluctuate in a time-dependent, nonlinear, and slower manner after the fluctuations in soil temperature had settled, and soil temperatures and volumetric water content increased the most in the areas closest to the heat source. Recently, Kaneza et al. [4] determined that unsaturated sand with a high moisture content achieved thermal equilibrium faster than samples with a lower moisture content. The researchers also noticed that gravity has an impact on the moisture movement in the soil, depending on the direction of the temperature gradient: when the bottom of the soil was heated, and the top cooled, less pore water moved away from the heated end, and the increased thermal conductivity affected the temperature near that end, resulting in a higher steady-state temperature.

Although many studies have been conducted analyzing thermally induced moisture flow, it is still challenging to accurately measure and predict the coupled moisture–heat flow process in unsaturated soils, particularly sandy soils, due to low moisture migration and temperature effects on soil moisture measurement. In this study, a silty sand at various initial moisture contents was tested in a heat cell at a constant temperature gradient. The heat cell was equipped with heat flux, thermocouples, thermal conductivity, and moisture sensors to monitor the thermal and moisture properties under a controlled 1-D temperature gradient. The moisture sensors were calibrated for moisture measurement with the test soil at room temperature; the temperature effect on the soil moisture sensor was also evaluated with the developed heat cell. This research brings new insight to the analysis of unsaturated soil behavior.

2. Materials and Methods

2.1. Soil Heating Test Cell

A fabricated soil heating test cell, originally developed by Kaneza et al. [4], was modified with additional sensors for conducting heating test on the soil. The modified heating cell, which consists of two concentric acrylic cylinders with a height of 10.16 cm and a wall thickness of 0.635 cm, with inside diameters of 8.89 cm and 20.96 cm, respectively, is shown in Figures 1 and 2. Two heat exchanger systems, consisting of copper plates and supporting rings, are placed at the top and bottom of the heating cell. The heat exchanger plates are 29.21 cm in diameter and 2.54 cm thick, with an inside spiral channel of 0.65 cm × 0.65 cm, extending up to a radius of 22.23 cm. The inner and outer diameters of the support rings are 22.23 cm and 29.21 cm, respectively, while the copper plates have a diameter of 29.21 cm and a thickness of 0.24 cm. Two O-rings were used to seal the outer column to the heat exchanger plates, and threaded rods were used to ensure a fixed soil heating system. The tubes, heat exchangers, and rings are made of clear cast acrylic. An illustration of the modified soil cell is provided in Figure 1. Via the inlet and outlet in the heat exchanger plates, warm and cold water is circulated from and to the temperature-controlled water bath (SD07R-20-A11B from PolyScience, Niles, IL, USA) to the heat exchangers. The features of the heat exchanger, including the water bath circulator and the engraved spiral channels with cross sections, are shown in Figure 3. To facilitate effective and uniform heat transfer from both the hot and cold ends, two copper plates are placed between the heat exchanger and the soil sample.

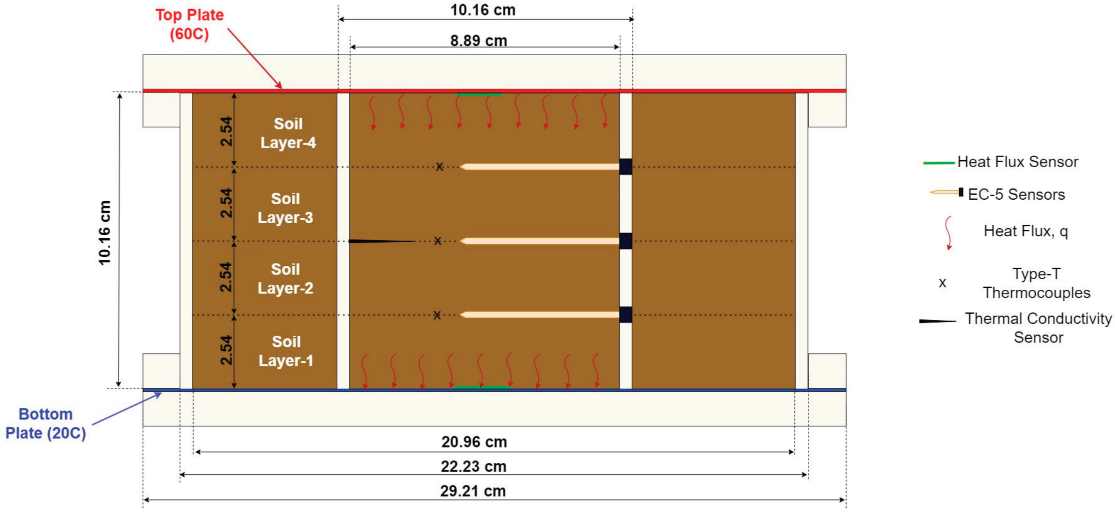

Figure 1. Schematics of the soil heating cell setup.

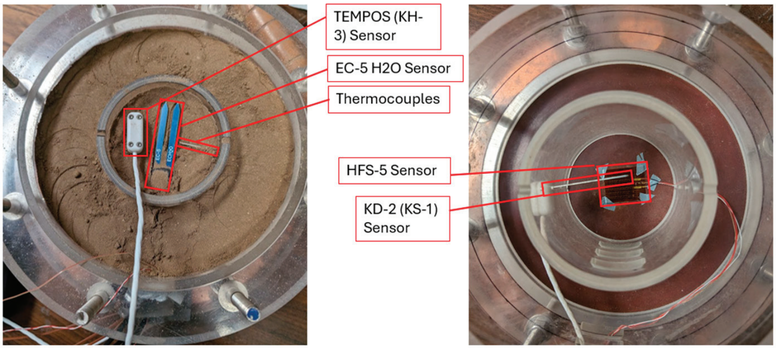

Figure 2. Photos of the heating cell during soil compaction placement.

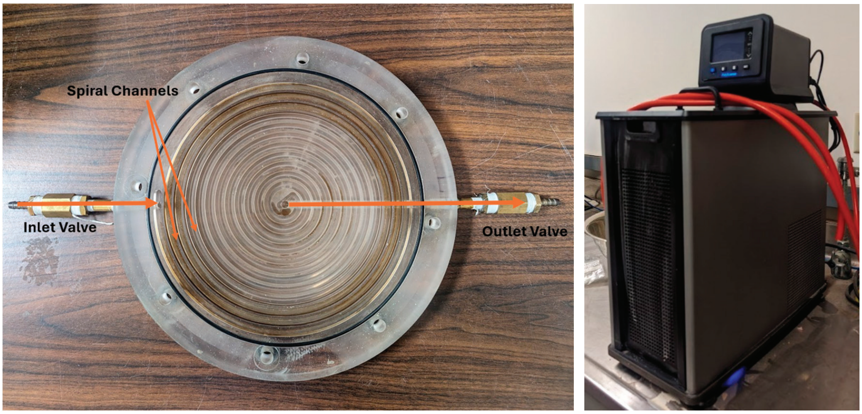

Figure 3. Heat exchanger plate with spiral channels (**Left**) and water circulator (**Right**).

The weight of the moist soil, based on the targeted density and the volume of the apparatus for each soil-layer, was obtained and equally distributed over the whole area of the testing apparatus, followed by the application of gentle compaction. The soil samples at different moisture contents were compacted on four layers of equal thickness for ease of compaction and sensor installation. The heat flux sensors were closely placed at the middle of the top and bottom copper plates and fixed at these position with the aid of tape at four corners of the heat flux sensors. The soil was compacted and slightly raised in the middle section to ensure proper contact of the heat flux sensor with the soil and the top copper plate. The remainder of the sensors were directly embedded in the soil sample; thus, had proper contact with the soil particles.

2.2. Test Sand

The test sand was collected from the riverbank of a bridge construction site in Benbrook, Texas, USA. A series of geotechnical tests were performed on the Benbrook sand, namely the wet sieve analysis [27], dry sieve analysis [28], hydrometer analysis [29], the Atterberg limits tests (liquid limit, LL, and plastic limit, PL [30,31], and the specific gravity (G_s) test [32]. The sieve analyses and hydrometer analyses established the particle size curves of the soil. The resulting soil index properties, including the percentage of particle sizes and specific gravity, are summarized in Table 1. The Benbrook sand is classified as silty sand (SM), with 35% non-plastic fine particles. The maximum dry density was determined to be 18.3 kN/m^3 (1.865 g/cm^3) at an optimum moisture of 12.3% (w/w) using the Standard Proctor Test.

Table 1. Particle size analysis and soil properties.

D_{60} (mm)	D_{30} (mm)	D_{10} (mm)	G_s	F_{200} (%)
0.186	0.064	0.005	2.66	35

The pressure plate and filter paper methods were adopted to measure low and high suction, respectively, to obtain the SWCC curve, followed by the determination of the best curve fitting to find the parameters for the van Genuchten model. The silty sand was compacted at 95% of the maximum dry density (1.865 g/cm^3) and the optimum moisture content (w_{opt}) determined from the standard proctor test to prepare the soil specimen for the proposed lab testing. The particle size distribution and standard proctor compaction curve are presented in Figures 4 and 5 respectively. The best-fit SWCC curve is illustrated in Figure 6. Ultimately, the residual and saturated volumetric moisture content (θ_{res} and θ_s) were estimated, and the van Genuchten's empirical parameters were determined. The residual and saturated volumetric moisture content (θ_r and θ_s) of 0.024 and 0.300 m^3/m^3 were estimated, and the van Genuchten empirical parameters of α = 4.527 m^{-1}, n = 1.246, and m = 0.197 were determined.

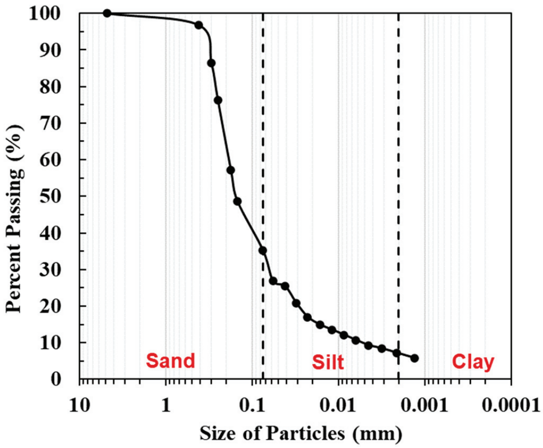

Figure 4. Soil particle size distribution curves of the silty sand.

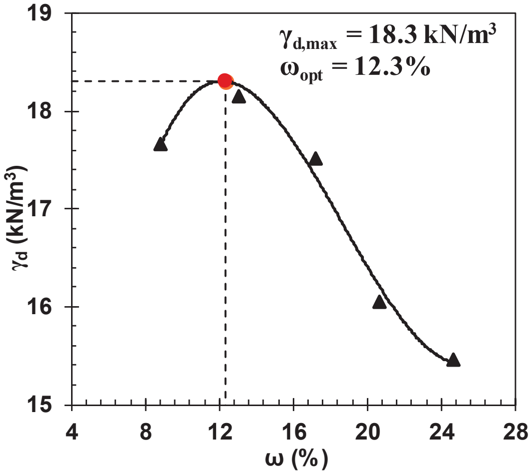

Figure 5. Soil compaction curve.

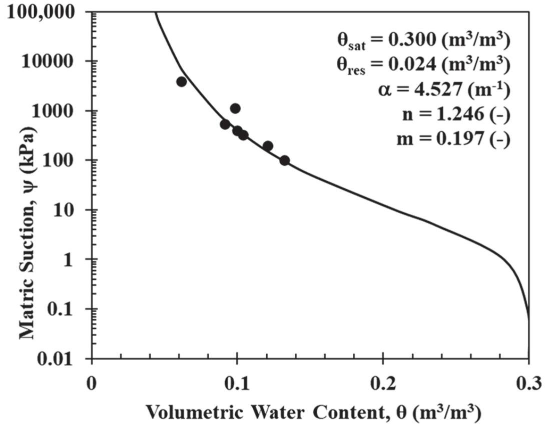

Figure 6. Soil water retention characteristics of the silty sand.

2.3. Sensors and Calibration

Temperature, moisture content, thermal conductivity, and heat flux measurements were obtained during the heating cell test using T-type thermocouples from Omega Engineering Inc., Norwalk, CT, USA, ECH2O EC-5 from Meter Group, Washington, DC, USA, KD2 Pro (KS-1) from Meter Group, Washington, USA, TEMPOS SH-3 Sensor from Meter Group, and HFS-5 from Omega Engineering Inc., Connecticut, USA, respectively. Two Omega HFS heat flux sensors, 34 mm × 27 mm × 0.36 mm, were attached to the top and bottom copper plates, respectively, to measure the temperature of the respective plates and the heat flux. A KD-2 Pro KS-1 single probe sensor, 60 mm in length and 1.27 mm in diameter, was installed at the middle height of the soil, and the thermocouples and moisture sensors were installed at 2.5 cm, 5.0 cm, and 7.5 cm from the bottom heat exchanger plate. The arrangement of the sensors is presented in the schematics and lab-test configuration in Figures 1 and 2, respectively.

The EC-5 sensors, with an overall dimension of 89 mm length, 18 mm wide, and 7 mm thick and a probe length of 50 mm, measure the soil dielectric permittivity of the soil, which is affected by mineralogy, texture, density, salinity, moisture content, and soil temperature [33,34]. Sensor-specific calibration must be performed to obtain the accurate soil moisture for sandy soil, since the effect of soil properties on EC-5 sensor readings is more pronounced [34]. The guidelines provided by Meter Group Inc., Washington, DC, USA have been followed for calibration tests to increase the accuracy of the EC-5 sensors to the ±1–2% range. Three EC-5 sensors were calibrated to the measure volumetric moisture content at room temperature. Soil samples were prepared at the same target gravimetric water content and dry density to calibrate the EC-5 moisture sensor, which was later used in the heating cell test. The VWC readings from the EC-5 sensor were recorded over a 1 h period at the mean room temperature of 21.69 °C, and the average readings were captured for calibration with the configuration as shown in Figure 7. Figure 8 presents the EC-5 sensor average readings vs. the oven-drying moisture content, and Table 2 explains the linear fitting equations for the EC-5 VWC correction at room temperature. The developed calibration equations show a close match between the EC-5 VWC and the correct VWC based on oven drying.

The moisture measurement obtained using the EC-5 capacitance sensor is affected by temperature, as the dielectric permittivity of the soil is also affected by temperature [34,35]. Therefore, the temperature effect on EC-5 was also calibrated using the heat cell. Two heating cell tests were performed to evaluate the effect of temperature on EC-5. In the first heating cell test, the soil was prepared at a VMC of =0.077 m^3/m^3, and three EC-5 sensors were used to capture its moisture readings, as shown in Figure 1. Two thermocouples were placed in the middle of the soil layers to record the soil temperature. The top and bottom heating plates were supplied with hot water of the same temperature and maintained for at least 6 h until a steady-state temperature was reached. The temperature was increased from 20 °C to 55 °C at an increment of 5 °C. The average temperature and VWC reading over an hour during the steady state were used for the calibration. The first temperature calibration test is shown in Figure 9, exhibiting no significant sensor dependency. Therefore, in the second heating cell test, three soil layers with different target moisture contents (0.055 m^3/m^3, 0.172 m^3/m^3, and 0.249 m^3/m^3) were prepared and separated with a plastic sheet between each layer to calibrate the three sensors simultaneously at different moisture contents.

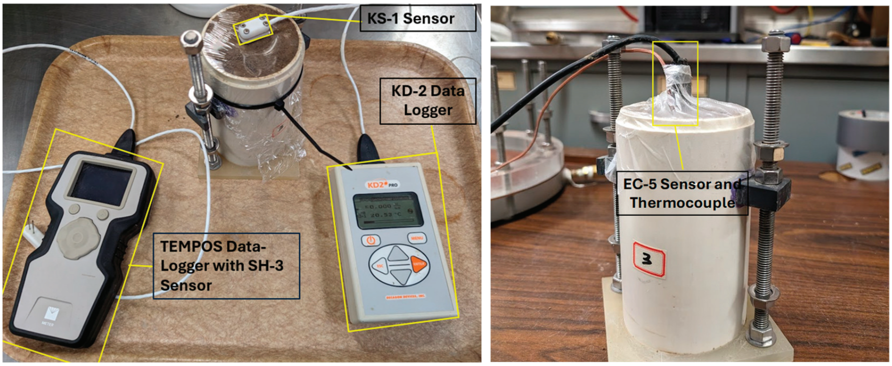

Figure 7. Setup for thermal conductivity (**Left**) and EC-5 VWC (**Right**) measurement at room temperature.

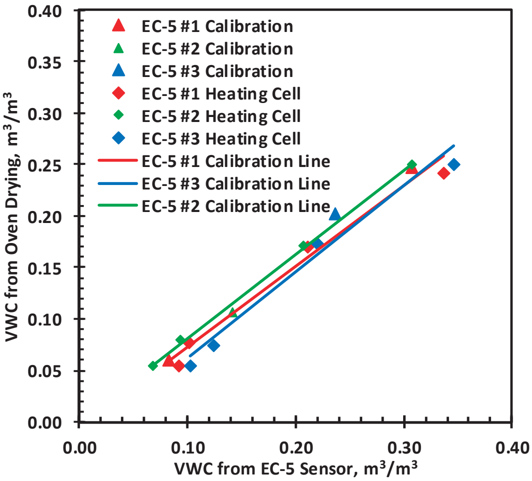

Figure 8. VWC readings for EC-5 sensor.

Table 2. VWC calibration for sensors.

Sensor Identification	Initial VWC Correction Equation	R^2	Equation
EC-5 #1	$VWC_{corrected} = VWC * 0.7501 - 0.0033$	0.9808	Equation (1)
EC-5 #2	$VWC_{corrected} = VWC * 0.8106 + 0.0024$	0.9992	Equation (2)
EC-5 #3	$VWC_{corrected} = VWC * 0.8163 - 0.0239$	0.9839	Equation (3)

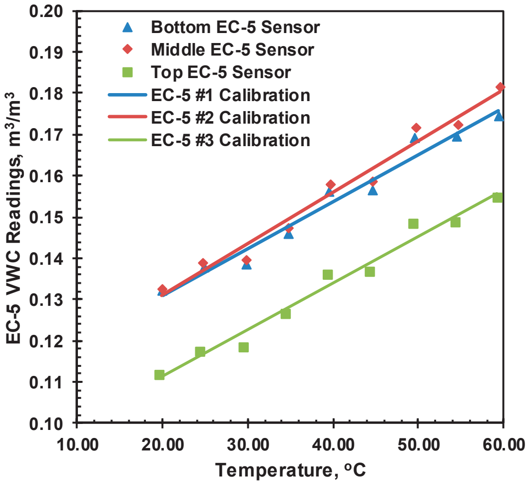

Figure 9. Temperature correction for EC-5 sensor for VWC = 0.077 m^3/m^3, dry density.

Individual temperature corrections for each sensor at each moisture content were proposed; however, the correction slopes for all EC-5 sensors were very close to each other, and single correction slopes were used for all sensors at a specific moisture content. The temperature calibration chart and the table for the same moisture content from different sensors are presented in Figure 9. The calibration results for the remaining volumetric moisture contents are presented in Figure 10, along with the calibration chart in Table 3.

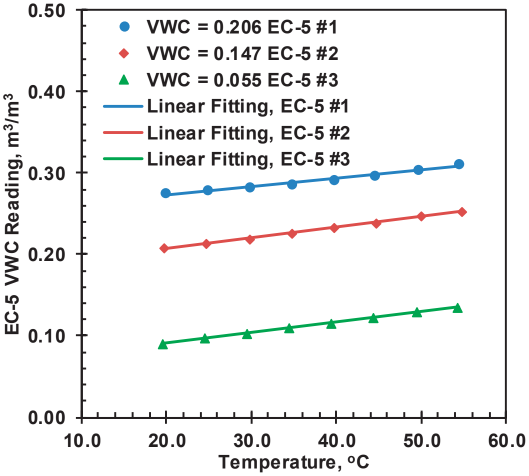

Figure 10. Temperature correction for VWC 0.055, 0.147, and 0.206.

Table 3. Temperature dependency of sensors.

Initial VWC	Sensor Identification	Temperature Correction Equation	R^2	Equation
0.055	EC-5 #3	$VWC_{T_0} = VWC_T - 0.0013(T - T_0)$	1.0000	Equation (4)
0.077	EC-5 #1, 2, 3	$VWC_{T_0} = VWC_T - 0.0012(T - T_0)$	0.9745	Equation (5)
0.147	EC-5 #2	$VWC_{T_0} = VWC_T - 0.0013(T - T_0)$	0.9983	Equation (6)
0.206	EC-5 #1	$VWC_{T_0} = VWC_T - 0.0010(T - T_0)$	0.9877	Equation (7)

2.4. Thermal Conductivity of Compacted Soil Samples

In this study, two thermal conductivity probes, KD-2 Pro (KS-1) and TEMPOS SH-3, were used for thermal conductivity measurement. KS-1 is a single needle sensor with a mean read time of one minute; and SH-3 is a dual-probe sensor, 30 mm in length, with 6 mm spacing, and a 1.3 mm diameter, with a mean read time of two minutes; however, both sensors have the same thermal conductivity measurement range up to 2.0 W/(m·K). The initial thermal conductivity of the soil was measured with a TEMPOS SH-3 sensor. The KS-1 was used to monitor the thermal conductivity in the heating cell. TEMPOS SH-3 was used for the initial thermal conductivity reading of the heating cell soil before the heating test. A noticeable difference was observed between the SH-3 and KS-1 sensors. Therefore, the thermal conductivity of the compacted soil at different moisture contents was measured with both sensors for comparison.

The thermal conductivity of the soil changes with moisture content [36]. A KD-2 Pro (KS-1) was utilized to monitor the thermal conductivity of the compacted soil samples at room temperature, with varying moisture contents and relatively constant dry density. The compacted soil samples were placed in the moisture equilibrium room for more than 12 h to facilitate further moisture equilibrium before measuring the thermal properties. Figures 11 and 12 represents the variation in thermal conductivity measured for the same soil using the KD-2 Pro and TEMPOS sensors, and the 1:1 line in Figure 12 represents the line of perfect agreement for both sensors.

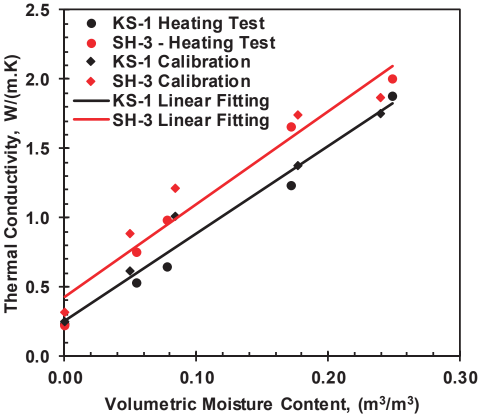

Figure 11. Comparison of the two thermal conductivity sensors.

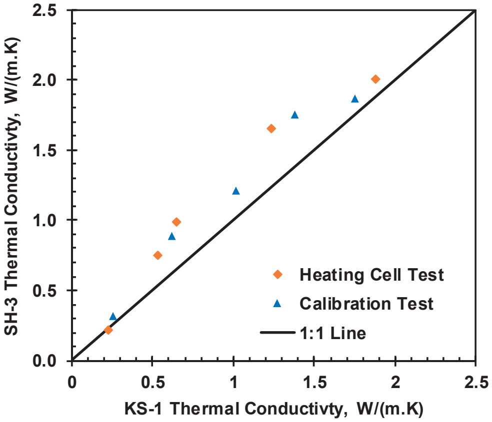

Figure 12. Thermal conductivity comparison of KS-1 and SH-3 sensors.

2.5. Soil Heating Tests

A series of soil heating tests were performed in the heating cell, where the soil was tested under different initial moisture contents at the same temperature gradient to measure the change in soil moisture content, temperature profile, and thermal conductivity of the soil. The test chamber's dual cell design and insulation with fiberglass ensure the 1-D heat transfer of the tested soil specimen in the inner soil column [4]. Three EC-5 sensors and three thermocouples (TCs) were used to measure water content and temperature variations during the heating process. The testing device, its dimensions, and all its main features are detailed in the work of [37], and the measuring devices are illustrated in Figure 1.

Moist soil samples with various target moisture contents and a constant target dry density were prepared and placed in a moisture room for 24 h to achieve moisture equilibrium. A constant target dry density of 1.6 g/cm was selected to represent about 86% of compaction, which can be achieved at all selected moisture content levels. The prepared moist soil sample was compacted in four layers, with each layer thickness measuring 2.54 cm, for sensor installation and uniform compaction. Proper care was taken to compact the soil around the sensors to achieve uniform compaction without damaging the sensors. Five soil samples, including dry soil with a consistent dry density, were prepared, whose geotechnical and thermal properties are presented in Table 4. The compacted soil sample in the heating cell setup was maintained at room temperature for 24 h to facilitate further moisture equilibrium. The temperature-controlled water baths were then initiated, with the temperature of the top and bottom heating plates set to 60 °C and 20 °C, respectively. The volumetric moisture, temperature, thermal conductivity, and heat flux readings were recorded during the heating test until moisture equilibrium was reached. Two steady-state types were encountered during the heating test: temperature equilibrium and moisture equilibrium. The temperature and moisture equilibrium reached the steady state during the heating cell test when the thermocouple and ECH2O EC-5 sensor's respective readings, temperature, and VWC, did not differ by more than 0.1 °C and 0.001 m^3/m^3 at an hourly interval. The test was terminated when the soil sample reached moisture equilibrium during the heating cell test. Table 5 indicates the time required for the test to attain a steady state, the moisture loss at the top, and the initial and steady-state thermal conductivity. Also, the onset of the steady state for the temperature and moisture plots is marked with arrows in the respective plots. The recorded soil heating test data can be found can be found in the Supplementary Materials.

Table 4. 1-D Heating test regarding the silty sand in the heating cell.

Soil	θ_{target} (m^3/m^3)	w_{target} (%)	$\theta_{measured}$ (m^3/m^3)	w_{oven} (%)	ρ_d g/cm^3	**S** (%)	ψ **kPa**	**λ (SH-3) W/(m·K)**
SM_0	0.00	0.00	0.000	0.00	1.555	0.00	-	0.220
SM_3.5	0.056	3.50	0.055	3.51	1.549	13.02	19,000	0.752
SM_4.5	0.080	5.00	0.078	4.69	1.655	20.51	2100	0.984
SM_10.5	0.160	10.00	0.172	10.51	1.634	44.52	28	1.732
SM_15	0.240	15.00	0.249	15.05	1.654	65.82	3	2.007

ρ_d, dry density; λ, thermal conductivity; S, degree of saturation; ψ, matric suction.

Table 5. Heating cell regarding the test steady-state time and the changed soil parameter.

$\theta_{measured}$	**Time to Reach Steady-State, min**		$\Delta\theta_{Top}$, m^3/m^3	**λ (SH-3), W/(m·K)**	
	Temperature	**Moisture**		**Initial**	**Steady-State**
0.000	420	-	-	0.242	0.244
0.055	1260	2100	0.034	0.536	0.442
0.078	1860	2600	0.067	0.748	0.642
0.172	180	1000	0.031	1.323	1.362
0.249	150	750	0.021	1.816	1.879

3. Results and Discussions

3.1. Temperature Response

The recorded temperature variations for specimens of different moisture contents are shown in Figure 13a–e represent the soil with initial volumetric moistures of 0.000, 0.055, 0.078, 0.172, and 0.249 m^3/m^3, respectively. The temperature at the hot end is slightly less than 60 °C, and that of the cold plate is slightly higher than 20 °C, which can be attributed to the temperature loss from the top and bottom copper plates, as well as imperfect contact between the copper plates and the soil column. For all moisture contents, the temperature reached equilibrium after 2000 min. The temperature readings of 0.055 m^3/m^3 and 0.078 m^3/m^3 showed a higher peak, which slowly decreased before reaching thermal equilibrium. The decrease in temperature after the peak is caused by moisture migration induced by the temperature gradient for all moisture soils. However, for the initial volumetric moisture of 0.172 m^3/m^3 and 0.249 m^3/m^3, no significant peak was observed during the heating test, which can be correlated to lower moisture migration. Figure 14 presents the temperature profile at different time steps, including the steady state. The steady-state temperature profile of the dry soil is almost linear, indicating a 1-D temperature gradient, whereas the soil samples with moisture content show concavity in the temperature profile. A linear temperature profile at a 1-D heat transfer indicates the uniform thermal properties of the dry soil. On the contrary, a concaved temperature profile indicates variations in thermal conductivity along the temperature gradient as the result of moisture migration.

3.2. Moisture Movement

The raw EC-5 moisture reading in the heating cell test for the initial moisture content of 0.078 m^3/m^3 is presented in Figure 15 as an example representing all the tested specimens. The initial and final moisture contents at different cross-sections of the soil column represent the equivalent volumetric moisture content measured by the oven-drying method. The EC-5 sensor determines the volumetric water content by measuring the dielectric constant of the soil using capacitance and frequency domain technology at a 70-MHz frequency to minimize salinity and textural effects. The sensor can only determine the liquid unbound water in the soil. The moisture vapor in the pore air has no noticeable impact on the dielectric constant of air (approximately 1) and is, therefore, negligible. The temperature impact on the EC-5 sensor, as shown in Figures 9 and 10, is attributed to the release of bound water from the fine soil particle surfaces [38].

The first sharp rise in EC-5 VWC readings at the initial stage, as shown in Figure 15, directly corresponds to the thermal effect on the EC-5 moisture readings. Thus, the VWC readings were first corrected for temperature based on the raw reading and temperature measured by the thermocouple using Equation (5) for 0.078 m^3/m^3. After the temperature correction, the moisture increase before the peak was close to zero, indicating that the temperature effect was correct, with nearly no moisture movement during this initial heating stage. Secondly, the temperature-corrected moisture content was corrected for the oven-drying moisture content measured before and after the heating cell tests, using correction Equations (1)–(3), depending on the sensor identification. The corrected VWC during the heating cell test is shown in Figure 16b, where the corrected VWC closely matches the final moisture obtained from oven drying. Similar moisture correction steps were applied to the moisture content data for soils of other moisture contents, and the corrected readings, along with initial and final oven drying VWC, are presented in Figure 16.

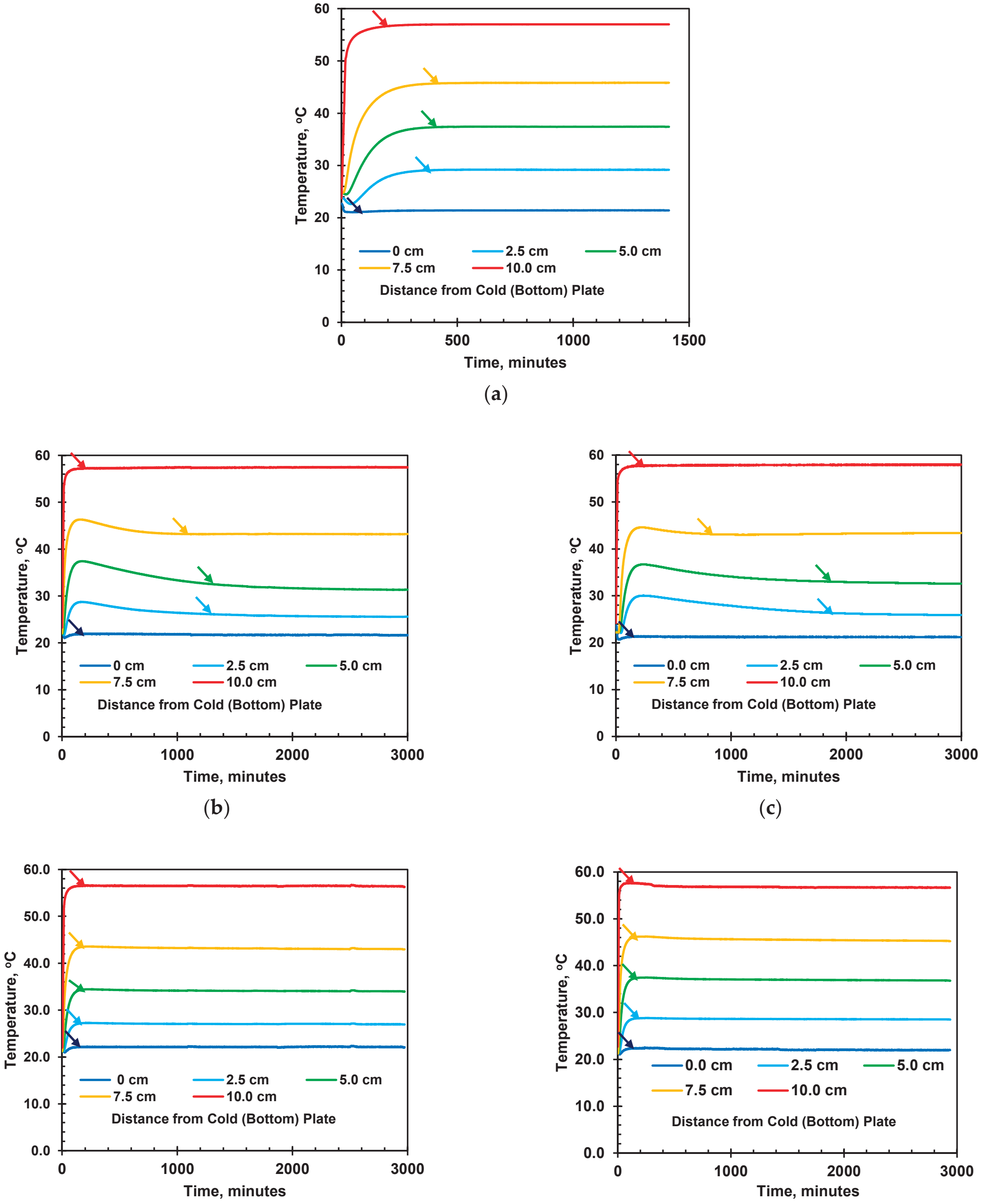

(**a**)

(**b**) (**c**)

(**d**) (**e**)

Figure 13. Temperature variations with time for (**a**) VWC = 0.000, (**b**) VWC = 0.055, (**c**) VWC = 0.078, (**d**) VWC = 0.172, and (**e**) VWC = 0.249 m^3/m^3.

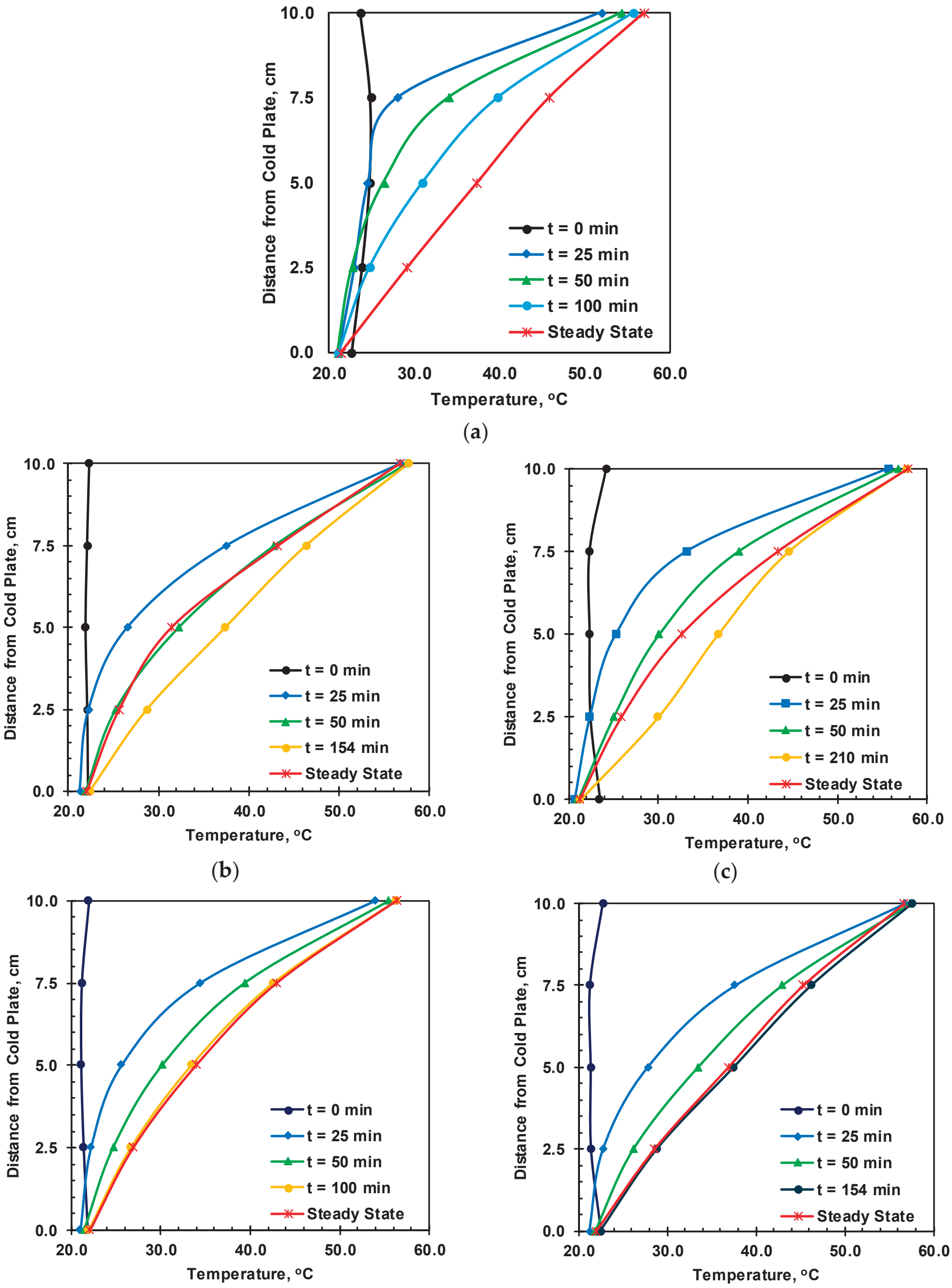

(**a**)

(**b**)

(**c**)

(**d**)

(**e**)

Figure 14. Temperature profile during different stages of the heating test for (**a**) 0.000, (**b**) 0.055, (**c**) 0.078, (**d**) 0.172, and (**e**) 0.249 m^3/m^3.

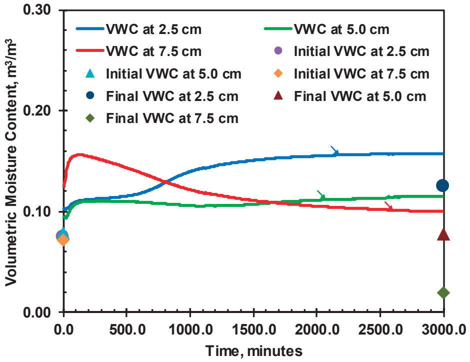

Figure 15. Raw EC-5 VWC data for initial VWC of 0.078 m^3/m^3.

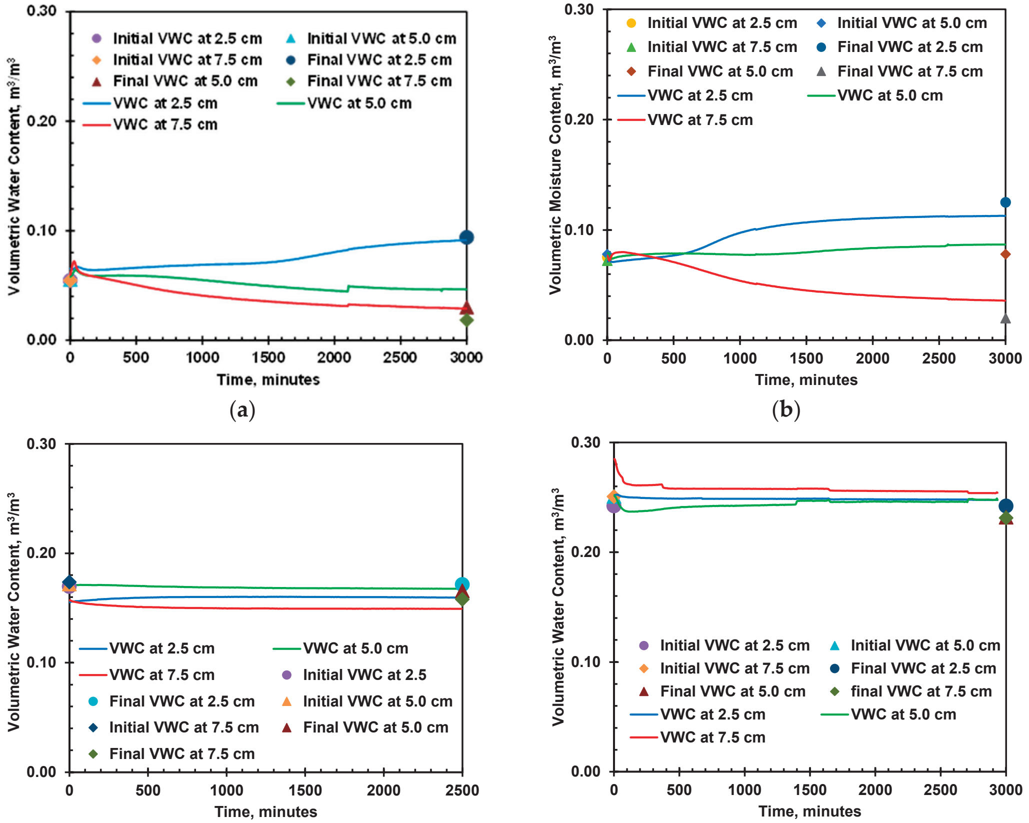

(**a**) (**b**)

(**c**) (**d**)

Figure 16. Soil moisture variation with time for initial VWC of (**a**) 0.055, (**b**) 0.078, (**c**) 0.172, and (**d**) 0.249 m^3/m^3.

The moisture variations in the soil column during the heating cell test for all the tested specimens are shown in Figure 16, which portrays the moisture migration during the heating cell test for initial volumetric moisture contents of 0.055, 0.078, 0.172, and 0.249 m^3/m^3 in (a), (b), (c), and (d), respectively. The graph represents migration of the pore water from hot region to the colder region, i.e., from the top (hot) plate toward the bottom (colder) plate. The initial and final volumetric moisture contents in different layers, based on the oven-drying method, are also presented in the graph. The corrected volumetric moisture content closely matches the volumetric moisture reading from the EC-5 sensor. The soil heating test reached the steady state at 2100, 2600, 1000, and 750 min for 0.055, 0.078, 0.172, and 0.249 m^3/m^3, respectively. Figure 17 shows the moisture profile of the soil column at different depths during steady state. A very large moisture migration has occurred for the initial moisture contents of 0.055 m^3/m^3 and 0.078 m^3/m^3. However, a very small moisture movement has occurred for an initial moisture content of 0.172 m^3/m^3 and 0.249 m^3/m^3. The interaction between temperature and suction gradients can explain the variations in moisture transport. Temperature gradients primarily induce moisture movement through the vapor phase, whereas suction gradients govern liquid-phase flow. Higher soil suction levels intensify the effects of temperature on capillary action, thereby increasing moisture flux. According to Taylor and Cavazza [23], under non-isothermal conditions, moisture predominantly migrates in the vapor phase. Figure 6 depicts the soil–water characteristic curve, illustrating suction levels of 19,000 kPa and 2100 kPa for initial moisture contents of 0.055 m^3/m^3 and 0.078 m^3/m^3, respectively. Conversely, moisture contents of 0.172 m^3/m^3 and 0.249 m^3/m^3 exhibit significantly lower suction levels at 28 kPa and 3 kPa, respectively. This observation shows the dominance of vapor-phase movement in unsaturated soils, where higher initial moisture content correlates with a reduced vapor phase. Consequently, moisture migration is less pronounced under high initial moisture conditions.

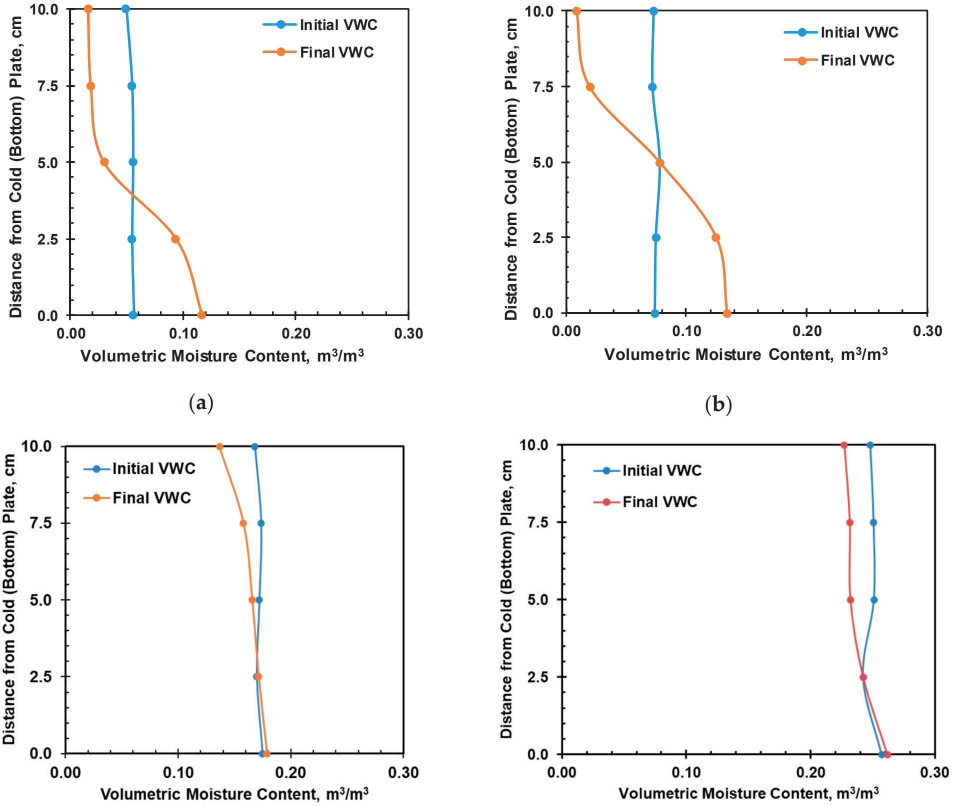

(a)

(b)

(c)

(d)

Figure 17. Initial and steady-state moisture profile from oven drying for initial moisture content of (**a**) 0.055, (**b**) 0.078, (**c**) 0.172, and (**d**) 0.249 m^3/m^3.

3.3. Thermal Critical Moisture Content

The maximum reduction or increase in the volumetric moisture in each tested soil specimen occurred at the top and bottom of the soil column after the moisture equilibrium was reached during the heating test. Figure 18a,b represent the volumetric moisture loss and gain at the hot and cold end of the soil columns at the conclusion of the heating test for each tested initial moisture content. Among all the tested soil specimens, the maximum moisture migration of 0.067 m^3/m^3 and 0.064 m^3/m^3, which occurred at the hot and cold end of the soil column, are observed in the soil specimen with the initial moisture content of 0.078 m^3/m^3, which is the thermal critical moisture content for this sandy soil.

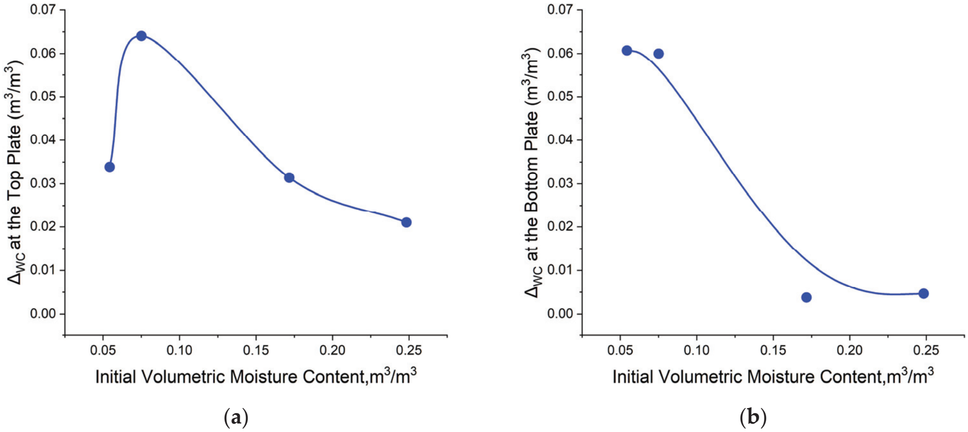

Figure 18. Moisture change at (**a**) 10.0 cm and (**b**) 0.0 cm.

The critical moisture content studied here is the moisture content that marks a decline in the drying or diffusion rate in unsaturated soil. When the initial moisture content is below this critical value, the moisture migration increases with the initial moisture content but then starts to decrease beyond this point. Typically, water retention of soil decreases with rising temperature due to the reduced adhesion of pore water to the soil solid particles, allowing heat-induced pore water movement from the heated source to a cooler region. This soil behavior is due to a decline in the surface tension and viscosity of pore water as the temperature increases. However, once the critical moisture content is surpassed, the behavior of the soil deviates from the conventional patterns. This could be attributed to the transition from partial to full saturation, where capillary forces that are responsible for significant water displacement start to dissipate, restricting moisture movement in saturated soil. This contrast arises because unsaturated soils contain a vapor phase that allows for moisture migration through the temperature gradients, whereas in saturated soils, water is tightly bound to soil particles, limiting its movement. Sandy soils are more sensitive to the critical moisture content due to their water retention limitations and narrow ranges. This explains the notable decrease in the difference in VWC compared to the initial VWC observed at both the top and bottom regions of the soil specimen. It should be noted that a critical moisture content of 0.078 was observed, based on the limited data points presented in Figure 18. Additional tests on soil samples with a gravimetric moisture content between 0.035 and 0.1 can provide a more accurate critical moisture content value.

3.4. Thermal Conductivity and Heat Flux

The soil column is depicted in 1D, as shown in Figure 19. Heat transfer only occurs in the vertical direction, as described in the previous section. Temperature measurements were captured at each layer boundary (T_1, T_2, . . ., T5), and heat flux was measured at the top and bottom surfaces.

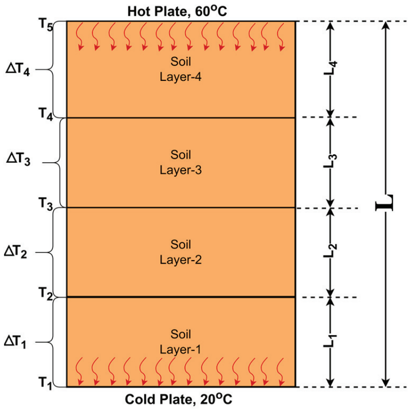

Figure 19. Schematics for the thermal conductivity analyses.

Thermal conductivity (k) for the soil sample with heat flux q, a thickness of layer Δx, represented by L_1, L_2, L_3, and L_4, and a temperature difference of ΔT is obtained by the following equation:

$$k_i = -q \times \frac{L_i}{\Delta T_i} \tag{8}$$

The negative sign represents the heat flux from the higher temperature to the lower temperature zone. The soil column is treated as four layered soils during the heating cell test to calculate the thermal conductivity of the soil layers, and the equivalent thermal conductivity of the entire soil column can be calculated based on the thermal resistance relationship for series connection, which can be given as follows:

$$k_{eq} = (\alpha_1/k_1 + \alpha_2/k_2 + \alpha_3/k_3 + \alpha_4/k_4)^{-1} \tag{9}$$

where, α_i and k_i represents the length ratio (L_i/L) and thermal conductivity of the soil layer, respectively.

The thermal conductivity of each soil layer and the equivalent thermal conductivity of the soil column were determined using Equations (8) and (9), as shown in Figure 20. The graph shows the thermal conductivity measured by the KS-1 sensor at the middle height of the soil column. At the steady state, thermal conductivity increases from top to bottom. Thermal conductivity profiles at the steady state for all soil specimens are plotted in Figure 21. The thermal conductivity measured by the KD-2 (KS-1) sensor, located at the interface of the second and third layers, is also presented in Figure 20. Thermal conductivity revealed by KS-1 first increases to a peak at about 200 min and decreases until reaching a steady state, reflecting the temperature effect on the rise before the peak and moisture migration after the peak, as shown in Figures 13b and 15.

The thermal conductivity and heat flux of different initial moisture soil columns at a steady state during the heating cell test are shown in Figure 21. The thermal conductivity profile at equilibrium for different initial moisture contents is presented in Figure 21a, where the thermal conductivity increases with initial moisture content. Soil thermal conductivity increases with the increased distance to the heat source due to thermally induced moisture migration. Thermal conductivity increases with the increase in temperature for the silty sand at constant moisture; thermal conductivity decreases slightly with the increase in temperature for the dry silty sand. The variation in thermal conductivity along the height of the soil column is due to the combined effect of temperature and moisture content. Figure 21b contrasts the measured thermal conductivity from KS-1 sensor with the soil column's equivalent thermal conductivity calculated based on steady state heat flux and thermocouple readings during heating test for varying initial saturation of the soil sample.

The equivalent thermal conductivity generally shows a close relationship with the thermal conductivity measured by the KS-1 sensor. The measured heat flux increases with the increase in the initial degree of saturation.

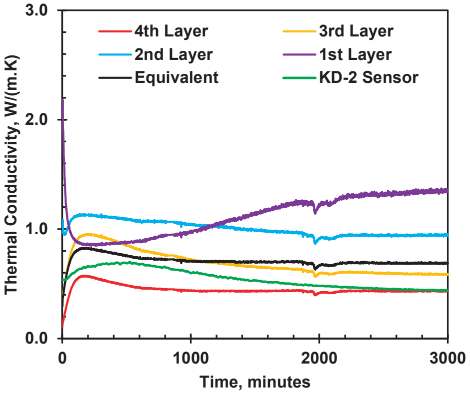

Figure 20. Thermal conductivity at 0.055 m^3/m^3 moisture content during heating test.

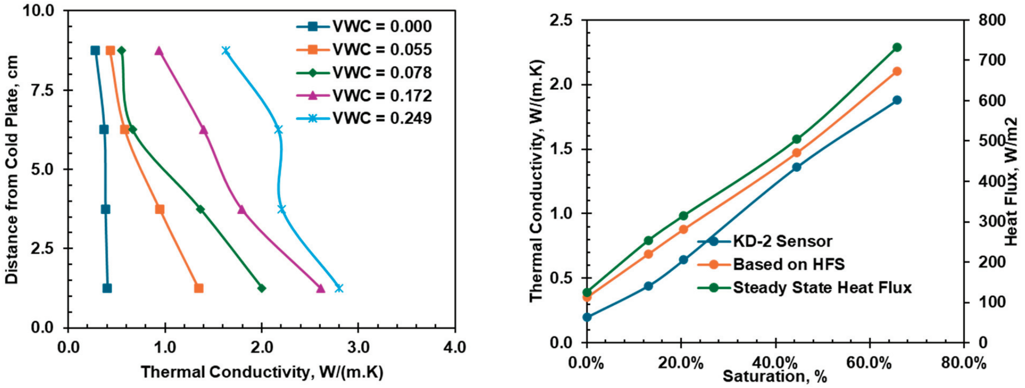

(**a**) (**b**)

Figure 21. (**a**) Thermal conductivity profile at steady state and (**b**) equivalent thermal conductivity and heat flux of the heating cell at steady state.

4. Conclusions

This study investigated the dynamic interactions between temperature, moisture content, and thermal conductivity in an unsaturated silty sand under a constant thermal gradient of 400 °C/m. Using a comprehensive array of sensors—three EC-5 moisture sensors, two heat flux sensors, three thermocouples, and a KS-1 sensor—the experiment continuously monitored key parameters across various sections of the soil column during controlled heating. In addition to real-time measurements during heating, thermal conductivity at room temperature was compared using different sensors to evaluate their reliability and accuracy under varying soil conditions.

The investigations showed significant temperature sensitivity of the EC-5 moisture sensors within the tested range of 20 °C to 60 °C. Therefore, correction of the temperature effects is essential for accurately measuring thermally induced moisture migration during transient states. Moreover, steady-state vertical temperature profiles within moist specimens exhibited concave shapes, indicating variations in thermal conductivity attributed to thermally induced moisture flow dynamics. Specimens with low initial moisture content exhibited notable thermally induced moisture flow due to high suction levels. A critical thermal moisture content of 0.078 m^3/m^3 was identified, marking the point at which a maximum moisture loss of 0.067 m^3/m^3 occurred. Increased suction levels amplified the effect of temperature on moisture migration, leading to more significant vapor-phase movement in soils with lower initial moisture contents. However, beyond a critical moisture content, the soil behavior changed as capillary forces decreased, restricting moisture movement.

Furthermore, it was observed that thermal conductivity increased proportionally along with the distance from the heating source under steady-state conditions, illustrating the impact of moisture migration away from the heat source on soil thermal properties. Under a constant thermal gradient, both the equivalent thermal conductivity and the heat flux of the soil column increased with a higher initial moisture content. Discrepancies observed between equivalent thermal conductivity readings from heat flux measurements and those from the KD-2 Pro (KS-1) sensor suggest influences such as soil compaction heterogeneity, inadequate sensor–soil contact, and temperature-induced variations affecting measurement accuracy.

Supplementary Materials: The following supporting information can be downloaded at: https://www.mdpi.com/article/10.3390/geosciences14080207/s1.

Author Contributions: Conceptualization, X.Y., N.K.; methodology, N.K., X.Y., A.P.; validation, X.Y., N.K., A.P.; formal analysis, A.P., X.Y., N.K.; investigation, N.K., A.P., X.Y.; resources, X.Y., L.R.H.; data curation, A.P., X.Y., N.K.; writing—original draft preparation, N.K., X.Y., A.P.; writing—review and editing, X.Y., L.R.H.; visualization, A.P., X.Y., N.K.; supervision, L.R.H., X.Y.; project administration, X.Y., A.P.; funding acquisition, X.Y. All authors have read and agreed to the published version of the manuscript.

Funding: The funding support from the University of Texas at Arlington to the authors A., Pokhrel, and N.K. is acknowledged.

Data Availability Statement: Data in the text and in the Supplementary Materials.

Conflicts of Interest: The authors declare no conflict of interest.

References

1. Raudkivi, A.J.; van U'u, N. Soil Moisture Movement by Temperature Gradient. *J. Geotech. Engrg. Div.* **1976**, *102*, 1225–1244. [CrossRef]
2. Oh, H. Thermal Resistivity Dry-Out Curves for Thirteen Sandy Soils. Master's Thesis, University of Wisconsin-Madison, Madison, WI, USA, 2014.
3. Oh, H.; Tinjum, J.M. Comparison of Two Laboratory Methods for Measuring Soil Critical Temperature. *Geotech. Test. J.* **2021**, *44*, 339–357. [CrossRef]
4. Kaneza, N.; Wang, X.; Yu, X. Moisture Migration in Unsaturated Sands under Controlled Thsermal Gradient: A Heat Cell Study. *Int. J. Geomech.* **2024**, *24*, 04024060. [CrossRef]
5. Abdel-Hadi, O.N.; Mitchell, J.K. Coupled Heat and Water Flows around Buried Cables. *J. Geotech. Eng. Div.* **1981**, *107*, 1461–1487. [CrossRef]
6. Mitchell, J.K.; Abdel-Hadi, O.N.; Chan, C.K.; Kao, T.C.; McMillan, J.C. *Backfill Materials for Underground Power Cables. Phase II. Backfill Treatments, Heat and Moisture Flow Analyses, and Field Tests. Interim Report*; No. EPRI-EL-1894; Department of Civil Engineering, California University: Berkeley, CA, USA, 1981.
7. Verschaffel-Drefke, C.; Balzer, C.; Schedel, M.; Hinrichsen, V.; Sass, I. Experiment for validation of numerical models of coupled heat and mass transfer around energy cables. *Vadose Zone J.* **2022**, *21*, e20173. [CrossRef]
8. Platts, A.B.; Cameron, D.A.; Ward, J. Improving the performance of Ground Coupled Heat Exchangers in unsaturated soils. *Energy Build.* **2015**, *104*, 323–335. [CrossRef]
9. Akrouch, G.A.; Sánchez, M.; Briaud, J.-L. An experimental, analytical and numerical study on the thermal efficiency of energy piles in unsaturated soils. *Comput. Geotech.* **2016**, *71*, 207–220. [CrossRef]
10. Lahoori, M.; Rosin-Paumier, S.; Jannot, Y.; Boukelia, A.; Masrouri, F. Thermal energy storage in embankments: Investigation of the thermal properties of an unsaturated compacted soil. *E3S Web Conf.* **2020**, *205*, 7011. [CrossRef]
11. McCartney, J.S.; Jafari, N.H.; Hueckel, T.; Sánchez, M.; Vahedifard, F. Emerging Thermal Issues in Geotechnical Engineering. In *Geotechnical Fundamentals for Addressing New World Challenges*; Lu, N., Mitchell, J., Eds.; Springer Series in Geomechanics and Geoengineering; Springer: Cham, Switzerland, 2019. [CrossRef]
12. Faizal, M.; Bouazza, A.; McCartney, J.S. Thermohydraulic Responses of Unsaturated Sand around a Model Energy Pile. *J. Geotech. Geoenviron. Eng.* **2021**, *147*, 04021105. [CrossRef]

13. Pham, T.A.; Sutman, M. A Simplified Method for Bearing-Capacity Analysis of Energy Piles Integrating Temperature-Dependent Model of Soil–Water Characteristic Curve. *J. Geotech. Geoenviron. Eng.* **2023**, *149*, 04023080. [CrossRef]
14. Başer, T.; McCartney, J.S.; Dong, Y.; Lu, N. Evaluation of Coupled Thermal and Hydraulic Relationships Used in Simulation of Thermally-Induced Water Flow in Unsaturated Soils. In *PanAm Unsaturated Soils 2017*; American Society of Civil Engineers: Reston, VA, USA, 2018. [CrossRef]
15. Radhakrishna, H.S.; Lau, K.-C.; Crawford, A.M. Coupled Heat and Moisture Flow through Soils. *J. Geotech. Engrg.* **1984**, *110*, 1766–1784. [CrossRef]
16. Bouyoucos, G.T. Effect of Temperature on the Movement of Water vapor and Capillary Moisture in Soils. *J. Agric. Res.* **1915**, *5*, 141–172.
17. Crawford, C.B. Soil temperature and thermal properties of soils. *Highw. Res. Board Spec. Rep.* **1951**, *2*, 17–41.
18. Gurr, C.G.; Marshall, T.J.; Hutton, J.T. Movement of Water in Soil due to a Temperature Gradient. *Soil Sci.* **1952**, *74*, 335–346. [CrossRef]
19. Jackson, R.D.; Rose, D.A.; Penman, H.L. Circulation of Water in Soil under a Temperature Gradient. *Nature* **1965**, *205*, 314–316. [CrossRef]
20. Kuzmak, J.M.; Sereda, P.J. The Mechanism by which Water Moves through a Porous Material Subjected to a Temperature Gradient, II: Salt Tracer and Streaming Potential to Defect Flow in the Liquid Phase. *Soil Sci.* **1957**, *84*, 419–422. [CrossRef]
21. Kuzmak, J.M.; Sereda, P.J. The Mechanism by Which Water Moves through a Porous Material Subjected to a Temperature Gradient, I: Introduction of a Vapor Gap into a Saturated System. *Soil Sci.* **1957**, *84*, 291–299. [CrossRef]
22. Maclean, D.J.; Gwatkin, P.M. *Moisture Movements Occurring in Soil Due to the Existence of a Temperature Gradient*; Road Research Laboratory: London, UK, 1953.
23. Taylor, S.A.; Cavazza, L. The Movement of Soil Moisture in Response to Temperature Gradients. *Soil Sci. Soc. Am.* **1954**, *18*, 351–358. [CrossRef]
24. Wang, T.-H.; Su, L.-J. Experimental Study on Moisture Migration in Unsaturated Loess under Effect of Temperature. *J. Cold Reg. Eng.* **2010**, *24*, 77–86. [CrossRef]
25. Hedayati-Dezfooli, M. Development of an Experimental Apparatus for Studying High-Temperature Heat and Mass Transfer in Soils. Ph.D. Thesis, Toronto Metropolitan University, Toronto, ON, Canada, 2016.
26. Dang, L. Experimental and Numerical Studies of Heat and Moisture Transfer in Soils at Various Conditions. Ph.D. Thesis, Toronto Metropolitan University, Toronto, ON, Canada, 2017.
27. *ASTM D1140-00*; Standard Test Methods for Amount of Material in Soils Finer than the No. 200 (75-μm) Sieve. American Society for Testing and Materials: West Conshohocken, PA, USA, 2000.
28. *ASTM D6913M-17*; Standard Test Methods for Particle-Size Distribution (Gradation) of Soils Using Sieve Analysis. American Society for Testing and Materials: West Conshohocken, PA, USA, 2017.
29. *ASTM D7928-21*; Standard Test Method for Particle-Size Distribution (Gradation) of Fine-Grained Soils Using the Sedimentation (Hydrometer) Analysis 1. American Society for Testing and Materials: West Conshohocken, PA, USA, 2021.
30. *ASTM D4318-17e1*; Standard Test Methods for Liquid Limit, Plastic Limit, and Plasticity Index of Soils 1. American Society for Testing and Materials: West Conshohocken, PA, USA, 2018. [CrossRef]
31. Texas Department of Transportation. *Test Procedure for Determining Plastic Limit of Soils*; Texas Department of Transportation: Austin, TX, USA, 1999.
32. *ASTM D0854-14*; Standard Test Methods for Specific Gravity of Soil Solids by Water Pycnometer 1. American Society for Testing and Materials: West Conshohocken, PA, USA, 2014. [CrossRef]
33. Campbell, C.S. *Response of the ECH$_2$O Soil Moisture Probe to Variation in Water Content, Soil Type, and Solution Electrical Conductivity*; Application note; Decagon Devices Inc.: Washington, DC, USA, 2001.
34. Cobos, D.; Campbell, C. *Correcting Temperature Sensitivity of ECH$_2$O Soil Moisture Sensors: Application Note*; Decagon Devices: Pullman, WA, USA, 2013.
35. Or, D.; Wraith, J.M. Temperature effects on soil bulk dielectric permittivity measured by time domain reflectometry: A physical model. *Water Resour. Res.* **1999**, *35*, 371–383. [CrossRef]
36. Abu-Hamdeh, N.H.; Reeder, R.C. Soil thermal conductivity effects of density, moisture, salt concentration, and organic matter. *Soil Sci. Soc. Am. J.* **2000**, *64*, 1285–1290. [CrossRef]
37. Kaneza, N. An Experimental Study of Coupled Thermo-Hydro Behavior in Unsaturated Soil. Master's Thesis, University of Texas at Arlington, Arlington, TX, USA, 2020.
38. Wraith, J.M.; Or, D. Temperature effects on soil bulk dielectric permittivity measured by time domain reflectometry: Experimental evidence and hypothesis development. *Water Resour. Res.* **1999**, *35*, 361–369. [CrossRef]

geosciences

MDPI

Article

Effect of Freeze–Thaw and Wetting–Drying Cycles on the Hydraulic Conductivity of Modified Tailings

Longlong Meng [1,2], Liangxiong Xia [1,2], Min Xia [1,2], Shaokai Nie [1,2], Jiakai Chen [1,2], Wenyuan Wang [1,2], Aifang Du [3], Haowen Guo [4] and Bate Bate [1,2,*]

1 Institute of Geotechnical Engineering, College of Civil Engineering and Architecture, Zhejiang University, Hangzhou 310058, China
2 MOE Key Laboratory of Soft Soils and Geoenvironmental Engineering, Zhejiang University, Hangzhou 310058, China
3 BGRIMM Technology Group, Beijing 100160, China
4 Department of Civil and Environmental Engineering, The Hong Kong University of Science and Technology, Kowloon, Hong Kong 999077, China
* Correspondence: batebate@zju.edu.cn

Abstract: Mine tailings have shown viability as the fine–grained layer in a capillary barrier structure for controlling acid mine drainage in a circular economy. Their saturated hydraulic conductivities (k_{sat}) under wetting–drying cycles and freeze–thaw cycles remain unexplored. In this study, modified tailings with a weight ratio of 95:5 (tailings/hydrodesulfurization (HDS) clay from waste–water treatment) and an initial water content of 12% were used. The k_{sat} of specimens was measured after up to 15 wetting–drying cycles, each lasting 24 h, with a drying temperature of 105 °C. The k_{sat} for wetting–drying cycles decreased from 3.9×10^{-6} m/s to 9.5×10^{-7} m/s in the first three cycles and then stabilized in the subsequent wetting–drying cycles (i.e., 5.7×10^{-7} m/s–6.3×10^{-7} m/s). Increased fine particles due to particle breakage are the primary mechanism for the k_{sat} trend. In addition, the migration of fines and their preferential deposition near the pore throat area may also promote this decreasing trend through the shrinking and potentially clogging–up of pore throats. This could be explained by the movement of the meniscus, increased salinity, and, subsequently, the shrinkage of the electrical diffuse layer during the drying cycle. Similar specimens were tested to measure k_{sat} under up to 15 freeze–thaw cycles with temperatures circling between −20 °C and 20 °C at 12 h intervals. Compared to the untreated specimen (i.e., 3.8×10^{-6} m/s), the k_{sat} after three freeze–thaw cycles decreased by 77.6% (i.e., 8.5×10^{-7} m/s) and then remained almost unchanged (i.e., 5.6×10^{-7} m/s–8.9×10^{-7} m/s) in subsequent freeze–thaw cycles. The increased fine grain content (i.e., 3.1%) can be used to explain the decreased k_{sat} trend. Moreover, the migration of fines toward the pore throat area, driven by the advancing and receding of ice lens fronts and subsequent deposition at the pore throat, may also contribute to this trend.

Keywords: freeze–thaw cycles; wetting–drying cycles; hydraulic conductivity; particle breaking

Citation: Meng, L.; Xia, L.; Xia, M.; Nie, S.; Chen, J.; Wang, W.; Du, A.; Guo, H.; Bate, B. Effect of Freeze–Thaw and Wetting–Drying Cycles on the Hydraulic Conductivity of Modified Tailings. *Geosciences* **2024**, *14*, 93. https://doi.org/10.3390/geosciences14040093

Academic Editors: Laureano R. Hoyos, Dunja Perić and Jesus Martinez-Frias

Received: 16 December 2023
Revised: 20 March 2024
Accepted: 22 March 2024
Published: 25 March 2024

1. Introduction

Mine waste rocks containing sulfur (e.g., waste of copper mine), which can significantly damage the environment and human health through acid mine drainage (AMD), are widely distributed and deposited in open–air fields worldwide [1–4]. AMD, produced by the chemical reaction of sulfide minerals with water and oxygen, is characterized by high concentrations of hydrogen ions and dissolved metals [2,3,5]. Recently, capillary barriers (e.g., a two–layer capillary barrier, as shown in Figure 1) have proven effective as a source control method in preventing water infiltration into waste rocks, thereby avoiding AMD [2,4]. The two–layer capillary barrier consists of a fine–grained layer and a coarse–grained layer. According to previous studies [2,4,6–10], the typical thicknesses of the fine–grained layer and coarse–grained layer are 0.4–1.0 m and 0.2–0.5 m, respectively

(Table 1). The mechanism of the capillary barrier is based on the difference in unsaturated hydraulic conductivities (k_{usat}) between fine and coarse particles [2,4,6–10]. As a key state of k_{usat} [7–9], the k_{sat} of the upper fine–grained layer is significantly affected by freeze–thaw cycles and wetting–drying cycles during climatic change [11–13]. Mine tailings are commonly used for the fine–grained layer of the mining capillary barrier (Figure 1) due to their remote location and cost [2,4]. So far, the k_{sat} under wetting–drying cycles and freeze–thaw cycles of mine tailings remain unexplored.

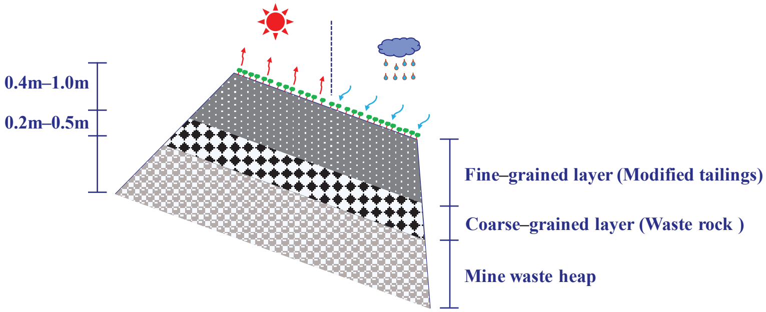

Figure 1. Schematic of the inclined two–layer mining capillary barrier system.

Table 1. Typical thickness of capillary barrier system in the literature.

References	Layer Thickness (m)	
	Fine–Grained Layer	Coarse–Grained Layer
Maqsoud et al. (2011) [6]	0.8	0.2
Harnas et al. (2014) [7]	0.5	0.5
Bossé et al. (2015) [2]	0.5–1.0	0.3
Ng et al. (2016) [8]	0.4	0.2
Zhan et al. (2017) [9]	0.6	0.3
Ng et al. (2022) [10]	0.6	0.4
Xia et al. (2023) [4]	0.6	0.4

Many previous studies have focused on the k_{sat} of soils, which are widely used in engineering practices under freeze–thaw and wetting–drying cycles [14–19]. For the freeze–thaw cycles, Kim and Daniel (1992) [14] studied the effects of compaction degree and water content on the k_{sat} of clay after 0 and 5 freeze–thaw cycles. The results showed that the k_{sat} on both the dry side and wet side of optimum water content after cycles increased by two to six times and one hundred times, respectively, compared to the untreated specimen, primarily due to increased pore volume. Tang and Yan (2015) [17] measured the k_{sat} of soft soil by the one–dimensional freeze–thaw setup. A similar increasing trend in k_{sat} was also observed following freeze–thaw cycles in this study, with differences attributed to an increased average pore diameter caused by aggregation. Shen et al. (2022) [20] compared the microstructure of saline soil with different compaction degrees. Both coarse particle breakage and fine particle aggregation were observed following freeze–thaw cycles, thereby altering the soil structure types. For the wetting–drying cycles, Albrecht and Benson (2001) [15] compared the k_{sat} of eight clayey soils used as clay liners and covers after wetting–drying cycles. An increase in k_{sat} was observed due to the volumetric shrinkage strain induced by the increased clay content. Thyagaraj and Julina (2019) [18] reported that the k_{sat} of compacted clay increased with the rise in pore fluid concentrations and the number of wetting–drying cycles. Xu et al. (2023) [19] studied compacted loess with 15% bentonite after wetting–drying cycles, finding that the k_{sat} initially increased and then stabilized after five cycles. It should be pointed out that the k_{sat} of modified tailings, subjected to freeze–thaw cycles and wetting–drying cycles, has not been deliberately studied, although it is crucial for water infiltration and the barrier effect of the capillary barrier structure.

This study aims to investigate the effects of freeze–thaw cycles and wetting–drying cycles on the k_{sat} of modified tailings. Two series of infiltration tests were conducted to measure k_{sat} on modified tailings after selected cycles. Mineralogical composition and particle size changes in the modified tailings were measured through X–ray diffraction (XRD) and laser particle size analyzer tests to unveil the fundamental mechanisms at the particulate level. More importantly, as a key indicator, the changes in k_{sat} subjected to freeze–thaw cycles and wetting–drying cycles play a crucial role in the k_{usat} of materials. This study could provide guidance for designing and maintaining mining capillary barriers.

2. Experimental Program

Two series of infiltration tests were carried out with modified tailings after several freeze–thaw cycles and wetting–drying cycles. The first series of tests was designed to study the effect of freeze–thaw cycles on the k_{sat} of modified tailings, including five infiltration tests after different freeze–thaw cycles, respectively. Each infiltration test included a specimen with a dry density of 1.50 g/cm^3, corresponding to the 85% degree of compaction. The five specimens prepared for the infiltration tests underwent freeze–thaw cycles of 0, 3, 6, 9, and 15 times, respectively. In the second series of tests, five infiltration tests were conducted on specimens similar to those in the first series, except that wetting–drying cycles were used. More details of the test programs and soil states are summarized in Table 2.

Table 2. Test programs and soil states in each test series.

Series	Test ID	Material Type	Initial State after Specimen Preparation		
			ρ_d (g/cm^3)	w_0 (%)	S_{r0} (%)
I (Infiltration tests after freeze–thaw cycles)	FT–0	Tailings/HDS clay (95:5)	1.50	11.8	39.6
	FT–3	Tailings/HDS clay (95:5)	1.50	11.8	39.6
	FT–6	Tailings/HDS clay (95:5)	1.50	11.8	39.6
	FT–9	Tailings/HDS clay (95:5)	1.50	11.8	39.6
	FT–15	Tailings/HDS clay (95:5)	1.50	11.8	39.6
II (Infiltration tests after wetting–drying cycles)	WD–0	Tailings/HDS clay (95:5)	1.50	11.8	39.6
	WD–3	Tailings/HDS clay (95:5)	1.50	11.8	39.6
	WD–6	Tailings/HDS clay (95:5)	1.50	11.8	39.6
	WD–9	Tailings/HDS clay (95:5)	1.50	11.8	39.6
	WD–15	Tailings/HDS clay (95:5)	1.50	11.8	39.6

Note: w_0, gravimetric water content; ρ_d, dry density; S_{r0}, degree of saturation.

In addition, to interpret the above k_{sat} results, the mineralogical compositions and particle size distributions were analyzed using the X–ray diffraction (XRD) and laser particle size analyzer, respectively. For XRD tests, the mineralogical compositions of the tailings and HDS clay in their natural states and after the 15th cycle were tested and analyzed. For the particle size distributions, similar specimens from the infiltration tests were prepared using oedometer rings. After that, the specimens, subjected to the ordered freeze–thaw cycles and wetting–drying cycles, were tested.

3. Soil Properties and Specimen Preparation

3.1. Soil Properties

Copper mine waste (i.e., tailings and HDS clay) was collected at the Copper Mine of Dexing, Jiangxi province, China (i.e., dotted lines in Figure 2b,c). After being oven–dried and sieved through a 2 mm standard sieve, the modified tailings were prepared by mixing at a weight ratio of 95:5 for tailings to HDS clay. According to the recommended guidelines for the fine–grained layer and coarse–grained layer of capillary cover [4,21,22], this mixing ratio satisfied the criteria for the cooperative properties of the coarse–grained layer (i.e., waste rock), which was proved by Xia et al. (2023) [4]. The particle size distributions of the modified tailings, tailings and HDS clay were measured by the laser particle size analyzer (APA2000, Malvern, UK). The fractions of sand, silt and clay in the modified tailings were 69.2%, 24.2% and 6.6%, respectively (Figure 3). Following ASTM D4318–10 (2010) [23], the liquid and plastic limits of the modified tailings were determined to be 22.4% and 3.8%, respectively. According to the Unified Soil Classification System [24], the modified tailings were classified as silty sand with the group symbol of SM, widely used for the fine–grained soil layer of the capillary cover system [2,4,25]. Furthermore, the maximum dry densities and optimum water content for the modified tailings were 1.73 g/cm^3 and 13.9%, respectively. Details of the physical properties of modified tailings, tailings and HDS clay are summarized in Table 3.

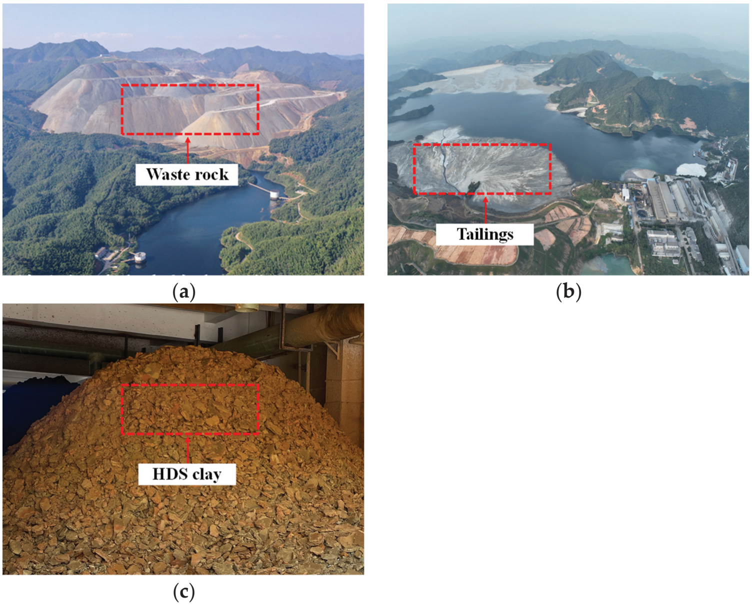

Figure 2. Copper mine waste: (**a**) waste rock; (**b**) tailings; (**c**) HDS clay (photo courtesy of Dr. Qiong Wang).

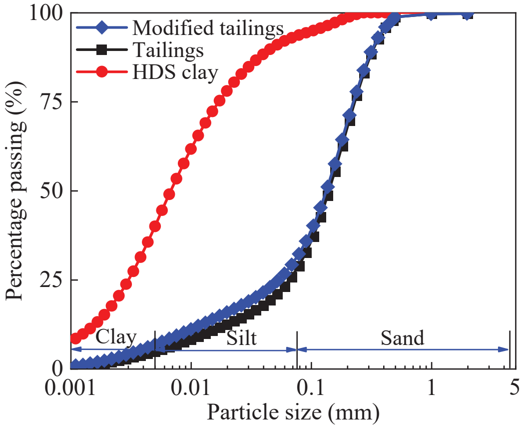

Figure 3. Particle size distributions of mining materials.

Table 3. Physical properties of mining materials.

Parameter	Modified Tailings	Tailings	HDS Clay
pH	6.7	6.7	7.9
Specific gravity	2.71	2.73	2.37
Particle size distribution			
Sand (0.075–4.75 mm, %)	69.2	72.5	6.6
Silt (0.005–0.075 mm, %)	24.2	22.6	53.5
Clay ($\leq$0.005 mm, %)	6.6	4.9	39.9
Atterberg limits			
Liquid limit (%)	22.4	20.5	61.6
Plastic limit (%)	3.8	1.8	40.4
Compaction parameters			
Standard maximum dry density (g/cm^3)	1.73	1.77	1.16
Optimum water content (%)	13.9	12.4	47.5
Unified soil classification			
(ASTM D 2487–11, 2011)	SM	SM	MH

3.2. Specimen Preparations

Ten compacted specimens were prepared for the infiltration tests. Following the compaction parameters of Xia et al. (2023) [4], the target dry density and water content were 1.50 g/cm^3 and 12%, corresponding to 85% of the maximum dry densities and optimum water content, respectively. The de–aired water was evenly sprayed and mixed with the modified tailings to gradually increase its water content to the target value. After approximately 48 h of moisture equalization, the mixture in a sealed plastic bag was compacted into oedometer rings (i.e., 7.2 cm in diameter and 5.2 cm in height) using the static compaction method. The measured dry density and water content for the prepared specimens were 1.50 g/cm^3 and 11.8%, respectively, closely matching the target values.

For the XRD specimens, the powder that passed through a 0.075 mm standard sieve was collected using a McCrone Micronising mill, mixing ethyl alcohol with air–dried materials (i.e., tailings and HDS clay). To reduce the influence of preferred orientation [26], the razor–tamped surface method was used to prepare the specimens. For the particle size distributions, specimens that underwent the wetting–drying and freeze–thaw cycle tests were collected using similar oedometer rings to the infiltration tests. After that, the specimens were oven–dried and passed the 2 mm standard sieve prior to laser particle size analyzer tests.

4. Test Apparatuses and Procedures

4.1. Test Apparatuses

For the freeze–thaw cycle tests, the Thermo Haake ARCTIC AC200 A40 immersion bath circulator with a Neslab RTE740 Digital Plus Replacement (Figure 4) was used to control the temperature and cycle time. The apparatus has a temperature range of −40 °C to 200 °C and includes a 12 L stainless steel immersion bath. The wetting–drying cycles were carried out by the combination of the vacuum saturator (−100–0 kPa) and air–blowing thermostatic oven (20–300 °C) (Figure 4). Considering the saturation degree and extreme conditions in the field (e.g., wildfires), the pore water pressure and drying temperature were limited to −80 kPa and 105 °C in this study, respectively. For the infiltration tests, the variable–head permeameter was used to measure the k_{sat}.

The XRD patterns of tailings and HDS clay were measured with the range from 5 to 60°2θ by the Bruker D8 Advance–X. During the test, the step size and time per step were set at 0.1°2θ and 2 s in this study, respectively. Furthermore, the mineralogical compositions were qualitatively identified by the Jade 9 Program.

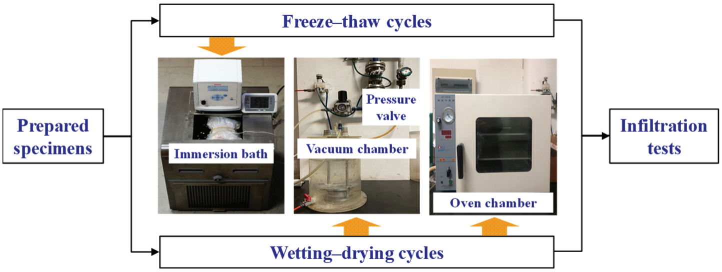

Figure 4. Schematic of the test apparatuses.

4.2. Test Procedures

For the first series of tests, a freeze–thaw cycle is defined as keeping the specimen in the container at 20 °C and −20 °C for 12 h, respectively [27]. The test paths of the freeze–thaw cycle tests are shown in Figure 5a. After specimen preparation, the initial state of the modified tailings is represented by point O. Subsequently, the specimens underwent the ordered freeze–thaw cycles before the infiltration tests (i.e., O→A, O→B, O→C, O→D, O→E), corresponding to 0, 3, 6, 9, and 15 cycles, respectively. After the freeze–thaw cycles, the specimens were saturated by the vacuum saturator for 12 h. The saturated specimens were then carefully placed in the variable–head permeameter. During the k_{sat} tests, the pressure head, water temperature and time were recorded. In addition, the k_{sat} of specimens was tested five times, and the average value was used.

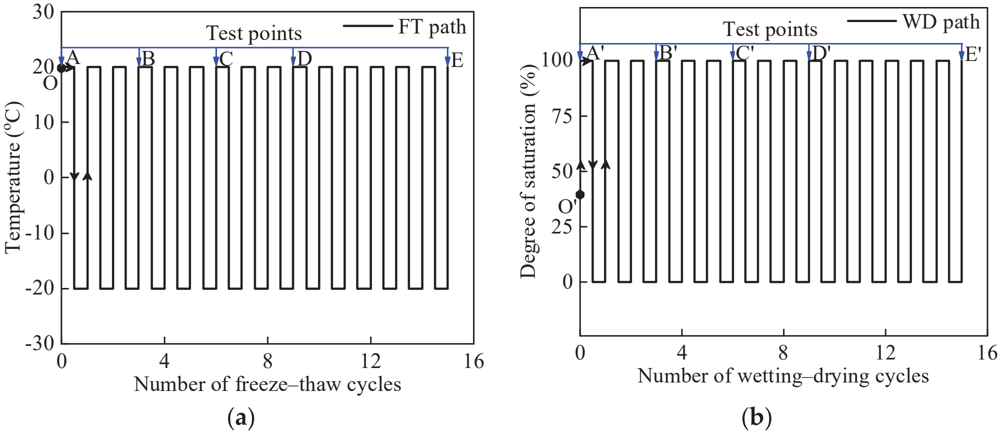

Figure 5. Test paths: (**a**) Freeze–thaw cycles; (**b**) wetting–drying cycles.

For the second series of tests, a wetting–drying cycle is defined as keeping the specimen in the vacuum saturator and the air–blowing thermostatic oven for 12 h, respectively (Figure 5b). The pore water pressure and drying temperature were maintained at −80 kPa and 105 °C, respectively. The initial state (i.e., O′) and the sequenced wetting–drying cycles (i.e., O′→A′, O′→B′, O′→C′, O′→D′, O′→E′) follow a pattern similar to that of the freeze–thaw cycle tests. After the wetting–drying cycle tests, the variable–head permeameter is also utilized to measure the k_{sat} of the modified tailings.

5. Interpretations of Experimental Results

5.1. Mineralogical Analysis of Tailings and HDS Clay

The XRD patterns of tailings and HDS clay are shown in Figure 6. For the tailings, the non–clay minerals, including quartz, albite, and microcline, were identified, while the clay minerals mainly consisted of muscovite and clinochlore. Compared to the mineralogical compositions of the tailings, calcite and kaolinite were additionally identified in the HDS clay as non–clay and clay minerals, respectively. Among the mineral compositions, muscovite, clinochlore, kaolinite and calcite are minerals with low hardness, whereas quartz, albite and microcline have high hardness. According to previous studies [28,29], minerals with low hardness are susceptible to physical weathering (i.e., disintegration and breakage). In addition, based on the studies of Garcia Giménez et al. (2012) [30], Liu et al. (2016) [31], and Yao et al. (2019) [32], muscovite and calcite are predominantly coarse–grained minerals, with the latter also being prone to chemical weathering due to its chemical composition. It is worth noting that the X–ray diffraction patterns after the freeze–thaw and wetting–drying cycles showed similar peaks to those observed before the cycles (i.e., peaks at natural states), thereby owning the identical mineralogical composition. Consequently, only the X–ray diffraction patterns before the cycles are shown in Figure 2. Similar results in soils and rocks (e.g., loess and slate rock) were also observed in previous studies [33–36].

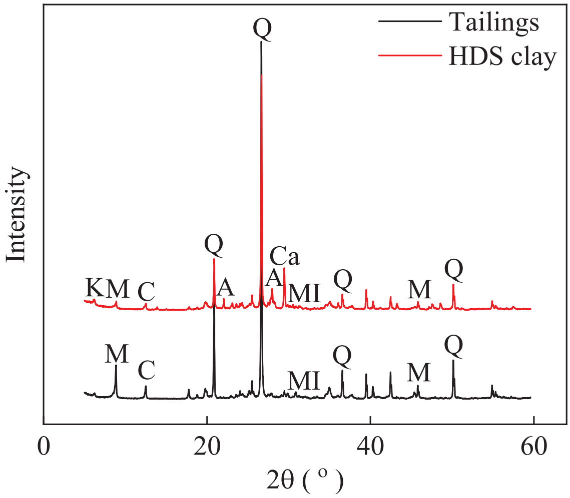

Figure 6. X–ray diffraction patterns of tailings and HDS clay (K: kaolinite; M: muscovite; C: clinochlore; Q: quartz; A: albite; Ca: calcite; and MI: microcline).

5.2. Freeze–Thaw Cycles

The fraction changes in clay, silt and sand in the modified tailings after freeze–thaw cycles are shown in Figure 7. The dotted line is used as reference line for the percentage change in particle groups. With the increasing number of freeze–thaw cycles, the fractions of clay and silt initially increased and then stabilized, while the fraction of sand decreased correspondingly. The fractions of clay and silt rose by 1.7% and 1.1% after three freeze–thaw cycles, corresponding to 25.8% and 4.5% of the initial content, respectively. The fractions of clay and silt both changed to less than ± 0.3% after the third freeze–thaw cycle. As shown in the XRD results, minerals with low hardness and coarse grains (i.e., muscovite and calcite) were likely fractured by the ice lens during the initial three freeze–thaw cycles [29,33]; meanwhile, the ice lenses had little effect on the high–hardness minerals with coarse grains.

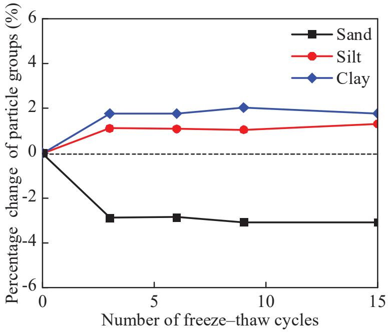

Figure 7. Percentage change in particle groups of modified tailings under freeze–thaw cycles.

The k_{sat} of modified tailings subjected to freeze–thaw cycles is shown in Figure 8. Similar to the changes in sand content, the k_{sat} of modified tailings initially decreased and then stabilized. Compared to the initial k_{sat} (i.e., 3.8×10^{-6} m/s), the value after three freeze–thaw cycles decreased by 77.6% (i.e., 8.5×10^{-7} m/s) and then remained nearly unchanged (i.e., 5.6×10^{-7} m/s–8.9×10^{-7} m/s) in subsequent cycles. This is attributed to the aforementioned increase in the fine grain content (3.1%), which decreases the k_{sat} of porous materials [15,20,37]. In addition, the potential clogging of pore throats by these fines may further decrease k_{sat} [37] (e.g., schematic drawing in Figure 9). During freeze–thaw cycles, the capillary water at the initial state ($S_r = 39.6\%$) is the source for ice phase generation. The growing ice lens can generate surface pressure (100–460 kPa), potentially causing the breakage of coarse grains and the creation of fine grains [20]. Both the redistribution of capillary water during subsequent thawing and the effects of stress (e.g., gravity and electrical forces) contribute to the migration of fine grains toward the pore throat area [20]. Subsequently, deposition and potentially clogging occur near pore throats.

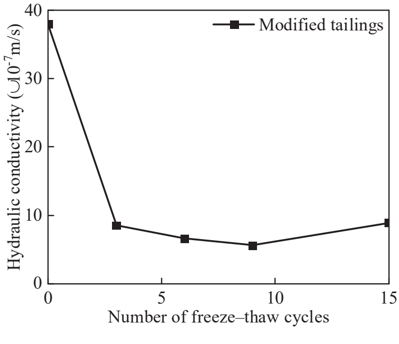

Figure 8. The k_{sat} of modified tailings under freeze–thaw cycles.

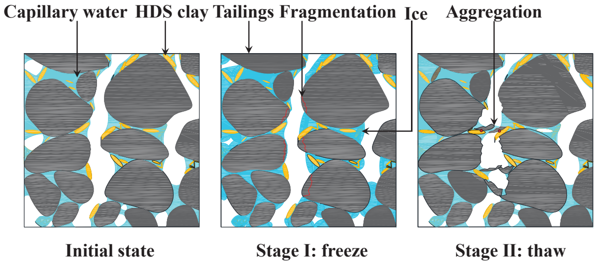

Figure 9. Conceptual illustration of the micro–particles of modified tailings under freeze–thaw cycles.

5.3. Wetting–Drying Cycles

The evolution of clay, silt and sand fractions in the modified tailings during 15 wetting–drying cycles is shown in Figure 10. The dotted line is used as reference line for the percentage change in particle groups. During the initial nine cycles, the fractions of clay and silt increased by 1.8% and 2.1%, respectively, and then stabilized (±0.3%). The sand fraction decreased by (3.9%) during the first nine cycles and then subsequently stabilized (±0.3%). The stabilization of particle group changes induced by wetting–drying cycles took longer than that of freeze–thaw cycles, mainly because of their different physical processes [38]. The fragmentation, denudation, dissolution–reprecipitation and aggregation occur during the wetting–drying cycles [11,31,34], while the freeze–thaw cycle process mainly involves fragmentation [33,39]. Consequently, a more prolonged stabilization process is needed for the wetting–drying cycles.

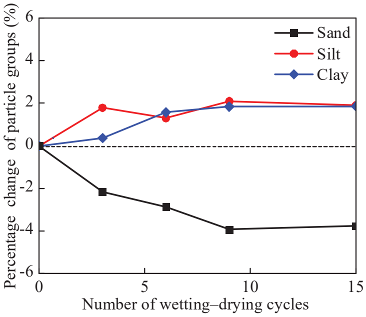

Figure 10. Percentage change in particle groups of modified tailings under wetting–drying cycles.

For the infiltration tests after wetting–drying cycles, the k_{sat} of modified tailings is shown in Figure 11. The k_{sat} decreased from 3.9×10^{-6} m/s to 9.5×10^{-7} m/s after three freeze–thaw cycles, corresponding to a 25.0% drop from the initial value. After that, the k_{sat} stabilized within the range of 5.7×10^{-7} m/s to 6.3×10^{-7} m/s. The increase in fine grain content (3.8%) contributed to the decrease in k_{sat}. In addition, the fines, the preferred deposition of which is near the pore throat area, may further exacerbate this decreasing trend through the narrowing and potential clogging of pore throats [11,13,40–42] (e.g., schematic drawing in Figure 12). During wetting–drying cycles, the fine portion (i.e., clay and silt) of the modified tailings at the initial state is fully hydrated upon saturation. In the subsequent drying process, the fine portion tends to accumulate at water–air interface (meniscus) and migrates with the receding meniscus. During drying, the meniscus preferentially resides near pore throats due to high matric suction (Laplace equation). Meanwhile, the fine portion accumulates and deposits near the pore throat area, driven by favorable attractive interparticle forces, namely van der Waals interactions and the Coulomb attraction. This could be explained by the shrinkage of the electrical diffuse layer at reduced water content and increased salinity.

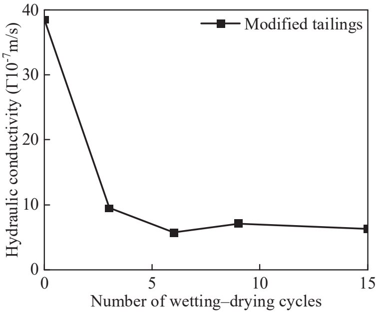

Figure 11. The k_{sat} of modified tailings under wetting–drying cycles.

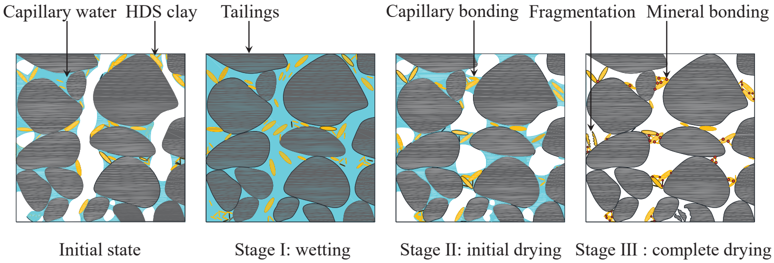

Figure 12. Conceptual illustration of the micro–particles of modified tailings under wetting–drying cycles.

5.4. Future Outlook

In this study, the k_{sat} of modified tailings was tested after specified freeze–thaw cycles and wetting–drying cycles. However, the mechanism of the capillary barrier is based on the k_{usat} of different materials, which is controlled by the water retention behavior and k_{sat}. According to previous studies [43–45], the water retention behaviors of soils (e.g., sand, silt and clay) are significantly changed by freeze–thaw cycles and wetting–drying cycles. Mu et al. (2020) [43] reported that both the air–entry value and degree of hysteresis of loess decreased with the increase in wetting–drying cycles. Zhao et al. (2021) [45] summarized that the water retention capacity of clay was reduced in the low suction range and remained unchanged after the 10th freeze–thaw cycle. It is clear that the parameters of water retention curves (e.g., air–entry value and degree of hysteresis) constitute the other critical aspect of this work. Consequently, the water retention behavior of modified tailings, subjected to the ordered freeze–thaw and wetting–drying cycles, is essential to future work.

6. Conclusions

Two–series infiltration tests, conducted after 0, 3, 6, 9, and 15 freeze–thaw cycles and wetting–drying cycles, were carried out in this study to investigate the k_{sat} of modified tailings. The following conclusions were drawn:

(1) For the changes in particle groups during freeze–thaw cycles, the fractions of clay and silt initially increased by 1.7% and 1.1% after three cycles and then changed by less than ± 0.3% in the subsequent cycles. As shown in the XRD results, this is probably because minerals with low hardness and coarse grains (i.e., muscovite and calcite) were broken by ice lenses during the initial several tests.

(2) Compared to the initial k_{sat} (i.e., 3.8×10^{-6} m/s) of modified tailings, the value after three freeze–thaw cycles decreased by 77.6% and then remained nearly unchanged in subsequent cycles. This is attributed to the increased fine content caused by ice lenses during freeze–thaw cycles. In addition, the potential clogging of pore throats by these fines may further reduce k_{sat} through the redistribution of capillary water upon thawing and the effect of stress (e.g., gravity and electrical forces).

(3) For the wetting–drying cycles, the fraction changes in clay and silt gradually stabilized (i.e., 1.8% and 2.1%) until the ninth wetting–drying cycle. The stabilization of particle group changes induced by wetting–drying cycles took longer than those from freeze–thaw cycles, mainly because of the more complex physical processes of the former.

(4) The k_{sat} first decreased after three wetting–drying cycles (i.e., 3.9×10^{-6} m/s to 9.5×10^{-7} m/s) and then almost remained unchanged. The increase in fines and their preferential deposition near the pore throat area are certainly and possibly the governing mechanisms for this decreasing trend, respectively. Furthermore, the trends of k_{sat} in wetting–drying cycles are similarly observed during freeze–thaw cycles, despite the longer stabilization process of particle groups for the former. This is probably because fragmentation is the main influencing factor for k_{sat}, regardless of the type of cycle.

(5) As another critical aspect of the present study, in further work, the water retention behavior of modified tailings will be investigated under different freeze–thaw cycles and wetting–drying cycles. The parameters of water retention curves (e.g., air–entry value and degree of hysteresis) will be discussed in detail.

Author Contributions: Conceptualization, L.X., L.M. and B.B.; Methodology, L.X., L.M. and B.B.; Validation, L.M.; Investigation, L.X. and L.M.; Data curation, L.M. and M.X.; Writing—original draft, L.M.; Writing—review and editing, L.M., M.X., S.N., J.C., W.W., A.D., H.G. and B.B. All authors have read and agreed to the published version of the manuscript.

Funding: This research was funded by the Ministry of Science and Technology of China, grant number 2019YFC1805002, the National natural Science Foundation of China, grant number 42177118, and the Basic Science Center Program for Multiphase Evolution in Hypergravity of the National Natural Science Foundation of China, grant number 51988101.

Data Availability Statement: Data sharing not applicable.

Acknowledgments: We would like to express our sincere gratitude to the anonymous reviewers for their feedback and constructive criticism, which have greatly improved the quality of this manuscript. We would also like to acknowledge the contributions of all those who have supported this research project.

Conflicts of Interest: The authors declare no conflicts of interest.

References

1. Zhan, G.S.; Keller, J.; Milczarek, M.; Giraudo, J. 11 years of evapotranspiration cover performance at the AA leach pad at Barrick Goldstrike Mines. *Mine Water Environ.* **2014**, *33*, 195. [CrossRef]
2. Bossé, B.; Bussière, B.; Hakkou, R.; Maqsoud, A.; Benzaazoua, M. Field experimental cells to assess hydrogeological behaviour of store-and-release covers made with phosphate mine waste. *Can. Geotech. J.* **2015**, *52*, 1255–1269. [CrossRef]
3. Dong, Y.B.; Liu, Z.R.; Liu, W.; Lin, H. A new organosilane passivation agent prepared at ambient temperatures to inhibit pyrite oxidation for acid mine drainage control. *J. Environ. Manag.* **2022**, *320*, 115835. [CrossRef]
4. Xia, L.X.; Chen, J.K.; Yang, Y.X.; Zhao, H.F.; Zhan, L.T.; Bate, B. Hydrogeochemical Responses of MTMS-Coated Capillary Cover Under Heavy Rainfalls. *Sustainability* **2023**, *15*, 6667. [CrossRef]
5. Chen, J.K.; Xia, L.X.; Yang, Y.X.; Mulati, D.; Zhang, S.; Zhan, L.T.; Chen, Y.M.; Bate, B. Polymer-modified bentonites with low hydraulic conductivity and improved chemical compatibility as barriers for Cu^{2+} containment. *Acta Geotech.* **2023**, *18*, 1629–1649.
6. Maqsoud, A.; Bussiere, B.; Aubertin, M.; Chouteau, M.; Mbonimpa, M. Field investigation of a suction break designed to control slope-induced desaturation in an oxygen barrier. *Can. Geotech. J.* **2022**, *48*, 53–71. [CrossRef]
7. Harnas, F.R.; Rahardjo, H.; Leong, E.C.; Wang, J.Y. Experimental study on dual capillary barrier using recycled asphalt pavement materials. *Can. Geotech. J.* **2014**, *51*, 1165–1177. [CrossRef]
8. Ng, C.W.; Coo, J.L.; Chen, Z.K.; Chen, R. Water infiltration into a new three-layer landfill cover system. *J. Environ. Manag.* **2016**, *142*, 04016007. [CrossRef]
9. Zhan, L.T.; Li, G.Y.; Jiao, W.G.; Wu, T.; Lan, J.W.; Chen, Y.M. Field measurements of water storage capacity in a loess–gravel capillary barrier cover using rainfall simulation tests. *Can. Geotech. J.* **2017**, *54*, 1523–1536. [CrossRef]
10. Ng, C.W.W.; Guo, H.W.; Ni, J.J.; Chen, R.; Xue, Q.; Zhang, Y.M.; Feng, Y.; Chen, Z.K.; Feng, S.; Zhang, Q. Long-term field performance of non-vegetated and vegetated three-layer landfill cover systems using construction waste without geomembrane. *Géotechnique* **2022**, *74*, 155–173. [CrossRef]
11. Mu, Q.Y.; Dong, H.; Liao, H.J.; Zhou, C.; Li, S.B.; Zhang, J.W. Effects of in situ wetting–drying cycles on the mechanical behaviour of an intact loess. *Can. Geotech. J.* **2022**, *59*, 1281–1284. [CrossRef]
12. Azizi, A.; Musso, G.; Jommi, C. Effects of repeated hydraulic loads on microstructure and hydraulic behaviour of a compacted clayey silt. *Can. Geotech. J.* **2020**, *57*, 100–114. [CrossRef]
13. Mu, Q.Y.; Meng, L.L.; Shen, Y.Q.; Zhou, C.; Gu, Z.L. Effects of clay content on the desiccation cracking behavior of low-plasticity soils. *Bull. Eng. Geol. Environ.* **2023**, *82*, 317. [CrossRef]
14. Kim, W.H.; Daniel, D.E. Effects of freezing on hydraulic conductivity of compacted clay. *J. Geotech. Geoenviron.* **1992**, *118*, 1083–1097. [CrossRef]
15. Albrecht, B.A.; Benson, C.H. Effect of desiccation on compacted natural clays. *J. Geotech. Geoenviron.* **2001**, *127*, 67–75. [CrossRef]
16. Ng, C.W.W.; Wong, H.N.; Tse, Y.M.; Pappin, J.W.; Sun, H.W.; Millis, S.W.; Leung, A.K. A field study of stress-dependent soil–water characteristic curves and permeability of a saprolitic slope in Hong Kong. *Geotechnique* **2011**, *61*, 511–521. [CrossRef]
17. Tang, Y.Q.; Yan, J.J. Effect of freeze–thaw on hydraulic conductivity and microstructure of soft soil in Shanghai area. *Environ. Earth Sci.* **2015**, *73*, 7679–7690. [CrossRef]

18. Thyagaraj, T.; Julina, M. Effect of pore fluid and wet-dry cycles on structure and hydraulic conductivity of clay. *Geotech. Lett.* **2019**, *9*, 348–354. [CrossRef]
19. Xu, J.; Li, Y.F.; Wang, B.; Wang, Z.F.; Wang, S.H. Microstructure and Permeability of Bentonite-Modified Loess after Wetting–Drying Cycles. *Int. J. Geomech.* **2023**, *23*, 04023052. [CrossRef]
20. Shen, J.J.; Wang, Q.; Chen, Y.T.; Han, Y.; Zhang, X.D.; Liu, Y.W. Evolution process of the microstructure of saline soil with different compaction degrees during freeze-thaw cycles. *Eng. Geol.* **2022**, *304*, 106699. [CrossRef]
21. Smesrud, J.K.; Selker, J.S. Effect of soil-particle size contrast on capillary barrier performance. *J. Geotech. Geoenviron. Eng.* **2001**, *127*, 885–888. [CrossRef]
22. Parent, S.-É.; Cabral, A. Design of inclined covers with capillary barrier effect. *Geotech. Geol. Eng.* **2006**, *24*, 689–710. [CrossRef]
23. *ASTM D4318-10*; Standard Test Methods for Liquid Limit, Plastic Limit, and Plasticity Index of Soils. ASTM International: West Conshohocken, PA, USA, 2010.
24. *ASTM D2487-11*; Standard Practice for Classification of Soils for Engineering Purposes (Unified Soil Classification System). ASTM International: West Conshohocken, PA, USA, 2011.
25. Scarfone, R.; Wheeler, S.J.; Smith, C.C. Numerical modelling of the application of capillary barrier systems for prevention of rainfall-induced slope instability. *Acta Geotech.* **2023**, *18*, 355–378. [CrossRef]
26. Zhang, G.P.; Germaine, J.T.; Martin, R.T.; Whittle, A.J. A simple sample-mounting method for random powder X-ray diffraction. *Clays Clay Miner.* **2003**, *51*, 218–225. [CrossRef]
27. Liu, Z.Y.; Liu, J.K.; Li, X.; Fang, J.H. Experimental study on the volume and strength change of an unsaturated silty clay upon freezing. *Cold Reg. Sci. Technol.* **2019**, *157*, 1–12. [CrossRef]
28. Villagran, X.S.; Poch, R.M. A new form of needle-fiber calcite produced by physical weathering of shells. *Geoderma* **2014**, *213*, 173–177. [CrossRef]
29. Wild, B.; Daval, D.; Guyot, F.; Knauss, K.G.; Pollet-Villard, M.; Imfeld, G. pH dependent control of feldspar dissolution rate by altered surface layers. *Chem. Geol.* **2016**, *442*, 148–159. [CrossRef]
30. Garcia Giménez, R.; Vigil de la Villa, R.; González Martín, J.A. Characterization of loess in central Spain: A microstructural study. *Environ. Earth Sci.* **2012**, *65*, 2125–2137. [CrossRef]
31. Liu, Z.; Liu, F.Y.; Ma, F.L.; Wang, M.; Bai, X.H.; Zheng, Y.L.; Yin, H.; Zhang, G.P. Collapsibility, composition, and microstructure of loess in China. *Can. Geotech. J.* **2016**, *53*, 673–686. [CrossRef]
32. Yao, G.; Zang, H.; Wang, J.X.; Wu, P.; Qiu, J.; Lyu, X.J. Effect of mechanical activation on the pozzolanic activity of muscovite. *Clays Clay Miner.* **2019**, *67*, 209–216. [CrossRef]
33. Zhai, J.B.; Zhang, Z.; Melnikov, A.; Zhang, M.Y.; Yang, L.Z.; Jin, D.D. Experimental study on the effect of freeze-thaw cycles on the mineral particle fragmentation and aggregation with different soil types. *Minerals* **2021**, *11*, 913. [CrossRef]
34. Zhou, W.; Cheng, J.L.; Zhang, G.K.; Li, H.B.; Cheng, Y.G.; Ma, G.; Ji, X. Effects of wetting–drying cycles on the breakage characteristics of slate rock grains. *Rock Mech. Rock Eng.* **2021**, *54*, 6323–6337. [CrossRef]
35. Li, X.M.; Di, S.J.; Shi, L.; Zhang, Y.; Huang, P.; Mu, Q.Y. Effects of in-situ drying–wetting cycles on the stress-dependent water retention behavior of intact loess. *Adv. Civ. Eng.* **2023**, *2023*, 2994986. [CrossRef]
36. Khanlari, G.; Abdilor, Y. Influence of wet–dry, freeze–thaw, and heat–cool cycles on the physical and mechanical properties of Upper Red sandstones in central Iran. *Bull. Eng. Geol. Environ.* **2015**, *74*, 1287–1300. [CrossRef]
37. Xu, W.S.; Li, K.S.; Chen, L.X.; Kong, W.H.; Liu, C.X. The impacts of freeze–thaw cycles on saturated hydraulic conductivity and microstructure of saline–alkali soils. *Sci. Rep.* **2021**, *11*, 18655. [CrossRef] [PubMed]
38. Zhao, G.T.; Han, Z.; Zou, W.L.; Wang, X.Q. Evolution of mechanical behaviours of an expansive soil during drying-wetting, freeze–thaw, and drying-wetting-freeze–thaw cycles. *Bull. Eng. Geol. Environ.* **2021**, *80*, 8109–8121. [CrossRef]
39. Eigenbrod, K.D. Effects of cyclic freezing and thawing on volume changes and permeabilities of soft fine-gained soils. *Can. Geotech. J.* **1996**, *33*, 529–537. [CrossRef]
40. Liu, P.F.; Nie, S.K.; Wang, W.Y.; Zhang, S.; Bate, B.; Chen, Y. CFD-DEM study on transport and retention behaviors of nZVI-clay colloids in porous media. *J. Hazard. Mater.* **2023**, *465*, 133048. [CrossRef]
41. Valdes, J.R.; Santamarina, J.C. Particle clogging in radial flow: Microscale mechanisms. *Spe J.* **2006**, *11*, 193–198. [CrossRef]
42. Liu, Q.; Zhao, B.; Santamarina, J.C. Particle migration and clogging in porous media: A convergent flow microfluidics study. *J. Geophys. Res. Solid Earth.* **2019**, *124*, 9495–9504. [CrossRef]
43. Mu, Q.Y.; Dong, H.; Liao, H.J.; Dang, Y.J.; Zhou, C. Water-retention curves of loess under wetting−drying cycles. *Geotech. Lett.* **2020**, *10*, 135–140. [CrossRef]
44. Ng, C.W.W.; Peprah-Manu, D. Pore structure effects on the water retention behaviour of a compacted silty sand soil subjected to drying-wetting cycles. *Eng. Geol.* **2023**, *313*, 106963. [CrossRef]
45. Zhao, G.T.; Zou, W.L.; Han, Z.; Wang, D.X.; Wang, X.Q. Evolution of soil-water and shrinkage characteristics of an expansive clay during freeze-thaw and drying-wetting cycles. *Cold Reg. Sci. Technol.* **2021**, *186*, 103275. [CrossRef]

geosciences

Article

Conceptual and Applied Aspects of Water Retention Tests on Tailings Using Columns

Fernando A. M. Marinho [1,*], Yuri Corrêa [1], Rosiane Soares [2], Inácio Diniz Carvalho [2] and João Paulo de Sousa Silva [2]

[1] Institute of Geoscience, University of São Paulo, São Paulo 05508-080, SP, Brazil; yuricorrea@usp.br
[2] Laboratório de Geotecnia da Vale (LGV), Santa Luzia 33040-900, MG, Brazil; rosiane.soares@vale.com (R.S.); inacio.carvalho@vale.com (I.D.C.); joao.paulo.silva@vale.com (J.P.d.S.S.)
* Correspondence: fmarinho@usp.br; Tel.: +55-1130914200

Abstract: The water retention capacity of porous materials is crucial in various geotechnical and environmental engineering applications such as slope stability analysis, landfill management, and mining operations. Filtered tailings stacks are considered an alternative to traditional tailings dams. Nevertheless, the mechanical behaviour and stability of the material under different water content conditions are of concern because these stacks can reach considerable heights. The water behaviour in these structures is poorly understood, particularly the effects of the water content on the stability and potential for liquefaction of the stacks. This study aims to investigate the water retention and flow characteristics of compacted iron ore tailings in high columns to better understand their hydromechanical behaviour. The research used 5 m high columns filled with iron ore tailings from the Quadrilátero Ferrífero region in Minas Gerais, Brazil. The columns were prepared in layers, compacted, and instrumented with moisture content sensors and suction sensors to monitor the water movement during various stages of saturation, drainage, infiltration, and evaporation. The sensors provided consistent data and revealed that the tailings exhibited high drainage capacity. The moisture content and suction profiles were effectively established over time and revealed the dynamic water retention behaviour. The comparison of the data with the theoretical soil water retention curve (SWRC) demonstrated a good correlation which indicates that there was no hysteresis in the material response. The study concludes that the column setup effectively captures the water retention and flow characteristics of compacted tailings and provides valuable insights for the hydromechanical analysis of filtered tailings stacks. These findings can significantly help improve numerical models, calibrate material parameters, and contribute to the safer and more efficient management of tailings storage facilities.

Keywords: water retention; iron ore tailing; columns; unsaturated material instrumentation

Citation: Marinho, F.A.M.; Corrêa, Y.; Soares, R.; Carvalho, I.D.; de Sousa Silva, J.P. Conceptual and Applied Aspects of Water Retention Tests on Tailings Using Columns. *Geosciences* **2024**, *14*, 273. https://doi.org/10.3390/geosciences14100273

Academic Editors: Dominic E. L. Ong, Dunja Perić and Laureano R. Hoyos

Received: 22 June 2024
Revised: 24 September 2024
Accepted: 8 October 2024
Published: 16 October 2024

1. Introduction

Particulate porous materials naturally occur and are also generated through mining processes to yield ore and tailings. These materials play a consistent role in infrastructure projects that involve road cuts or embankments for dams and levees. Ores are typically transported by ships or other means, whereas tailings are deposited in dams or stored in expansive "dry" stacks. However, the inherent porous nature of these materials and the variable yet consistent presence of water pose various challenges to the safety of associated activities. The risks include potential hazards to ships during ore transport, stability concerns for dams, large tailings embankments, and other structural elements.

The eventual saturation of the material can lead to failure. When porous materials become saturated with water, their stability and mechanical properties can be significantly compromised, which may result in liquefaction. Rico et al. [1], Santamarina et al. [2], Koppe [3], Nwigwe and Minami [4], and other studies underscore these risks due to the saturation of those materials. The present study stands out for its originality by addressing a highly relevant and contemporary topic, which has been the subject of limited experimental research. Given the increasing attention to environmental and geotechnical challenges related to filtered tailings and their hydraulic behaviour, this research fills a crucial gap by providing experimental insights that are often overlooked in the literature. The scarcity of empirical studies on re-saturation processes and moisture redistribution in tailings stacks makes this work particularly significant for both academic and practical applications. This work presents experimental data from monitored columns and elucidates the fundamental concepts of water retention in porous media, particularly in ores and tailings. To illustrate this process, Figure 1a depicts an open-air ore pile undergoing drainage with water retention at the time of deposition. The accompanying graph in Figure 1b illustrates the drainage process over time, which tends toward equilibrium in the absence of atmospheric interference.

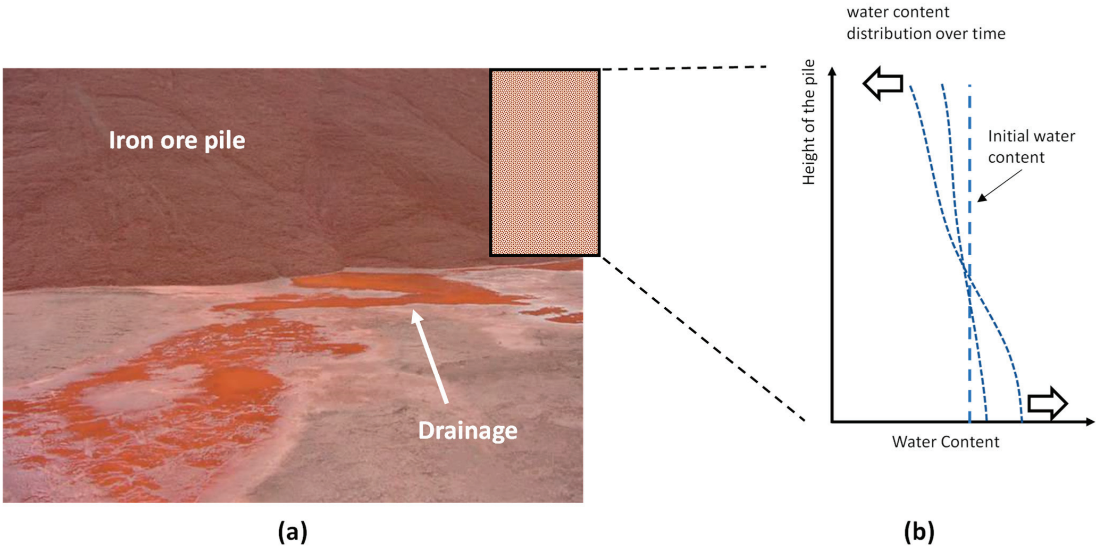

Figure 1. (**a**) Ore-pile draining and (**b**) water content variation along the pile.

In the example in Figure 1, the boundary condition at the base enables unrestricted drainage, which ensures that there is no water accumulation at the base.

2. Water Retention in Porous Media

The definitions in this section may appear elementary but can help the reader become familiar with certain characteristics of porous materials and understand the relationships among three phases in these materials: solid (particle), liquid (typically water), and gas (typically air). Table 1 shows useful definitions to interpret data related to water retention in porous media [5,6].

Water Retention Curves in Porous Media

The water retention capacity of particulate porous materials is influenced by factors such as the particle size distribution, mineralogy, and material structure. Of particular significance is the fine content, which is composed of particles smaller than 0.074 mm, or more specifically, the clay content, which consists of particles smaller than 2 µm. Capillarity and adsorption forces in clayey materials are primarily responsible for water retention phenomena. Figure 2 shows the relationship between water content and proportion of fines in the material or its plasticity. Figure 2 illustrates two phenomena that drive the variations in moisture content. When initially saturated, water in the soil is primarily drained by gravitational forces, which are counteracted by capillary and physicochemical forces, until it reaches the field capacity. Below this water content threshold, water is only depleted through evapotranspiration (solar and/or vegetation) energy. Beyond the threshold, the water content cannot be reduced under typical environmental conditions. Importantly, materials without fines may struggle to retain water, which limits their ability to maintain a high degree of saturation.

Table 1. Interrelations of indices involving water.

$\theta=$	$G_s(1-n)w$	$\frac{h_w}{h_T}$	nS
$w=$	$\frac{\theta}{G_s(1-n)}$	$\frac{h_w \rho_w}{h_T \rho_d}$	$\frac{n\left(\frac{G_s \rho_w}{\rho_d}-1\right)}{\theta G_s}$
$S=$	$\frac{wG_s}{e}$	$\frac{h_w}{nh_T}$	$\frac{\theta}{n}$
$h_w=$	θh_T	nSh_T	$\frac{wh_T \rho_d}{\rho_w}$

Where θ is the volumetric water content ($\frac{\text{Volumeofwater}}{\text{Totalvolumeofthesoil}}$). $\rho_d = \frac{M_s}{V_t}$ is the dry density. $G_s = \frac{\rho_s}{\rho_w}$ is the specific gravity. S is the degree of saturation. n is the porosity. e is the void ratio. h_w is the water height at a specific soil depth. h_T is the soil height.

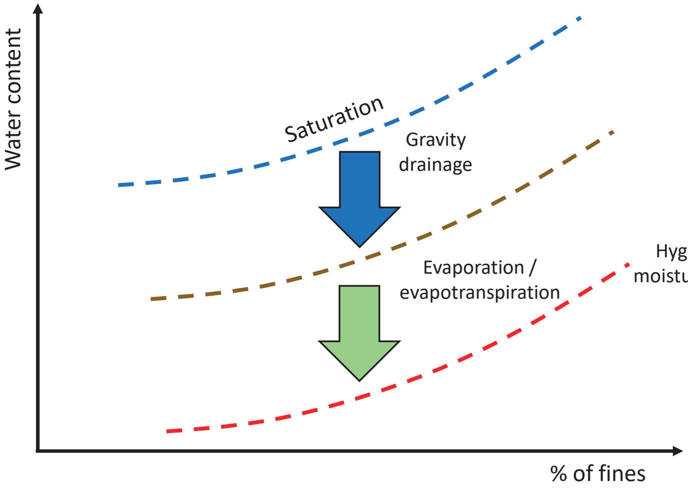

Figure 2. Relationship between the water content and the amount of fines.

The water distribution in a soil profile is influenced by the material properties and boundary conditions of the problem, particularly the potential presence of free water, such as a water table or another system of free water access. Figure 3a shows a soil column with free water access at the base, which simulates a water table. Water has energy above the water level, which is called free energy [7]. The variation in this energy is numerically equal to the variation in hydrostatic pressure when the density of water is 1 g/cm^3. Therefore, we can express it as follows:

$$\Delta f = -h\rho g = suction \tag{1}$$

Thus, suction represents the negative pressure of water in the pores. Figure 3b shows the distribution of free energy along a soil column under constant temperature. The rate of change in free energy along the column remains constant and equal to $-$g. Regardless of the soil type, the distribution of free energy resembles that in Figure 3b when the system is in equilibrium. Figure 3c schematically depicts the change in water content with the column height. This relationship depends on the granulometric, mineralogical, and structural characteristics of the soil.

The profile of the free energy, i.e., the suction profile, can be coupled with the determination of the water content and volume variation of the material to establish the water retention curve. This curve relates the amount of water (w, θ, S) to suction. However, this condition holds true only under equilibrium situations where there is no flow of water or water vapour in the system. Under field conditions, the suction profile is as shown in Figure 4a, which illustrates potential seasonal variations that correlate with the fluctuations in water content (Figure 4b). Figure 4 highlights the active zone, which is the depth at which atmospheric environmental factors can influence the suction profile [8,9].

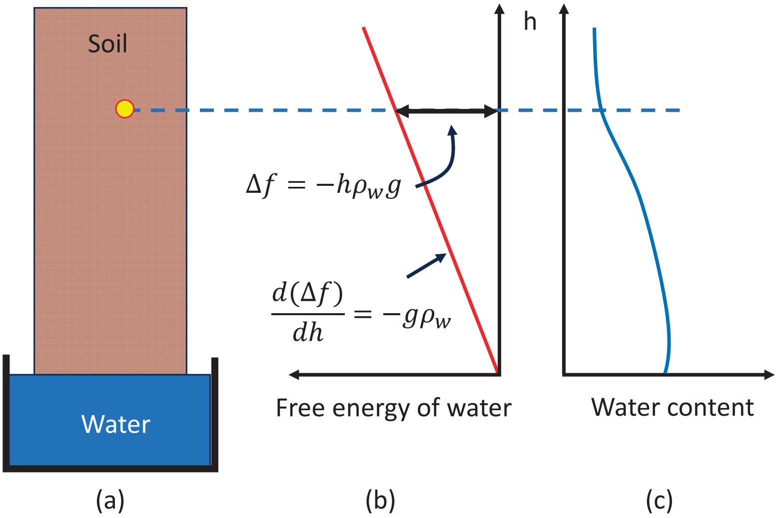

Figure 3. (**a**) Physical model of a soil column with a water table (**b**) Relationships between free energy and water content in a soil column with a fixed water table (**c**) Variation of water content with the height of the column (modified from Edlefesen and Anderson [7]).

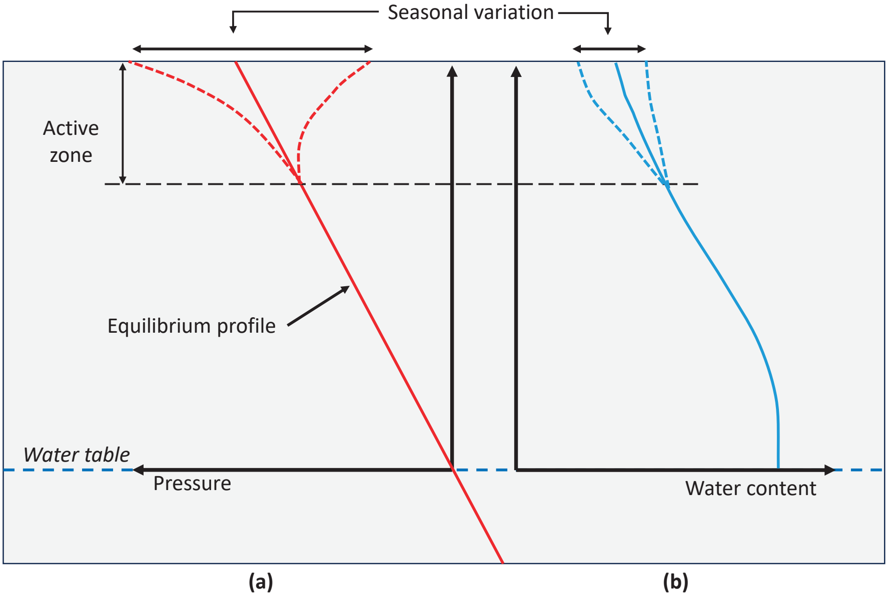

Figure 4. Suction (**a**) and water content (**b**) profile in the field.

3. Use of Columns for Water Retention Studies

Some authors consider Philippe de La Hire the inventor of the lysimeter [10–12]. De La Hire pioneered the use of columns to study the hydrogeological behaviour of soils in 1703 and constructed a series of lysimeters that resembled columns of different heights. After 15 years of experimentation in the field, he concluded that the infiltration was minimal, and vegetation played an important role in the interaction with the atmosphere. Buckingham [13] could be one of the first to use soil columns in the laboratory to study the water retention and movement in soils. Recently, other researchers successfully used this technique [14–20]. As described, a column of porous material in contact with free water at the base reaches suction equilibrium and forms a hydrostatic profile. Combined with water content data, this profile enables the determination of the water retention curve. This method is suitable for materials that do not significantly change in volume when subjected to changes in water content. However, it has limitations such as the column height and equilibrium time. Columns taller than 3 m make the assembly procedure difficult and require a robust support structure. The 3 m high columns enable equilibrium suctions of up to 30 kPa, according to Equation (8). Nevertheless, there are cases where longer columns should be used, such as investigations of the active zone. The use of longer columns is particularly interesting for fine materials, such as tailings used for dry stack piles.

Figure 5 presents the concepts in obtaining the retention curve through columns. Columns in general and short columns in particular provide an accurate method to obtain the soil water retention curve (SWRC), especially for lower suction levels. Figure 5a shows a photo of a straightforward column system made of PVC segments. Figure 5b shows an example of a column with a constant water level system at the base. There is a cap at the top of the column to prevent evaporation while maintaining atmospheric pressure. Figure 5c shows the resulting equilibrium profile.

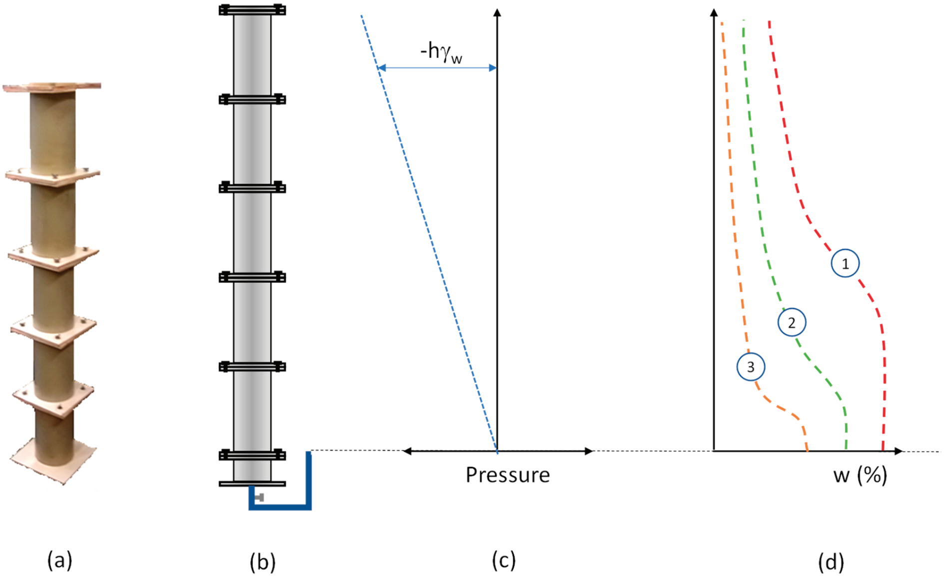

Figure 5. (**a**) PVC column; (**b**) schematic drawing of the column; (**c**) suction equilibrium profile, and (**d**) water content profiles for three hypothetical materials [15].

The equilibrium profile is associated with the water content profiles in Figure 5d, which represent three hypothetical materials. The preparation procedure involves defining the assembly density in the column and the column saturation process. The density depends on the simulated conditions and is associated with the specific problem in investigation.

Saturation is achieved from bottom to top by raising the water level through a hose connected to the base. After saturation has been complete, the drainage process can be initiated, and the loss of water from the base is monitored over time to determine the time at which equilibrium is attained. In this scenario, the columns lack instruments, and the SWRC determination involves dismantling the columns. The water content is measured along the column and then correlated with the column height.

4. Columns with Compacted Iron Ore Tailings

As previously mentioned, the construction of filtered tailings stacks has been an alternative to deposition in dams. These stacks generally have large heights of hundreds of metres [21]. The considerable heights of these stacks raise doubts regarding the stress state of the material, mechanical behaviour of the material, and the effects of the presence of water and eventual saturation of the compacted material on this behaviour. Understanding the behaviour of water in the stacks in terms of infiltration, evaporation, and capillary rise is crucial to avoid creating additional conditions for liquefaction.

Columns filled with compacted tailings are an alternative to simulate the one-dimensional behaviour of tailings piles in terms of water flow and water retention. This work used columns with a height of 5 m, which enables the understanding of water behaviour associated with precipitation and evaporation to evaluate the active zone. The columns were instrumented to better characterize the water movement process.

4.1. Materials

The material in the studied column was an iron ore tailing from the Quadrilátero Ferrífero in the state of Minas Gerais, Brazil. According to the unified classification, it is a nonplastic silt composed of approximately 90% quartz and 10% iron oxide. Table 2 presents the characteristics of the material.

Table 2. General characteristics of the material.

Specific gravity (G_s)	3.35
Fine sand	13.5%
Silt	83.7%
% < 2 mm	2.8%
w_{opt}	11.9%
θ_{opt}	24.0%
S_{opt}	58.0%
Maximum dry unit weight	19.77 kN/m^3
θ_{sat}	40%
Quartz	89.1%
Fe_2O_3	10.9%

w_{opt}—Optimum gravimetric water content; θ_{opt}—Optimum volumetric water content; θ_{sat}—Saturated volumetric water content.

Figure 6 shows the SWRC of the material. The data were obtained via different techniques, as presented by Jesus et al. [22].

The parameters of the curve were adopted based on Van Genuchten's [23] equation (Equation (2)) and are shown in Table 3.

$$\theta(suction) = \theta_r + \frac{\theta_{sat} - \theta_{residual}}{[1 + \alpha \times suction^n]^m} \quad (2)$$

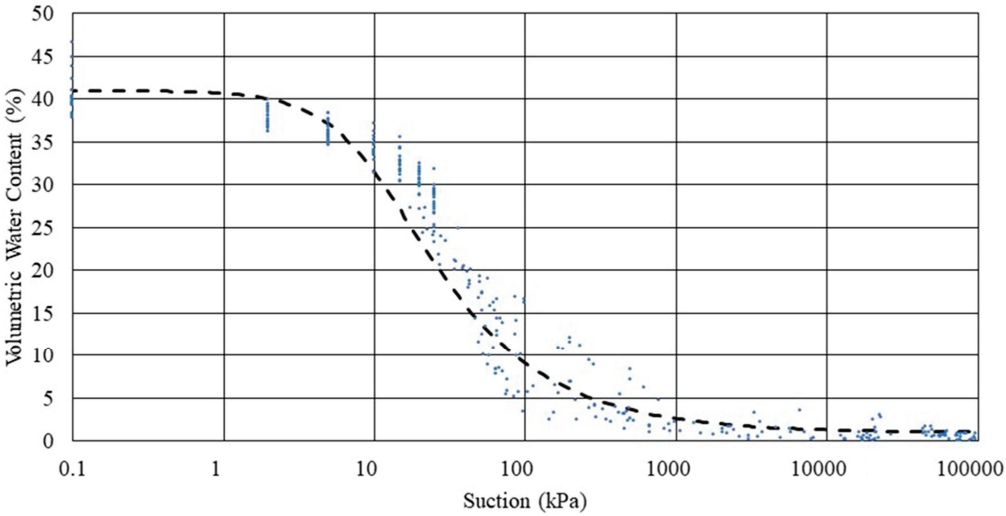

Figure 6. Soil water retention curve of the material (data from Jesus et al. [22]).

Table 3. Parameters for the SWRC.

a	0.09
n	1.7
m = (1-1/n)	0.4118
θ_{sat}	41%
$\theta_{residual}$	1%

4.2. Column Assembly

To connect the segments, a rubber ring was used to seal them and prevent leakage, and bolts with nuts were employed. The material for the segments was PEAD. The segments were produced with a diameter of 25 cm and in two heights: 30 cm and 20 cm, as shown in Figure 7.

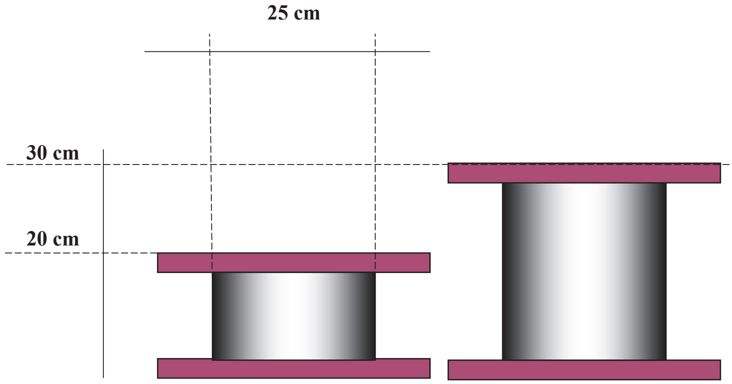

Figure 7. Segments for the column assembly.

It was necessary to build a steel structure to install the columns. The steel structure was supported and fixed on a concrete slab. The first segment of the column was the drainage system, which consisted of gravel and medium sand. Figure 8 shows the drain preparation, where one can observe the valve that controls the water outlet.

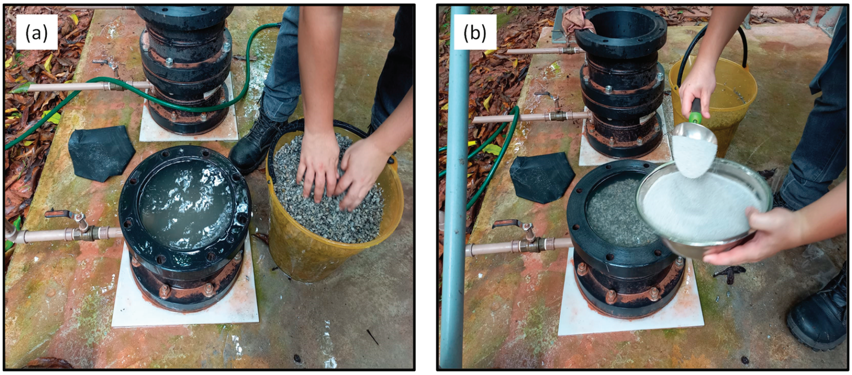

Figure 8. Drainage segment. Placement of (**a**) gravel and (**b**) medium sand.

The segments following the drain were compacted according to the characteristics of the material. The main objective was to simulate the field conditions. Water content sensors and suction sensors were installed in some of the segments, as described in detail below.

4.3. Material Preparation and Compaction

Considering the required volume of material to assemble the column, it was necessary to prepare the material for each individual segment. The material was prepared at the optimal water content of the standard Proctor test. The tailings required the addition of water to reach the water content that was used. The material was homogenized using a mortar mixer. After the mixing process had been completed, the material was placed in plastic bags for equilibration for at least 24 h. After this period, the material was divided into six parts for six layers of compaction for each segment. The amount of material per segment was calculated to achieve the maximal dry density specified by the standard Proctor test, which is the target density for the field. Figure 9a illustrates the compaction procedure, and Figure 9b presents the column with six compacted segments. The tailings were compacted with an average water content of 11.11% and a degree of saturation of 52%.

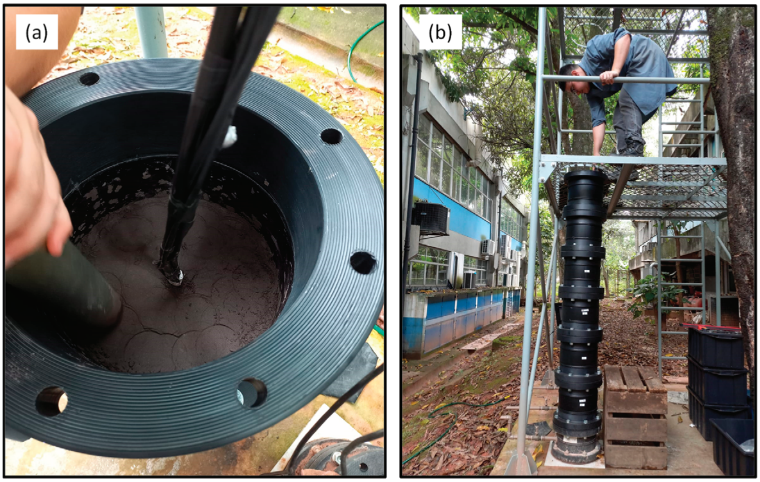

Figure 9. Column compaction process: (**a**) Details of the compaction; (**b**) column at its 6th segment.

4.4. Sensors and Installation

In the columns in this paper, two types of sensors were used: Teros 12 (for the water content) and Teros 21 (for the suction). Considering the operating principle of the Teros 12 sensor and characteristics of the material, a specific calibration for the tailings was applied [24]. Equation (3) was adopted to obtain the volumetric water content.

$$\theta = 0.037 \times (\mathrm{RAW}) - 75.354 \tag{3}$$

where RAW denotes the raw data readings provided by the sensors.

Similar to all sensors designed to measure the volumetric water content, Teros 12 requires very careful installation. Significant variations in contact between rods and soil can compromise the measurement. In the present study, where the material was compacted over the sensor, this aspect was less relevant.

The Teros 21 sensor is composed of two ceramics with a designed pore distribution to cover a range of possible water content values, which can be inferred through the measured dielectric constant of the ceramic. When installed, the sensor (its porous ceramic) reaches equilibrium with the surrounding material, and suction is inferred through calibration (the SWRC of the ceramic). In this type of sensor, installation is not critical, and the sensor can be simply buried in the material to be measured. For Teros 21, there is no material influence, although there may be effects associated with the water characteristics.

Figure 10a shows a photo of a completed column. Figure 10b shows the positions of the sensors to measure the water content (WC) and suction (TE), which were installed along the column.

The sensors were installed as close to the centre of the segments as possible and on opposite sides. The wiring was adjusted to run through the centre of the column to the top. All sensors had a data logger to record the data at specific time intervals.

The temperature measurements revealed a variation of approximately 2 °C between the top and the base during the compaction and saturation phases. After drainage, the temperature variation between the top and the base was approximately 1 °C. Throughout the entire experiment, the biweekly average variation was 7 °C.

An important aspect of the analysis of the obtained data is the response time or time lag of the sensors. The time lag of a sensor is the delay between the occurrence of an event (e.g., a change in water content or suction) and the response of the sensor to that change. In other words, it is the time for a sensor to detect the change at the point where the sensor is installed. This delay depends on factors associated with the sensor design and operating principle. The response time of a sensor can determine whether it can be used for safety alerts. Generally, water content sensors such as Teros 12 can measure changes as soon as they occur and only depend on the measurement capacity of the data acquisition system. Meanwhile, Teros 21 requires the ceramic to reach equilibrium with the surrounding material before accurately measuring the suction, so there is a time lag.

With this understanding, the water content sensor is expected to respond before the suction sensor, which results in a time lag between the two types of sensors. Assuming that the water content sensor instantaneously responds, it is relatively straightforward to identify the time lag of the suction sensor in the same region. However, measuring this response time (time lag) depends on the sensitivity of the sensors to the imposed changes. Therefore, the obtained time lag is approximate.

In anticipation of one of the analyses performed with the data from the column, Figure 11 presents the measured volumetric water content and suction during specific intervals of four events (not necessarily the end or the beginning of the events): the saturation process (Figure 11a), drainage process (Figure 11b), infiltration process (Figure 11c), and evaporation process (Figure 11d). In the graphs, the response time of the suction sensor to the events was not entirely clear, although some events suggest an immediate response. The values in the data sheets indicate that the response time of the suction sensor was approximately 5 min. This value was used to correct the suction values over time. Immediately after the installation of the moisture sensor, the soil/sensor system may take more than an hour to reach equilibrium. After this period, the responses follow the estimated response time of 5 min. The sensor response depends on the shape of the SWRC. Sections of the curve can be more or less sensitive to different variables.

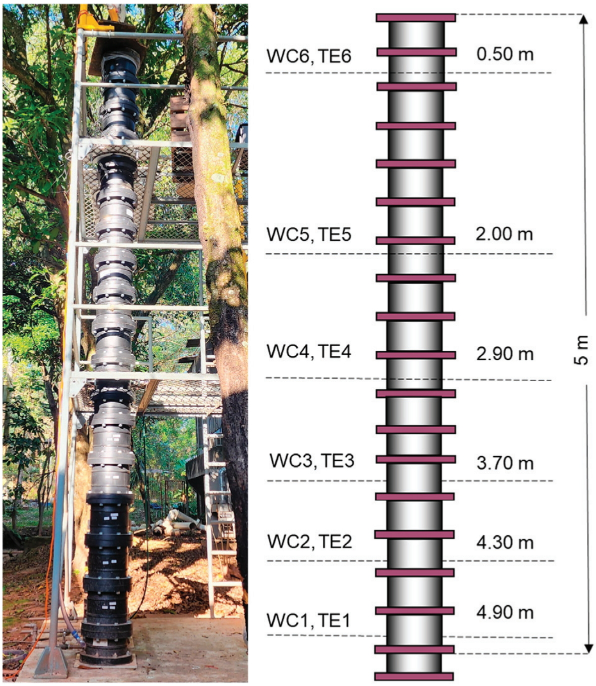

(a) (b)

Figure 10. First completed column: (**a**) Image of the completed column; (**b**) sensor positions.

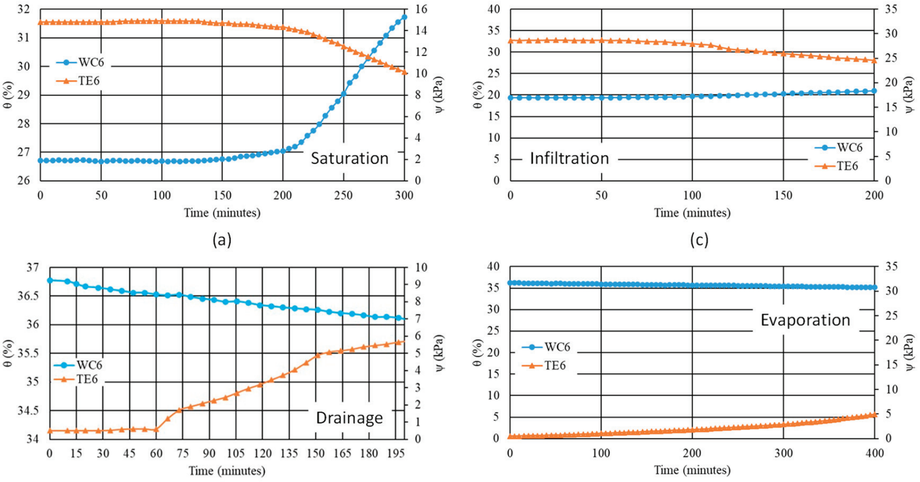

(a) (c)

(b) (d)

Figure 11. Time lag graphical analysis between sensors WC6 and TE6 during (**a**) saturation, (**b**) drainage, (**c**) infiltration, and (**d**) evaporation.

5. Experiments

To understand the processes that the columns experienced, five stages were specified: Stage 1, immediately after compaction (as compacted); Stage 2, column saturation; Stage 3, drainage after saturation; Stage 4, induced infiltration; Stage 5, evaporation. Figure 12 shows the various stages.

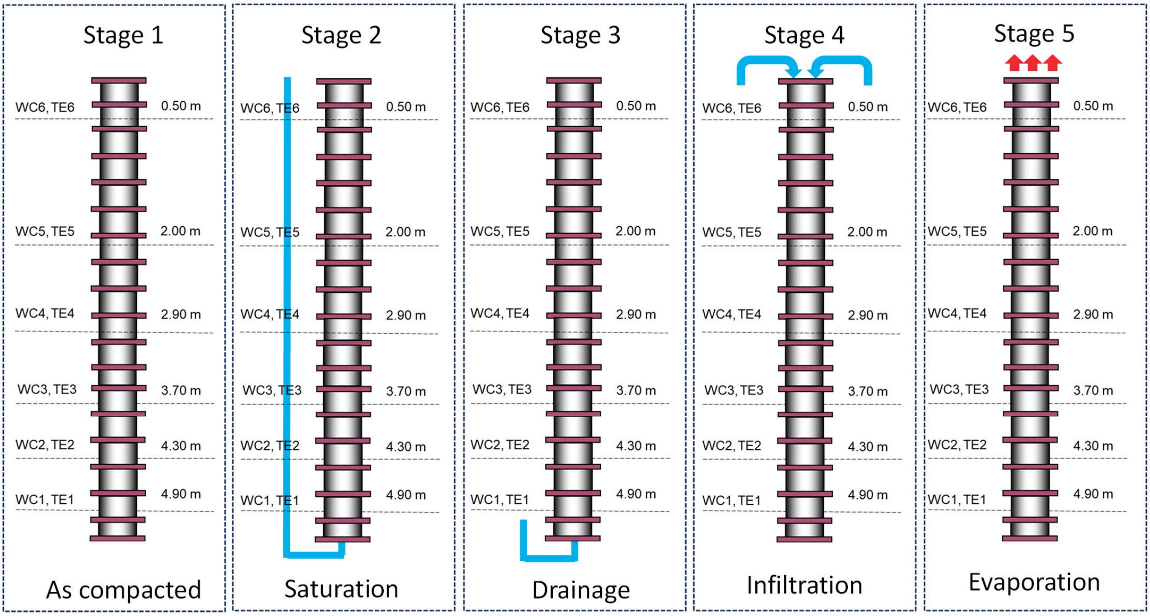

Figure 12. Stages imposed in the columns.

The saturation process (Stage 2) was conducted by introducing water through the base of the column. The water level was monitored by an external hose until the water emerged at the top of the column. The drainage process was executed by opening the valve at the base of the column while maintaining the level at the top of the filter segment. The drained volume was systematically measured by weighing the drained water at the base. The infiltration process was performed on two occasions, interspersed with evaporation.

The infiltration induced through the top of the column was conducted as follows:

Infiltration 1—1.8 l was manually added every 24 h for one hour per day over 7 days. This value corresponds to a low-intensity rainfall of 0.075 mm/h.

Infiltration 2—12.6 l was added over 8 h for one day, which corresponds to a rainfall intensity of 1.58 mm/h.

The evaporation was induced using a closed PVC box at the top of the column with a continuously operating exhaust fan. This system induced a total evaporation of 1.0–1.4 mm/day.

5.1. Profiles at Different Stages

Each stage of the column experiments is presented in the form of profiles of volumetric water content and suction. The reference position in the column is in terms of depth, i.e., the top of the column is the zero reference. Figure 13 shows the profile obtained immediately after the completion of the column (after installation), end of construction, and before saturation. The volumetric water content at the compaction of the material was 24% (w = 11.9%).

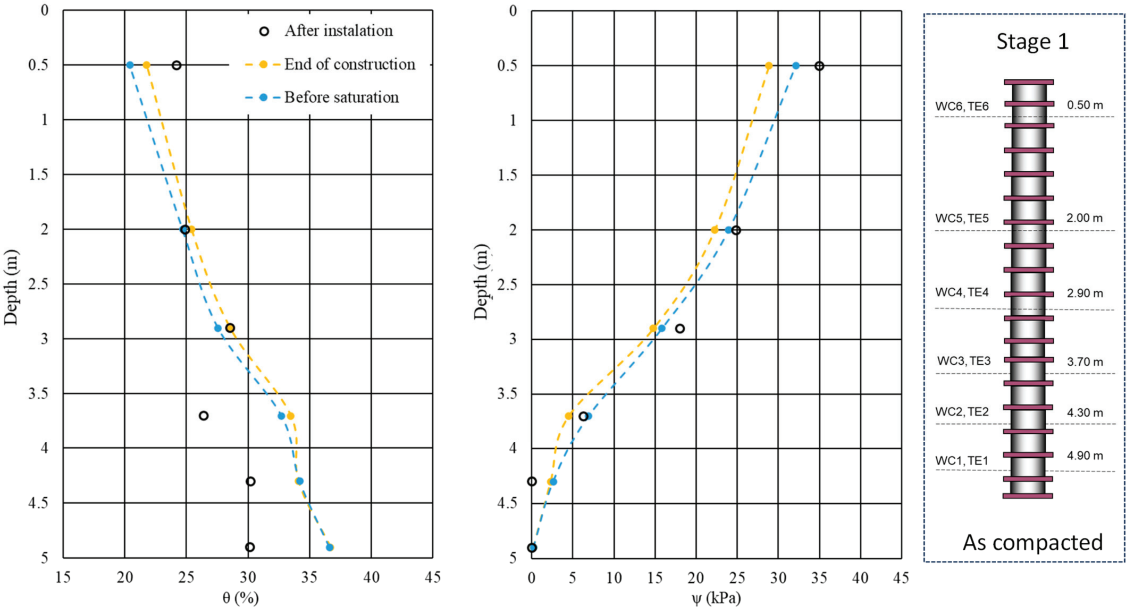

(a) **(b)**

Figure 13. Profiles at the end of construction and before saturation: (**a**) Volumetric water content and (**b**) suction.

Ten days after the column assembly, the water content profile tended to increase with depth, but the point at a depth of 2.9 m had a lower value than the general trend. This deviation was not observed in terms of suction. Considering the soil water retention curve (SWRC), the values are reasonably consistent with the curve.

Figure 14 shows the profile immediately before the saturation process began, the profiles at 2, 4, and 16 days, and the final saturation profile (39 days). The saturated volumetric water content for the compacted material was 42% (porosity of 0.42). At a depth of 2.9 m, θ remained lower than expected. A leak immediately below this level was observed. Leakage occurred through the wires of the electro-resistivity measurement system, which was installed up to this level. This leakage might have interfered with the saturation process, but after drainage and leakage repair, there was no longer a reason for further influence. The suction profile indicates a value very close to zero. However, this low level of suction (<10 kPa) is not accurate for the sensor.

5.2. Results After Drainage

The readings of Stage 3 (drainage) are shown in Figure 15. This stage was the longest with 190 days of free drainage. The readings were expected to show a decrease in water content values and an increase in suction over time. Figure 15 shows the changes in volumetric water content and suction over time at the beginning of this process. As expected, the volumetric water content at the top of the column decreased over time, which demonstrates a vertical downward flow of water. In accordance with the volumetric water content, the suction increased over time. However, even after a long period of drainage, equilibrium was not achieved.

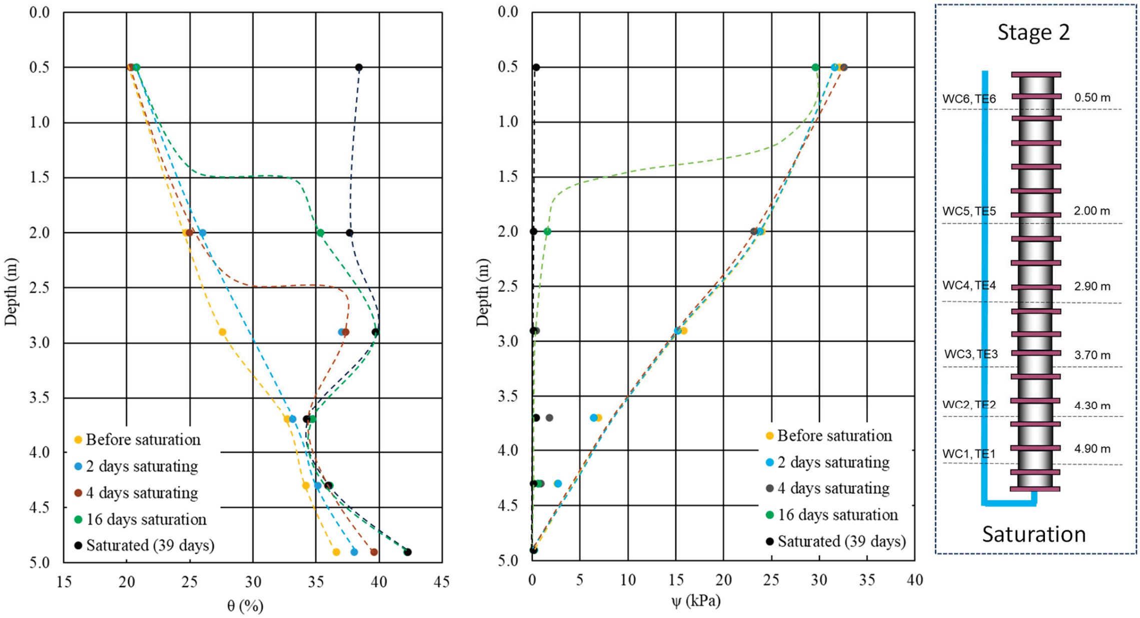

Figure 14. Profiles during saturation: (**a**) Volumetric water content and (**b**) suction.

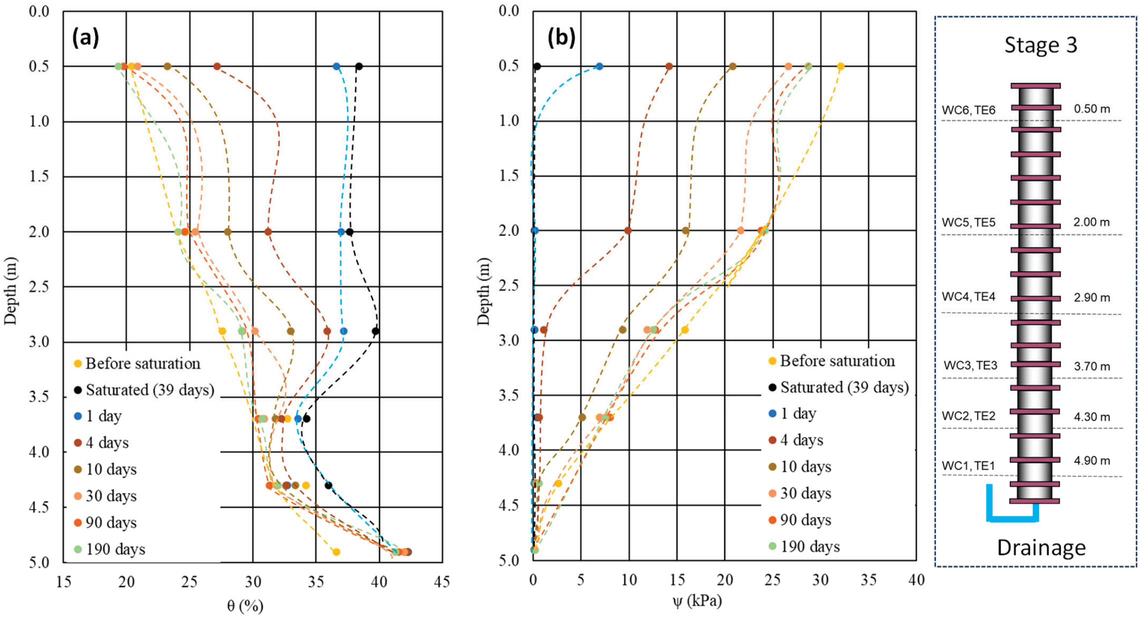

Figure 15. Profiles during drainage: (**a**) Volumetric water content and (**b**) suction.

To evaluate the active zone and observe the water response to infiltration days or dry periods, a simulation was conducted with constant infiltration at the surface of the column followed by a period of evaporation from the top of the column.

To illustrate the effects of the initial infiltration and subsequent evaporation, Figure 16 presents the measured suction and volumetric water content over time for the sensor closest to the top of the column. The numbers in Figure 16 are the days of water inlets. The first cycle of water application increased the water content and correspondingly reduced the suction. Within one day, the suction tended to recover due to drainage and without induced evaporation (the top of the column remained covered after the water application). The decrease in suction decreased with subsequent cycles until the sixth cycle when a greater decrease in suction and a more significant recovery of suction were observed. This phenomenon is associated with the retention curve and permeability of the material for that water content.

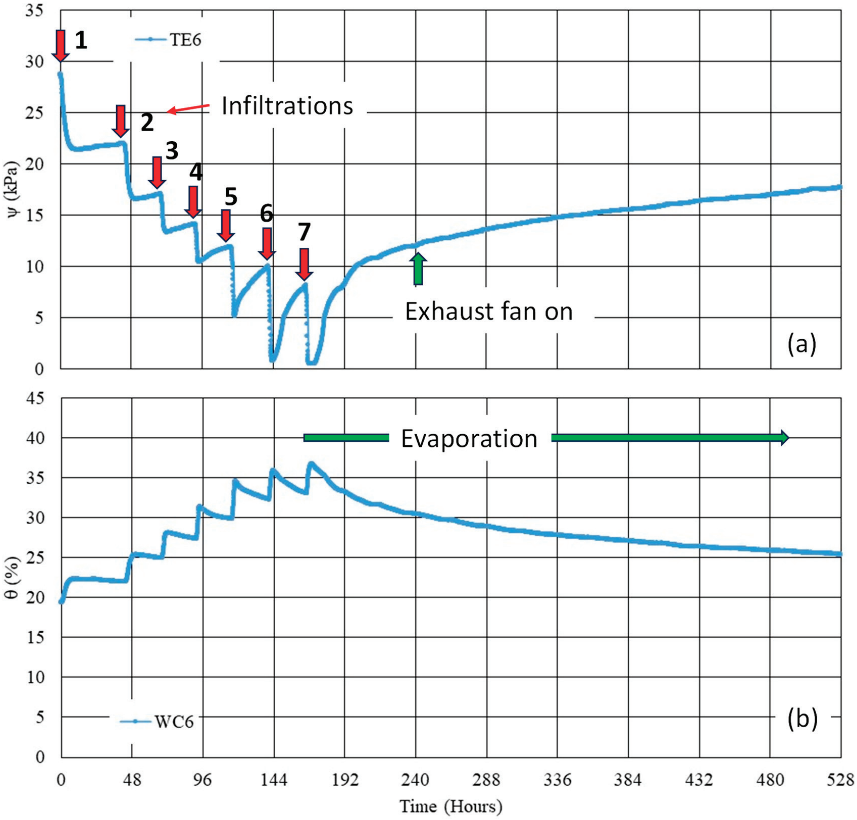

Figure 16. Responses of the TE6 (**a**) and WC6 (**b**) sensors to the first infiltration and evaporation.

As soon as the last water application (7) passed through the sensor in Figure 16, the water drained and simultaneously began to interact with the atmosphere, which initiated an evaporation process. Figure 18a shows the moment when the exhaust system was turned on. Apparently, no significant effect of the system was observed, but it prevented an increase in relative humidity in the upper segment of the column.

The second infiltration cycle was performed with the same volume of water but was continuously applied. However, the water accumulation on the surface did not exceed 1 cm, and the saturation front was not allowed to break. The first 2 litres was applied in the first 12 min without the formation of a layer thicker than 1 cm. The water was subsequently added in two 500 mL portions to always maintain a water layer of less than 1 cm in thickness. Eight hours after the process began, 1.1 litres was added, which increased the water accumulation level. After 24 h, a 2.5 cm layer remained. To compare the infiltration processes induced by different water feeding times, Figure 17 presents infiltration cycle 2. The continuous water inlet rapidly increased the water content and quickly decreased the suction at the sensors near the top (0.5 m). This finding indicates that the surface drainage system plays a fundamental role in the infiltration process. The drainage and evaporation that followed the water application had almost identical rates of increase in suction during both infiltration cycles.

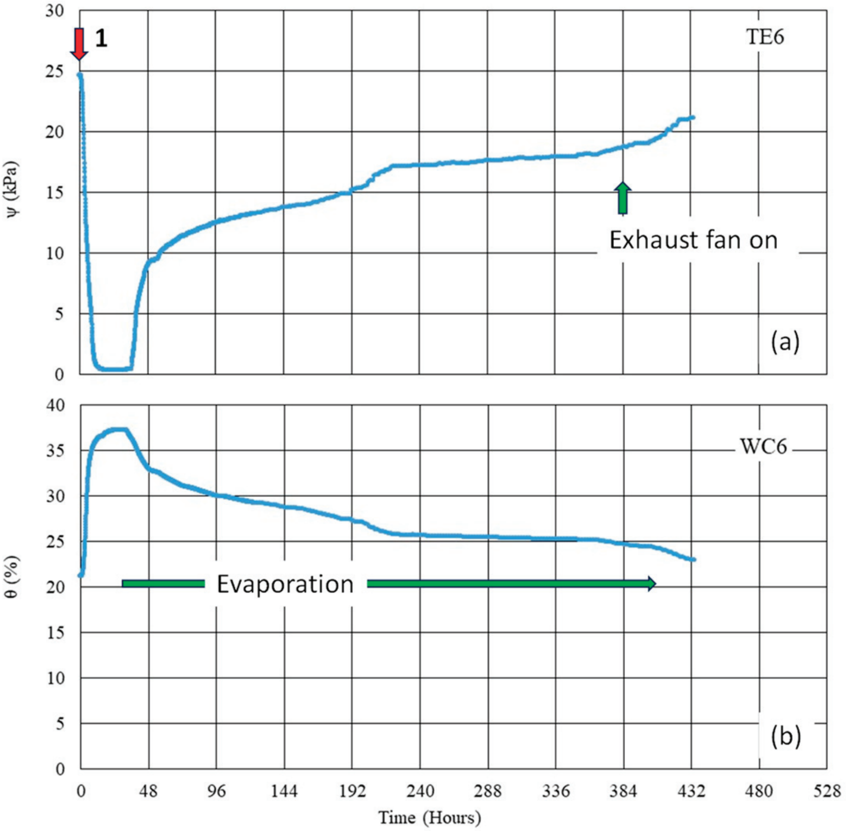

Figure 17. Responses of the TE6 (**a**) and WC6 (**b**) sensors to the second infiltration and evaporation.

Figure 18 presents the suction and water content profiles for the first infiltration cycle. The profile before the infiltration began indicates a water content slightly below 20% and a suction of approximately 28 kPa. One day after the first portion of water had been applied, an increase in water content was observed only at the shallowest sensor. Water was detected at the sensor at 0.5 m only on the seventh day. Afterwards, the profile became more vertical, but there were no changes in water content or suction.

Figure 19 shows the profiles associated with the evaporation process. As expected, a decrease in moisture content and an increase in suction were observed, which only affected the sensors at depths of 0.5 m and 2.0 m during the monitored period.

The described second infiltration process is presented in the form of moisture content and suction profiles in Figure 20. Figure 21 shows the data of Day 48, which indicates the number of days after the first infiltration. Since the water was continuously applied in this case, the profiles refer to the number of hours after the infiltration began. Notably, the water took more than 2 h to reach the sensor at the 0.5 m depth.

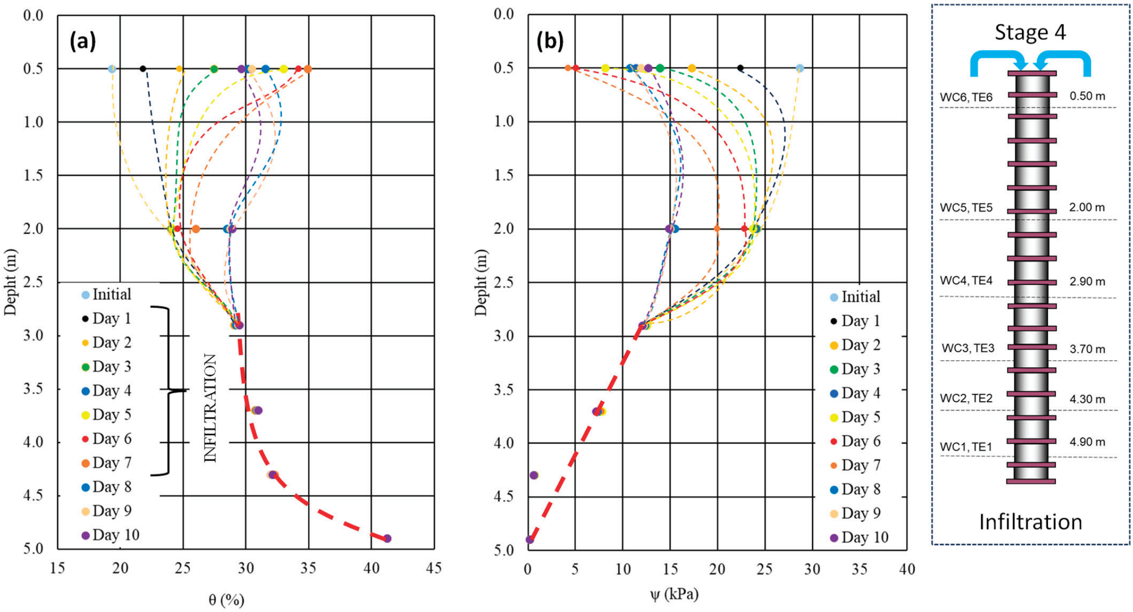

Figure 18. Profiles during the first infiltration: (**a**) volumetric water content and (**b**) suction.

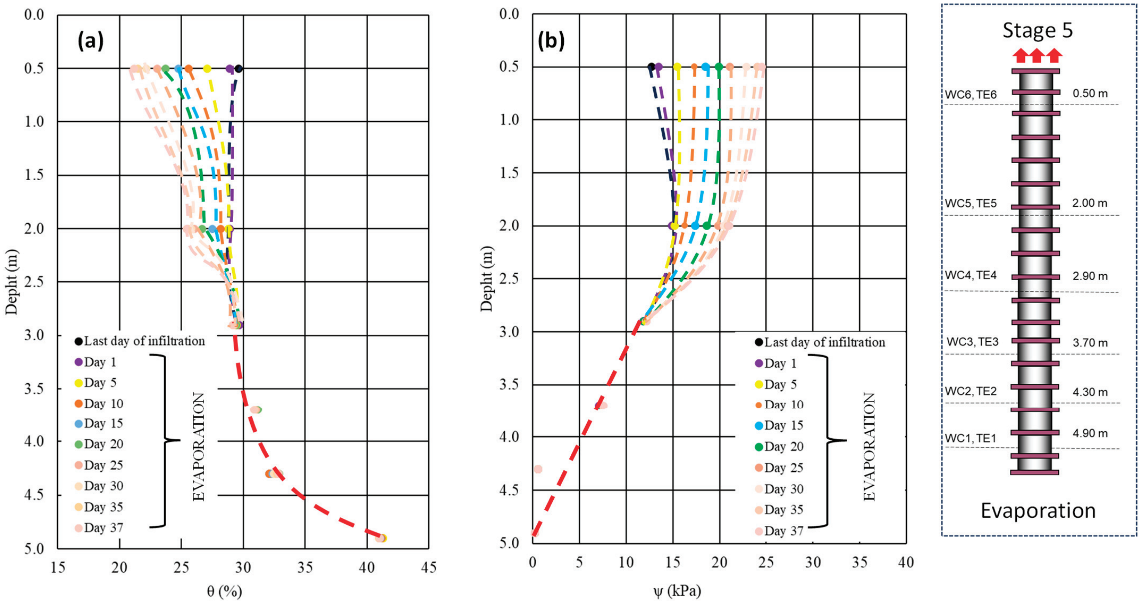

Figure 19. Profiles during the first evaporation: (**a**) volumetric water content and (**b**) suction.

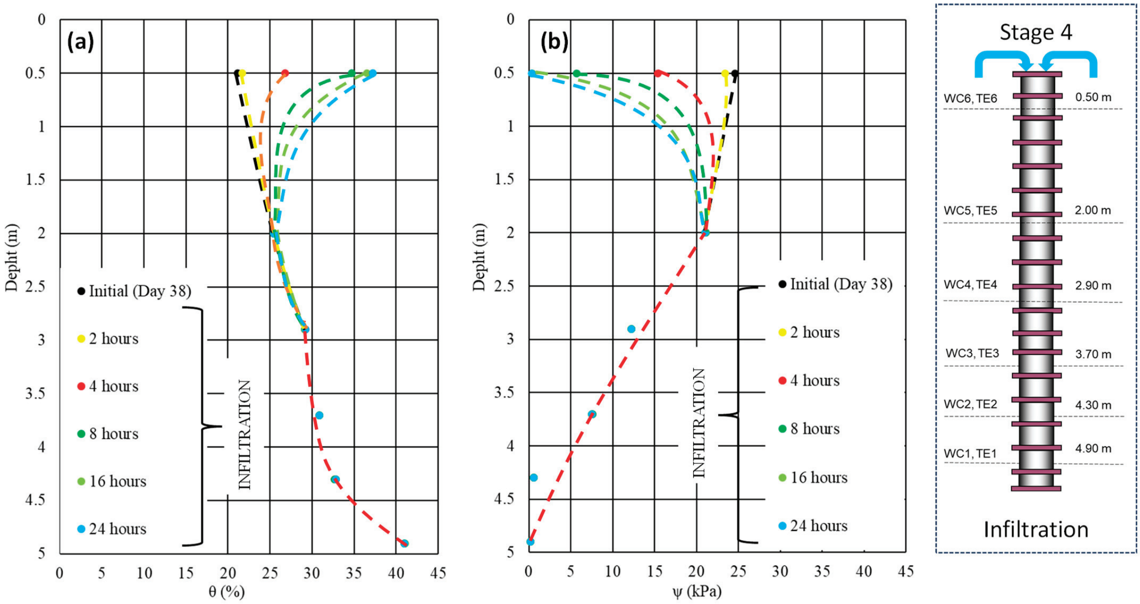

Figure 20. Profiles during the second infiltration: (**a**) volumetric water content and (**b**) suction.

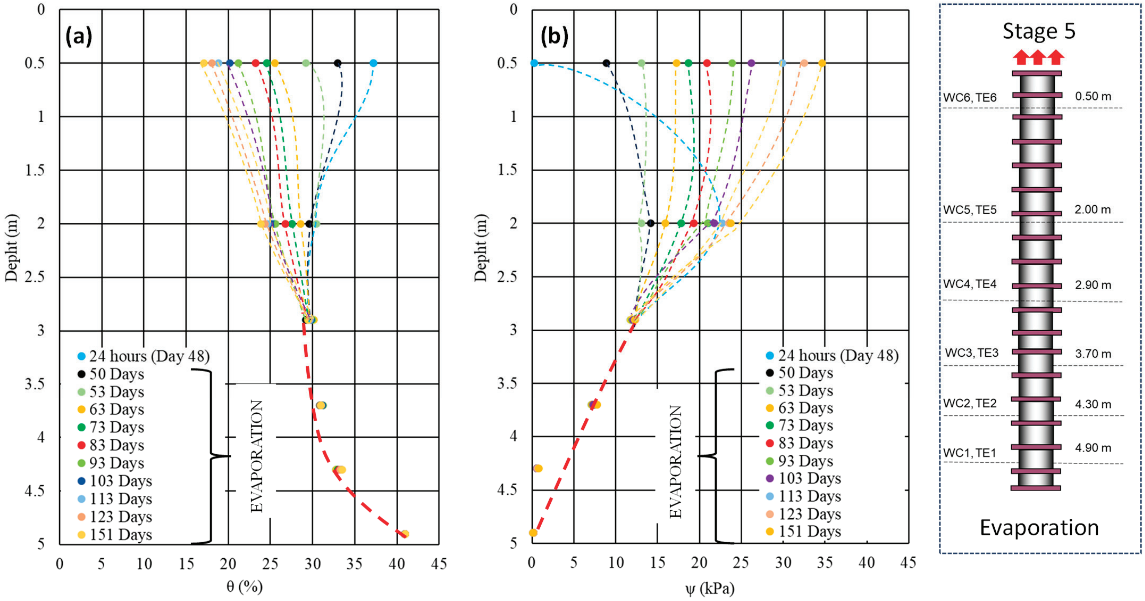

Figure 21. Profiles during the second evaporation: (**a**) Volumetric water content and (**b**) suction.

Based on the data and interpretation, the active zone for induced infiltration and evaporation was 3 m thick.

Part of the infiltrated water drained through the base of the column and was collected and measured throughout all processes. Figure 22 shows the water discharge from the drain following saturation and the induced infiltration. The volume of water drained after saturation was approximately 42 litres. Using a hyperbolic fitting, the final volume to be drained was estimated to be 43.5 litres. The theoretical total volume of water that the material in the column can retain is 103.1 litres, and the value obtained via the water content sensors was 93 litres. Subsequent infiltration (infiltration 1) drained 10.3 litres, and the second infiltration drained 14.9 litres, which indicates that each infiltration introduced 12.6 litres. The total water drained considering only the volume of water that was placed (infiltration stage) was 25.2 litres, which is exactly the amount of water introduced into the column.

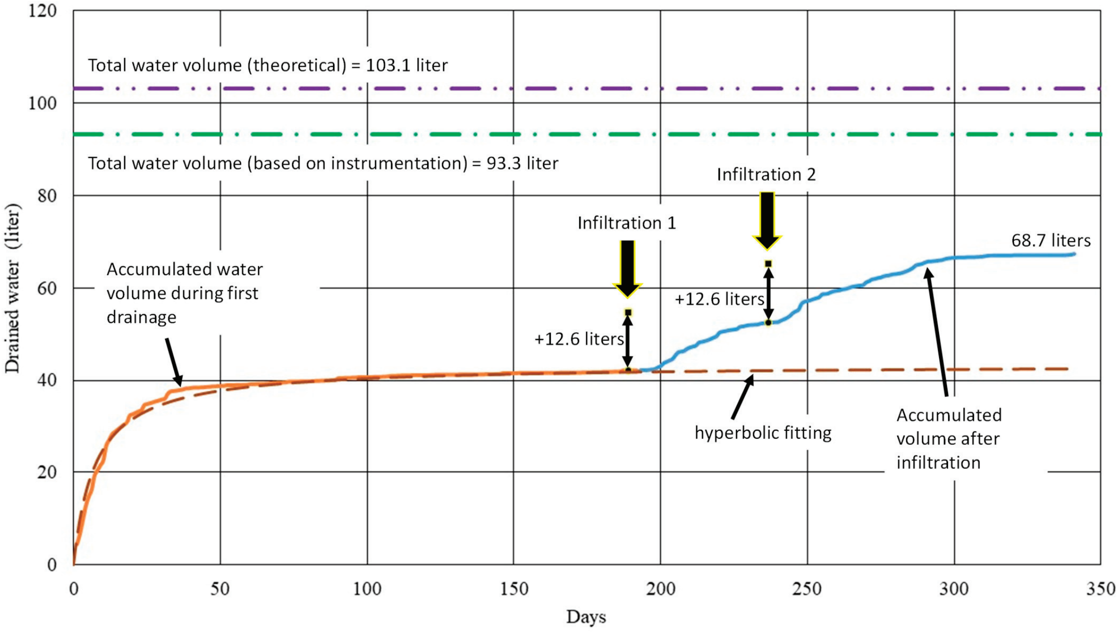

Figure 22. Measured water flux at the base of the column.

To describe the water volume balance of the experiment in the column, it is important to analyse the process at each phase of the experiment, considering the volumes of drained, infiltrated, and retained water in the porous medium over time. After saturation, the water was allowed to drain under the influence of gravity. This drainage process was monitored by sensors and by collecting water at the base of the column. The drainage continued until near-equilibrium was reached, where there was no significant flow of water. Subsequently, infiltration events were induced to simulate the addition of water to the system from the top in a controlled manner, as if they were rainfall.

The volume balance in the system can be expressed as follows:

$$V_{initial} + V_{infiltration} = V_{drained} + V_{retained} \tag{4}$$

where $V_{initial}$ is the volume of water in the column after saturation, $V_{infiltration}$ is the volume of water added during the two infiltrations, $V_{drained}$ is the volume of water drained from the system, and $V_{retained}$ is the volume of water that remained in the tailings after the drainage and infiltration processes.

Table 4 presents the values of the volume of water involved in the experiment. The total volume of water in the system, when saturated, can be calculated based on the average porosity of the column or sensor-measured moisture content. The determined values were 103.1 litres and 93.3 litres, respectively. During the drainage process, part of the water was removed from the column by gravity, as illustrated in Figure 22. The amount of water drained by Day 190 was 42 litres. The hyperbolic fitting indicates that the final drained volume was 42 litres, which indicates that the system was very close to equilibrium.

Table 4. Water volumes of the experiment.

Description	Volume (Litres)
Theoretical pore saturation volume	103.1
Sensor-estimated saturation volume	93.3
Volume of water drained after 190 days	42
Estimated volume for initial drainage (hyperbolic fitting)	43.5
Volume of water in the first infiltration	12.6
Volume of water in the second infiltration	12.6
Drainage after the first infiltration (47 days)	10.3
Drainage after the second infiltration (103 days)	14.7
Total volume of water present in the column since the start	118.5
Total increase in drained water after induced infiltrations	23.6
Volume to be drained over time	0.9

Each infiltration process introduced 12.6 litres of water. Measurements and drained water after infiltration indicated drained volumes of 10.3 litres and 14.7 litres for each infiltration. The total volume drained after infiltration was 23.6 litres.

After the drainage and infiltration processes, a certain amount of water remained in the column due to the water retention capacity of the material. This retained water volume was calculated by the difference of the initial mass, infiltrations, and drained volume. The sum of the initial water volume (using the theoretical value) and the induced infiltration was 118.5 litres. The sum of the total drained volume by Day 190 plus the retained volume was 117.6 litres. The water volume balance indicates that 0.9 litres remained to be drained.

The volume balance reveals that the column experiment has significant potential for inferring important information about water flow and retention and assessing the possibility of saturation in filtered tailing piles.

Based on Nguyen et al. [25], the permeability coefficient as a function of suction was calculated using the volumetric moisture content and suction profiles that were determined during infiltration. Unfortunately, the suction variations were not sufficient to cover a significant range of suctions. The permeability coefficient was 2.5×10^{-8}–1×10^{-7} m/s for suctions of 19–26 kPa. The permeability coefficient for an average suction of 22 kPa was 2.2×10^{-7} m/s.

5.3. Soil Water Retention Curve and Column Data

Figures 23–25 present the data obtained through the volumetric moisture content and suction sensors and retention curves obtained in the laboratory for various stages of the study.

Figure 23 shows the continuously obtained data from Stages 1 and 2 (during the compaction and saturation process). The deepest sensor had a relatively high saturated water content, whereas the other sensors had water content approximately 7% below the saturation value. The water content and suction trajectories followed a segment with little variation in water content until a suction of approximately 10 kPa was reached. Beyond this point, the data consistently followed the soil water retention curve (SWRC). Importantly, during these two stages, the wetting path was followed.

For suction values of approximately 0–10 kPa, the SWRC showed little variation in volumetric water content. Additionally, the suction sensor is not sufficiently sensitive to these small variations at this suction level. However, the data clearly followed the SWRC when the suction values approached 10 kPa.

In the stages associated with climatic events (Stages 4 and 5), there was minimal variation in moisture content up to a suction of approximately 10 kPa, as noted in previous stages. This finding was indicated in the soil water retention curve (SWRC) in the laboratory and confirms that the water content was not recorded by the moisture sensor. Interestingly, no hysteresis was detected. Only the upper sensor (6) showed variations. As previously described, water can infiltrate to greater depths without altering the suction or water content. However, more intense infiltration and/or evaporation may affect deeper sensors.

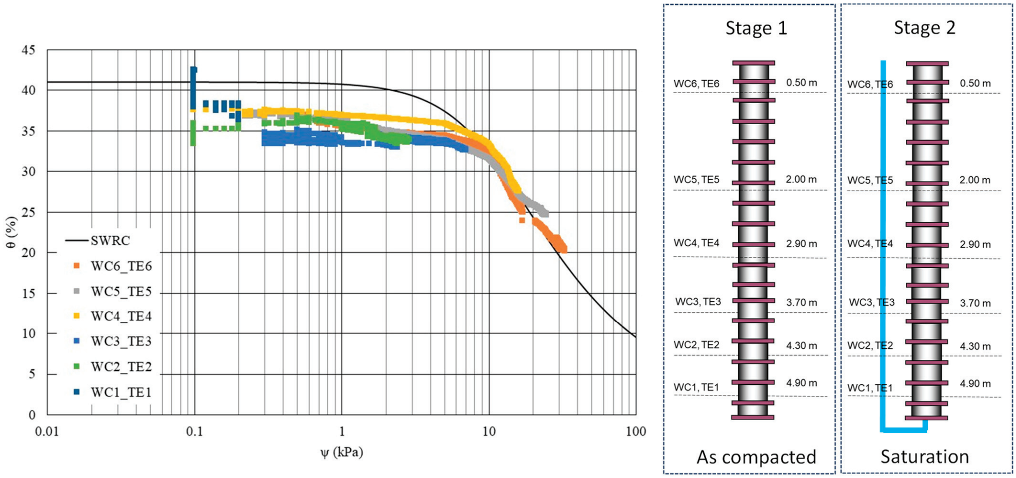

Figure 23. A closer look at the sensor readings plotted with the retention curve.

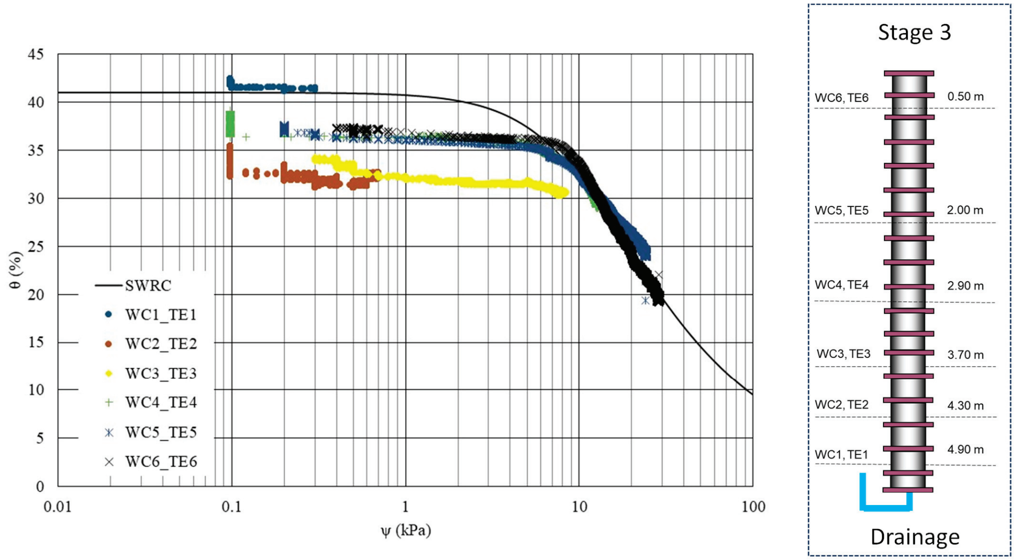

Figure 24. Water retention curve with the sensor readings.

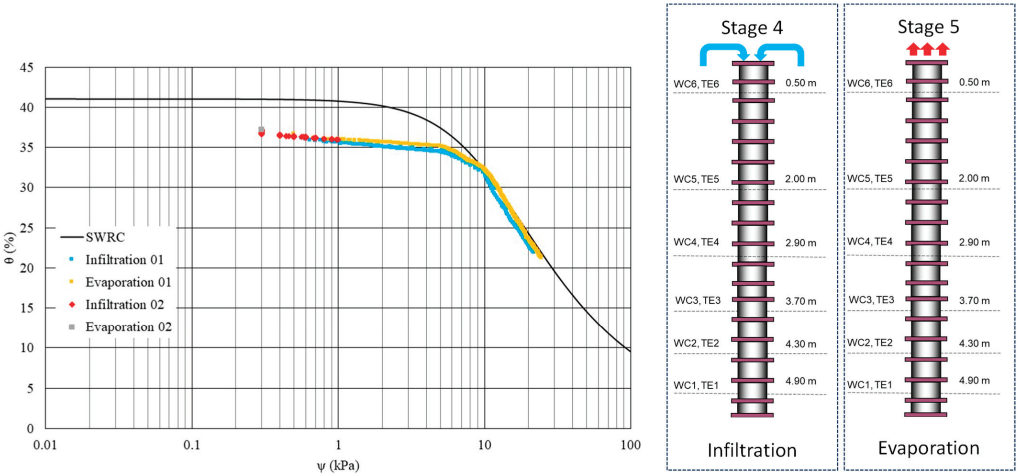

Figure 25. SWRC versus infiltration and evaporation data.

6. Conclusions

This study presented the initial findings from an experiment using a 5 m high column filled with compacted iron ore tailings. The volumetric water content and suction were monitored using sensors to evaluate the water retention behaviour and define the active zone in the material. After saturation, drainage, and two cycles of infiltration and evaporation, the experiment provided insights into the complex water dynamics in compacted tailings. The experiment highlighted the critical role of infiltration, drainage, and evaporation processes for effective tailings management, particularly in preventing water-induced instabilities such as liquefaction in tall tailings stacks.

A key aspect of the experiment was the calibration of the volumetric water content sensor, which was specifically tailored for the iron-rich material to account for the influence of iron oxide on the sensor readings. With an instantaneous response time, the moisture content sensor provided immediate data, whereas the suction sensor with a determined response time of 5 min required careful correction to ensure accuracy.

The collected data yielded consistent water content and suction profiles, which clearly defined an active zone of approximately 3 m under simulated climatic conditions. A significant conclusion was the reasonable consistency between laboratory-obtained soil water retention curves (SWRCs) and field data, although further investigation is recommended near saturation levels.

The experiment also provided a detailed water balance and demonstrated that although some infiltrated water was quickly drained, a portion remained in the tailings due to the water retention capacity of the material. This retention is crucial for understanding the long-term stability and assessing potential risks associated with water in tailings stacks. Overall, the experiments are demonstrated to be highly effective in evaluating the behaviour of compacted filtered tailings and serve as a robust basis for precise numerical analyses to calibrate material parameters.

Author Contributions: All authors have contributed extensively to the work presented in this paper. Conceptualization, F.A.M.M., Y.C. and J.P.d.S.S. Methodology, all the authors. Data curation, all the authors. Writing—original draft preparation, F.A.M.M., Y.C. and J.P.d.S.S. Writing—review and editing, all the authors. All authors have read and agreed to the published version of the manuscript.

Funding: The studies were funded by Vale S.A. in partnership with the University of São Paulo (cov. USP 1012802).

Data Availability Statement: The original contributions presented in the study are included in the article material; further inquiries can be directed to the corresponding author.

Acknowledgments: The authors would like to express their thanks to the workers who collaborated in the construction of the experiment, and the students Talita Menegaz and Ana Paula André for their precious collaboration during the activities of the experiment.

Conflicts of Interest: There are no conflicts of interest.

References

1. Rico, M.; Benito, G.; Salgueiro, A.R.; Díez-Herrero, A.; Pereira, H.G. Reported tailings dam failures: A review of the European incidents in the worldwide context. *J. Hazard. Mater.* **2008**, *152*, 846–852. [CrossRef] [PubMed]
2. Santamarina, J.C.; Torres-Cruz, L.A.; Bachus, R.C. Why coal ash and tailings dam disasters occur. *Science* **2019**, *364*, 526–528. [CrossRef] [PubMed]
3. Koppe, J.C. Lessons learned from the two major tailings dam accidents in Brazil. *Mine Water Environ.* **2021**, *40*, 166–173. [CrossRef]
4. Nwigwe, T.; Minami, K. Assessment of factors contributing to the risks of cargo liquefication accident in bulk carriers (a qualitative approach). *TransNav Int. J. Mar. Navig. Saf. Sea Transp.* **2022**, *16*, 149–152. [CrossRef]
5. Marshall, T.J.; Holmes, J.W.; Rose, C.W. *Soil Physics*; Cambridge University Press: Cambridge, UK, 1996.
6. Murray, E.J.; Sivakumar, V. *Unsaturated Soils: A Fundamental Interpretation of Soil Behaviour*; John Wiley & Sons: New York, NY, USA, 2010.
7. Edlefsen, N.; Anderson, A. Thermodynamics of soil moisture. *Hilgardia* **1943**, *15*, 31–298. [CrossRef]
8. Nelson, J.D.; Miller, D.J. *Expansive Soils*; Wiley: New York, NY, USA, 1992.
9. Blight, G.E. *Unsaturated Soil Mechanics in Geotechnical Practice*; CRC Press: Boca Raton, FL, USA, 2013.
10. Goss, M.J.; Ehlers, W. The role of lysimeters in the development of our understanding of soil water and nutrient dynamics in ecosystems. *Soil Use Manag.* **2009**, *25*, 213–223. [CrossRef]
11. Lewis, J.; Sjöstrom, J. Optimizing the experimental design of soil columns in saturated and unsaturated transport experiments. *J. Contam. Hydrol.* **2010**, *115*, 1–13. [CrossRef] [PubMed]
12. Pütz, T.; Fank, J.; Flury, M. Lysimeters in vadose zone research. *Vadose Zone J.* **2018**, *17*, 180035. [CrossRef]
13. Buckingham, E. *Studies on the Movement of Soil Moisture*; US Department of Agriculture, Bureau of Soils: Washington, DC, USA, 1907.
14. Marinho, F.A.M.; Stuermer, M.M. Aspects of the storage capacity of a compacted residual soil. In Proceedings of the Second International Conference on Unsaturated Soils Beijing, Beijing, China, 27–30 August 1998; International Academic Publishers: Beijing, China, 1998; pp. 581–585.
15. Marinho, F.A.M.; Pinto, C.D.S. Investigating the water retention in iron ore. In *Proceeding of the 3rd International Conference on Unsaturated Soils, Recife, Brazil, 10–13 March 2002*; CRC Press: Boca Raton, FL, USA, 2004; pp. 1143–1146.
16. Oliveira, O.M.; Marinho, F.A.M. Simulação de chuva em coluna de solo residual compactado. In Proceedings of the VI Simpósio Brasileiro de Solos Não Saturados, Salvador, Brazil, 1–3 November 2007; pp. 291–297.
17. Teixeira, P.F.; Marinho, F.A.; Oliveira, O.M.D. Efeito do fluxo de ar no perfil de umidade de uma areia. In Proceedings of the XIV Congresso Brasileiro de Mecânica dos Solos e Engenharia Geotécnia, Búzios, Brazil, 23–26 August 2008.
18. Reinert, D.J.; Reichert, J.M. Coluna de areia para medir a retenção de água no solo: Protótipos e teste. *Ciênc. Rural* **2006**, *36*, 1931–1935. [CrossRef]
19. McCartney, J.S.; Zornberg, J.G. Effects of infiltration and evaporation on geosynthetic capillary barrier performance. *Can. Geotech. J.* **2010**, *47*, 1201–1213. [CrossRef]
20. Ng, C.W.W.; Leung, A.K. Measurements of drying and wetting permeability functions using a new stress-controllable soil column. *J. Geotech. Geoenviron. Eng.* **2012**, *138*, 58–68. [CrossRef]
21. Crystal, C.; Hore, C.; Ezama, I. Filter-pressed dry stacking: Design considerations based on practical experience. In Proceedings of the Tailings and Mine Waste, Brisbane, Australia, 23–24 July 2018; pp. 209–219.
22. Jesus, M.H.; Silva, J.P.D.S.; Marinho, F.A.M. Soil water retention curve of a compacted iron ore tailing obtained by various methods. In Proceedings of the 17th Pan-American Conference on Soil Mechanics and Geotechnical Engineering (XVII PCSMGE), La Serena, Chile, 12–17 November 2024.
23. Van Genuchten, M.T. A closed-form equation for predicting the hydraulic conductivity of unsaturated soils. *Soil Sci. Soc. Am. J.* **1980**, *44*, 892–898. [CrossRef]
24. De Sá Landim, A.; Corrêa, Y.; Silva, J.P.; Marinho, A.M.F. Evaluation a volumetric water content sensor to be used for compacted filtered iron ore tailings. In *E3S Web of Conferences*; EDP Sciences: Les Ulis, France, 2023; p. 16003.
25. Nguyen, B.T.; Ishikawa, T.; Zhu, Y.; Subramanian, S.S.; Nguyen, T.T. New simplified transient method for determining the coefficient of permeability of unsaturated soil. *Eng. Geol.* **2022**, *300*, 106564. [CrossRef]

geosciences

Article

A Hyperelastic Bounding Surface Plasticity Model for Unsaturated Granular Soils

Mehdi Kadivar [1], Kalehiwot Nega Manahiloh [2,*] and Victor N. Kaliakin [1]

[1] Department of Civil & Environmental Engineering, University of Delaware, Newark, DE 19716, USA; mehdika@udel.edu (M.K.); kaliakin@udel.edu (V.N.K.)
[2] Civil Engineering Department, Liberty University, Lynchburg, VA 24515, USA
* Correspondence: kmanahiloh@liberty.edu; Tel.: +1-434-592-4243

Abstract: In this paper, a state-dependent, bounding surface plasticity model that simulates the behavior of unsaturated granular soils is presented. An unsaturated, soil mechanics-compatible elastoplastic response is adopted in which no part of the response occurs in a purely elastic fashion. To create an appropriate hydro-mechanical coupling, a newer generation stress framework, consisting of the Bishop-type effective stress and a second stress variable, is used in conjunction with a soil-water characteristic curve function. Details regarding the model development, parameter estimation, and assessment of the model's predictive capabilities are outlined. With a single set of parameter values, the model realistically simulates the main features that characterize the shear and volumetric behavior of unsaturated granular soils over a wide range of matric suction, density, and net confining pressure.

Keywords: unsaturated granular soil; constitutive modeling; bounding surface plasticity; matric suction; axis translation; hyperelasticity; soil water characteristic curve

Citation: Kadivar, M.; Manahiloh, K.N.; Kaliakin, V.N. A Hyperelastic Bounding Surface Plasticity Model for Unsaturated Granular Soils. *Geosciences* **2024**, *14*, 148. https://doi.org/10.3390/geosciences14060148

Academic Editors: Jesus Martinez-Frias, Dunja Perić and Laureano R. Hoyos

Received: 31 March 2024
Revised: 13 May 2024
Accepted: 28 May 2024
Published: 30 May 2024

1. Introduction

Environmental conditions such as precipitation, infiltration, and evaporation influence the location of the groundwater table and, therefore, the thickness of the unsaturated soil zone. In this zone, the soil is characterized by variations in moisture content and in the associated water pressure. Ignoring conditions in the tightly adsorbed water layer in the unsaturated zone, the pore-water pressure is negative. Depending on the type and permeability of the soil, the magnitude of the pore pressure can vary over six orders of magnitude. Reports indicate that, in the USA alone, problems associated with unsaturated soils (e.g., volume change, pressure generation, and moisture transport) annually inflict over $15 billion in damage to buildings, roads, and pipelines, e.g., [1].

Constitutive modeling of unsaturated soils has drawn attention since the 1990s. Research in this field was pioneered by the likes of Alonso, et al. [2], who extended the modified Cam-Clay model [3] to one based on the concept of two independent stress state variables. In this concept, the behavior of unsaturated soils is governed by matric suction and net stress [4,5]. Based on the concept of two stress state variables and using the extended critical state concept, several constitutive models were subsequently developed and used to simulate the behavior of unsaturated soils, e.g., [6–10]. However, Gens, et al. [11] postulated that the framework of two independent stress state variables is successful only in cases where one of these variables is kept constant. According to Nuth and Laloui [12], separating the mechanical stress from the hydraulic stress prevents the proper simulation of the hydro-mechanical coupling phenomena observed in unsaturated soils. Sheng [13] indicated that, in the two-stress state variable approach, a smooth transition between saturated and unsaturated states was missing. Using energy principles, Houlsby [14] rigorously demonstrated that two sets of stress–strain variables (e.g., the effective stress and matric suction as stress variables and the strain of the solid skeleton and degree of saturation as kinematic variables) are adequate to describe unsaturated soil behavior.

The Bishop-type [15] effective stress has been extensively used in describing unsaturated soil behavior, as evident in the works of [16–30]. The constitutive relationships presented in the aforementioned studies fall within the framework of standard rate-independent elastoplasticity. They predict path-dependent elastic response for stress states within a yield surface, which is counter to the framework of elastoplasticity. In such formulations, the elastic response should be path-independent. Additional details regarding these observations will be provided in the Strain Decomposition section of this paper.

The effective stress framework allows the direct incorporation of the soil water characteristic curve (SWCC) and the intrinsic coupling between the mechanical and hydraulic behavior. In addition, when the state of the soil changes to full saturation, the associated effective stress reduces to Terzaghi’s effective stress. This characteristic makes such a framework a viable choice for implementing a constitutive model for unsaturated soils into new or existing finite element or finite difference computer programs, as most of these are written in terms of effective stress for saturated soils. Consequently, a natural transition to unsaturated states can be realized by simply replacing Terzaghi’s effective stress with Bishop’s definition [12].

In elastoplastic models for unsaturated soils employing the effective stress framework, the yield surface can be made a function of the matric suction and/or the degree of saturation [19,24,26,31,32]. This gives such models the ability to correctly simulate the influence of unsaturated conditions on plastic straining, including the possible occurrence of collapse compression during wetting.

The concept of a bounding surface in stress space was independently introduced by Krieg [33] and Dafalias and Popov [34] to more accurately simulate the cyclic response of metals. The basic idea underlying bounding surface models is a smooth transition from elastic to plastic states. In such models, there is a yield surface whose size and location may vary within an outer or “bounding” surface. The plastic stiffness decreases as the material state approaches the bounding surface. This beneficial characteristic has led to the development of several bounding surface models for saturated soils [35–40].

Russell and Khalili [32] first applied the bounding surface concept to simulate the rate-independent behavior of unsaturated soils. They combined the framework of critical state soil mechanics with Bishop’s effective stress definition for such soils. Their model also accounted for possible particle crushing at high stresses. The capabilities of this model were assessed by simulating the axisymmetric triaxial response of both clean sand and pure clay.

By extending the bounding surface plasticity model of Bardet [36], which was originally developed for saturated sands, Morvan, et al. [41] proposed a bounding surface-based constitutive model for unsaturated soils. More recently, Patil, Hoyos, Morvan and Puppala [28] refined this model, taking into account the hysteretic behavior of a water retention curve and its dependence on the void ratio. A common trait of the aforementioned bounding surface constitutive models is that they all assume a hypoelastic response. However, as pointed out by Lashkari and Golchin [42], the lack of conservation of energy in hypoelasticity poses challenges in proving the accuracy of such models.

In the present work, a state-dependent, critical state-compatible constitutive model that accounts for the effect of matric suction on the hydro-mechanical response of unsaturated granular soils is described. The model is formulated in a rate-independent bounding surface plasticity framework and incorporates a newer generation of effective stress definition. The model represents an enhanced extension of the hyperelastic bounding surface model for fully saturated granular soils originally proposed by Lashkari, et al. [43]. In the unsaturated, soil mechanics-compatible elastoplastic response associated with the present model, no part of the response occurs in a purely elastic fashion. The elastic portion of the elastoplastic response is computed from a Gibbs free energy function suitable for unsaturated granular soil, thus satisfying the law of conservation of energy. Using a single set of parameter values, this model simulates the hydro-mechanical response of unsaturated granular soils with various ranges of density, normal stress, and matric suction. The model's predictive capabilities are assessed by comparing its simulations with experimental data for clean sand, as reported by Russell and Khalili [32], and silty sand, as reported by Patil, Hoyos and Puppala [29]. The model is also compared with the bounding surface-based models of Russell and Khalili [32], Morvan, Wong and Branque [41], and Patil, Hoyos, Morvan and Puppala [28]. To rigorously assess the model's performance, the statistical technique of Li and Zhu [44] is employed, wherein the normalized residual sum of squares ($\mathrm{RSS}_{\mathrm{mono}}$) serves as the benchmark for comparison.

The authors deeply appreciate the importance of evaluating the model performance with varying stress paths, other test types, and plastic volumetric strains induced by wetting and drying cycles under isotropic loading conditions. However, due to page limit issues, the details pertaining to these issues must be deferred to future publications.

2. Model Development

The following sections present the development of the model. For simplicity, the model is formulated in axisymmetric triaxial space in terms of the mean normal effective stress (p') and the deviator stress (q). Although implementing the model into general research and commercial computer programs would necessitate a more general, three-invariant framework, such development is beyond the scope of the present paper.

2.1. Effective Stress Definition

Following the principles of saturated soil mechanics, the effective stress vector (σ') is written as follows:

$$\boldsymbol{\sigma}' = \begin{Bmatrix} p' \\ q \end{Bmatrix}, \tag{1}$$

where p' and q are defined above. By adopting Bishop's relationship, p' is defined as follows:

$$p' = p_{net} + \chi s, \tag{2}$$

where $p_{net} = (p_t - u_a)$ is the net confining stress, p_t is the total confining stress, u_a is the pore air pressure, $s = (u_a - u_w)$ is the matric suction, and u_w is the pore water pressure. In this work, matric suction signifies the component of the total suction, excluding the osmotic fraction. In Equation (2), χ is Bishop's effective stress parameter, which varies between a value of zero (corresponding to dry conditions) and one (corresponding to water-saturated conditions).

Several functional relationships have been proposed for χ, most of which relate it to the degree of saturation (S_r). Schefler [45] suggested that χ be equal to S_r. The use of this definition, in conjunction with experimental data for unsaturated soils with different values of matric suction, showed that a unique critical state line (CSL) was, however, not achieved in p'-q space. This observation is evident in Figure 1a, where it can be seen that for each value of matric suction (s), a different critical state line must be defined.

To avoid the need for defining multiple CSLs in p'-q space, Manzanal, Pastor and Merodo [24] suggested that the effective degree of saturation, S_{re}, be used in the definition of χ as follows:

$$\chi = S_{re} = \frac{S_r - S_{r0}}{1 - S_{r0}}, \tag{3}$$

where S_r is the current degree of saturation and S_{r0} is the residual state degree of saturation, which can be estimated from the SWCC. The symbols $\langle\ \rangle$ represent Macaulay brackets; for some quantity x, they give $\langle x \rangle = x$ if $x > 0$ and $\langle x \rangle = 0$ if $x \leq 0$. As evident from Figure 1b, Equation (3) eliminates the need for defining multiple CSLs in p'-q space.

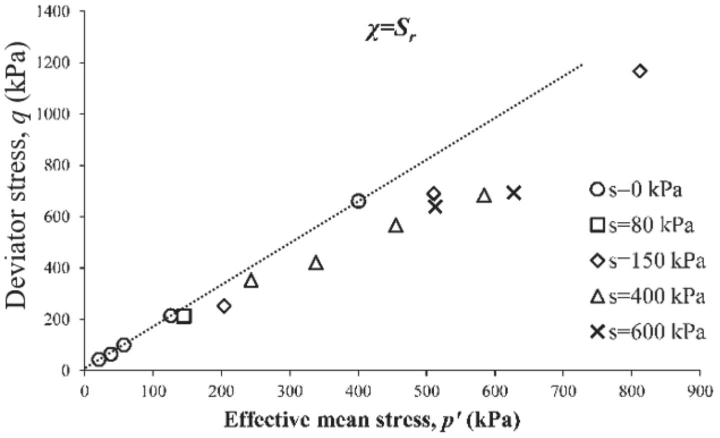

(**a**)

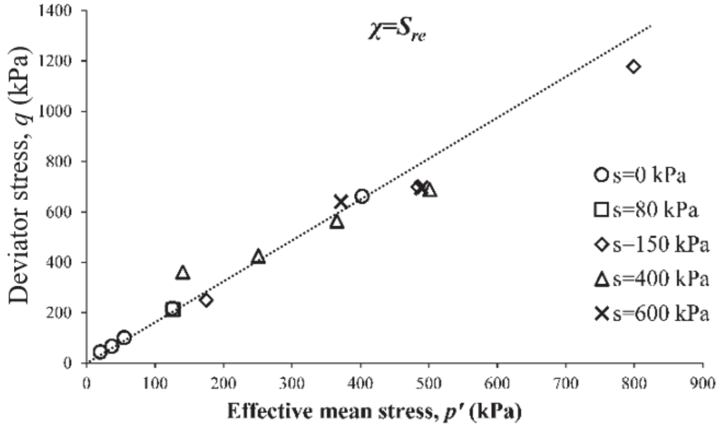

(**b**)

Figure 1. Critical states in p'-q space for different values of matric suction (s) when (**a**) $\chi = S_r$; (**b**) $\chi = S_{re}$ (experimental data from Maatouk, et al. [46]).

2.2. The Idealization of the Soil Water Characteristic Curve (SWCC)

The constitutive relationship between matric suction and the water content (or degree of saturation) of soils is commonly described using the SWCC. A number of functional forms have been suggested for SWCCs, (e.g., [47–54]). The SWCC of a given soil varies depending on the direction and history of wetting considered. This variation in SWCCs is referred to as hysteresis [55]; its physical description was pioneered by Poulovassilis [56]. Past investigations have shown that the SWCC of natural soil differs from the SWCC of the same soil recompacted to the same density at the same water content [57,58]. Similar studies have reported that additional factors such as stress state, loading and wetting history, and soil structure affect the SWCC. In addition, many studies have investigated the dependence of the SWCC on a soil's initial density, (e.g., [6,32,57–63]). For example, from Figure 2, it is evident that different SWCCs are obtained for different densities, as quantified by the void ratio (e).

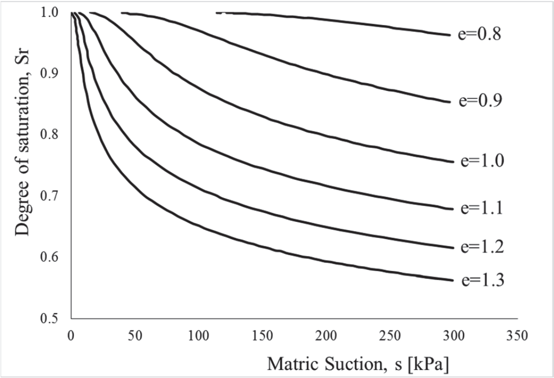

Figure 2. Density dependence of SWCC (data from [63]).

Following the work of Wheeler [62] but adopting a simplified approach, Gallipoli, Wheeler and Karstunen [63] proposed a normalization technique that yields a unique SWCC for different values of density. In this technique, the degree of saturation is correlated with not only the matric suction but also the density (i.e., specific volume). Adopting such a technique, Manzanal, Pastor and Merodo [24] defined a modified suction (s*) that is a function of the void ratio according to the following:

$$s* = se^{\Omega}, \tag{4}$$

where Ω is a curve-fitting parameter.

In the present model, the relationship of Fredlund and Xing [47] for the SWCC is adopted and combined with the aforementioned normalization technique of Gallipoli, Wheeler and Karstunen [63]. The resulting normalized SWCC function thus takes the following form:

$$S_r = S_{r0} + (1 - S_{r0})\left(1 - \frac{ln\left(1 + \frac{s}{s_0}\right)}{ln\left(1 + \frac{10^6}{s_0}\right)}\right)\left[ln\left(exp(1) + \left(\frac{s*}{a_v.p_{ref}}\right)\right)^{n_v}\right]^{-m_v}, \tag{5}$$

In Equation (5), a_v, n_v, and m_v are model parameters, and S_{r0} and S_0 are the residual values of the degree of saturation and matric suction, respectively. The value of 10^6 corresponds to the suction of 1 GPa, which is the value at which the degree of saturation, S_r, reaches the residual value, S_{r0}, in the SWCC expression proposed by Fredlund and Xing [47].

2.3. Strain Decomposition

The strain vector ($\boldsymbol{\varepsilon}$) that is work-conjugate to the effective stress vector given in Equation (1) is as follows:

$$\boldsymbol{\varepsilon} = \begin{Bmatrix} \varepsilon_v \\ \varepsilon_q \end{Bmatrix}, \tag{6}$$

where ε_v and ε_q are, respectively, the volumetric and distortional components of the strain vector.

Assuming infinitesimal displacements and displacement gradients, the total strain rate vector is additively decomposed into an elastic and plastic part as follows:

$$\dot{\boldsymbol{\varepsilon}} = \begin{Bmatrix} \dot{\varepsilon}_v \\ \dot{\varepsilon}_q \end{Bmatrix} = \dot{\boldsymbol{\varepsilon}}^{\boldsymbol{e}} + \dot{\boldsymbol{\varepsilon}}^{\boldsymbol{p}} = \begin{Bmatrix} \dot{\varepsilon}_v \\ \dot{\varepsilon}_q \end{Bmatrix}^e + \begin{Bmatrix} \dot{\varepsilon}_v \\ \dot{\varepsilon}_q \end{Bmatrix}^p, \tag{7}$$

where the superscripts e and p denote the elastic and plastic parts, respectively, of $\boldsymbol{\varepsilon}$. A superposed dot indicates a material time derivative or rate, which is used here in lieu of incremental notation as a convenience since the formulation is rate-independent.

Within a conventional elastoplasticity framework, the response associated with stress states within the elastic region is, by definition, independent of the stress path. However, Zhang and Lytton [64] and Sheng, et al. [65] showed that for unsaturated soils, the "elastic" volumetric change is stress-path dependent. As Figure 3 illustrates, a closed loop of net stress and suction changes within the elastic region does not necessarily lead to a closed loop of effective mean stress changes. This is because of the material state dependency of the effective stress [13]. The lack of a closed-loop means that, even for seemingly elastic stress states, the response is stress-path dependent. A model that exhibits stress-path-dependent elastic behavior is inconsistent with classical elastoplasticity theory and thermodynamic considerations.

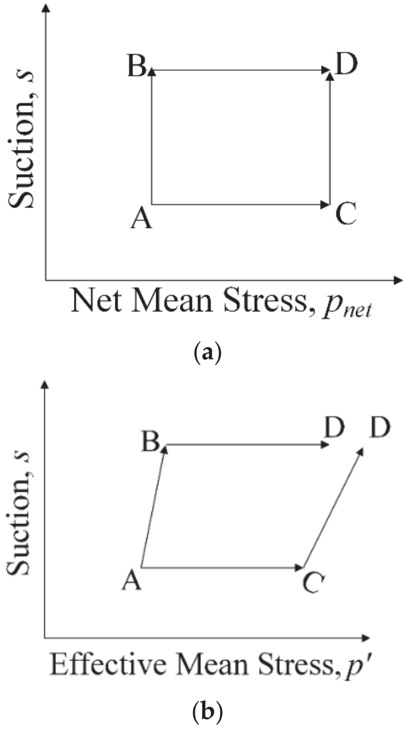

Figure 3. (**a**) Closed loop in net stress space vs. (**b**) open loop in effective stress space (adopted from Sheng [13]).

According to Collins and Houlsby [66], for materials in which elastic parameters are dependent on internal parameters due to elastic-plastic coupling, the traditional elastic-plastic strain decomposition is not valid. Following the work of Maier and Hueckel [67], Collins and Houlsby [66] postulated that instead of using "elastic" and "plastic", the terms "reversible" and "irreversible" should instead be used when describing strain rates. In their definition, the elastic strain was assumed to be affected by the plastic strain; coupled elastic-plastic strain rates were thus added to the elastic strain rates. Collins and Houlsby [66] thus decomposed the elastic strain rate into reversible and irreversible (coupled) portions. Table 1 summarizes their strain decomposition. In this table, the superscripts "r" and "i" denote the reversible and irreversible parts, respectively, of the infinitesimal strain vector.

Table 1. Strain decomposition for unsaturated granular soils.

Total strain rate	$\dot{\varepsilon}$		
Elastic + Plastic	$\dot{\varepsilon}^{e}$		$\dot{\varepsilon}^{p}$
Reversible elastic + Coupled (Irreversible) elastic + Plastic	$\dot{\varepsilon}^{er}$	$\dot{\varepsilon}^{ei}$	$\dot{\varepsilon}^{p}$
Reversible elastic + Coupled (Irreversible)	$\dot{\varepsilon}^{er}$	$\dot{\varepsilon}^{i}$	

(Adopted from Collins and Houlsby [66]).

In the present model, due to the aforementioned path dependence of the elastic strains in unsaturated soils (Figure 3), it is assumed that no purely elastic strains can develop at any time; the elastic strain is thus inherently coupled with the plastic strain. In light of the above discussion, the term "irreversible elastic strain vector" is adopted for the elastic strain that is coupled with the plastic strain.

2.4. Definition of the Elastic Response

The constitutive relation used by Golchin and Lashkari [68] and Alipour and Lashkari [69] is likewise adopted herein, i.e.:

$$\begin{Bmatrix} \dot{p}' \\ \dot{q} \end{Bmatrix} = \begin{bmatrix} K & J \\ J & 3G \end{bmatrix} \begin{Bmatrix} \dot{\varepsilon}_v \\ \dot{\varepsilon}_q \end{Bmatrix}^{er}, \tag{8}$$

where K, G, and J are the hyperelastic moduli, which are non-linear functions of p'. Following the approach of Golchin and Lashkari [68], expressions for these moduli are calculated by partial differentiation of the Gibbs free energy function proposed by Einav and Puzrin [70], which guarantees the conservation of energy in any arbitrary closed loop. As derived by Golchin and Lashkari [68], this function is as follows:

$$\Gamma(p', q, X) = \frac{p'^{2-X} - (2-X)p' p_0^{1-X}}{K_0 F(e)(2-X)(1-X)p_{ref}^{1-X}} + \frac{q^2}{6G_0 F(e) p'^{X} p_{ref}^{1-X}} - \frac{q_0(2qp_0 - Xq_0 p')}{6G_0 F(e) p_0^{1+X} p_{ref}^{1-X}}, \tag{9}$$

where K_o and G_o are model parameters, P_{ref} is a reference pressure that is normally assumed to be equal to the atmosphere pressure ($P_{atm} = 101$ kPa), p_0 and q_0 are the values of p' and q at zero elastic strain, respectively, and $F(e)$ is a function of the void ratio (e) and particle shape. Lashkari, Karimi, Fakharian and Kaviani-Hamedani [43] proposed the following expression for granular soils with angular particles:

$$F(e) = \frac{(2.97 - e)^2}{1 + e}, \tag{10}$$

The comparable expression for granular soils with well-rounded particles is as follows:

$$F(e) = \frac{(2.17 - e)^2}{1 + e}, \tag{11}$$

In Equation (9), the elastic variable X, which evolves with plastic hardening, is defined as follows:

$$X = X(\eta) = X_{min} + \frac{X_{max} - X_{min}}{1 + B\left[\left(\frac{M}{\eta}\right)exp(-n^b\psi) - 1\right]}, \tag{12}$$

where values of $X_{max} = 0.95$, $X_{min} = 0.50$, and $B = 0.10$ are adopted from Lashkari, Karimi, Fakharian and Kaviani-Hamedani [43]. In Equation (12), M is the slope of the CSL in p'-q space that takes on values of M_c and M_e for axisymmetric triaxial compression and extension, respectively. The quantity $\eta = q/p'$ is the stress ratio, n^b is a model parameter (to be discussed in the next section), and ψ is the Been and Jefferies state parameter [71] that represents the state dependency of the proposed model by relating a given state of soil with its critical state according to the following:

$$\psi = e - e_c, \tag{13}$$

where e_c is the value of the void ratio (e) at critical state for the current value of p'.

As mentioned above, the moduli K, G, and J appearing in Equation (8) are obtained by suitable partial differentiation of the Gibbs free energy function, giving the following

$$K = \frac{1}{1 - \frac{X(X-1)}{6} \cdot \left(\frac{K_0}{G_0}\right) . \eta^2} K_0 p_{ref} F(e) \left(\frac{p'}{p_{ref}}\right)^X, \tag{14}$$

$$G = \frac{1}{1 - \frac{X(X-1)}{6} \left(\frac{K_0}{G_0}\right) \eta^2} \left(G_0 F(e) + \frac{X(X+1)}{6} K_0 F(e) \eta^2\right) p_{ref} \left(\frac{p'}{p_{ref}}\right)^X, \tag{15}$$

$$J = \frac{1}{1 - \frac{X(X-1)}{6} \cdot \left(\frac{K_0}{G_0}\right) . \eta^2} X \eta K_0 p_{ref} F(e) \left(\frac{p'}{p_{ref}}\right)^X = X \eta K, \tag{16}$$

For the special case of isotropic loading, η = 0. The above moduli then reduce to the following functional forms, originally proposed by Hardin and Richart [72]:

$$K = K_0 p_{ref}\ F(e) \left(\frac{p'}{p_{ref}}\right)^X, \tag{17}$$

$$G = G_0 p_{ref}\ F(e) \left(\frac{p'}{p_{ref}}\right)^X, \tag{18}$$

$$J = 0, \tag{19}$$

2.5. Definition of the Bounding Surface

In p'-q space, the bounding surface is represented by a straight line with the slope of M^b (see Figure 4). M^b is related to the slope of the CSL, M, according to the following:

$$M^b = M\, exp\left(-n^b \psi\right), \tag{20}$$

where n^b is a model parameter by which the peak shear stress is simulated (also see Equation (12)).

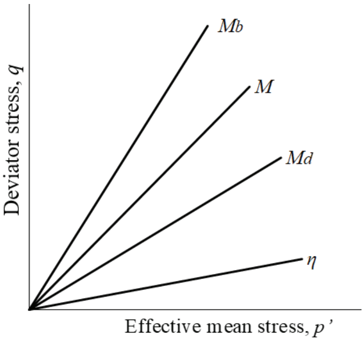

Figure 4. Bounding, critical, and dilatancy surfaces and stress ratio η in p'-q space.

2.6. Definition of the Dilatancy Surface

Similar to the bounding surface, the dilatancy surface is defined as a straight line in p'-q space with a slope of M^d (Figure 4). M^d is also a function of the slope of the CSL according to the following:

$$M^d = M\,exp\left(-n^d\psi\right), \tag{21}$$

where n^d is a model parameter by which the volume phase transformation is simulated.

2.7. Definition of the Critical State Void Ratio

Li and Wang [73], Lashkari and Yaghtin [74], and Lashkari, Karimi, Fakharian and Kaviani-Hamedani [43] used the following relationship to define critical state void ratio for fully saturated soils:

$$e_c = e_0 - \lambda\left(\frac{p'}{p_{ref}}\right)^{\zeta}, \tag{22}$$

where e_0, λ, and ζ are model parameters and p_{ref} is as previously defined. One important attribute of Equation (22) is that, for fully saturated granular soils with various initial densities and stress states, it yields a unique CSL in the space of e versus $\left(\frac{p'}{p_{ref}}\right)^{\zeta}$.

For unsaturated states, critical state experimental data in this space are, however, dependent on the values of matric suction. Consequently, as shown in Figure 5a, a unique line cannot fit all of the experimental data [10]. Indeed, different CSLs need to be defined in this space for different levels of matric suction.

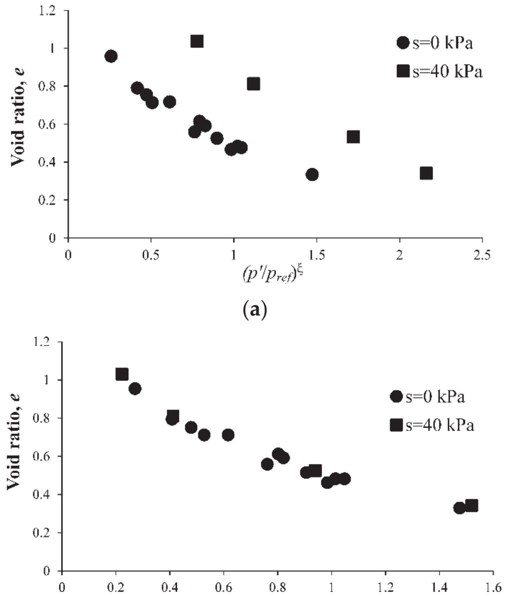

(**a**)

(**b**)

Figure 5. (**a**) Critical state data for an unsaturated soil at different suction values (*s*) and (**b**) normalization of critical state data using Equation (23) (data from Chiu and Ng [10]).

Gallipoli, et al. [75] proposed a normalization approach that brings critical state data with different values of matric suction into a unique line. Their approach, which is adopted in the present model, consists of the following normalization, which relates the critical state effective stress for saturated conditions to its value for unsaturated conditions according to the following:

$$\frac{\left(p_n'\right)_{cs}^{unsat}}{\left(p_n'\right)_{cs}^{sat}} = 1 + g(\xi), \tag{23}$$

where $\left(p_n'\right)_{cs}^{sat}$ and $\left(p_n'\right)_{cs}^{unsat}$ are the critical state effective confining pressures at saturated and unsaturated conditions, respectively.

In Equation (23), the function $g(\xi)$ is given by the following:

$$g(\xi) = a.[exp(b.\xi) - 1], \tag{24}$$

where a and b are model parameters and ξ is a "cementation" parameter. The latter is defined by the following relationship [75]:

$$\xi = f(s).(1 - S_r), \tag{25}$$

where S_r is again the degree of saturation. The term $(1 - S_r)$ takes into account the number of water menisci per unit volume of the soil. The suction-dependent function $f(s)$ represents the magnitude of the inter-particle contact force due to the matric suction.

Referring to the theoretical expression derived by Fisher [76], the maximum value for $f(s)$ is 1.5 (for infinite suction), while its minimum value is 1.0 (for zero suction). In the present model, the following relationship, proposed by Lashkari and Kadivar [77], is used for $f(s)$:

$$f(s) = 1 + \frac{s^{0.75}}{2(125 + s^{0.75})}, \tag{26}$$

Figure 6 shows the variation of $f(s)$ with suction s.

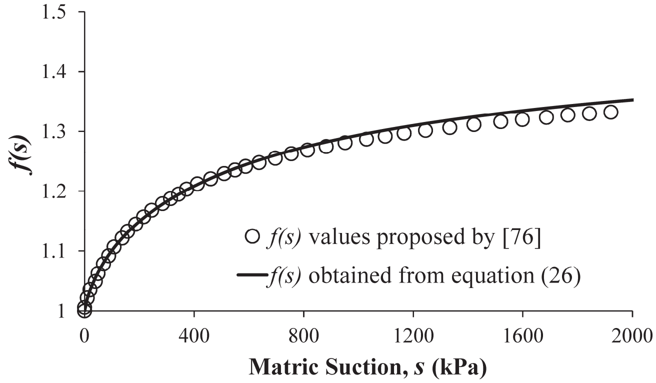

Figure 6. Variation of the function f(s) with matric suction.

Recalling that Equation (22) applies for fully saturated conditions, in light of Equation (23), this expression is modified for unsaturated granular soils, giving the following:

$$e_c = e_0 - \lambda\left(\frac{p'}{p_{ref}(1 + g(\xi))}\right)^{\zeta}, \tag{27}$$

where, e_0, λ, and ζ are again model parameters. Unlike Equation (22), Equation (27) provides a unique CSL in $e - \left(\frac{p'}{p_{ref}(1+g(\xi))}\right)^{\zeta}$ space for unsaturated soils at different initial conditions. Figure 5b illustrates the normalization effect of Equation (27). It is evident that this normalization transforms the scattered experimental data shown in Figure 5a more nearly into a unique line.

2.8. Definition of the Flow Rule, Hardening Rule, and Dilatancy Function

The plastic shear strain rate is obtained using the non-associative flow rule of Dafalias and Manzari [39], which is written as follows:

$$\dot{\varepsilon}_q^p = \langle \Lambda \rangle \frac{\dot{\eta}}{K_p}, \tag{28}$$

where Λ is a scalar loading index, η is again the stress ratio, and K_p is the dimensionless plastic-hardening modulus given by the following:

$$K_p = h_0(1 - c_h e)\left(\frac{M^b}{\eta} - 1\right)\left(\frac{p_{ref}}{p'}\right)^{1-X}, \tag{29}$$

where h_0 and c_h are dimensionless model parameters, M^b is given by Equation (20), and X is the elastic variable defined in Equation (12).

The total irreversible strain vector is then calculated from the following equation:

$$\begin{Bmatrix} \varepsilon_v \\ \varepsilon_q \end{Bmatrix}^i = \begin{Bmatrix} \varepsilon_v \\ \varepsilon_q \end{Bmatrix}^{ei} + \begin{Bmatrix} \varepsilon_v \\ \varepsilon_q \end{Bmatrix}^p = \begin{Bmatrix} \Gamma_{,pX} X_{,\eta} K_p \dot{\boldsymbol{\varepsilon}}_q^p + \dot{\boldsymbol{\varepsilon}}_v^p \\ (\Gamma_{,qX} X_{,\eta} K_p + 1)\dot{\boldsymbol{\varepsilon}}_q^p \end{Bmatrix}, \tag{30}$$

where $\Gamma_{,pX} = \frac{\partial^2 \Gamma}{\partial p' \partial X}$, $\Gamma_{,qX} = \frac{\partial^2 \Gamma}{\partial q \partial X}$, and $X_{,\eta} = \frac{\partial X}{\partial \eta}$, with Γ being the Gibbs free energy function given by Equation (9).

For isotropic loading ($J = 0$), by imposing the consistency condition and combining it with Equations (8) and (30), the scalar loading index is calculated from the following equation:

$$\Lambda = \frac{3G\dot{\varepsilon}_q - K\eta\dot{\varepsilon}_v}{p'K_p + (1 + \Gamma_{,q}\chi \mathrm{X}_{,\eta} K_p)(3G - K\eta d)}, \tag{31}$$

which has the form of the loading index originally given by Dafalias and Manzari [39]. In Equation (31), d is the following dilatancy function:

$$d = A^d \left[2 - \sqrt{\frac{\langle M^d - \eta \rangle}{(1 + c)M}}\right]\left(M^d - \eta\right), \tag{32}$$

In Equation (32), A_d is a model parameter, and $c = M_e/M_c$, where M_c and M_e are again the slopes of critical state lines in axisymmetric triaxial compression and extension, respectively [39]. According to Lashkari, Karimi, Fakharian and Kaviani-Hamedani [43], for practical problems, a value of $c = 0.7$ provides reasonable results. As such, this value is adopted in this work. Knowing that $d = \frac{\dot{\varepsilon}_v^i}{\dot{\varepsilon}_q^i}$ and considering Equation (30), the plastic volumetric strain rate is given by the following:

$$\dot{\varepsilon}_v^p = \left[(d\Gamma_{,q\chi} - \Gamma_{,p\chi})\chi_{,\eta} K_p + d\right]\dot{\varepsilon}_q^p, \tag{33}$$

3. Determination of Model Parameters

Associated with the most general form of the present model are 14 parameters (K_0, G_0, e_0, λ, a, b, ζ, M_c, M_e, n^b, n^d, A^d, h_0, and c_h) whose values must be determined for a particular soil. There are also four parameters with default values of p_{ref} = 101 kPa, X_{max} = 0.95, X_{min} = 0.50, and B = 0.10 that can be used for all soils. Six additional parameters (a_v, Ω, n_v, m_v, S_{r0}, and s_0) characterize the SWCC function that was adopted in the present model (recall Equations (4) and (5)). The values of these six parameters are obtained by regression-based curve fitting of the SWCC experimental data for a particular soil.

The following sections describe how values for the aforementioned 14 model parameters are determined from experimental data.

3.1. Elastic Parameters

The parameters K_0 and G_0 enter the formulation through the Gibbs free energy function given by Equation (9). They are used in the definition of the elastic moduli K, G, and J as given by Equations (14)–(19). A value for the parameter K_0 can be determined from an isotropic compression test in which p' increases but $q = 0$, thus rendering $J = 0$ from Equation (16). From this test, the bulk modulus K is equal to the slope of the line tangent to the initial portion of the mean effective stress (p') versus volumetric strain curve, from which K_0 can be determined by employing Equation (17). The parameter G_0 is best determined from a test in which q is increased from zero at constant p'. Since the test starts at $q = 0$, η is small initially, thus rendering small values of J from Equation (16). From this test, the value of G is determined from the initial slope of the curve of deviator stress versus distortional strain. In such a test, the value of G_0 is approximately equal to $3G$. Values of K_0 and G_0 can also be determined from the results of resonant column or bender element tests [42].

3.2. Critical State Related Parameters

The seven parameters e_0, λ, a, b, ζ, M_c, and M_e are associated with the definition of the critical state. Values of e_0, λ, a, b, and ζ are determined by fitting a straight line to data plotted in $e - \left(\frac{p'}{p_{ref}(1+g(\xi))}\right)^{\zeta}$ space. The parameters a, b, and ζ are then obtained using Equations (23)–(27). Values of e_0 and λ correspond to the slope and intercept, respectively, of the aforementioned straight line. Finally, the values of M_c and M_e correspond to the slopes of the CSLs that best fit the ultimate states of undrained stress paths, plotted in p'-q space, for axisymmetric triaxial compression and extension tests, respectively.

3.3. Parameters Controlling State-Dependency

The parameters n^b and n^d control the state dependency. At peak shear stress, the state of the soil is on the bounding surface. Here the stress ratio (η) is equal to M^b. Using Equation (20), n^b is computed as follows:

$$n^b = -(1/\psi)\ln(M^b/M) \tag{34}$$

At the point of phase transformation from compressive to dilatational response, the stress point lies on the dilatancy surface, where the dilatancy function given by Equation (32) is zero.

Using Equation (21), n^d is computed as follows:

$$n^d = (1/\psi)\ln\left(M^d/M\right) \tag{35}$$

3.4. Dilatancy Parameter

The dilatancy function, d, is obtained by dividing the irreversible volumetric strain increment by the irreversible distortional strain increment. Following Li and Dafalias [38], it is assumed that the irreversible strain increments are approximately equal to the total strain increments. Therefore $d = \frac{\dot{\varepsilon}_v^i}{\dot{\varepsilon}_q^i} \approx \frac{\dot{\varepsilon}_v}{\dot{\varepsilon}_q}$, which can be obtained from the results of drained axisymmetric triaxial compression tests [68]. With d, M^d, and h known, the value of A^d is then computed from Equation (32), giving the following:

$$A^d = \frac{d}{\left[2 - \sqrt{\frac{\langle M^d - \eta \rangle}{(1+c)M}}\right]\left(M^d - \eta\right)} \tag{36}$$

3.5. Hardening Parameters

Finally, suitable values of the parameters h_0 and c_h, which enter the formulation through Equation (29), are determined by fitting model simulations to deviator stress versus distortional strain data from axisymmetric triaxial tests.

4. Assessment of Predictive Capabilities

The predictive capabilities of the model are next assessed by comparing its simulations with two sets of axisymmetric triaxial test results. Included in these comparisons are simulations obtained using three other bounding surface plasticity models that were previously developed for unsaturated soils.

4.1. Simulation of the Behavior of Clean Sand

Russell and Khalili [32] performed suction-controlled axisymmetric triaxial compression tests on Kurnel sand, which is clean with no fines. For this sand, the specific gravity of the soil particles (G_s) is 2.65, the mean grain size (D_{50}) is 0.31 mm, the uniformity coefficient (C_u) is 1.83, and the minimum and maximum void ratios are 0.60 and 0.92, respectively. Experimental data for the SWCC, along with the best-fit curve given by Equation (5), are presented in Figure 7. CSLs in the space of q-p' and $e - \left(\frac{p'}{p_{ref}(1+g(\xi))}\right)^{\zeta}$ are shown in Figure 8a,b, respectively. The complete set of model parameter values used in simulating the behavior of Kurnel sand is presented in Table 2.

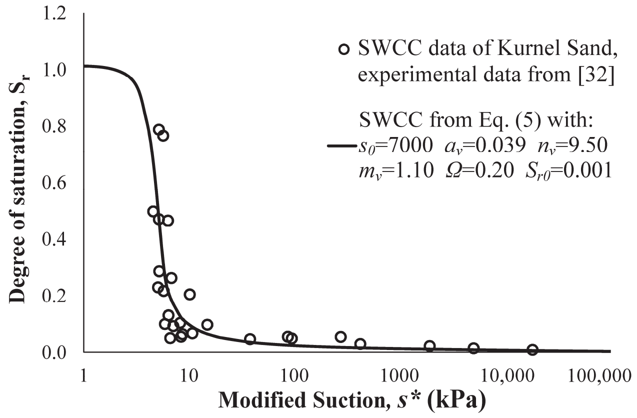

Figure 7. Experimental and analytical soil-water characteristic curves for Kurnel sand.

Table 2. Model parameters used to simulate the behavior of unsaturated Kurnel sand.

Parameter Category	**Elastic**		**Critical State**						**State**		**Dilatancy**	**Hardening**	
Symbol	K_0	G_0	e_0	λ	a	b	ζ	M_c	n^b	n^d	A^d	h_0	c_h
Value	250	200	1.422	0.508	0	0	0.07	1.77	0.5	2.7	0.35	95	0.1

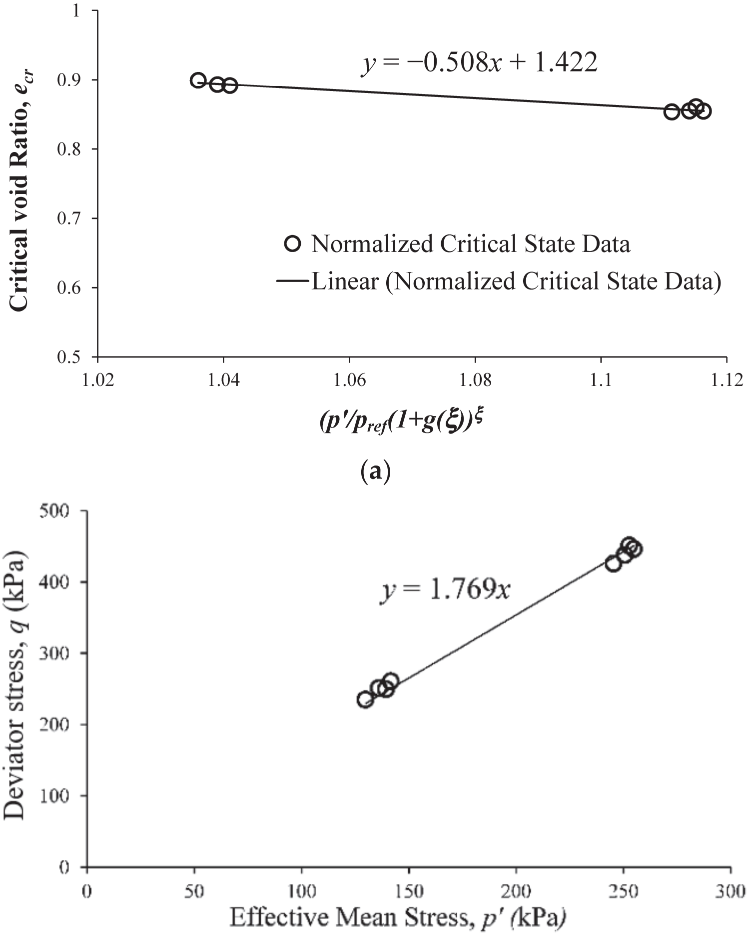

(**a**)

(**b**)

Figure 8. Critical state line for unsaturated Kurnel sand in the space of (**a**) $e-\left(\frac{p'}{p_{ref}(1+g(\xi))}\right)^{\zeta}$ and (**b**) $q-p'$ (experimental data from Russell and Khalili [32]).

Figures 9–12 compare the model simulations with experimental data and with the simulations obtained using the bounding surface models of Russell and Khalili [32] and Morvan, Wong and Branque [41]. The matric suction was maintained constant in these tests. Associated with the results shown in Figures 9–12 were suctions of 51, 100, and 200 kPa, respectively. In these tests, the radial net stress varied from approximately 50 to approximately 100 kPa, and the initial void ratio varied between 0.658 and 0.780.

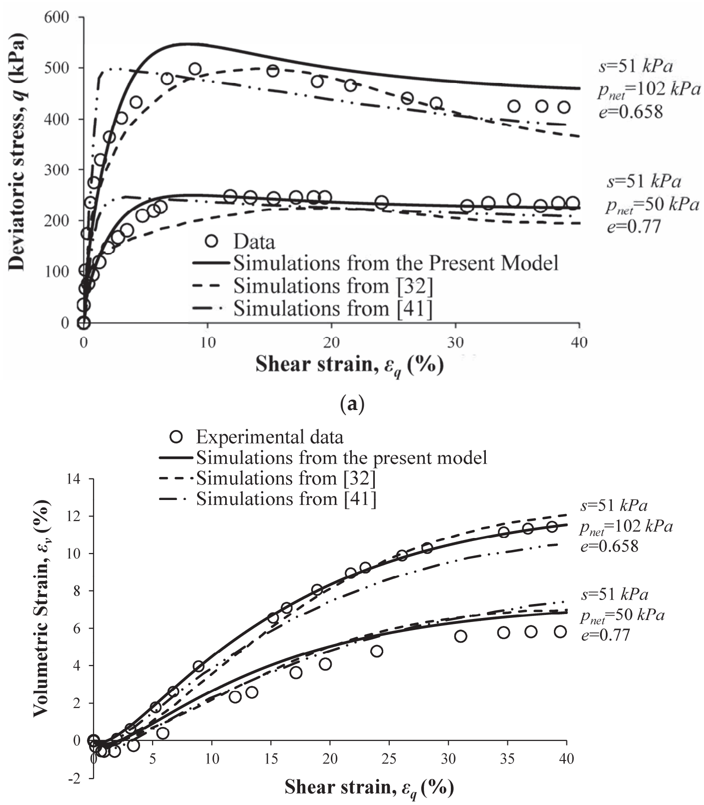

(**a**)

(**b**)

Figure 9. Simulations from multiple bounding surface models for unsaturated soils at constant matric suction of s = 51 kPa: (**a**) deviator stress vs. shear strain, and (**b**) volumetric strain vs. distortional strain (experimental data from Russell and Khalili [32]).

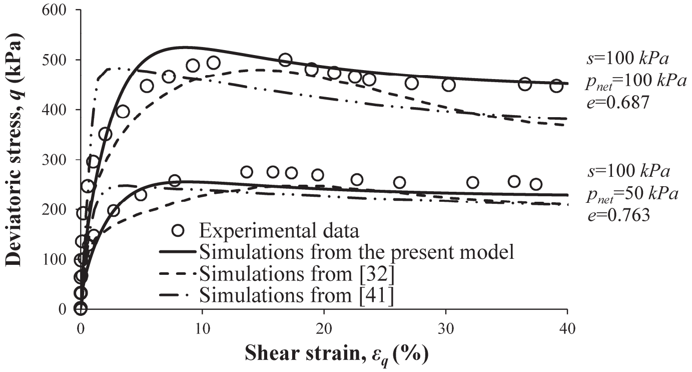

(**a**)

Figure 10. *Cont.*

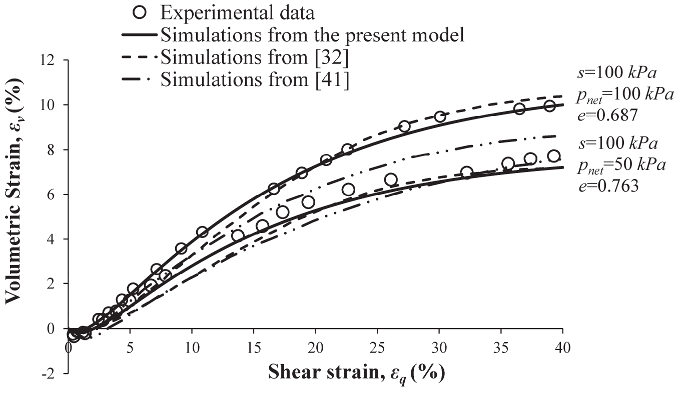

(**b**)

Figure 10. Simulations from multiple bounding surface models for unsaturated soils at constant matric suction of s = 100 kPa: (**a**) deviator stress vs. distortional strain, and (**b**) volumetric strain vs. distortional strain (experimental data from Russell and Khalili [32]).

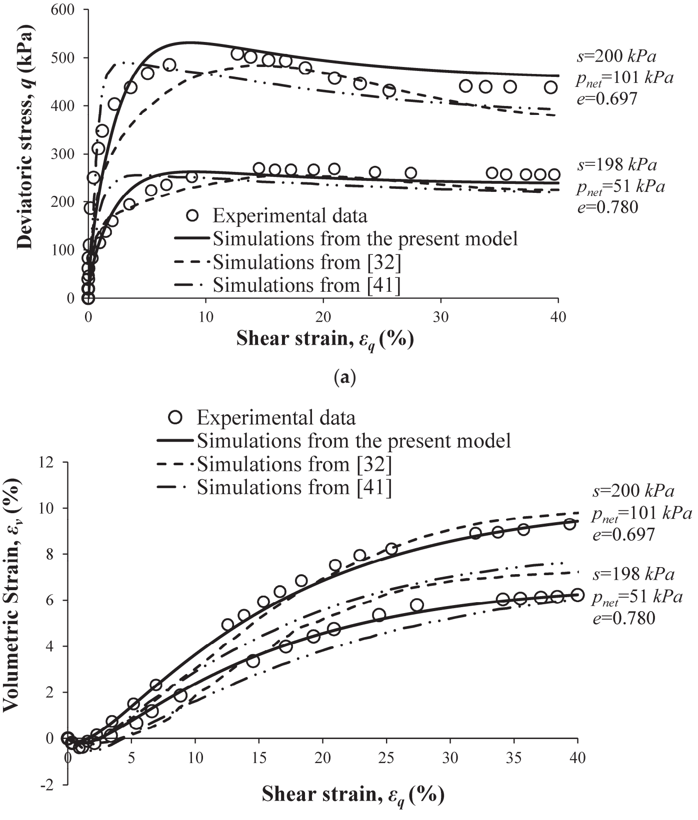

(**a**)

(**b**)

Figure 11. Simulations from multiple bounding surface models for unsaturated soils at constant matric suction of s = 200 kPa: (**a**) deviator stress vs. distortional strain, and (**b**) volumetric strain vs. distortional strain (experimental data from Russell and Khalili [32]).

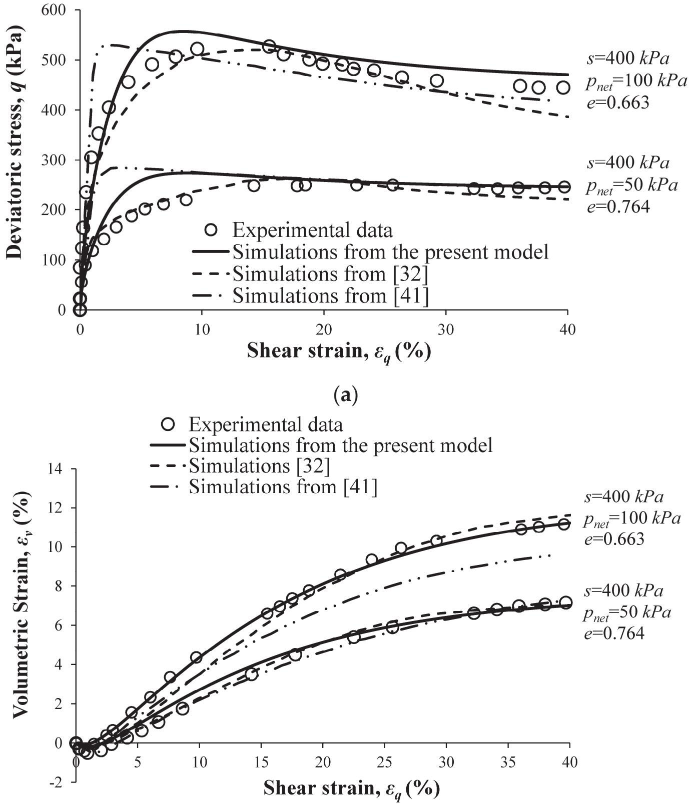

(**a**)

(**b**)

Figure 12. Simulations from multiple bounding surface models for unsaturated soils at constant matric suction of s = 400 kPa: (**a**) deviator stress vs. distortional strain, and (**b**) volumetric strain vs. distortional strain (experimental data from Russell and Khalili [32]).

From Figures 9–12, it is evident that the present model accurately simulates the experimental deviator stress versus distortional strain and volumetric strain versus distortional strain results. Comparing these simulations to those obtained using the bounding surface models of [32,41], it is evident that they are in better agreement with the experimental results. In particular, simulations from the model of Morvan, Wong and Branque [41] give a “stiffer” stress–strain response. This model is also unable to reproduce the critical state data, in terms of either volumetric strain or shear strength, especially at the higher radial net stress of 100 kPa. The model of Russell and Khalili [32], on the other hand, simulates a “softer” behavior as compared to the experimental data. Compared to the present model, it is less accurate at critical state. In addition, for the radial net stress of 50 kPa, the model predicted the peak deviatoric stress more accurately than the other two models. However, at the higher radial net stress of approximately 100 kPa, the Russell and Khalili [32] model provides a somewhat more accurate simulation.

4.2. Simulation of the Behavior of a Silty Sand

The present model is next used to simulate the axisymmetric triaxial behavior of silty sand. The experimental data for this soil have been reported by Patil et al. [29]. The soil consists of 55% sand, 37% silt, and 8% non-plastic clay-size fraction. For this soil, G_s is 2.67. The maximum dry density and optimum water content of the soil are

1.87 g/cm^3 and 12.2%, respectively. Experimental data for the SWCC, along with the best-fit curve given by Equation (5), are presented in Figure 13. Critical state lines in q-p' and $e-\left(p'/p_{ref}(1+g(\xi))\right)^{\zeta}$ spaces are shown in Figure 14a,b, respectively. The complete set of model parameter values used in simulating the behavior of the silty sand is presented in Table 3.

Table 3. Model parameters used to simulate the behavior of unsaturated silty sand.

Parameter Category	**Elastic**		**Critical State**						**State**		**Dilatancy**	**Hardening**	
Parameter Symbol	K_0	G_0	e_0	λ	a	b	ζ	M_c	n^b	n^d	A^d	h_0	c_h
Value	250	200	0.83	0.32	0.57	1.73	1.18	1.33	4.4	0.75	0.6	105	0.2

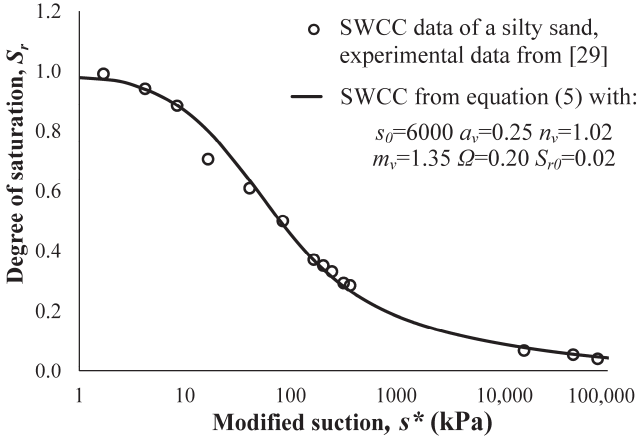

Figure 13. Soil-water characteristic curve for silty sand [29].

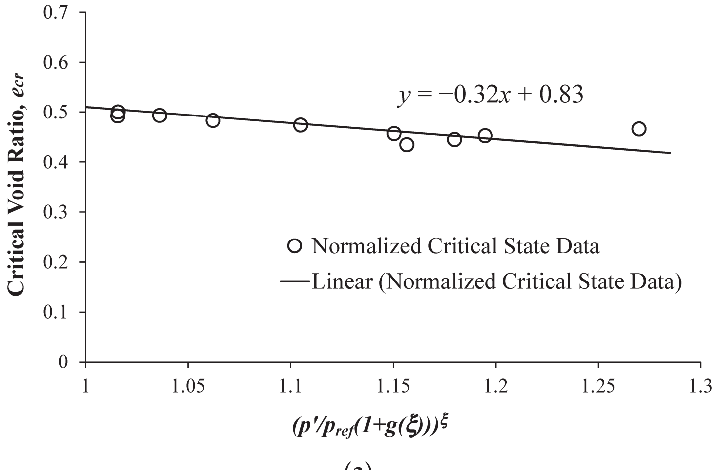

(**a**)

Figure 14. *Cont.*

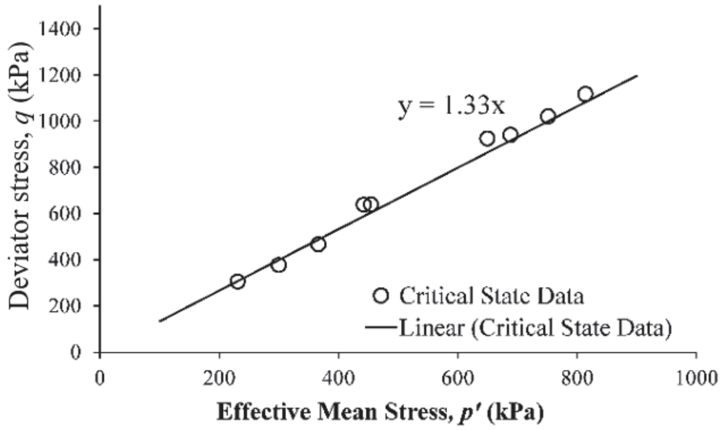

(**b**)

Figure 14. Critical state line for unsaturated silty sand in the space of (**a**) $e - \left(\frac{p'}{p_{ref}(1+g(\xi))}\right)^{\zeta}$ and (**b**) q-p' (data from [29]).

The triaxial compression tests were performed at four different suction values (50, 250, 500, and 750 kPa) and three different values of radial net stress (100, 200, and 300 kPa). In Figures 15–18, the simulations obtained using the present model are compared with experimental data and with the simulations reported by Patil et al. [28]. Values of suction, radial net stress, and initial void ratio for each test are indicated on these figures.

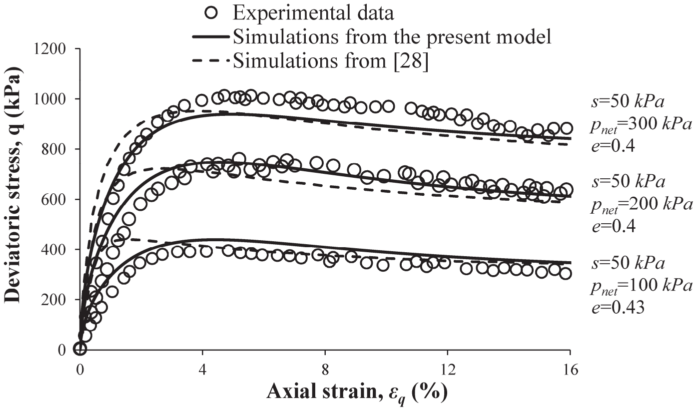

(**a**)

Figure 15. *Cont.*

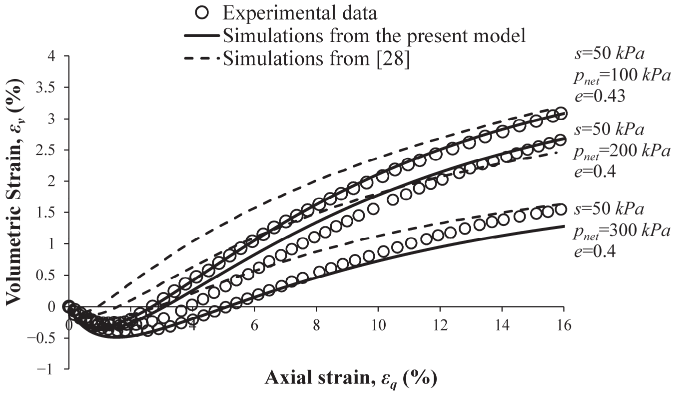

(**b**)

Figure 15. Simulations from two bounding surface models for unsaturated soils at constant matric suction of s = 50 kPa: (**a**) deviator stress vs. axial strain, and (**b**) volumetric strain vs. axial strain (data from Patil, Hoyos and Puppala [29]).

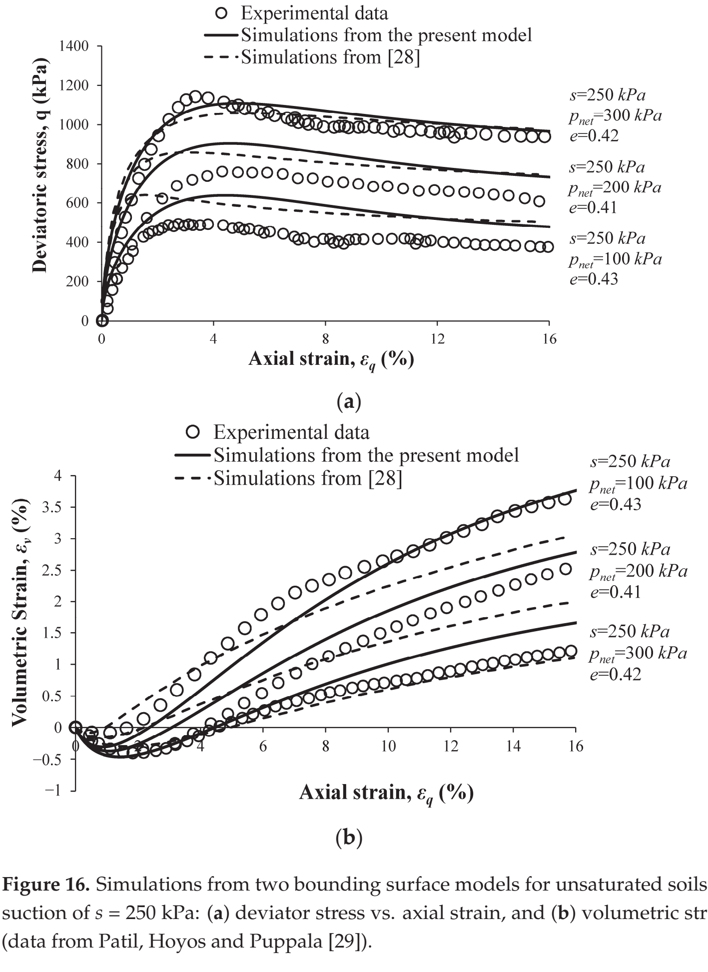

(**a**)

(**b**)

Figure 16. Simulations from two bounding surface models for unsaturated soils at constant matric suction of s = 250 kPa: (**a**) deviator stress vs. axial strain, and (**b**) volumetric strain vs. axial strain (data from Patil, Hoyos and Puppala [29]).

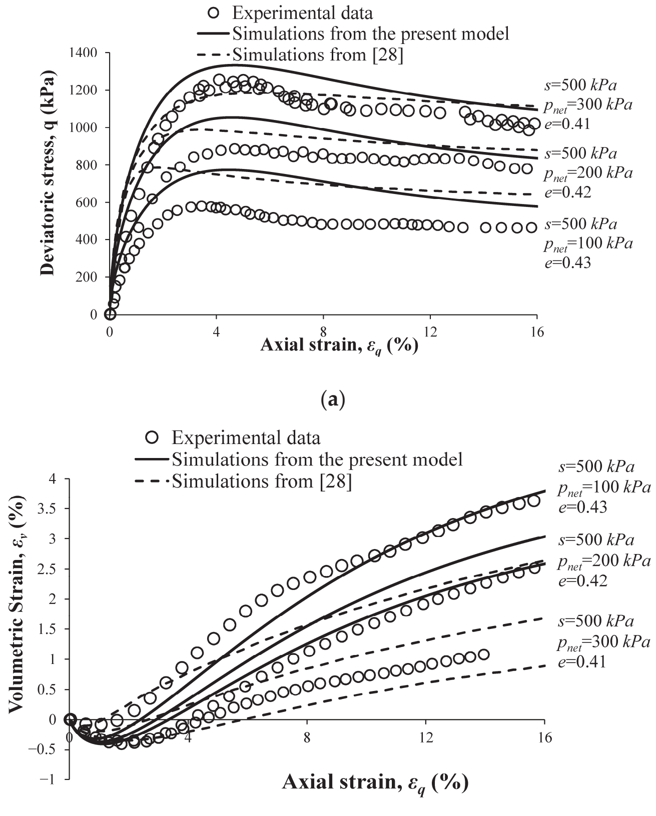

(**a**)

(**b**)

Figure 17. Simulations from two bounding surface models for unsaturated soils at constant matric suction of s = 500 kPa: (**a**) deviator stress vs. axial strain, and (**b**) volumetric strain vs. axial strain (data from Patil, Hoyos and Puppala [29]).

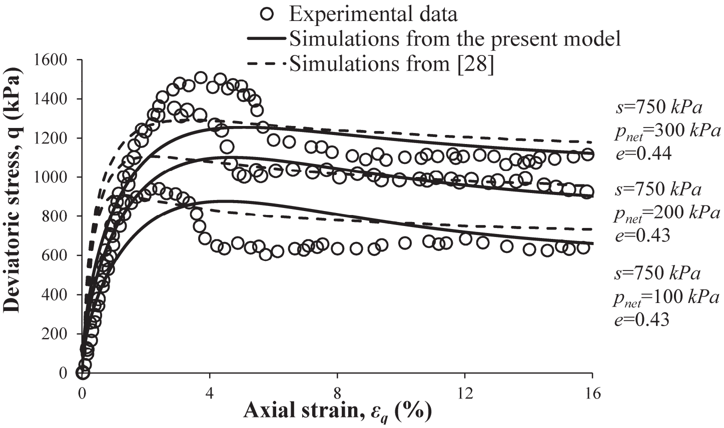

(**a**)

Figure 18. *Cont.*

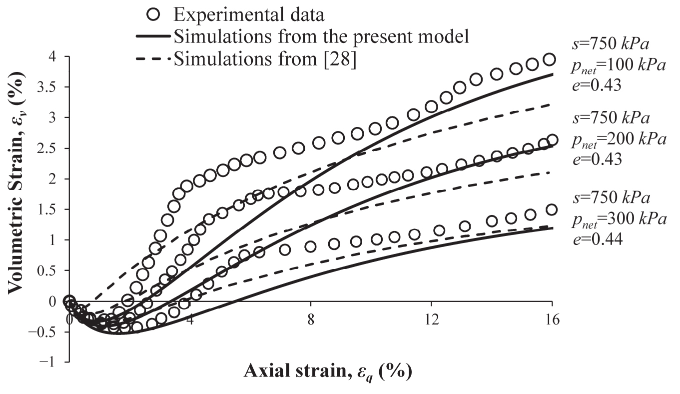

(**b**)

Figure 18. Simulations from two bounding surface models for unsaturated soils at constant matric suction of s = 750 kPa: (**a**) deviator stress vs. axial strain, and (**b**) volumetric strain vs. axial strain (data from Patil, Hoyos and Puppala [29]).

The data of Patil et al. [29] provided in Figures 15–17 shows that the post-peak softening increases with the increasing amount of suction. In particular, the tests at the highest suction value of 750 kPa (Figure 18) show apparent anomalies in the experimental deviator stress and volumetric behavior. The post-peak softening for this test has led to strain localization (i.e., the formation of a shear band). The displayed behavior precludes the simulation of all features of the behavior using any existing model for unsaturated soils. However, to be consistent, the results of the present model are presented for all the data. It can be observed that the present model is able to simulate the trend of the deviator stress and volumetric behavior shown in Figures 15–17. Compared to the bounding surface model of Patil et al. [28], the present model yields better agreement with the experimental data. In particular, the model of Patil et al. [28] predicts a stiffer initial deviator stress–axial strain response, while the present model is smooth and close to the experimental data. Also, at the critical state, the present model shows a better overall agreement with the experimental data.

5. Conclusions

A state-dependent, critical state-compatible constitutive model that accounts for the effect of matric suction on the hydro-mechanical response of unsaturated granular soils was presented in this paper. The model is formulated in a rate-independent bounding surface plasticity framework and incorporates a newer generation definition of effective stress. The model is an enhanced extension of the hyperelastic model for fully saturated granular soils that was originally proposed by Lashkari, Karimi, Fakharian and Kaviani-Hamedani [43]. Based on the observations of physical phenomena during laboratory testing of unsaturated granular soils, the stress–strain response of the unsaturated soil is assumed to be exclusively elastoplastic, with no purely elastic region. To satisfy the law of conservation of energy, the elastic components of the elastoplastic strains are calculated from a Gibbs free energy function in a hyperelastic formulation. Associated with the most general form of the present model are fourteen parameters whose values must be determined for a particular soil. Six additional parameters characterize the SWCC. The model was calibrated for two different sets of unsaturated experimental results, one for pure sand and one for silty sand. The predictive capabilities of the model were assessed by comparing simulations generated using the model with experimental data and with the simulations of the same data from three previously developed bounding surface constitutive models for unsaturated soils. The present model was shown to accurately simulate the behavior of unsaturated granular soils at various levels of initial matric suction, confining pressure, and void ratio. In addition, in many instances, the present model gave more accurate simulations than earlier bounding surface models for unsaturated soils.

Author Contributions: Conceptualization, M.K., K.N.M. and V.N.K.; methodology, M.K., K.N.M. and V.N.K.; software, M.K., K.N.M. and V.N.K.; validation, M.K., K.N.M. and V.N.K.; formal analysis, M.K., K.N.M. and V.N.K.; investigation, M.K., K.N.M. and V.N.K.; resources, M.K., K.N.M. and V.N.K.; data curation, M.K., K.N.M. and V.N.K.; writing—original draft preparation, M.K., K.N.M. and V.N.K.; writing—review and editing, M.K., K.N.M. and V.N.K.; visualization, M.K., K.N.M. and V.N.K.; supervision, K.N.M. and V.N.K.; project administration, K.N.M. and V.N.K.; funding acquisition, K.N.M. All authors have read and agreed to the published version of the manuscript.

Funding: This research received no external funding.

Data Availability Statement: Some or all data, models, or code that support the findings of this study are available from the corresponding author upon reasonable request.

Conflicts of Interest: The authors declare no conflicts of interest.

References

1. Wray, W.K.; Meyer, K.T. Expansive Clay Soil—A Widespread and Costly GeoHazard. *Geo-Strat.—Geo Inst. ASCE* **2004**, *5*, 24–28.
2. Alonso, E.E.; Gens, A.; Josa, A. A constitutive model for partially saturated soils. *Géotechnique* **1990**, *40*, 405–430. [CrossRef]
3. Roscoe, K.H.; Burland, J. *On the Generalized Stress-Strain Behavior of Wet Clay*; Heyman, J., Leckie, F., Eds.; Cambridge University Press: Cambridge, UK, 1968; pp. 535–609.
4. Fredlund, D.G.; Morgenstern, N.R.; Widger, R.A. The shear strength of unsaturated soils. *Can. Geotech. J.* **1978**, *15*, 313–321. [CrossRef]
5. Fredlund, D.G.; Morgenstern, N.R. Stress state variables for unsaturated soils. *J. Geotech. Eng. Div.* **1977**, *103*, 447–466. [CrossRef]
6. Wheeler, S.J.; Sivakumar, V. An elasto-plastic critical state framework for unsaturated soil. *Géotechnique* **1995**, *45*, 35–53. [CrossRef]
7. Sheng, D.; Fredlund, D.G.; Gens, A. A new modelling approach for unsaturated soils using independent stress variables. *Can. Geotech. J.* **2008**, *45*, 511–534. [CrossRef]
8. Cui, Y.J.; Delage, P. Yielding and plastic behaviour of an unsaturated compacted silt. *Géotechnique* **1996**, *46*, 291–311. [CrossRef]
9. Thomas, H.R.; He, Y. Analysis of coupled heat moisture and air transfer in a deformable unsaturated soil. *Géotechnique* **1994**, *44*, 667–689.
10. Chiu, C.F.; Ng, C.W.W. A state-dependent elasto-plastic model for saturated and unsaturated soils. *Géotechnique* **2003**, *53*, 809–829. [CrossRef]
11. Gens, A.; Sánchez, M.; Sheng, D. On constitutive modelling of unsaturated soils. *Acta Geotech.* **2006**, *1*, 137. [CrossRef]
12. Nuth, M.; Laloui, L. Effective stress concept in unsaturated soils: Clarification and validation of a unified framework. *Int. J. Numer. Anal. Methods Geomech.* **2008**, *32*, 771–801. [CrossRef]
13. Sheng, D. Review of fundamental principles in modelling unsaturated soil behaviour. *Comput. Geotech.* **2011**, *38*, 757–776. [CrossRef]
14. Houlsby, G.T. The work input to an unsaturated granular material. *Géotechnique* **1997**, *47*, 193–196. [CrossRef]
15. Bishop, A.W. The principle of effective stress. *Tec. Ukebl.* **1959**, *39*, 859–863.
16. Sheng, D.; Sloan, S.W.; Gens, A. A constitutive model for unsaturated soils: Thermomechanical and computational aspects. *Comput. Mech.* **2004**, *33*, 453–465. [CrossRef]
17. Sun, D.a.; Sheng, D.; Sloan, S.W. Elastoplastic modelling of hydraulic and stress–strain behaviour of unsaturated soils. *Mech. Mater.* **2007**, *39*, 212–221. [CrossRef]
18. Sun, D.A.; Sheng, D.C.; Cui, H.B.; Sloan, S.W. A density-dependent elastoplastic hydro-mechanical model for unsaturated compacted soils. *Int. J. Numer. Anal. Methods Geomech.* **2007**, *31*, 1257–1279. [CrossRef]
19. Loret, B.; Khalili, N. An effective stress elastic–plastic model for unsaturated porous media. *Mech. Mater.* **2002**, *34*, 97–116. [CrossRef]
20. Pereira, J.M.; Wong, H.; Dubujet, P.; Dangla, P. Adaptation of existing behaviour models to unsaturated states: Application to CJS model. *Int. J. Numer. Anal. Methods Geomech.* **2005**, *29*, 1127–1155. [CrossRef]
21. Bolzon, G.; Schrefler, B.A.; Zienkiewicz, O.C. Elastoplastic soil constitutive laws generalized to partially saturated states. *Géotechnique* **1996**, *46*, 279–289. [CrossRef]
22. Zhou, C.; Ng, C.W.W.; Chen, R. A bounding surface plasticity model for unsaturated soil at small strains. *Int. J. Numer. Anal. Methods Geomech.* **2015**, *39*, 1141–1164. [CrossRef]
23. Hu, R.; Liu, H.-H.; Chen, Y.; Zhou, C.; Gallipoli, D. A constitutive model for unsaturated soils with consideration of inter-particle bonding. *Comput. Geotech.* **2014**, *59*, 127–144. [CrossRef]
24. Manzanal, D.; Pastor, M.; Merodo, J.A.F. Generalized plasticity state parameter-based model for saturated and unsaturated soils. Part II: Unsaturated soil modeling. *Int. J. Numer. Anal. Methods Geomech.* **2011**, *35*, 1899–1917. [CrossRef]

25. Mašín, D.; Khalili, N. Swelling phenomena and effective stress in compacted expansive clays. *Can. Geotech. J.* **2015**, *53*, 134–147. [CrossRef]
26. Wheeler, S.J.; Sharma, R.S.; Buisson, M.S.R. Coupling of hydraulic hysteresis and stress–strain behaviour in unsaturated soils. *Géotechnique* **2003**, *53*, 41–54. [CrossRef]
27. Maleki, M.; Pouyan, H. A kinematic hardening based model for unsaturated soils considering different hydraulic conditions. *Int. J. Numer. Anal. Methods Geomech.* **2016**, *40*, 2271–2290. [CrossRef]
28. Patil, U.D.; Hoyos, L.R.; Morvan, M.; Puppala, A.J. Bounding surface-based modeling of compacted silty sand exhibiting suction dependent postpeak strain softening. *Int. J. Numer. Anal. Methods Geomech.* **2018**, *42*, 1741–1761. [CrossRef]
29. Patil, U.D.; Hoyos, L.R.; Puppala, A.J. Modeling Essential Elastoplastic Features of Compacted Silty Sand via Suction-Controlled Triaxial Testing. *Int. J. Geomech.* **2016**, *16*, D4016012. [CrossRef]
30. Kadivar, M.; Manahiloh, K.N.; Kaliakin, V.N. A Bounding Surface Based Constitutive Model for Unsaturated Granular Soils. In Proceedings of the Geo-Congress 2019, Philadelphia, PA, USA, 24–27 March 2019.
31. Santagiuliana, R.; Schrefler, B.A. Enhancing the Bolzon–Schrefler–Zienkiewicz Constitutive Model for Partially Saturated Soil. *Transp. Porous Media* **2006**, *65*, 1–30. [CrossRef]
32. Russell, A.R.; Khalili, N. A unified bounding surface plasticity model for unsaturated soils. *Int. J. Numer. Anal. Methods Geomech.* **2006**, *30*, 181–212. [CrossRef]
33. Krieg, R.D. A Practical Two Surface Plasticity Theory. *J. Appl. Mech.* **1975**, *42*, 641–646. [CrossRef]
34. Dafalias, Y.F.; Popov, E.P. Cyclic loading for materials with a vanishing elastic region. *Nucl. Eng. Des.* **1977**, *41*, 293–302. [CrossRef]
35. Kaliakin, V.N.; Dafalias, Y.F. Simplifications to the bounding surface model for cohesive soils. *Int. J. Numer. Anal. Methods Geomech.* **1989**, *13*, 91–100. [CrossRef]
36. Bardet, J.P. Bounding Surface Plasticity Model for Sands. *J. Eng. Mech.* **1986**, *112*, 1198–1217. [CrossRef]
37. Manzari, M.T.; Dafalias, Y.F. A critical state two-surface plasticity model for sands. *Géotechnique* **1997**, *47*, 255–272. [CrossRef]
38. Li, X.S.; Dafalias, Y.F. Dilatancy for cohesionless soils. *Géotechnique* **2000**, *50*, 449–460. [CrossRef]
39. Dafalias, Y.F.; Manzari, M.T. Simple Plasticity Sand Model Accounting for Fabric Change Effects. *J. Eng. Mech.* **2004**, *130*, 622–634. [CrossRef]
40. Kaliakin, V.N.; Nieto-Leal, A.; Mashayekhi, M. Modeling the Time- and Temperature-Dependent Response of Cohesive Soils in a Generalized Bounding Surface Framework. *Transp. Infrastruct. Geotechnol.* **2018**, *5*, 250–286. [CrossRef]
41. Morvan, M.; Wong, H.; Branque, D. An unsaturated soil model with minimal number of parameters based on bounding surface plasticity. *Int. J. Numer. Anal. Methods Geomech.* **2010**, *34*, 1512–1537. [CrossRef]
42. Lashkari, A.; Golchin, A. On the influence of elastic-plastic coupling on sands response. *Comput. Geotech.* **2014**, *55*, 352–364. [CrossRef]
43. Lashkari, A.; Karimi, A.; Fakharian, K.; Kaviani-Hamedani, F. Prediction of Undrained Behavior of Isotropically and Anisotropically Consolidated Firoozkuh Sand: Instability and Flow Liquefaction. *Int. J. Geomech.* **2017**, *17*, 04017083. [CrossRef]
44. Li, Q.; Zhu, Z. Calibration of an elastoplastic model of sand liquefaction using the swarm intelligence with a multi-objective function. *J. Rock Mech. Geotech. Eng.* **2023**, *15*, 789–802. [CrossRef]
45. Schefler, B. The Finite Element Method in Soil Consolidation (with Applications to Surface Subsidence). Doctoral Dissertation, University College of Swansea, Swansea, UK, 1984.
46. Maatouk, A.; Leroueil, S.; Rochelle, P.L. Yielding and critical state of a collapsible unsaturated silty soil. *Géotechnique* **1995**, *45*, 465–477. [CrossRef]
47. Fredlund, D.G.; Xing, A. Equations for the soil-water characteristic curve. *Can. Geotech. J.* **1994**, *31*, 521–532. [CrossRef]
48. van Genuchten, M.T. A Closed-form Equation for Predicting the Hydraulic Conductivity of Unsaturated Soils. *Soil Sci. Soc. Am. J.* **1980**, *44*, 892–898. [CrossRef]
49. Gallipoli, D.; Bruno, A.W.; D'onza, F.; Mancuso, C. A bounding surface hysteretic water retention model for deformable soils. *Géotechnique* **2015**, *65*, 793–804. [CrossRef]
50. Lu, N.; Godt, J.W.; Wu, D.T. A closed-form equation for effective stress in unsaturated soil. *Water Resour. Res.* **2010**, *46*, 2009WR008646. [CrossRef]
51. Brooks, R.H.; Corey, A.T. *Hydraulic Properties of Porous Media*; Colorado State University: Fort Collins, CO, USA, 1964.
52. Gardner, W.R. Some steady state solutions of the unsaturated moisture flow equation with application to evaporation from a water table. *Soil Sci. Am.* **1958**, *85*, 228–232. [CrossRef]
53. Mualem, Y. A new model for predicting the hydraulic conductivity of unsaturated porous media. *Water Resour. Res.* **1976**, *12*, 513–522. [CrossRef]
54. Burdine, N.T. Relative permeability calculations from pore size distribution data. *Trans. AIME* **1952**, *198*, 71–77. [CrossRef]
55. Haines, W.B. Studies in the physical properties of soils. V. The hysteresis effect in capillary properties and the modes of moisture distribution associated therewith. *J. Agric. Sci.* **1930**, *20*, 97–116. [CrossRef]
56. Poulovassilis, A. Hysteresis of pore water, an application of the concept of independent domains. *J. Soil Sci.* **1962**, *93*, 405–412. [CrossRef]
57. Ng, C.W.W.; Pang, Y.W. Experimental investigation of soil–water characteristics of a volcanic soil. *Can. Geotech. J.* **2000**, *37*, 1252–1264. [CrossRef]

58. Ng, C.W.W.; Pang, Y.W. Influence of stress state on soil–water characteristics and slope stability. *J. Geotech. Geoenviron. Eng.* **2000**, *26*, 157–166. [CrossRef]
59. Vanapalli, S.K.; Fredlund, D.G.; Pufahl, D.E. The influence of soil structure and stress history on the soil-water characteristics of a compacted till. *Géotechnique* **1999**, *49*, 143–159. [CrossRef]
60. Romero, E.; Vaunat, J. Retention curves of deformable clays. In *International Workshop on Unsaturated Soils: Experimental Evidence and Theoretical Approaches in Unsaturated Soils*; CRC Press: Boca Raton, FL, USA, 2000; pp. 91–106.
61. Sivakumar, V.A. A Critical State Framework for Unsaturated Soil. Doctoral Dissertation, University of Sheffield, Sheffield, UK, 1993.
62. Wheeler, S.J. Inclusion of specific water volume within an elasto-plastic model for unsaturated soil. *Can. Geotech. J.* **1996**, *33*, 42–57. [CrossRef]
63. Gallipoli, D.; Wheeler, S.J.; Karstunen, M. Modelling the variation of degree of saturation in a deformable unsaturated soil. *Géotechnique* **2003**, *53*, 105–112. [CrossRef]
64. Zhang, X.; Lytton, R.L. Discussion of "A new modelling approach for unsaturated soils using independent stress variables". *Can. Geotech. J.* **2008**, *45*, 1784–1787. [CrossRef]
65. Sheng, D.; Fredlund, D.G.; Gens, A. Reply to the discussion by Zhang and Lytton on 'A new modelling approach for unsaturated soils using independent stress variables'. *Can. Geotech.* **2008**, *45*, 1788–1794. [CrossRef]
66. Collins, I.F.; Houlsby, G.T. Application of thermomechanical principles to the modelling of geotechnical materials. *Proc. R. Soc. Lond. Ser. A Math. Phys. Eng. Sci.* **1997**, *453*, 1975–2001. [CrossRef]
67. Maier, G.; Hueckel, T. Nonassociated and coupled flow rules of elastoplasticity for rock-like materials. *Int. J. Rock Mech. Min. Sci. Geomech. Abstr.* **1979**, *16*, 77–92. [CrossRef]
68. Golchin, A.; Lashkari, A. A critical state sand model with elastic–plastic coupling. *Int. J. Solids Struct.* **2014**, *51*, 2807–2825. [CrossRef]
69. Alipour, M.J.; Lashkari, A. Sand instability under constant shear drained stress path. *Int. J. Solids Struct.* **2018**, *150*, 66–82. [CrossRef]
70. Einav, I.; Puzrin, A.M. Pressure-Dependent Elasticity and Energy Conservation in Elastoplastic Models for Soils. *J. Geotech. Geoenviron. Eng.* **2004**, *130*, 81–92. [CrossRef]
71. Been, K.; Jefferies, M.G. A state parameter for sands. *Géotechnique* **1985**, *35*, 99–112. [CrossRef]
72. Hardin, B.O.; Richart, F.E. Elastic Wave Velocities in Granular Soils. *J. Soil Mech. Found. Div.* **1963**, *89*, 33. [CrossRef]
73. Li, X.S.; Wang, Y. Linear Representation of Steady-State Line for Sand. *J. Geotech. Geoenviron. Eng.* **1998**, *124*, 1215–1217. [CrossRef]
74. Lashkari, A.; Yaghtin, M.S. Sand flow liquefaction instability under shear–volume coupled strain paths. *Géotechnique* **2018**, *68*, 1002–1024. [CrossRef]
75. Gallipoli, D.; Gens, A.; Sharma, R.; Vaunat, J. An elasto-plastic model for unsaturated soil incorporating the effects of suction and degree of saturation on mechanical behaviour. *Géotechnique* **2003**, *53*, 123–135. [CrossRef]
76. Fisher, A.R. On the Capillary Forces in an Ideal Soil; Correction of Formulae Given by W. B. Haines. *J. Agric. Sci.* **1926**, *16*, 492–505. [CrossRef]
77. Lashkari, A.; Kadivar, M. A constitutive model for unsaturated soil–structure interfaces. *Int. J. Numer. Anal. Methods Geomech.* **2016**, *40*, 207–234. [CrossRef]

geosciences

Article

Shear Banding and Cracking in Unsaturated Porous Media through a Nonlocal THM Meshfree Paradigm

Hossein Pashazad and Xiaoyu Song *

Engineering School of Sustainable Infrastructure and Environment, University of Florida,
Gainesville, FL 32611, USA; hossein.pashazad@ufl.edu
* Correspondence: xysong@ufl.edu

Abstract: The mechanical behavior of unsaturated porous media under non-isothermal conditions plays a vital role in geo-hazards and geo-energy engineering (e.g., landslides triggered by fire and geothermal energy harvest and foundations). Temperature increase can trigger localized failure and cracking in unsaturated porous media. This article investigates the shear banding and cracking in unsaturated porous media under non-isothermal conditions through a thermo–hydro–mechanical (THM) periporomechanics (PPM) paradigm. PPM is a nonlocal formulation of classical poromechanics using integral equations, which is robust in simulating continuous and discontinuous deformation in porous media. As a new contribution, we formulate a nonlocal THM constitutive model for unsaturated porous media in the PPM paradigm in this study. The THM meshfree paradigm is implemented through an explicit Lagrangian meshfree algorithm. The return mapping algorithm is used to implement the nonlocal THM constitutive model numerically. Numerical examples are presented to assess the capability of the proposed THM mesh-free paradigm for modeling shear banding and cracking in unsaturated porous media under non-isothermal conditions. The numerical results are examined to study the effect of temperature variations on the formation of shear banding and cracking in unsaturated porous media.

Keywords: shear banding; cracking; unsaturated porous media; THM; periporomechanics

Citation: Pashazad, H.; Song, X. Shear Banding and Cracking in Unsaturated Porous Media through a Nonlocal THM Meshfree Paradigm. *Geosciences* **2024**, *14*, 103. https://doi.org/10.3390/geosciences14040103

Academic Editors: Laureano R. Hoyos, Dunja Perić and Jesus Martinez-Frias

Received: 20 January 2024
Revised: 3 April 2024
Accepted: 4 April 2024
Published: 9 April 2024

1. Introduction

The thermo–hydro–mechanical (THM) behavior of unsaturated porous media, such as soils, plays a crucial role in various engineering applications, including nuclear waste disposal storage, pavement design, fault propagation, landslides, geothermal energy utilization, and the performance of buried high-voltage cables (e.g., [1–8]). Temperature variations can significantly impact the mechanical and physical properties of unsaturated soils, influencing parameters such as shear strength, deformation characteristics, fluid flow behavior, and mass transport properties at multiple length scales [9–16]. For instance, temperature changes can lead to complex behaviors in unsaturated soils, including volumetric strain or dilation, which may vary depending on factors like the overconsolidation ratio of the soil. Consequently, both physical experiments and numerical simulations are essential tools for investigating and understanding the coupled multi-physical processes involved in solid deformation, fluid flow, and heat conduction within thermally unsaturated soils (e.g., [10,11,17,18]). These studies, such as the mesoscale finite element modeling of shear banding in thermal unsaturated soils [11] provide valuable insights into the behavior of unsaturated soils under the influence of temperature variations, contributing to more accurate and reliable engineering designs and assessments. Meanwhile, the heat transfer mechanism in porous media at the pore scale and nanosacale [19–21] have been studied in recent years. For instance, in [19], the authors conducted a critical review of the heat transfer enhancement methods in the presence of porous media, nanofluids, and microorganisms. Bai et al. [20] studied the coupled THM mechanism considering the soil particle rearrangement of granular thermodynamics. Farahani et al. [19] investigated the heat transfer in unfrozen and frozen porous media on the pore scale. In this study, as a new contribution, we develop a nonlocal mesh-free THM paradigm for modeling shear banding and cracking in unsaturated soils under elevated temperatures. For this purpose, we formulate a nonlocal THM constitutive model for unsaturated soils and implement the THM constitutive model into the meshfree periporomechanics (PPM) paradigm [22–27]. We refer to the related literature for other numerical methods such as the discrete element method, the extended finite element method (XFEM), and the phase-field method for modeling shear banding and cracking in unsaturated soils (e.g., [28–33], among others). It is worth noting that in [25,34], the authors presented an in-depth review of these methods for modeling unsaturated soils. Next, we sequentially review the constitutive modeling of thermal unsaturated soils and the PPM paradigm.

Significant progress has been made in thermal constitutive modeling for unsaturated soils in recent decades, addressing the intricate interplay between thermal, mechanical, and hydraulic behavior under non-isothermal conditions [35–40]. These advancements are pivotal in understanding the response of unsaturated soils in a wide range of geotechnical applications. Numerous constitutive models have been formulated, each tailored to capture specific aspects of thermal–mechanical coupling in unsaturated soils (e.g., [17,41,42]). Some constitutive models have integrated thermal effects into established critical state theories [43], while others have explicitly accounted for temperature-induced alterations in the water retention curve [38]. Unified models have emerged, combining both mechanical and thermal aspects, e.g., leveraging concepts from bounding surface theory [35,42]. In addition, micro-structural-based constitutive models have been developed to elucidate the influence of temperature on capillary stress at solid–water–air interfaces [39]. Noteworthy contributions include hierarchical models that hierarchically incorporate hydro–mechanical hardening and thermal softening and models tailored to study cyclic behavior under varying thermal conditions [17,42]. Collectively, these thermal constitutive models provide invaluable tools for comprehensively characterizing the behavior of unsaturated soils in response to temperature fluctuations, contributing to safer and more efficient engineering designs and geotechnical assessments. These advanced constitute models for thermal unsaturated soils have been implemented into the finite element program [44], which is robust for modeling continuous deformation in unsaturated soils but not for discontinuities such as shear bands and cracks. In the present study, we formulate a nonlocal thermal constitutive model for unsaturated soils and implement it into the mesh-free PPM paradigm to better study shear banding and cracking in thermal unsaturated soils.

PPM is a nonlocal formulation of classical coupled poromechanics through the peridynamic state concept and the effective force concept for unsaturated porous media [45,46], which is robust for modeling continuous and discontinuous mechanical and physical behavior of porous media [22–26,34,47,48]. In PPM, equations of motion and mass balance are expressed as integral–differential equations [46–48]. PPM stands out for its natural ability to simulate multiphase discontinuities through field equations and material models [25]. By using the stabilized multiphase correspondence principle, classical advanced constitutive models and physical laws are readily incorporated into PPM, enabling the modeling of coupled deformation, shear banding, and fracturing in porous media [22]. In PPM, the energy-based bond breakage criterion has been formulated for modeling cracks leveraging the effective force state concept [25]. Furthermore, the large-deformation PPM through the updated Lagrangian framework was developed for unsaturated porous media in [24]. The μPPM has been formulated to model dynamic shear bands and crack branching in porous media considering the rotational degree of freedom of the solid skeleton of porous media in [49,50]. In the present study, we investigate the shear banding and cracking in thermal unsaturated soils leveraging PPM. The PPM paradigm [22] is used by incorporating a thermal constitutive model for unsaturated soils.

In this study, we delve into the intricate phenomena of shear banding and cracking within unsaturated porous media under non-isothermal conditions. A notable contribution of this study is the implementation of a classical THM material model tailored for unsaturated porous media into the computational meshfree PPM paradigm. A pivotal aspect of this integration is the utilization of a stabilized multiphase correspondence principle that effectively mitigates the zero-energy mode instability. Our implementation of the THM PPM paradigm is realized through an explicit Lagrangian meshfree algorithm in which the unsaturated soil is represented by a collection of a finite number of material points. Each material point has its own displacement, pore pressure, and temperature. At each material point, the return mapping algorithm in computational plasticity is used to numerically implement the THM constitutive model. To assess the capabilities of our proposed THM meshfree paradigm, we present numerical examples that illustrate its efficacy in modeling shear banding and cracking phenomena within unsaturated porous media under non-isothermal conditions. The second-order work criterion for instability of unsaturated soils [51] is adopted to validate our numerical results of shear banding in thermal unsaturated soils. Our numerical results offer valuable insights into the intricate interplay between temperature variations and the formation of shear bands and cracks within unsaturated porous media.

The remainder of this article is organized as follows. Section 2 presents the mathematical formulation of the THM PPM framework, including the thermal elastoplastic material model. Section 3 is dedicated to the numerical implementation of the proposed PPM paradigm. Section 4 presents numerical examples to assess the accuracy of the numerical implementation at the material point level and utilize the THM PPM paradigm to model dynamic shear banding and fracturing in unsaturated porous media under non-isothermal conditions, followed by a summary in Section 5. Throughout this work, we adopt the sign convention in continuum mechanics, wherein tensile forces and deformations under tension are considered positive. For pore fluid pressure, compression is positive, and tension is negative.

2. Mathematical Formulation

In this section, we introduce the governing equation, the stabilized constitutive correspondence principle, the thermal elastoplastic material model, and the energy-based bond breakage criterion. In this study, we assume that the matric suction and temperature are known variables, i.e., one-way coupling. We also assume that no phase change exists between the three phases, i.e., solid, water, and air.

2.1. Governing Equation

In PPM, the porous media is represented by a set of mixed material points. A material point $\boldsymbol{X}$ has mechanical and physical interactions with any material point $\boldsymbol{X}'$ within its neighborhood, i.e., a spherical domain $\mathscr{H}$ with a radius of δ called horizon. The bond between material points $\boldsymbol{X}$ and $\boldsymbol{X}'$ is defined as $\underline{\boldsymbol{\xi}} = \boldsymbol{X}' - \boldsymbol{X}$ in the reference configuration. For notation simplicity, the variables with no prime are associated with $\boldsymbol{X}$ and the variables with a prime means the variables associated with $\boldsymbol{X}'$. For a partially saturated porous medium (i.e., solid, water, and air), assuming a weightless air phase, the total density is defined as

$$\rho = (1 - \phi)\rho_s + \phi S_r \rho_w, \tag{1}$$

where ϕ is the porosity, ρ_s is the intrinsic density of the solid skeleton, S_r is the degree of saturation, and ρ_w is the intrinsic density of water. In this study, the degree of saturation is determined through a temperature-dependent water retention model for unsaturated soils at elevated temperatures [17], which reads

$$S_r = \left\{ \frac{1}{1 + \left[a_1 \gamma_\theta (\nu - 1)^{b_1} s \right]^{\widetilde{n}}} \right\}^{-m}, \tag{2}$$

where ν is the specific volume of unsaturated porous media, s is matric suction, a_1, b_1, $\widetilde{n}$, and m are material parameters, and γ_θ is a temperature-dependent air-entry matric suction. This variable can be determined by

$$\gamma_\theta = \left(\frac{a_2 + b_2\theta_0}{a_2 + b_2\theta} \right)^{b_2}, \tag{3}$$

where a_2 and b_2 are material parameters, θ_0 is a reference temperature, and θ is the temperature of the mixture.

The motion equation for this porous medium in the PPM framework is written as

$$\rho\ddot{\boldsymbol{u}} = \int_{\mathscr{H}} \left(\underline{\mathscr{T}} - \underline{\mathscr{T}}'\right) d\mathscr{V}' - \rho\boldsymbol{g}, \tag{4}$$

where ρ is the total density as defined in (1), $\ddot{\boldsymbol{u}}$ is the acceleration, $\underline{\mathscr{T}}$ and $\underline{\mathscr{T}}'$ are the total force vector states (i.e., associated with the bond $\underline{\boldsymbol{\xi}}$), and $\boldsymbol{g}$ is gravitational acceleration. Through the effective state concept [46] and assuming that matric suction and temperature are given, the motion equation for the porous media can degenerate into the motion equation for the solid phase as

$$\rho^s\ddot{\boldsymbol{u}} = \int_{\mathscr{H}} \left(\overline{\underline{\mathscr{T}}} - \overline{\underline{\mathscr{T}}}'\right) d\mathscr{V}' - \rho^s\boldsymbol{g}, \tag{5}$$

where $\rho^s = (1-\phi)\rho_s$ is the partial density of the solid phase, and $\overline{\underline{\mathscr{T}}}$ and $\overline{\underline{\mathscr{T}}}'$ are the effective force states. Assuming the passive air pressure (i.e., zero air pressure), the effective force state [25] at $\boldsymbol{X}$ is defined as

$$\overline{\underline{\mathscr{T}}} = \underline{\mathscr{T}} - S_r\underline{\mathscr{T}}_w. \tag{6}$$

It is noted that the impact of temperature and matric suction on the mechanical behavior of unsaturated soils is considered through the thermal constitutive model given the temperature and matric suction. In what follows, we present the kinematics of the solid phase.

2.2. Kinematics

In PPM, the Lagrangian coordinate is used to model the solid phase [25]. Let $\boldsymbol{y}$ and $\boldsymbol{y}'$ be the positions of material points $\boldsymbol{X}$ and $\boldsymbol{X}'$ in the current configuration, respectively. Let $\boldsymbol{u}$ and $\boldsymbol{u}'$ be the displacements of material points $\boldsymbol{X}$ and $\boldsymbol{X}'$, respectively. The deformation and displacement states are defined as

$$\underline{\mathscr{Y}} = \boldsymbol{y}' - \boldsymbol{y}, \tag{7}$$

$$\underline{\mathscr{U}} = \boldsymbol{u}' - \boldsymbol{u}. \tag{8}$$

Given $\underline{\mathscr{Y}}$, the deformation gradient tensor in PPM [24] is defined as

$$\boldsymbol{F} = \left[\int_{\mathscr{H}} \underline{\omega} \left(\underline{\mathscr{Y}} \otimes \underline{\boldsymbol{\xi}} \right) d\mathscr{V}' \right] \mathscr{K}^{-1}, \tag{9}$$

where $\underline{\omega}$ is a weighting function, and $\mathscr{K}$ is the shape tensor [46]. The shape tensor is defined as

$$\mathscr{K} = \int_{\mathscr{H}} \underline{\omega} \left(\underline{\boldsymbol{\xi}} \otimes \underline{\boldsymbol{\xi}} \right) d\mathscr{V}'. \tag{10}$$

It is noted that the shape tensor $\mathscr{K}$ is defined referring to the initial configuration. Then, the rate form of the deformation gradient tensor follows from (10), (9), and (8), and can be written as

$$\dot{\boldsymbol{F}} = \left[\int_{\mathscr{H}} \underline{\omega}\left(\underline{\dot{\mathscr{U}}} \otimes \underline{\boldsymbol{\xi}}\right) d\mathscr{V}'\right]\mathscr{K}^{-1}. \tag{11}$$

From (9) and (11), the velocity gradient tensor is determined as

$$\boldsymbol{L} = \dot{\boldsymbol{F}}\boldsymbol{F}^{-1}. \tag{12}$$

Given (12), the rate of deformation tensor $\boldsymbol{D}$ can be computed as

$$\boldsymbol{D} = \frac{1}{2}\left(\boldsymbol{L} + \boldsymbol{L}^T\right), \tag{13}$$

where the superscript T is the transpose operator.

According to the polar decomposition theorem, the nonlocal deformation gradient $\boldsymbol{F}$ can be decomposed as

$$\boldsymbol{F} = \boldsymbol{R}\boldsymbol{U}, \tag{14}$$

where $\boldsymbol{R}$ is the rotation tensor that is a proper orthogonal tensor, and $\boldsymbol{U}$ is the right stretch tensor that is a symmetric positive-definite tensor. The unrotated rate of deformation tensor $\hat{\boldsymbol{d}}$ can be obtained by

$$\hat{\boldsymbol{d}} = \boldsymbol{R}\boldsymbol{D}\boldsymbol{R}^T. \tag{15}$$

Given the unrotated rate of deformation tensor, the strain increment can be written as

$$\Delta\boldsymbol{\varepsilon} = \Delta t\hat{\boldsymbol{d}}, \tag{16}$$

where Δt is the time increment. Finally, given (9), the porosity [52,53] in the current configuration is written as

$$\phi = 1 - \frac{(1-\phi_0)}{J}, \tag{17}$$

where J is the Jacobian of the nonlocal deformation gradient, and ϕ_0 is the initial porosity. We note that in this study, the soil water retention curve is dependent on the porosity, as introduced in Section 2.3.2. Next, we introduce the stabilized constitutive correspondence principle through which the advanced thermal constitutive model is implemented into the meshfree PPM paradigm.

2.3. *Correspondence THM Constitutive Model*

To complete (5), a constitutive model is needed to determine the effective force state. In this study, the stabilized constitutive correspondence principle [22] is used to implement an advanced thermal constitutive model for unsaturated soils.

2.3.1. Constitutive Correspondence Principle

The constitutive correspondence principle is based on the notion that the internal energy in a porous body from the local formulation in classical poromechanics is equal to that from the nonlocal formulation in periporomechanics. We refer to [22,26,46] for the detailed derivation. The effective force state in PPM can be written in terms of the effective Piola stress as

$$\overline{\underline{\mathscr{T}}} = \underline{\omega}\overline{\boldsymbol{P}}\mathscr{K}^{-1}\underline{\boldsymbol{\xi}}, \tag{18}$$

where $\overline{\boldsymbol{P}}$ is the effective Piola stress, which can be obtained from the local constitutive model given the nonlocal deformation gradient. It is noted that, assuming passive air pressure (i.e., atmospheric air pressure), the effective stress $\overline{\boldsymbol{\sigma}}$ is written as

$$\overline{\boldsymbol{\sigma}} = \boldsymbol{\sigma} - S_r p_w \mathbf{1}, \tag{19}$$

where $\boldsymbol{\sigma}$ is the total Cauchy stress tensor, p_w is pore water pressure, and $\mathbf{1}$ is the second-order identity tensor. Thus, it follows from (18), (6), and (19), that the fluid force state can be written as

$$\underline{\overline{\mathscr{T}}}_w = \underline{\omega} p_w \mathbf{1} \mathscr{K}^{-1} \underline{\boldsymbol{\xi}}. \tag{20}$$

Note that in (20), the small deformation of a solid is assumed.

From (18), the effective force state can be computed from a thermal elasto-plastic constitutive model for unsaturated soils given matric suction, temperature change, and the nonlocal deformation gradient. The effective Piola stress can be written in terms of the unrotated Cauchy stress as

$$\boldsymbol{P} = J \hat{\overline{\boldsymbol{\sigma}}} \boldsymbol{F}^{-T}. \tag{21}$$

The unrotated effective Cauchy stress reads

$$\hat{\overline{\boldsymbol{\sigma}}} = \boldsymbol{R} \overline{\boldsymbol{\sigma}} \boldsymbol{R}^T, \tag{22}$$

where $\overline{\boldsymbol{\sigma}}$ can be determined from an advanced thermal constitutive model for unsaturated soils. Next, we introduce the thermal elastoplastic model for unsaturated soils.

2.3.2. Thermal Elastoplastic Model for Unsaturated Soils

In this study, the thermal elastoplastic constitutive model is formulated based on the critical state soil mechanics. Following the small strain theory, the total strain is additively decomposed to elastic and plastic components as

$$\boldsymbol{\varepsilon} = \boldsymbol{\varepsilon}^e + \boldsymbol{\varepsilon}^p, \tag{23}$$

where $\boldsymbol{\varepsilon}^e$ is the elastic strain tensor and $\boldsymbol{\varepsilon}^p$ is the plastic strain tensor. For the thermal elastic model, the total elastic strain is assumed to consist of the mechanical elastic strain and the thermal elastic strain. Thus, the total elastic strain is additively decomposed into mechanical and thermal parts as

$$\boldsymbol{\varepsilon}^e = \boldsymbol{\varepsilon}^e_{me} + \boldsymbol{\varepsilon}^e_{\theta}, \tag{24}$$

where $\boldsymbol{\varepsilon}^e_{me}$ is the mechanical elastic strain, and $\boldsymbol{\varepsilon}^e_{\theta}$ is the thermal elastic strain. Given a temperature change, the thermal elastic strain is determined as

$$\boldsymbol{\varepsilon}^e_{\theta} = \beta_\theta (\theta - \theta_0) \mathbf{1}, \tag{25}$$

where β_θ is the volumetric thermal expansion coefficient, which is assumed to be a constant in this study, θ is the temperature of soils, and θ_0 is a reference temperature. Given the total elastic strain, the effective stress can be written through a linear thermal elastic model as

$$\overline{\boldsymbol{\sigma}} = \boldsymbol{C} : \boldsymbol{\varepsilon}^e, \tag{26}$$

where $\boldsymbol{C}$ is the fourth-order linear elastic stiffness tensor that reads

$$C_{ijkl} = K \, \delta_{ij} \, \delta_{kl} + \mu \, (\delta_{ik} \delta_{jl} + \delta_{il} \delta_{jk} - \tfrac{2}{3} \, \delta_{ij} \, \delta_{kl}), \tag{27}$$

where $i, j, k, l = 1, 2, 3$, K is the elastic bulk modulus, and μ is the shear modulus.

Next, we present the thermal plastic model. First, we define the effective mean stress $\overline{p}$ and the deviatoric stress q as

$$\overline{p} = \frac{1}{3} \mathrm{tr}(\overline{\boldsymbol{\sigma}}), \tag{28}$$

$$q = \sqrt{\frac{3}{2}} || \overline{\boldsymbol{\sigma}} - \overline{p} \mathbf{1} ||, \tag{29}$$

where $|| \ ||$ is the norm of a tensor. Following the modified Cam–Clay model [17], the yield function is written as

$$f = \overline{p}^2 - \overline{p} p_c + \frac{q^2}{M^2}, \tag{30}$$

where M is the slope of the critical state line and p_c is the apparent preconsolidation pressure. In this study, the apparent preconsolidation pressure depends on the volumetric plastic strain, matric suction, and temperature changes [17]. Specifically, the apparent preconsolidation pressure reads

$$p_c = -\exp(\hat{a})(-p_{c,0})^{\hat{b}}\left[1 - \alpha_\theta \log\left(\frac{\theta}{\theta_0}\right)\right], \tag{31}$$

where

$$\hat{a} = \frac{N(\hat{c} - 1)}{\widetilde{\lambda}\hat{c} - \widetilde{\kappa}}, \tag{32}$$

$$\hat{b} = \frac{\widetilde{\lambda} - \widetilde{\kappa}}{\widetilde{\lambda}\hat{c} - \widetilde{\kappa}}, \tag{33}$$

$$\hat{c} = 1 - c_1[1 - \exp(c_2\zeta)], \tag{34}$$

and ζ is a bonding variable related to water meniscus between grains, N is the specific volume of the soil under a unit saturated preconsolidaiton pressure, c_1 and c_2 are constants [54], $p_{c,0}$ is the apparent preconsolidation pressure at the reference temperature, θ_0, and α_θ is a thermal parameter that characterizes the impact of temperature variation on the apparent preconsolidation pressure. It is noted that the parameter $\hat{c}$ is the ratio between the specific volume of the virgin compression curve in the partially saturated state to the corresponding specific volume in the fully saturated state. The bonding variable ζ [17] at the reference temperature (i.e., ambient temperature) is defined as

$$\zeta = (1 - S_r)\hat{f}(s), \tag{35}$$

where $(1 - S_r)$ accounts for the number of water menisci per unit soil volume and $\hat{f}(s)$ is the stabilizing normal force exerted by a single water meniscus. The latter is written as

$$\hat{f}(s) = 1 + \frac{s/p_{\text{atm}}}{10.7 + 2.4(s/p_{\text{atm}})}, \tag{36}$$

where p_{atm} is the atmospheric pressure.

Adopting the associative flow rule, the total THM plastic strain is written as

$$\dot{\boldsymbol{\varepsilon}}^p = \dot{\lambda}\frac{\partial f}{\partial \overline{\boldsymbol{\sigma}}}, \tag{37}$$

where $\dot{\lambda}$ is a plastic multiplier, which is determined by the consistency condition [55]. Next, we introduce the energy-based bond breakage criterion.

2.4. Energy-Based Bond Breakage Criterion

In this study, the energy-based bond breakage criterion [26] is adopted to detect the bond breakage in the THM PPM framework. The effective force state is used to determine the deformation energy. Thus, the energy density in bond $\underline{\boldsymbol{\xi}}$ is obtained as

$$\mathcal{W} = \int_0^t \left(\underline{\mathscr{T}} - \underline{\mathscr{T}}'\right)\dot{\mathscr{U}}\, dt, \tag{38}$$

where t is the load time. In PPM, the broken bond is modeled through the influence function at the constitutive model level. In this study, the influence function for bond $\boldsymbol{\xi}$ is defined as

$$\underline{\omega} = \begin{cases} 1 & \text{for } \mathcal{W} < \mathcal{W}_{cr}, \\ 0 & \text{for } \mathcal{W} \geq \mathcal{W}_{cr}, \end{cases} \tag{39}$$

where $\mathcal{W}_{cr}$ is the critical bond energy density. Following linear elastic fracture mechanics, the critical bond energy density can be calculated from the critical energy release rate as

$$\mathcal{W}_{cr} = \frac{4\mathcal{G}_{cr}}{\pi\delta^4}, \tag{40}$$

where $\mathcal{G}_{cr}$ is the critical energy per unit fracture area. In PPM, when a bond breaks, it will not sustain any mechanical load. The local damage parameter $\mathscr{D}$ at a material point is defined as

$$\mathscr{D} = 1 - \frac{\int_{\mathscr{H}} \underline{\omega} d\mathscr{V}'}{\int_{\mathscr{H}} d\mathscr{V}'}. \tag{41}$$

In this study, it is assumed that the crack initiates when $\mathscr{D} > 0.5$ at a material point. In the following section, we present the numerical implementation of the THM PPM paradigm.

3. Numerical Implementation

The THM PPM paradigm is implemented numerically through an explicit Newmark scheme [44,56] in time and a Lagrangian meshfree method in space. The return mapping algorithm in computational plasticity is adopted for implementing the nonlocal thermal elasto-plastic constitutive model at the material point level. Figure 1 presents the flowchart of the explicit numerical scheme of the implementation of the THM PPM paradigm. Algorithm 1 summarizes the global explicit meshfree numerical scheme and the local return mapping algorithm at the material point.

3.1. Global Integration in Time

In this part, we present the time integration of the governing equations at each material point. In this study, the explicit Newmark scheme is adopted. Let $\boldsymbol{u}_n$, $\dot{\boldsymbol{u}}_n$, and $\ddot{\boldsymbol{u}}_n$ be the displacement, velocity, and acceleration vectors at time step n. The predictors of displacement and velocity in a general Newmark scheme read

$$\dot{\tilde{\boldsymbol{u}}}_{n+1} = \dot{\boldsymbol{u}}_n + (1-\beta_1)\Delta t \ddot{\boldsymbol{u}}_n, \tag{42}$$

$$\tilde{\boldsymbol{u}}_{n+1} = \boldsymbol{u}_n + \Delta t \dot{\boldsymbol{u}}_n + (1-2\beta_2)\Delta t^2 \ddot{\boldsymbol{u}}_n, \tag{43}$$

where β_1 and β_2 are the numerical integration parameters. Given (42) and (43), the effective force state can be determined from the thermal elasto-plastic constitutive model introduced in Section 2.3.2. Then, the acceleration at time step $n+1$ is determined by

$$\ddot{\boldsymbol{u}}_{n+1} = \mathcal{M}_{n+1}^{-1}\left(\widetilde{\mathscr{T}}_{n+1} - \mathcal{M}_{n+1}\boldsymbol{g}\right), \tag{44}$$

where $\mathcal{M}_{n+1}$ is the mass of the solid at time step $n+1$ and $\widetilde{\mathscr{T}}_{n+1}$ is the effective force at time step $n+1$. The two terms for a material point i are written as

$$\mathcal{M}_{n+1} = \rho_s(1-\phi_{n+1,i})\mathscr{V}_i, \tag{45}$$

$$\widetilde{\mathscr{T}}_{n+1} = \sum_{j=1}^{\mathscr{N}_i}\left(\underline{\widetilde{\mathscr{T}}}_{n+1,ij} - \underline{\widetilde{\mathscr{T}}}'_{n+1,ji}\right)\mathscr{V}_j\mathscr{V}_i, \tag{46}$$

where $\mathscr{N}_i$ is the number of neighbor material points of material point i. From (44), the displacement and velocity at time step $n+1$ can be obtained as

$$\dot{\boldsymbol{u}}_{n+1} = \tilde{\dot{\boldsymbol{u}}}_{n+1} + \beta_1 \Delta t \ddot{\boldsymbol{u}}_{n+1}, \tag{47}$$

$$\boldsymbol{u}_{n+1} = \tilde{\boldsymbol{u}}_{n+1} + \beta_2 \Delta t^2 \ddot{\boldsymbol{u}}_{n+1}. \tag{48}$$

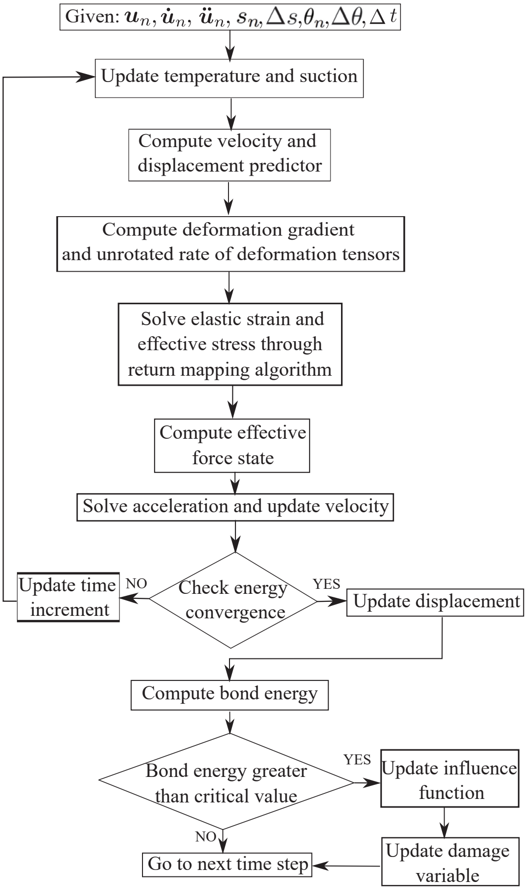

Figure 1. Flowchart for the explicit numerical implementation of the thermo–hydro–mechanical (THM) periporomechanic (PPM) paradigm.

In this study, the explicit central difference solution scheme is adopted, i.e., $\beta_1 = 1/2$ and $\beta_2 = 0$. The energy balance check is used to ensure the numerical stability of the algorithm in time. The internal energy, external energy, and kinetic energy of the system at time step $n+1$ are written as

$$\mathscr{W}_{\text{int},n+1} = \mathscr{W}_{\text{int},n} + \frac{\Delta t}{2}\left(\dot{\boldsymbol{u}}_n + \frac{\Delta t}{2}\ddot{\boldsymbol{u}}_n\right)(\mathscr{T}_n + \mathscr{T}_{n+1}), \tag{49}$$

$$\mathscr{W}_{\text{ext},n+1} = \mathscr{W}_{\text{ext},n} + \frac{\Delta t}{2}\left(\dot{\boldsymbol{u}}_n + \frac{\Delta t}{2}\ddot{\boldsymbol{u}}_n\right)(\mathcal{M}_n \boldsymbol{g} + \mathcal{M}_{n+1}\boldsymbol{g}), \tag{50}$$

$$\mathscr{W}_{\text{kin},n+1} = \frac{1}{2}\dot{\boldsymbol{u}}_{n+1}\mathcal{M}_{n+1}\dot{\boldsymbol{u}}_{n+1}. \tag{51}$$

The energy conservation criterion requires

$$|\mathscr{W}_{\text{kin},n+1} - \mathscr{W}_{\text{ext},n+1} + \mathscr{W}_{\text{int},n+1}| \leq \hat{\varepsilon}\max(\mathscr{W}_{\text{kin},n+1}, \mathscr{W}_{\text{int},n+1}, \mathscr{W}_{\text{ext},n+1}), \tag{52}$$

where $\hat{\varepsilon}$ is a small tolerance on the order of 10^{-2} [56].

Algorithm 1 Summary of the numerical integration algorithm of the thermo–hydro–mechanical (THM) periporomechanic (PPM) paradigm

```
Given: $\boldsymbol{u}_n, \dot{\boldsymbol{u}}_n, \ddot{\boldsymbol{u}}_n, \theta_n, s_n, \Delta\theta, \Delta s, \Delta t$ and compute: $\boldsymbol{u}_{n+1}, \dot{\boldsymbol{u}}_{n+1}, \ddot{\boldsymbol{u}}_{n+1}, \theta_{n+1}, s_{n+1}$
 1: Update time $t_{n+1} = t_n + \Delta t$
 2: while $t_{n+1} \leq t_f$ do
 3:     for all points do
 4:         Compute the velocity predictor $\tilde{\dot{\boldsymbol{u}}}_{n+1}$ using (42)
 5:         Apply boundary conditions
 6:         Compute displacement predictor $\widetilde{\boldsymbol{u}}_{n+1}$ using (43)
 7:         for each neighbor do
 8:             Update deformation state $\underline{\mathscr{Y}}_{n+1}$ using (53)
 9:             Compute deformation gradient tensor $\boldsymbol{F}_{n+1}$ using (54)
10:         end for
11:         Compute unrotated rate of deformation tensor $\boldsymbol{d}_{n+1}$ using (57)
12:         Update temperature $\theta_{n+1}$ using (60) and suction $s_{n+1}$ using (59)
13:         Update preconsolidation pressure $p_{c,n+1}$
14:         Compute trial elastic strain tensor $\boldsymbol{\varepsilon}^{e,\text{tr}}_{n+1}$ using (62)
15:         Compute the trial effective stress $\overline{\boldsymbol{\sigma}}^{tr}_{n+1}$
16:         Compute the trial yield function $f^{tr}_{n+1}$
17:         if $f^{tr}_{n+1} \leq 0$ then
18:             Update effective stress $\overline{\boldsymbol{\sigma}}_{n+1} = \overline{\boldsymbol{\sigma}}^{tr}_{n+1}$
19:         else if $f^{tr}_{n+1} > 0$ then
20:             Compute the residual $\boldsymbol{r}^k_{n+1}$
21:             if $||\boldsymbol{r}^k_{n+1}|| \leq$ Tol then
22:                 Go to line 30
23:             else if $||\boldsymbol{r}^k_{n+1}|| >$ Tol then
24:                 Compute $(\partial \boldsymbol{r}/\partial \boldsymbol{x})^k_{n+1}$ using (73)
25:                 Solve $\delta \boldsymbol{x}^k_{n+1}$ using (71)
26:                 Update the $\boldsymbol{x}^{k+1}_{n+1}$ using (72)
27:                 $k \leftarrow k+1$
28:                 Go to line 20
29:             end if
30:             Update effective stress $\overline{\boldsymbol{\sigma}}_{n+1}$ using (26)
31:         end if
32:         Compute the effective force state using (75)
33:         Compute $\mathcal{M}_{n+1}$ using (45)
34:         Solve acceleration $\ddot{\boldsymbol{u}}_{n+1}$ using (44)
35:         Update velocity $\dot{\boldsymbol{u}}_{n+1}$ using (47)
36:         Update displacement $\boldsymbol{u}_{n+1}$ using (48)
37:         Compute kinematic energy $\mathscr{W}_{kin,n+1}$ using (51)
38:         Compute internal energy $\mathscr{W}_{\text{int},n+1}$ using (49) and external energy $\mathscr{W}_{\text{ext},n+1}$ using (50)
39:         Check energy balance
40:         for each neighbor do
41:             Compute bond energy $\mathcal{W}$
42:             if $\mathcal{W} > \mathcal{W}_{cr}$ then
43:                 Update influence function
44:                 Update damage variable $\mathscr{D}_{n+1}$
45:             end if
46:         end for
47:     end for
48: end while
49: $n \leftarrow n+1$
```

3.2. Implementation of the Material Model

This part deals with the numerical implementation of the thermal elasto-plastic model at the material point level through the return mapping algorithm (e.g., [11,18]). First, we present the procedure for determining the strain increment at a material point i. Given (43), the deformation state on bond ij at time step $n+1$ is written as

$$\underline{\widetilde{\mathscr{Y}}}_{n+1,ij} = \underline{\mathscr{Y}}_{n,ij} + \Delta\underline{\widetilde{\mathscr{Y}}}_{n+1,ij}. \tag{53}$$

Then, the nonlocal deformation gradient at material point i at time step $n+1$ is computed by

$$\widetilde{\boldsymbol{F}}_{n+1,i} = \left[\sum_{j=1}^{\mathscr{N}_i} \underline{\omega}\left(\underline{\widetilde{\mathscr{Y}}}_{n+1,ij} \otimes \underline{\boldsymbol{\xi}}_{ij}\right)\mathscr{V}_j\right]\mathscr{K}_i^{-1}. \tag{54}$$

The spatial velocity gradient at material point i at time step $n+1$ is written as

$$\widetilde{\boldsymbol{L}}_{n+1,i} = \left[\left(\sum_{j=1}^{\mathscr{N}_i} \underline{\omega\dot{\widetilde{\mathscr{U}}}}_{n+1,ij} \otimes \underline{\boldsymbol{\xi}}_{ij}\mathscr{V}_j\right)\mathscr{K}_{\boldsymbol{i}}^{-1}\right]\widetilde{\boldsymbol{F}}_{n+1,i}^{-1}. \tag{55}$$

The rate of deformation tensor at time step $n+1$ is written as

$$\widetilde{\boldsymbol{D}}_{n+1,i} = \frac{1}{2}\left(\widetilde{\boldsymbol{L}}_{n+1,i} + \widetilde{\boldsymbol{L}}_{n+1,i}^{T}\right), \tag{56}$$

Given (56), the unrotated rate of deformation tensor $\boldsymbol{d}_{n+1,i}$ can be written as

$$\widetilde{\boldsymbol{d}}_{n+1,i} = \boldsymbol{R}_{n+1,i}\widetilde{\boldsymbol{D}}_{n+1,i}\boldsymbol{R}_{n+1,i}^{T}. \tag{57}$$

where $\boldsymbol{R}_{n+1,i}$ is rigid body rotation at material point i at time step $n+1$. Then, the incremental strain tensor at material point i at time step $n+1$ is computed as

$$\Delta\boldsymbol{\varepsilon}_i = \Delta t\widetilde{\boldsymbol{d}}_{n+1,i}. \tag{58}$$

Second, we present the procedure for updating the effective stress, given the increments of mechanical strain, temperature, and/or matric suction, through the return mapping algorithm. For brevity in notation, the subscript i of the material point is omitted in the following presentation. Let s_n, θ_n, and $\boldsymbol{\varepsilon}_n^e$ be the suction, temperature, and elastic strain, respectively, at material point i at time step n. Let $\Delta\boldsymbol{\varepsilon}_{me}$, $\Delta\theta$, and Δs be incremental mechanical strain tensor, temperature, and matric suction from time steps n to $n+1$. Here, we assume no return mapping on the suction and temperature [17,54]. In this case, the matric suction and temperature at time step $n+1$ can be written as

$$s_{n+1} = s_n + \Delta s, \tag{59}$$

$$\theta_{n+1} = \theta_n + \Delta\theta. \tag{60}$$

Given (60), the incremental thermal elastic strain $\Delta\boldsymbol{\varepsilon}_\theta^e$ is defined as

$$\Delta\boldsymbol{\varepsilon}_\theta^e = \frac{1}{3}\beta_\theta\Delta\theta\boldsymbol{1}. \tag{61}$$

By freezing plastic deformation, the trial elastic strain is written as

$$\boldsymbol{\varepsilon}_{n+1}^{e,\mathrm{tr}} = \boldsymbol{\varepsilon}_n^e + \Delta\boldsymbol{\varepsilon} + \Delta\boldsymbol{\varepsilon}_\theta^e, \tag{62}$$

Then, the trial-specific volume, degree of saturation, and bonding variable at time step $n+1$ can be updated as

$$\nu_{n+1} = \nu_n \exp\left(1 + tr(\boldsymbol{\varepsilon}^{e,\mathrm{tr}}_{n+1})\right), \tag{63}$$

$$S_{r,n+1} = \left[\frac{1}{1 + \left[a_1 \gamma_\theta (\nu_{n+1} - 1)^{b_1} s_{n+1}\right]^{\widetilde{n}}}\right]^{-m}, \tag{64}$$

$$\zeta_{n+1} = (1 - S_{r,n+1})\hat{f}(s_{n+1}). \tag{65}$$

The trial preconsolidatation pressure at time step $n+1$ can be obtained from Equation (31). To conduct the return mapping algorithm in the elastic strain space, we define the unknown vector as

$$\boldsymbol{x}_{n+1} = \{\varepsilon^e_{v,n+1}, \varepsilon^e_{d,n+1}, \Delta\lambda\}^T, \tag{66}$$

where $\varepsilon^e_{v,n+1}$ is the elastic volume strain, $\varepsilon^e_{d,n+1}$ is the elastic deviatoric strain, and $\Delta\lambda$ is the plastic multiplier at time step $n+1$. The residual vector is defined as

$$\boldsymbol{r}_{n+1} = \{r_{1,n+1}, r_{2,n+1}, r_{3,n+1}\}^T, \tag{67}$$

The elements of the residual vector are defined as

$$r_{1,n+1} = \varepsilon^e_{v,n+1} - \varepsilon^{e,\mathrm{tr}}_{v,n+1} + \Delta\lambda \left(\frac{\partial f}{\partial \overline{p}}\right)_{n+1} \tag{68}$$

$$r_{2,n+1} = \varepsilon^e_{d,n+1} - \varepsilon^{e,\mathrm{tr}}_{d,n+1} + \Delta\lambda \left(\frac{\partial f}{\partial q}\right)_{n+1} \tag{69}$$

$$r_{3,n+1} = f^{tr}_{n+1} \tag{70}$$

where $\varepsilon^{e,\mathrm{tr}}_{v,n+1}$ is the trial elastic volume strain and $\boldsymbol{\varepsilon}^{e,\mathrm{tr}}_{d,n+1}$ is the trial elastic deviatoric strain at time step $n+1$. The unknown vector $\boldsymbol{x}$ can be solved following the Newton's method as follows.

$$\delta \boldsymbol{x}^k_{n+1} = -\left(\left.\frac{\partial \boldsymbol{r}}{\partial \boldsymbol{x}}\right|^k_{n+1}\right)^{-1} \boldsymbol{r}^k_{n+1} \tag{71}$$

$$\boldsymbol{x}^{k+1}_{n+1} = \boldsymbol{x}^k_{n+1} + \delta \boldsymbol{x}^k_{n+1} \tag{72}$$

where k is the iteration number. The tangent matrix in (71) reads

$$\left.\frac{\partial \boldsymbol{r}}{\partial \boldsymbol{x}}\right|^k_{n+1} = \begin{bmatrix} \frac{\partial r_1}{\partial \varepsilon^e_v} & \frac{\partial r_1}{\partial \varepsilon^e_d} & \frac{\partial r_1}{\partial \Delta\lambda} \\ \frac{\partial r_2}{\partial \varepsilon^e_v} & \frac{\partial r_2}{\partial \varepsilon^e_d} & \frac{\partial r_2}{\partial \Delta\lambda} \\ \frac{\partial r_3}{\partial \varepsilon^e_v} & \frac{\partial r_3}{\partial \varepsilon^e_d} & \frac{\partial r_3}{\partial \Delta\lambda} \end{bmatrix}^k_{n+1}. \tag{73}$$

After solving the elastic strain, the effective stress at time step $n+1$ can be updated through (26). The unrotated effective stress is

$$\overline{\boldsymbol{\sigma}}'_{n+1} = R^T_{n+1} \overline{\boldsymbol{\sigma}}_{n+1} R_{n+1}. \tag{74}$$

From (21), the effective Piola stress at time step $n+1$ can be computed. Then, the effective force state at time step $n+1$ can be written as

$$\underline{\overline{\mathscr{T}}}_{n+1} = \underline{\omega}\overline{\boldsymbol{P}}_{n+1}\mathscr{K}^{-1}\underline{\boldsymbol{\xi}}. \tag{75}$$

4. Numerical Examples

In this section, we present three numerical examples to showcase the effectiveness of the THM PPM paradigm in modeling shear banding and cracking in unsaturated porous media under THM conditions. Example 1 focuses on the isoerror map to assess the accuracy of the proposed return mapping algorithm at the material point level. Example 2 addresses shear banding in an unsaturated elasto-plastic porous material under biaxial compression and varying temperature conditions. Example 3 examines crack formation in a disk specimen of an unsaturated elastic porous material under displacement control loading with increasing temperature.

4.1. Accuracy Assessment with Isoerror Maps

This example evaluates the precision of the return mapping algorithm at the material point level through numerical testing. To gauge the accuracy of our proposed implicit algorithm, we employ isoerror maps [55]. The relative error is defined as follows:

$$\text{Error} = \frac{\sqrt{(\boldsymbol{\sigma} - \boldsymbol{\sigma}^{\star}) : (\boldsymbol{\sigma} - \boldsymbol{\sigma}^{\star})}}{\sqrt{\boldsymbol{\sigma}^{\star} : \boldsymbol{\sigma}^{\star}}} \times 100, \tag{76}$$

where $\boldsymbol{\sigma}$ represents the algorithm's output, and $\boldsymbol{\sigma}^{\star}$ denotes the exact solution, determined for specific strain and temperature increments. Following the methodology in [55], the exact solution is attained by repeatedly subdividing increments until further division yields negligible changes in the numerical result. It is important to note, as pointed out in [55], that while this approach effectively evaluates the algorithm's overall accuracy, it is not a substitute for a comprehensive analysis of accuracy and stability [55].

For this numerical test, the input material parameters [17,54] are as follows: bulk modulus $K = 83$ MPa, shear modulus $\mu = 18$ MPa, reference pressure $p_{c,0} = -35$ kPa, reference specific volume $\nu_0 = 1.9$, elastic thermal coefficient $\beta_\theta = 6.67 \times 10^{-4}$, swelling/recompression index $\widetilde{\kappa} = 0.03$, compression index $\widetilde{\lambda} = 0.11$, critical state line slope $M = 1$, and plastic thermal parameters $\alpha_\theta = -0.23$, $a_1 = 0.038$ kPa^{-1}, $b_1 = 3.49$, $a_2 = -335$ °C, $b_2 = 1$, $\widetilde{n} = 0.718$, $m = 0.632$, $N = 2.76$, $\theta_0 = 25$ °C, $c_1 = 0.185$, and $c_2 = 1.42$.

We consider three distinct cases, each with specific initial conditions. For all cases, the initial effective isotropic stress is set uniformly at $\sigma_{11} = \sigma_{22} = \sigma_{33} = -150$ kPa, and the preconsolidation pressure is established at -250 kPa. For Case 1, the initial temperature is 25 °C, with a constant matric suction of 50 kPa. For Cases 2 and 3, the initial temperature is raised to 50 °C, and the constant matric suction is increased to 100 kPa. For all three cases, the maximum temperature increment is set at 10 °C, and the maximum volumetric strain increment is -2%. To visualize the accuracy, we utilize isoerror maps plotted on a plane defined by the volumetric strain increment and the temperature increment. These maps employ a color bar to represent the error percentage. Figure 2 displays the isoerror maps for Case 1. Figure 3 illustrates the isoerror maps for Case 2. Figure 4 shows the isoerror maps for Case 3. The results in Figures 2–4 indicate that greater algorithmic accuracy can be achieved by adopting smaller increments in both temperature and strain.

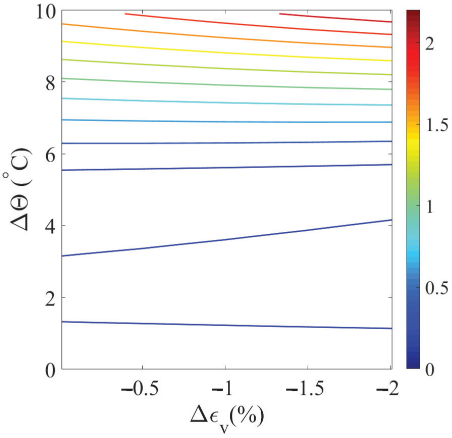

Figure 2. Isoerror map for Case 1.

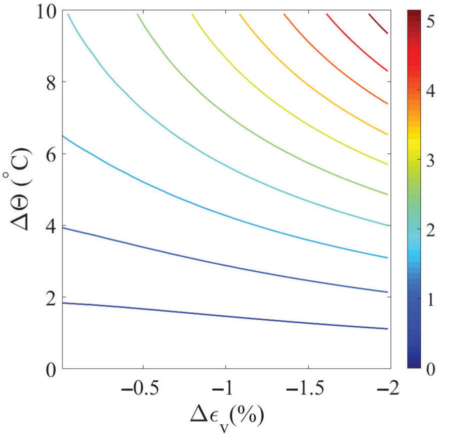

Figure 3. Isoerror map for Case 2.

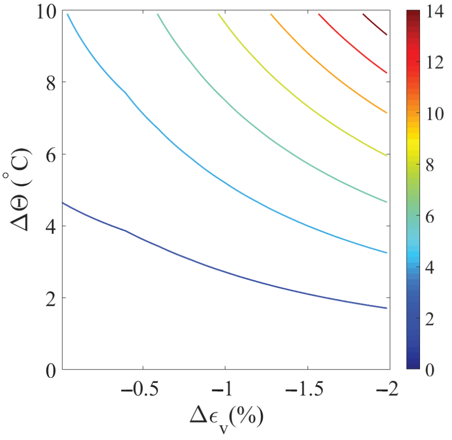

Figure 4. Isoerror map for Case 3.

4.2. Shear Banding Under Non-Isothermal Conditions

This example deals with the shear banding in thermal unsaturated porous media under dynamic loading conditions. Specifically, we investigate the influence of the effects of temperature and matric suction on shear banding. Figure 5 illustrates the model setup for this example. A vertical displacement of $u_y = 10$ mm is applied to the top boundary at a rate of 5 mm/s. A constant lateral confining pressure of 35 kPa is enforced on the left and right boundaries. The thermal elastoplastic constitutive model is utilized for this example. The second-order work criterion can be used to detect material instability, including shear banding in porous media [24,51]. It states that the material loses stability (e.g., shear banding) if the second-order work becomes zero. In this example, we use the second-order work as a sufficient condition for shear banding to validate our numerical results of shear banding in thermal unsaturated soils. The PPM second-order work [24] in terms of the effective force state can be written as

$$d^2\mathscr{E} = \int_{\mathscr{H}} \left(\Delta\underline{\overline{\mathscr{T}}} \cdot \Delta\underline{\mathscr{Y}}\right) d\mathscr{V}'. \tag{77}$$

The input material parameters for the base simulation are: solid phase density $\rho_s = 2000$ kg/m^3, bulk modulus $K = 83$ MPa, shear modulus $\mu = 18$ MPa, elastic thermal coefficient $\beta_\theta = 6.67 \times 10^{-4}$, reference pressure $p_{c,0} = -20$ kPa, reference specific volume $v_0 = 1.9$, swelling index $\widetilde{\kappa} = 0.03$, compression index $\widetilde{\lambda} = 0.11$, critical state line slope $M = 1$, and plastic thermal parameters $\alpha_\theta = -0.23$, $a_1 = 0.038$ kPa^{-1}, $b_1 = 3.49$, $a_2 = -335$ °C, $b_2 = 1$, $\widetilde{n} = 0.718$, $m = 0.632$, $N = 2.76$, $\theta_0 = 25$°C, $c_1 = 0.185$, and $c_2 = 1.42$. The specimen is discretized into a grid of 25 × 50 material points using a uniform grid spacing of $\Delta x = 4$ mm. The horizon δ is set to 8 mm, and the time increment Δt is 1×10^{-4} s.

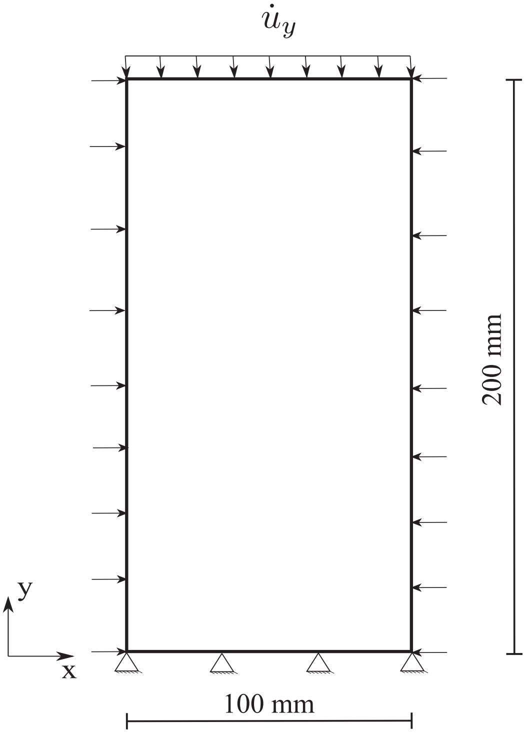

Figure 5. Model setup for the example of shear banding.

For the base simulation, a constant temperature of 25 °C is prescribed within the problem domain. The matric suction decreases from 25 kPa to 10 kPa at a rate of 7.5 kPa/s. The results of the base simulation are presented in Figures 6–9. Figure 6 plots the loading curve on the top boundary, demonstrating a softening stage after the peak load due to the reduction of matric suction. Figure 7 displays the curve of deviatoric stress with vertical strain and the stress path (in the $p - q$ space) of the point at the specimen center. The results indicate that the deviator stress increases with mean stress until it reaches the critical state line, after which it starts to decrease due to softening. Figure 8 presents snapshots of the equivalent plastic shear strain in the deformed configuration at three loading stages. Figure 9 provides snapshots of the plastic volumetric strain at the same three loading stages. It is important to note that a magnification factor of 5 is applied to all contours in this example. The results in Figures 8 and 9 demonstrate the development of two conjugate shear bands originating from the specimen center. Notably, in our nonlocal PPM framework, the initiation of shear banding does not require a weak element, as typically seen in finite element modeling of shear banding. Figure 9 shows that the plastic volumetric strain in the shear zone is positive, indicating dilatation. Figure 10 shows the snapshots of the second-order work in the deformed configuration at the three loading stages. As shown in Figure 10, the second-order work within the shear band zone is zero, which confirms our numerical modeling result.

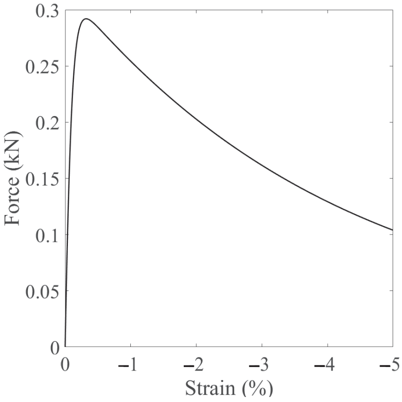

Figure 6. Loading curve on the top boundary.

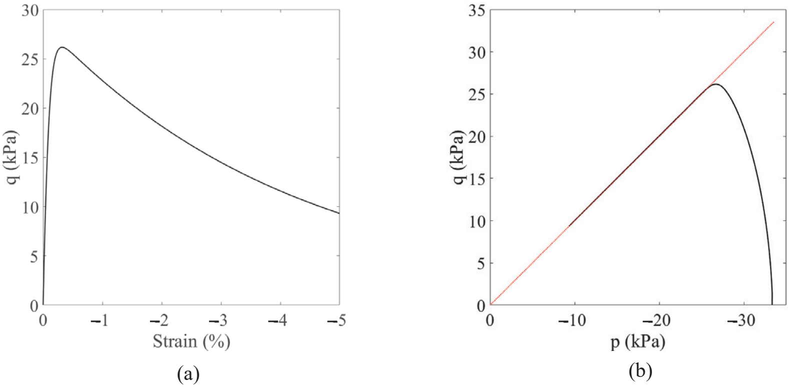

(a)

(b)

Figure 7. (**a**) Plot of the deviator stress versus the vertical strain and (**b**) the stress path in the $p - q$ space at the point of the specimen center. Note: The dashed line in red is the critical state line and the same holds for the following figures in the $p - q$ space.

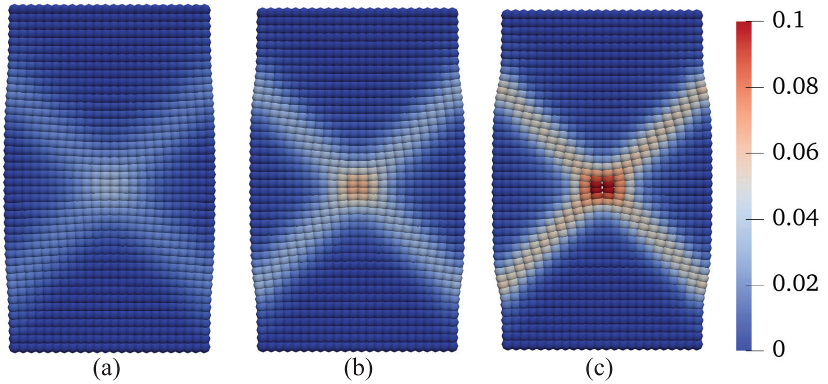

Figure 8. Contours of the equivalent plastic shear strain superimposed on the deformed configuration at (**a**) $u_y = 4$ mm, (**b**) $u_y = 7$ mm, and (**c**) $u_y = 10$ mm.

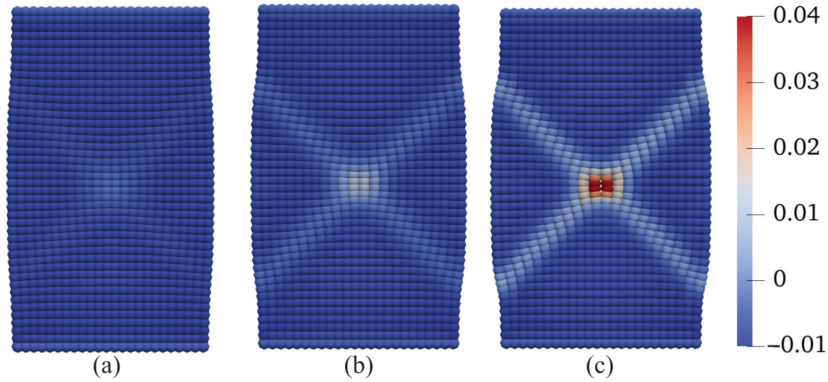

Figure 9. Contours of the plastic volume strain on the deformed configuration at (**a**) $u_y = 4$ mm, (**b**) $u_y = 7$ mm, and (**c**) $u_y = 10$ mm.

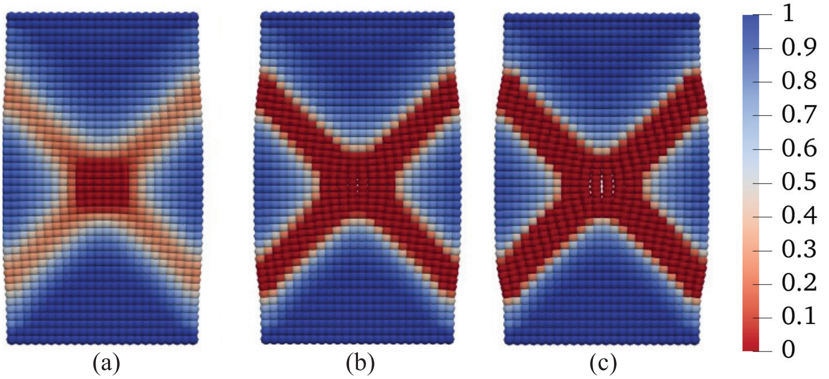

Figure 10. Contours of the second-order work on the deformed configuration at (**a**) $u_y = 4$ mm, (**b**) $u_y = 7$ mm, and (**c**) $u_y = 10$ mm. Note: The second-order work is normalized with the maximum value and the same holds for the following contours of the second-order work.

To investigate the impact of spatial discretization on the results, we examine two different spatial discretization schemes: one with a grid of 25 × 50 points and $\Delta x = 4$ mm (grid 1), and the other with a grid of 40 × 80 points and $\Delta x = 2.5$ mm (grid 2). Both simulations utilize the same horizon value of $\delta = 8$ mm, while all other conditions and parameters remain consistent with the base simulation. Figure 11 presents a comparison of the loading curves obtained from the two simulations. These two loading curves are identical until the onset of the softening stage. Figure 12 displays the contours of equivalent plastic shear strain at $u_y = 10$ mm for both simulations, while Figure 13 shows the contours of plastic volumetric strains at the same displacement level. The results from Figures 9 and 12 suggest that the choice of spatial discretization has a relatively minor influence on shear band formation, primarily due to the adoption of the same nonlocal length scale. Figure 14 compares the contour of the second-order work at $u_y = 10$ mm for the two simulations. In the subsequent sections, we investigate the impact of temperature on shear banding in unsaturated porous media at elevated temperatures. Three scenarios are considered: (i) elevated constant temperature (Scenario 1), (ii) increasing temperature at constant suction (Scenario 2), and (iii) increasing temperature under decreasing suction (Scenario 3).

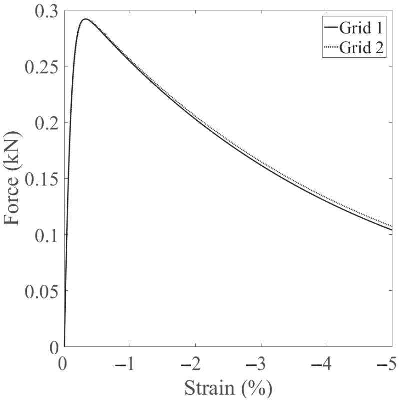

Figure 11. Comparison of the loading curves on the top boundary from the simulations with two spatial discretizations.

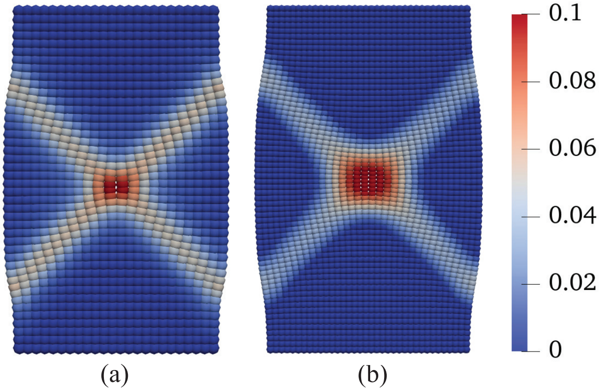

(a) (b)

Figure 12. Contours of the equivalent plastic shear strain on the deformed configuration at $u_y = 10$ mm from the simulations with (**a**) Grid 1 and (**b**) Grid 2.

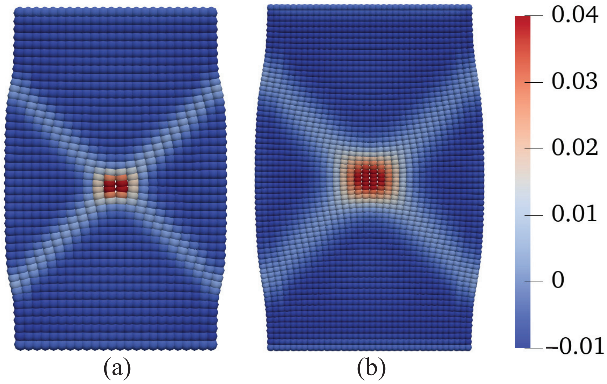

Figure 13. Contours of the plastic volume strain on the deformed configuration at $u_y = 10$ mm from the simulations with (**a**) Grid 1 and (**b**) Grid 2.

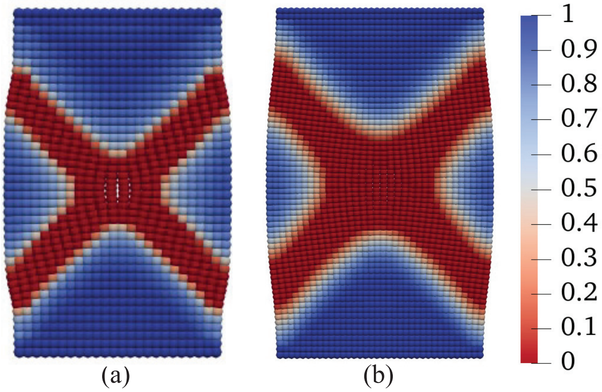

Figure 14. Contours of the second-order work on the deformed configuration at $u_y = 10$ mm from the simulations with (**a**) Grid 1 and (**b**) Grid 2.

4.2.1. Scenario 1: Elevated Constant Temperature

In this scenario, we explore the influence of temperature on shear banding under constant suction conditions. To achieve this, we conduct numerical simulations at three different temperatures, 25 °C, 50 °C, and 75 °C, all while maintaining a constant matric suction of 25 kPa. All other conditions and parameters remain consistent with the base simulation. The results of these simulations are presented in Figures 15–18. Figure 15 compares the loading curves obtained from the three simulations. As shown in Figure 15, the loading capacity of the specimen decreases at higher temperatures due to the temperature-induced softening effect. Figure 16 illustrates the curves of deviator stress versus vertical strain and the stress paths at the specimen center from the three simulations. Regardless of the temperature, the stress paths at the same point demonstrate that the soil element reaches the same critical state line under loading. It is noteworthy that the critical state line remains consistent due to the adoption of the Bishop-type effective stress model for unsaturated soils. Figure 17 displays the contours of equivalent plastic shear strain at $u_y = 10$ mm from the three simulations, while Figure 18 presents the contours of plastic volumetric strain at the same displacement level. Figure 19 compares the contours of the second-order work at $u_y = 10$ mm for the three simulations. These results imply that temperature affects the magnitudes of dilation and shear strain within the specimen under the same mechanical load. Specifically, higher temperatures lead to more significant dilation and shear strain compared to lower temperatures.

In the subsequent section, we further investigate the impact of varying temperatures on the formation of shear banding.

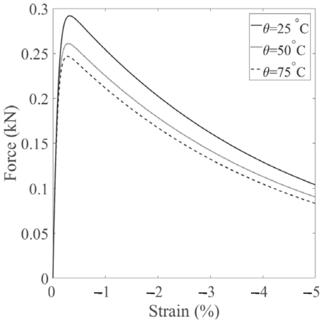

Figure 15. Comparing of the loading curves from the simulations at three temperatures.

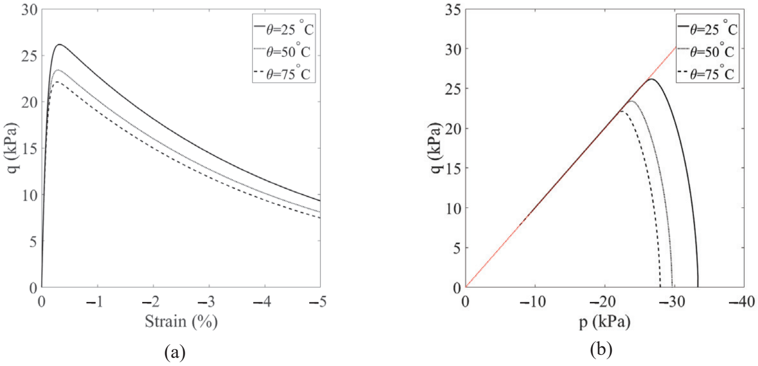

Figure 16. (**a**) Plot of deviatoric stress versus vertical strain, and (**b**) the stress paths in the $p - q$ space for the material point at the specimen center.

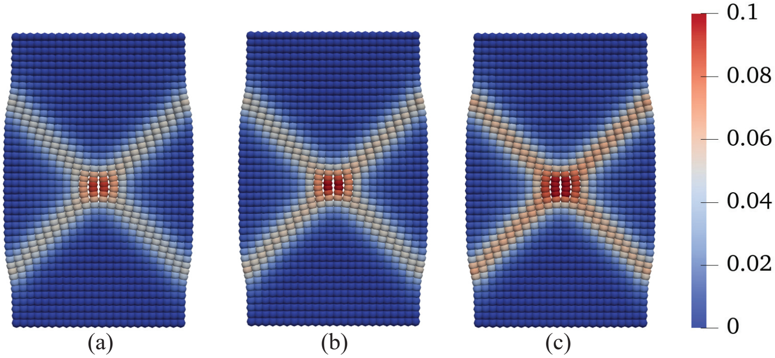

Figure 17. Contours of the equivalent plastic shear strain on the deformed configuration: (**a**) $\theta =$ 25 °C, (**b**) $\theta = 50$ °C, and (**c**) $\theta = 75$ °C.

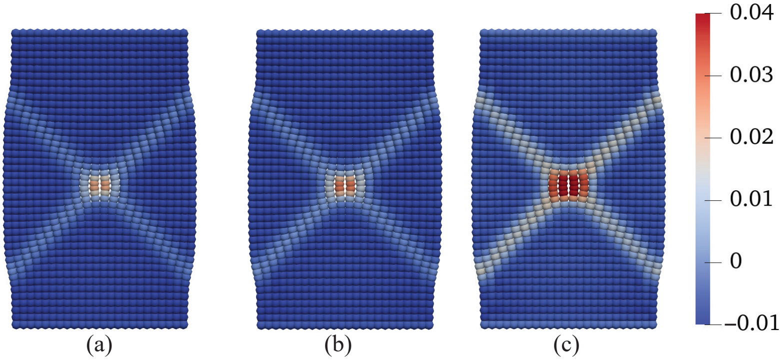

Figure 18. Contours of the plastic volume strain on the deformed configuration at $u_y = 10$ mm: (**a**) $\theta = 25$ °C, (**b**) $\theta = 50$ °C, and (**c**) $\theta = 75$ °C.

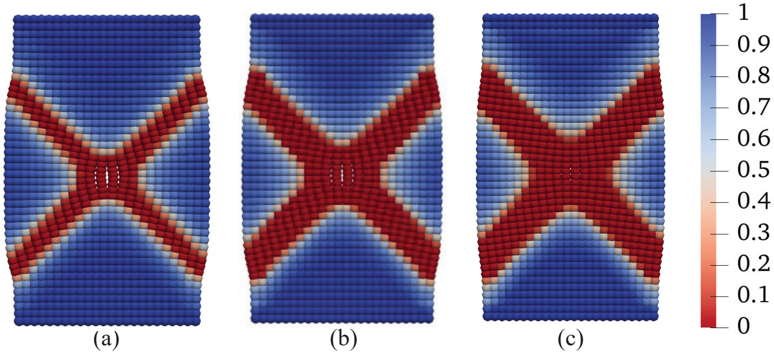

Figure 19. Contours of the second-order work on the deformed configuration at $u_y = 10$ mm: (**a**) $\theta = 25$ °C, (**b**) $\theta = 50$ °C, and (**c**) $\theta = 75$ °C.

4.2.2. Scenario 2: Increasing Temperature

In this scenario, we examine the effect of temperature increase on the development of shear banding in unsaturated soils after the peak load. Specifically, we consider three different temperature changes applied after reaching the peak load of the base simulation, $\Delta\theta = 25$ °C, 25 °C, and 50 °C, all while maintaining a constant suction level of 25 kPa. It is important to note that the simulation with $\Delta\theta = 25$ °C is included for comparison purposes. All other conditions and input parameters remain consistent with the base simulation. The results are presented in Figures 20–23. Figure 20 provides a comparison of the loading curves obtained from the three simulations. As depicted in Figure 20, increasing the temperature after the peak load has a notable effect on the post-localization regime in unsaturated soils, with a larger temperature increase resulting in a more significant reduction in strength. Figure 21 displays the curves of deviatoric stress versus vertical strain and the stress paths at the specimen center from the three simulations. The results in Figures 20 and 21 reinforce the influence of temperature increase on the post-localization behavior in unsaturated soils, where a larger temperature increase leads to a more pronounced strength reduction. Figure 22 presents the contours of equivalent plastic shear strain at $u_y = 10$ mm from the three simulations, while Figure 23 plots the contours of plastic volumetric strain at the same displacement level. Figure 24 compares the contours of the second-order work at $u_y = 10$ mm for the three simulations. These results, as shown in Figures 22 and 23, illustrate that a larger temperature increase, under the same conditions, results in more significant dilation and shear strain within the shear banding zone. In the subsequent section, we delve into the combined effect of varying temperature and suction on shear banding.

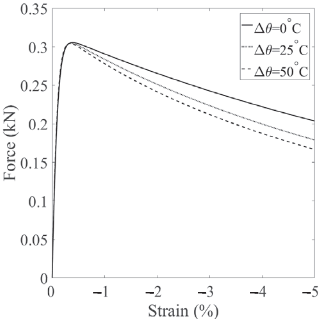

Figure 20. Comparison of the loading curves from the simulations with three temperature changes.

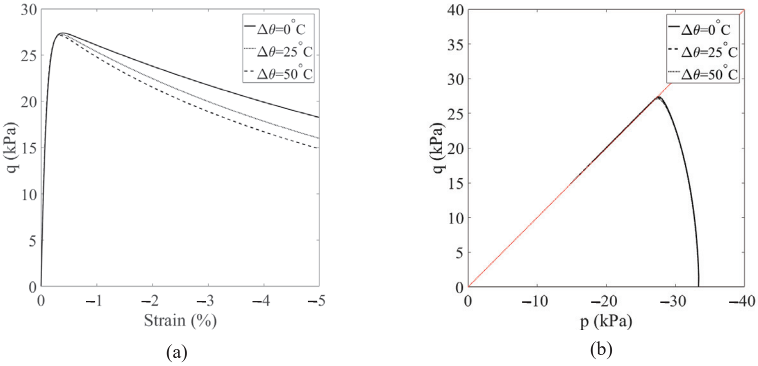

Figure 21. (**a**) Plot of the deviatoric stress versus the vertical strain, and (**b**) the stress paths in the $p - q$ space at the specimen center under three temperature changes.

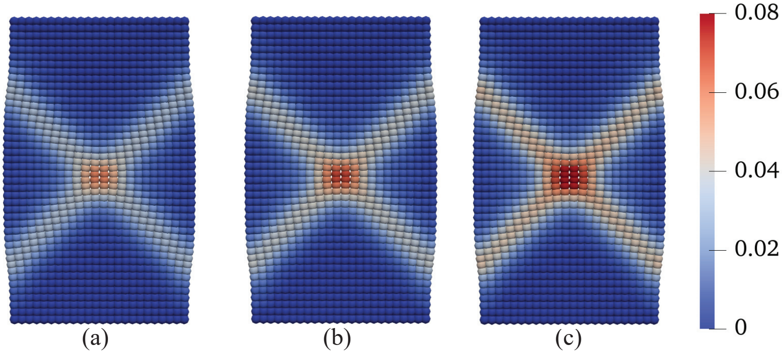

Figure 22. Contours of the equivalent plastic shear strain on the deformed configuration at $u_y = 10$ mm: (**a**) $\Delta\theta = 0$ °C, (**b**) $\Delta\theta = 25$ °C, and (**c**) $\Delta\theta = 50$ °C.

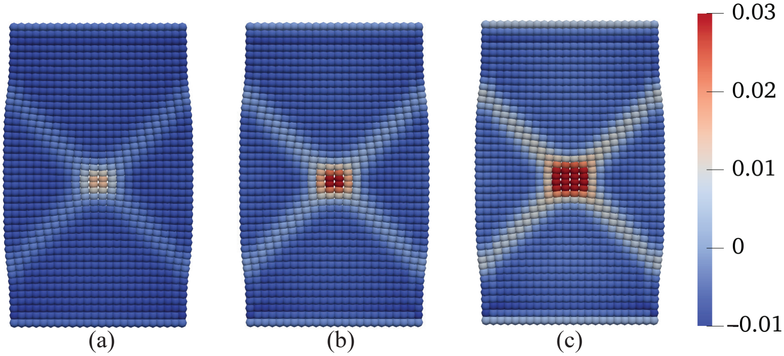

Figure 23. Contours of the plastic volume strain on the deformed configuration at $u_y = 10$ mm: (**a**) $\Delta\theta = 0$ °C, (**b**) $\Delta\theta = 25$ °C, and (**c**) $\Delta\theta = 50$ °C.

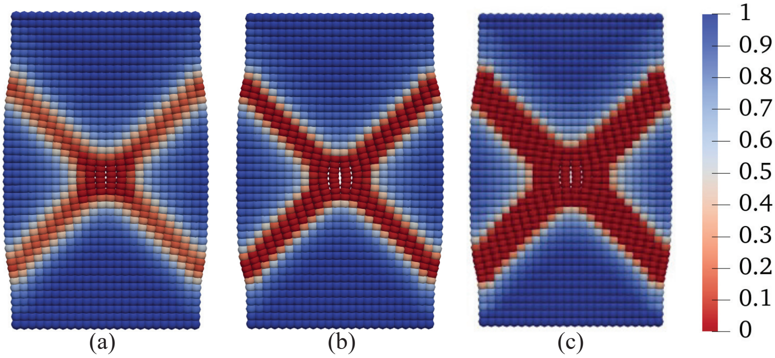

Figure 24. Contours of the second-order work on the deformed configuration at $u_y = 10$ mm: (**a**) $\Delta\theta = 0$ °C, (**b**) $\Delta\theta = 25$ °C, and (**c**) $\Delta\theta = 50$ °C.

4.2.3. Scenario 3: Increasing Temperature and Decreasing Suction

In this scenario, we investigate the combined effect of increasing temperature and decreasing suction on shear banding instability in unsaturated soils. To achieve this, we consider three different temperature changes, $\Delta\theta = 0$ °C, 25 °C, and 50 °C, while concurrently decreasing suction from 25 kPa to 10 kPa. All other parameters and loading conditions are kept consistent with the base simulation, and the results are presented in Figures 25–28. Figure 25 displays the loading curves obtained from the three simulations. As shown in Figure 25, there is a notable reduction in loading capacity under the combined effect of temperature increase and suction reduction during the post-localization regime of unsaturated soils. Figure 26 presents the curves of deviatoric stress versus vertical strain and the stress paths from the three simulations. These results, depicted in Figure 26, further emphasize the impact of the coupling effect, showing that the soil reaches a critical state line at the same point for all three temperature–suction scenarios. Figure 27 compares the contours of equivalent plastic shear strain at $u_y = 10$ mm in the deformed configuration for the three simulations. Meanwhile, Figure 28 compares the contours of plastic volumetric strain at $u_y = 10$ mm. Figure 29 presents the contours of the second-order work at $u_y = 10$ mm for the three simulations. The results in Figures 25–28 illustrate a significant reduction in loading capacity under the coupling effect of temperature increase and suction reduction during the post-localization regime in unsaturated soils. In summary, these findings highlight the complex interplay between temperature and suction on shear banding instability in unsaturated soils.

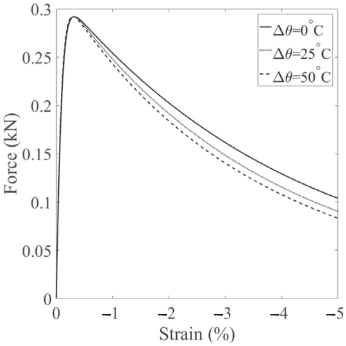

Figure 25. Comparison of the loading curves on the top boundary for Scenario 3.

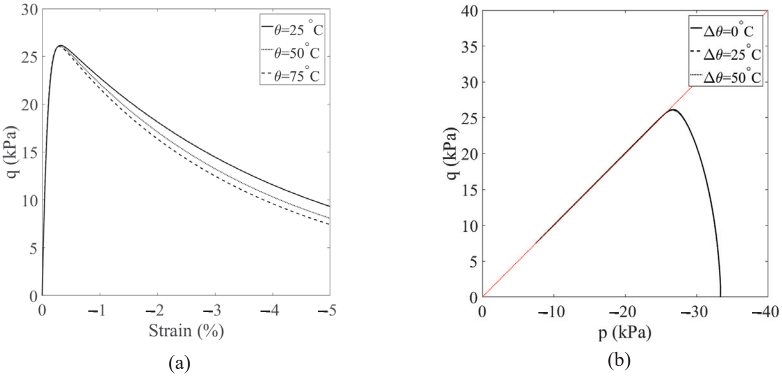

Figure 26. (**a**) Plot of the deviatoric stress versus the vertical strain, and (**b**) the stress loading path in the p versus q space at the specimen center for Scenario 3.

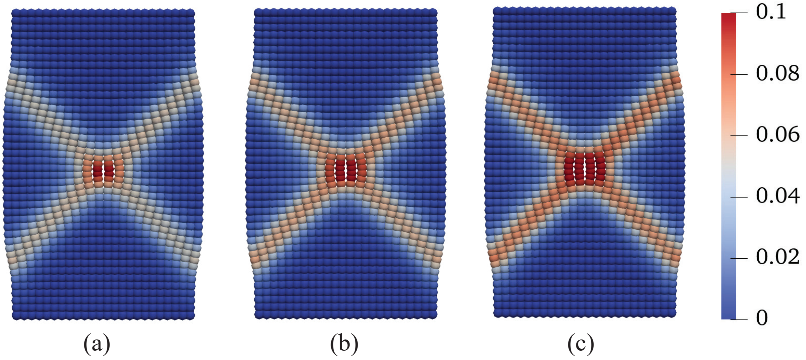

Figure 27. Contours of the equivalent plastic shear strain on the deformed configuration at $u_y = 10$ mm for Scenario 3: (**a**) $\Delta\theta = 0$ °C, (**b**) $\Delta\theta = 25$ °C, and (**c**) $\Delta\theta = 50$ °C.

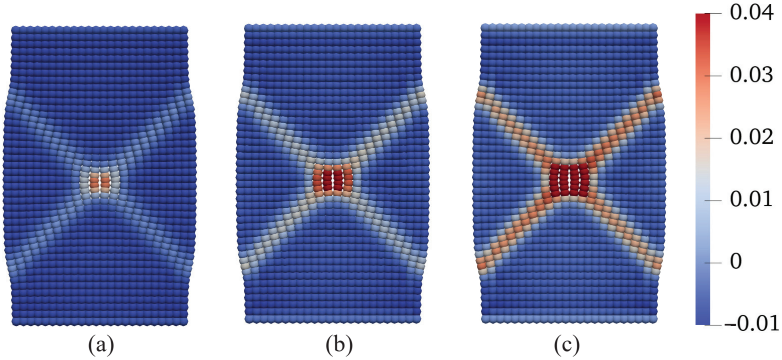

(a) (b) (c)

Figure 28. Contours of the plastic volume strain on the deformed configuration at $u_y = 10$ mm for Scenario 3: (**a**) $\Delta\theta = 0$ °C, (**b**) $\Delta\theta = 25$ °C, and (**c**) $\Delta\theta = 50$ °C.

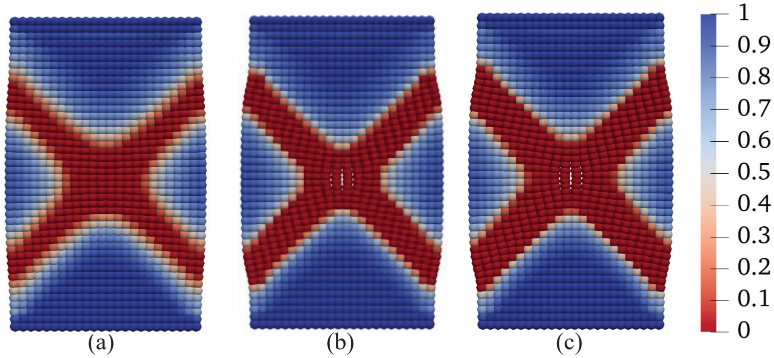

(a) (b) (c)

Figure 29. Contours of the second-order work on the deformed configuration at $u_y = 10$ mm for Scenario 3: (**a**) $\Delta\theta = 0$ °C, (**b**) $\Delta\theta = 25$ °C, and (**c**) $\Delta\theta = 50$ °C.

4.3. Cracking in an Elastic Unsaturated Disk Specimen

In this example, we focus on cracking phenomena in unsaturated elastic porous materials. The modeling of cracking is based on an energy-based bond breakage criterion. Specifically, we simulate cracking in a disk specimen. Figure 30 illustrates the disk specimen and its loading scheme. The disk has a radius of 200 mm and a thickness of 5 mm. As depicted in Figure 30, vertical displacement loads are applied to the top and bottom plates of the disk. The displacement load on each plate is set at $u = 2.0$ mm, with a loading rate of $\dot{u} = 200$ mm/s. The short-range forces within the PPM framework are employed to simulate the contact between the disk and the rigid plates [23]. The matric suction present in the specimen is $s = 10$ kPa. For this example, we adopt the thermo-elastic material model. The material parameters include: solid phase density $\rho_s = 2000$ kg/m^3, bulk modulus $K = 83$ MPa, shear modulus $\mu = 18$ MPa, and an elastic thermal expansion coefficient $\beta_\theta = 6.67 \times 10^{-4}$/°C. In the base simulation scenario, the temperature is increased by 50 °C. The energy-based bond breakage criterion is implemented with a critical energy release rate, $G_{cr} = 20$ N/m. The specimen discretization involves 10,408 points arranged in a uniform grid, with a spacing of $\Delta x = 2.5$ mm. The horizon size is set to $\delta = 4\Delta x$. The simulation uses a time increment of $\Delta t = 1 \times 10^{-5}$ s.

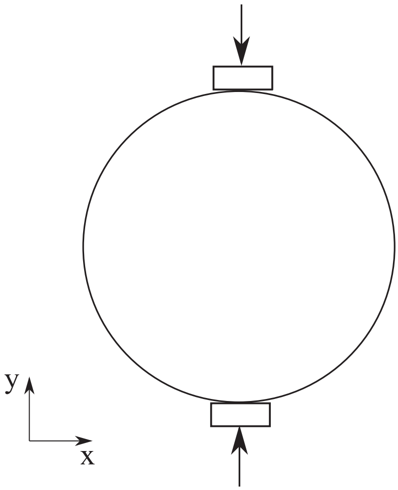

Figure 30. Model setup for the disk specimen under compression.

First, we present the results of the base simulation conducted under ambient temperature conditions. Figure 31 displays the loading curve applied to the top plate of the specimen, revealing a peak load of approximately 0.2 kN. To illustrate the progression of crack formation within the specimen, we provide contours of displacements at three distinct loading stages. Figure 32 depicts the vertical displacement contours on the deformed specimen at these stages, with a uniform magnification factor of 5 applied to all contours in this example. Similarly, Figure 33 presents the horizontal displacement contours under the same conditions. Analysis of the results shown in Figures 32 and 33 indicates the initiation of a crack at the specimen's center, which then extends towards the top and bottom of the disk. Notably, there is a discontinuity in the x-direction displacement along the vertical center line, whereas the vertical displacement remains continuous along the horizontal center line. This observation aligns with the expectations set by classical Brazilian testing, suggesting that the crack results from the discontinuous deformation in the x direction, as further evidenced by the deformed configurations depicted in Figures 32 and 33. Furthermore, Figure 34 illustrates the vertical stress contours (σ_{yy}) on the deformed specimen at the three stages, highlighting the maximum compression stress occurring under the plate. Figure 35 focuses on the contours of horizontal stress (σ_{xx}), elucidating that the specimen experiences tension in the x direction, with the crack process zone around the crack tip being under horizontal tension and vertical compression. Figure 36 shows the contours of the damage parameter at the same three loading stages. It is noted that the damage variable is a post-processing variable (see Equation (41)). The contour in Figure 36a represents the initial damage zone (in the sense of the damage parameter) in the disk specimen under compression. For the crack pattern, it would be more accurate to refer to the contour of displacement (e.g., Figure 33). The results from Figures 34–36 collectively indicate that the crack formation is primarily due to tensile stress perpendicular to the specimen's vertical center line.

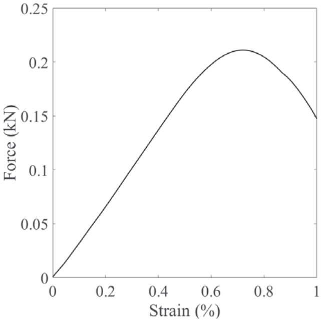

Figure 31. Loading curve on the top plate.

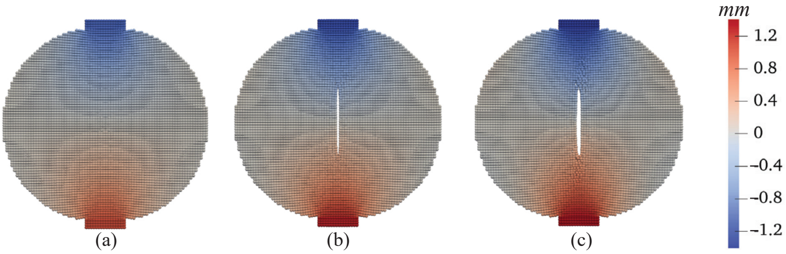

Figure 32. Contours of the vertical displacement (mm) superimposed on the deformed configuration at (**a**) $u = 1.1$ mm, (**b**) $u = 1.25$ mm, and (**c**) $u = 1.4$ mm.

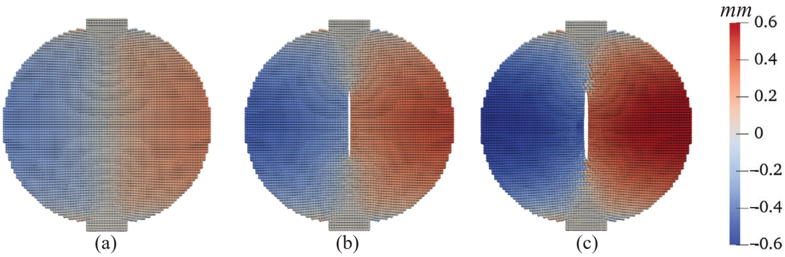

Figure 33. Contours of the horizontal displacement (mm) on the deformed configuration at (**a**) $u = 1.1$ mm, (**b**) $u = 1.25$ mm, and (**c**) $u = 1.4$ mm.

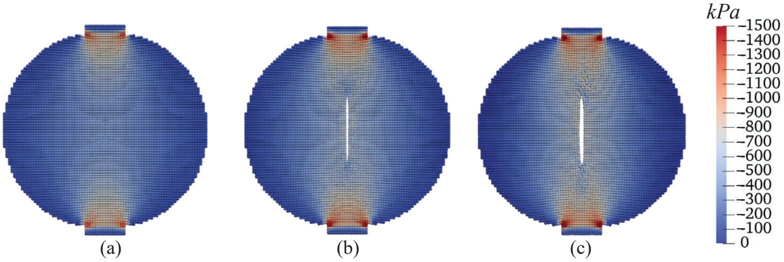

Figure 34. Contours of stress σ_{yy} (kPa) on the deformed configuration at (**a**) $u = 1.1$ mm, (**b**) $u = 1.25$ mm, and (**c**) $u = 1.4$ mm.

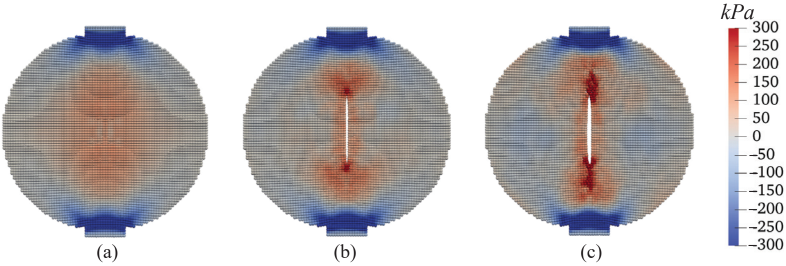

Figure 35. Contours of stress σ_{xx} (kPa) on the deformed configuration at (**a**) $u = 1.1$ mm, (**b**) $u = 1.25$ mm, and (**c**) $u = 1.4$ mm.

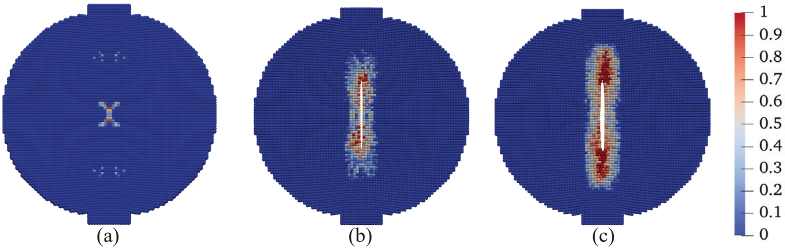

Figure 36. Contours of the damage parameter on the deformed configuration at (**a**) $u = 1.1$ mm, (**b**) $u = 1.25$ mm, and (**c**) $u = 1.4$ mm.

Second, in the base simulation, we also investigate the influence of spatial discretization on the results by employing two distinct spatial discretization schemes. The first scheme utilizes 6224 points with a grid spacing (Δx) of 3.3 mm (referred to as grid 1), while the second scheme involves 10,408 points with $\Delta x = 2.5$ mm (referred to as grid 2). Both schemes adopt the same horizon size, $\delta = 10$ mm. The comparative results of these two discretization schemes are presented in Figures 37–42. Figure 37 displays the vertical loading curves obtained from simulations using both spatial discretization schemes. For a detailed comparison, we present contours of displacement and stress at a uniform displacement load ($u = 1.25$ mm) for both simulations as follows. Figure 38 compares the vertical displacement contours. Figure 39 contrasts the horizontal displacement contours. Figure 40 showcases the differences in vertical stress contours (σ_{yy}). Figure 41 illustrates the comparison in horizontal stress contours (σ_{xx}). Figure 42 compares the damage parameter contours at the same displacement load for both discretization schemes. The results from these comparisons suggest that, given a consistent horizon size, the choice of spatial discretization scheme exerts a minimal influence on the crack formation in the disk specimen under vertical compression loading.

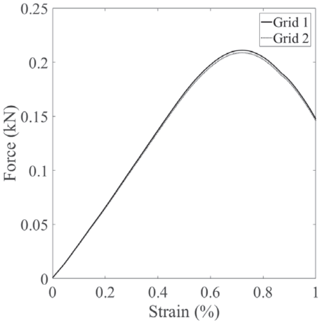

Figure 37. Comparison of the loading curve from the simulations with two spatial discretization schemes.

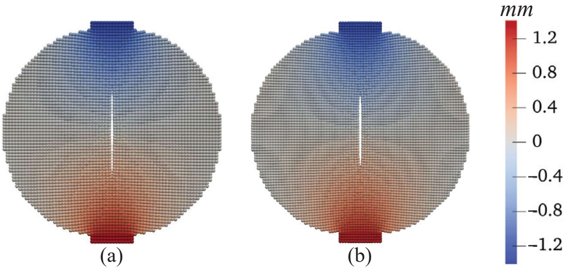

Figure 38. Contours of the vertical displacement (mm) on the deformed configuration at $u = 1.25$ mm: (**a**) Grid 1 and (**b**) Grid 2.

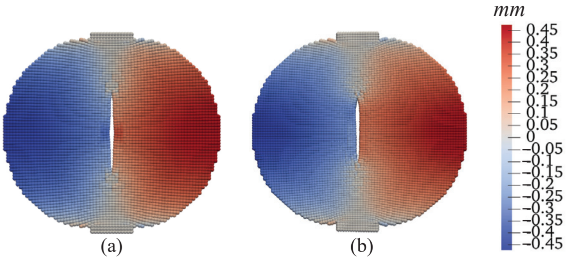

Figure 39. Contours of the horizontal displacement (mm) on the deformed configuration at $u = 1.25$ mm: (**a**) Grid 1 and (**b**) Grid 2.

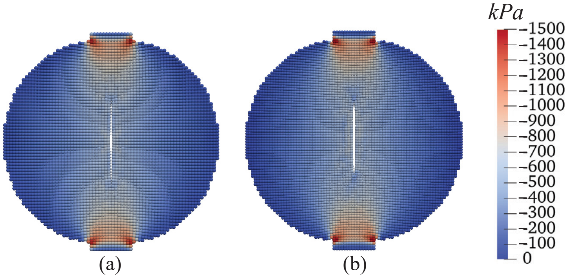

Figure 40. Contours of stress σ_{yy} (kPa) on the deformed configuration at $u = 1.25$ mm: (**a**) Grid 1 and (**b**) Grid 2.

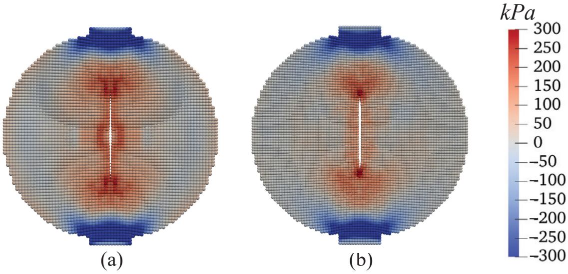

Figure 41. Contours of stress σ_{xx} (kPa) on the deformed configuration at $u = 1.25$ mm: (**a**) Grid 1 and (**b**) Grid 2.

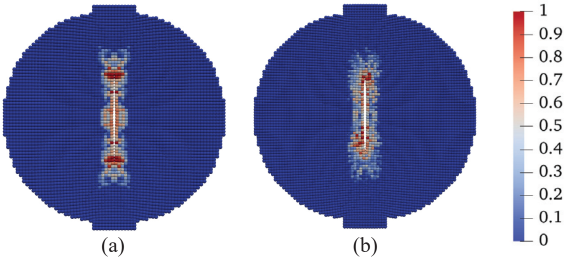

Figure 42. Contours of the damage parameter on the deformed configuration at $u = 1.25$ mm: (**a**) Grid 1 and (**b**) Grid 2.

Third, we investigate the effect of temperature variations on the cracking behavior in unsaturated elastic porous materials, specifically, at $\Delta\theta = 0$ °C, 25 °C, and 50 °C. The other simulation parameters, including loading and spatial discretization, remain identical to those in the base simulation. The outcomes of this investigation are showcased in Figures 43–48. Figure 43 compares the loading curves from the simulations conducted at the three different temperatures, revealing a decrease in the peak load of the disk specimen with increasing temperature. The contours of vertical displacement at a uniform displacement load ($u = 1.25$ mm) across the three simulations are compared in Figure 44, while Figure 45 does the same for horizontal displacement. These figures illustrate that the rise in temperature increases the horizontal displacement, leading to a longer crack, whereas the vertical displacement is comparatively less influenced by temperature changes under the same loading conditions. The contours of vertical and horizontal stresses (σ_{yy} and σ_{xx}, respectively) at $u = 1.25$ mm for the three simulations are presented in Figures 46 and 47. Finally, Figure 48 compares the contours of the damage variable at the same displacement load. Collectively, the results from Figures 46–48 indicate that the combination of temperature increase and mechanical loading significantly impacts the timing and progression of crack initiation and development in the specimen.

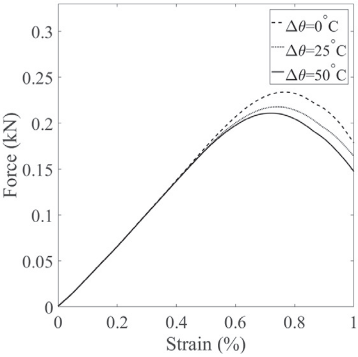

Figure 43. Comparison of the loading curves from the simulation with $\Delta\theta = 0$ °C, $\Delta\theta = 25$ °C, and $\Delta\theta = 50$ °C.

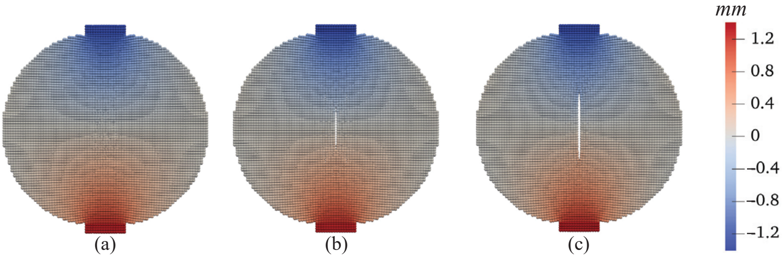

Figure 44. Contours of the vertical displacement (mm) on the deformed configuration at $u = 1.25$ mm: (**a**) $\Delta\theta = 0$ °C, (**b**) $\Delta\theta = 25$ °C, and (**c**) $\Delta\theta = 50$ °C.

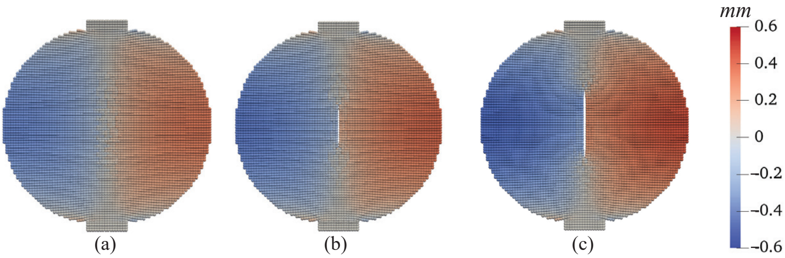

Figure 45. Contours of the horizontal displacement (mm) on the deformed configuration at $u = 1.25$ mm: (**a**) $\Delta\theta = 0$ °C, (**b**) $\Delta\theta = 25$ °C, and (**c**) $\Delta\theta = 50$ °C.

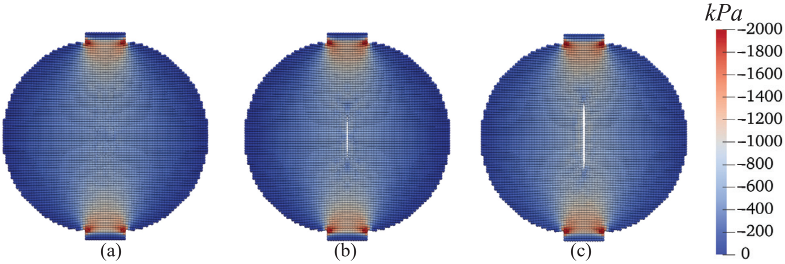

Figure 46. Contours of stress σ_{yy} (kPa) on the deformed configuration at $u = 1.25$ mm: (**a**) $\Delta\theta = 0$ °C, (**b**) $\Delta\theta = 25$ °C, and (**c**) $\Delta\theta = 50$ °C.

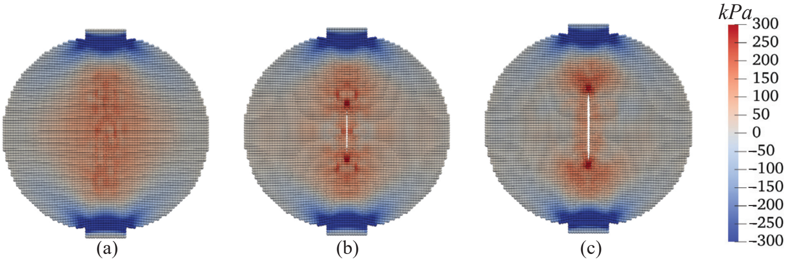

Figure 47. Contours of stress σ_{xx} (kPa) on the deformed configuration at $u = 1.25$ mm: (**a**) $\Delta\theta = 0$ °C, (**b**) $\Delta\theta = 25$ °C, and (**c**) $\Delta\theta = 50$ °C.

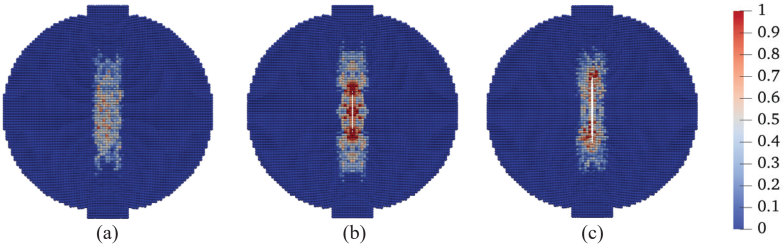

Figure 48. Contours of the damage variable on the deformed configuration at $u = 1.25$ mm: (**a**) $\Delta\theta = 0$ °C, (**b**) $\Delta\theta = 25$ °C, and (**c**) $\Delta\theta = 50$ °C.

4.4. Discussions

In this part, we briefly discuss the limitations of the present study and future work. The present study focused on the impact of temperature on shear banding formation and mode I cracking in unsaturated soils. In the nonlocal THM framework, the temperature variation in the specimen is assumed to be uniform, and the temperature change caused by the plastic deformation is not considered, which should be resolved in a future study. The numerical simulations in this study should be further validated against physical testing results on shear banding and cracking in thermal unsaturated soils. The improvement of the present work includes implementing a fully coupled THM PPM model following the authors' previous work on the fully coupled hydro–mechanical PPM model, which is an ongoing effort. It is worth noting that the proposed THM PPM model can be applied to modeling failure in frozen soils by implementing a constitutive model for frozen soils through the stabilized multiphase correspondence principle.

5. Summary

In this article, our investigation centers on shear banding and cracking in unsaturated porous media under non-isothermal conditions, utilizing a THM framework within PPM. A significant advancement of this study is the development of a nonlocal THM constitutive model specifically designed for unsaturated porous media in the PPM context. We have implemented the THM paradigm using an explicit Lagrangian meshfree algorithm, complemented by a return mapping algorithm for the numerical implementation of the nonlocal THM constitutive model. We have evaluated the performance and applicability of our proposed THM meshfree paradigm through a series of numerical examples. The results from these examples demonstrate the effectiveness and reliability of our THM PPM approach in accurately modeling the complex behaviors of shear banding and cracking in unsaturated porous media under varying thermal conditions. Importantly, our findings provide deep insights into the sophisticated relationship between temperature changes and the development of shear bands and cracks in such porous media under THM loading, highlighting the nuanced interdependencies in these phenomena.

Author Contributions: Conceptualization, H.P. and X.S.; methodology, H.P. and X.S.; software, H.P. and X.S.; validation, H.P. and X.S.; formal analysis, H.P. and X.S.; investigation, H.P. and X.S.; resources, X.S.; data curation, H.P. and X.S.; writing—original draft preparation, H.P.; writing—review and editing, H.P. and X.S.; visualization, H.P. and X.S.; supervision, X.S.; project administration, X.S.; funding acquisition, X.S. All authors have read and agreed to the published version of the manuscript.

Funding: This research was funded by the US National Science Foundation grant number 1944009.

Data Availability Statement: The data that support the findings of this study are available from the corresponding author upon reasonable request.

Acknowledgments: This work has been supported by the US National Science Foundation under contract number 1944009. The support is gratefully acknowledged. Any opinions or positions expressed in this article are those of the authors only and do not reflect any opinions or positions of the NSF. The authors thank the three anonymous reviewers for their constructive reviews of the original version of this article.

Conflicts of Interest: The authors declare no conflict of interest.

References

1. Terzaghi, K.; Peck, R.B.; Mesri, G. *Soil Mechanics in Engineering Practice*; John Wiley & Sons: Hoboken, NJ, USA, 1996.
2. Lambe, T.W.; Whitman, R.V. *Soil Mechanics*; John Wiley & Sons: Hoboken, NJ, USA, 1991; Volume 10.
3. Cheng, A.H.D. *Poroelasticity*; Springer: Berlin/Heidelberg, Germany, 2016; Volume 27.
4. Coussy, O. *Poromechanics*; John Wiley & Sons: Hoboken, NJ, USA, 2004.
5. Matasovic, N.; Kavazanjian, E., Jr.; Augello, A.J.; Bray, J.D.; Seed, R.B. Solid waste landfill damage caused by 17 January 1994 Northridge earthquake. *Northridge Calif. Earthq.* **1994**, *17*, 221–229.
6. Zoback, M.D. *Reservoir Geomechanics*; Cambridge University Press: Cambridge, UK, 2010.
7. Wartman, J.; Montgomery, D.R.; Anderson, S.A.; Keaton, J.R.; Benoît, J.; dela Chapelle, J.; Gilbert, R. The 22 March 2014 Oso landslide, Washington, USA. *Geomorphology* **2016**, *253*, 275–288. [CrossRef]
8. Kramer, S.L. *Geotechnical Earthquake Engineering*; Pearson Education India: Chennai, India, 1996.
9. Mitchell, J.K.; Soga, K. *Fundamentals of Soil Behavior*; John Wiley & Sons: New York, NY, USA, 2005; Volume 3.
10. Gens, A. Soil–environment interactions in geotechnical engineering. *Géotechnique* **2010**, *60*, 3–74. [CrossRef]
11. Wang, K.; Song, X. Strain localization in non-isothermal unsaturated porous media considering material heterogeneity with stabilized mixed finite elements. *Comput. Methods Appl. Mech. Eng.* **2020**, *359*, 112770. [CrossRef]
12. Song, X.; Wang, M.C. Molecular dynamics modeling of a partially saturated clay-water system at finite temperature. *Int. J. Numer. Anal. Methods Geomech.* **2019**, *43*, 2129–2146. [CrossRef]
13. Zhang, Z.; Song, X. Nonequilibrium molecular dynamics (NEMD) modeling of nanoscale hydrodynamics of clay-water system at elevated temperature. *Int. J. Numer. Anal. Methods Geomech.* **2022**, *46*, 889–909. [CrossRef]
14. Sánchez, M.; Gens, A.; Olivella, S. THM analysis of a large-scale heating test incorporating material fabric changes. *Int. J. Numer. Anal. Methods Geomech.* **2012**, *36*, 391–421. [CrossRef]
15. Coccia, C.R.; McCartney, J. A thermo-hydro-mechanical true triaxial cell for evaluation of the impact of anisotropy on thermally induced volume changes in soils. *Geotech. Test. J.* **2012**, *35*, 227–237. [CrossRef]
16. Zhang, X.; Briaud, J.L. Three dimensional numerical simulation of residential building on shrink–swell soils in response to climatic conditions. *Int. J. Numer. Anal. Methods Geomech.* **2015**, *39*, 1369–1409. [CrossRef]
17. Song, X.; Wang, K.; Bate, B. A hierarchical thermo-hydro-plastic constitutive model for unsaturated soils and its numerical implementation. *Int. J. Numer. Anal. Methods Geomech.* **2018**, *42*, 1785–1805. [CrossRef]
18. Song, X.; Wang, K.; Ye, M. Localized failure in unsaturated soils under non-isothermal conditions. *Acta Geotech.* **2018**, *13*, 73–85. [CrossRef]
19. Habibishandiz, M.; Saghir, M. A critical review of heat transfer enhancement methods in the presence of porous media, nanofluids, and microorganisms. *Therm. Sci. Eng. Prog.* **2022**, *30*, 101267. [CrossRef]
20. Bai, B.; Zhou, R.; Cai, G.; Hu, W.; Yang, G. Coupled thermo-hydro-mechanical mechanism in view of the soil particle rearrangement of granular thermodynamics. *Comput. Geotech.* **2021**, *137*, 104272. [CrossRef]
21. Vasheghani Farahani, M.; Hassanpouryouzband, A.; Yang, J.; Tohidi, B. Heat transfer in unfrozen and frozen porous media: Experimental measurement and pore-scale modeling. *Water Resour. Res.* **2020**, *56*, e2020WR027885. [CrossRef]
22. Menon, S.; Song, X. A stabilized computational nonlocal poromechanics model for dynamic analysis of saturated porous media. *Int. J. Numer. Methods Eng.* **2021**, *122*, 5512–5539. [CrossRef]
23. Menon, S.; Song, X. Updated Lagrangian unsaturated periporomechanics for extreme large deformation in unsaturated porous media. *Comput. Methods Appl. Mech. Eng.* **2022**, *400*, 115511. [CrossRef]
24. Menon, S.; Song, X. Computational coupled large-deformation periporomechanics for dynamic failure and fracturing in variably saturated porous media. *Int. J. Numer. Methods Eng.* **2023**, *124*, 80–118. [CrossRef]
25. Menon, S.; Song, X. A computational periporomechanics model for localized failure in unsaturated porous media. *Comput. Methods Appl. Mech. Eng.* **2021**, *384*, 113932. [CrossRef]
26. Menon, S.; Song, X. Computational multiphase periporomechanics for unguided cracking in unsaturated porous media. *Int. J. Numer. Methods Eng.* **2022**, *123*, 2837–2871. [CrossRef]
27. Menon, S.; Song, X. Shear banding in unsaturated geomaterials through a strong nonlocal hydromechanical model. *Eur. J. Environ. Civ. Eng.* **2022**, *26*, 3357–3371. [CrossRef]
28. Cundall, P.A.; Strack, O.D. A discrete numerical model for granular assemblies. *Geotechnique* **1979**, *29*, 47–65. [CrossRef]
29. Sukumar, N.; Moës, N.; Moran, B.; Belytschko, T. Extended finite element method for three-dimensional crack modelling. *Int. J. Numer. Methods Eng.* **2000**, *48*, 1549–1570. [CrossRef]

30. Moës, N.; Belytschko, T. Extended finite element method for cohesive crack growth. *Eng. Fract. Mech.* **2002**, *69*, 813–833. [CrossRef]
31. Khoei, A.R. *Extended Finite Element Method: Theory and Applications*; John Wiley & Sons: Hoboken, NJ, USA, 2014.
32. Miehe, C.; Welschinger, F.; Hofacker, M. Thermodynamically consistent phase-field models of fracture: Variational principles and multi-field FE implementations. *Int. J. Numer. Methods Eng.* **2010**, *83*, 1273–1311. [CrossRef]
33. De Borst, R. *Computational Methods for Fracture in Porous Media: Isogeometric and Extended Finite Element Methods*; Elsevier: Amsterdam, The Netherlands, 2017.
34. Menon, S.; Song, X. Coupled analysis of desiccation cracking in unsaturated soils through a non-local mathematical formulation. *Geosciences* **2019**, *9*, 428. [CrossRef]
35. François, B.; Laloui, L. ACMEG-TS: A constitutive model for unsaturated soils under non-isothermal conditions. *Int. J. Numer. Anal. Methods Geomech.* **2008**, *32*, 1955–1988. [CrossRef]
36. Bolzon, G.; Schrefler, B.A. Thermal effects in partially saturated soils: A constitutive model. *Int. J. Numer. Anal. Methods Geomech.* **2005**, *29*, 861–877. [CrossRef]
37. Gens, A.; Jouanna, P.; Schrefler, B. *Modern Issues in Non-Saturated Soils*; Number BOOK; Springer: Berlin/Heidelberg, Germany, 1995.
38. Wu, W.; Li, X.; Charlier, R.; Collin, F. A thermo-hydro-mechanical constitutive model and its numerical modelling for unsaturated soils. *Comput. Geotech.* **2004**, *31*, 155–167. [CrossRef]
39. Dumont, M.; Taibi, S.; Fleureau, J.M.; Abou-Bekr, N.; Saouab, A. A thermo-hydro-mechanical model for unsaturated soils based on the effective stress concept. *Int. J. Numer. Anal. Methods Geomech.* **2011**, *35*, 1299–1317. [CrossRef]
40. Mašín, D.; Khalili, N. A thermo-mechanical model for variably saturated soils based on hypoplasticity. *Int. J. Numer. Anal. Methods Geomech.* **2012**, *36*, 1461–1485. [CrossRef]
41. Xiong, Y.; Ye, G.; Zhu, H.; Zhang, S.; Zhang, F. Thermo-elastoplastic constitutive model for unsaturated soils. *Acta Geotech.* **2016**, *11*, 1287–1302. [CrossRef]
42. Zhou, C.; Ng, C.W.W. Simulating the cyclic behaviour of unsaturated soil at various temperatures using a bounding surface model. *Géotechnique* **2016**, *66*, 344–350. [CrossRef]
43. Schofield, A.N.; Wroth, P. *Critical State Soil Mechanics*; McGraw-Hill: London, UK, 1968; Volume 310.
44. Zienkiewicz, O.C.; Chan, A.; Pastor, M.; Schrefler, B.; Shiomi, T. *Computational Geomechanics*; Citeseer: University Park, PA, USA, 1999; Volume 613.
45. Silling, S.A.; Epton, M.; Weckner, O.; Xu, J.; Askari, E. Peridynamic states and constitutive modeling. *J. Elast.* **2007**, *88*, 151–184. [CrossRef]
46. Song, X.; Silling, S.A. On the peridynamic effective force state and multiphase constitutive correspondence principle. *J. Mech. Phys. Solids* **2020**, *145*, 104161. [CrossRef]
47. Song, X.; Khalili, N. A peridynamics model for strain localization analysis of geomaterials. *Int. J. Numer. Anal. Methods Geomech.* **2019**, *43*, 77–96. [CrossRef]
48. Song, X.; Menon, S. Modeling of chemo-hydromechanical behavior of unsaturated porous media: A nonlocal approach based on integral equations. *Acta Geotech.* **2019**, *14*, 727–747. [CrossRef]
49. Song, X.; Pashazad, H. Computational Cosserat periporomechanics for strain localization and cracking in deformable porous media. *Int. J. Solids Struct.* **2023**, *288*, 112593. [CrossRef]
50. Pashazad, H.; Song, X. Computational multiphase micro-periporomechanics for dynamic shear banding and fracturing of unsaturated porous media. *Int. J. Numer. Methods Eng.* **2023**, *125*, e7418. . [CrossRef]
51. Kakogiannou, E.; Sanavia, L.; Nicot, F.; Darve, F.; Schrefler, B.A. A porous media finite element approach for soil instability including the second-order work criterion. *Acta Geotech.* **2016**, *11*, 805–825. [CrossRef]
52. Song, X.; Borja, R.I. Mathematical framework for unsaturated flow in the finite deformation range. *Int. J. Numer. Methods Eng.* **2014**, *97*, 658–682. [CrossRef]
53. Song, X. Transient bifurcation condition of partially saturated porous media at finite strain. *Int. J. Numer. Anal. Methods Geomech.* **2017**, *41*, 135–156. [CrossRef]
54. Borja, R.I. Cam-Clay plasticity. Part V: A mathematical framework for three-phase deformation and strain localization analyses of partially saturated porous media. *Comput. Methods Appl. Mech. Eng.* **2004**, *193*, 5301–5338. [CrossRef]
55. Simo, J.C.; Hughes, T.J. *Computational Inelasticity*; Springer Science & Business Media: New York, NY, USA, 1998; Volume 7.
56. Hughes, T.J. *The Finite Element Method: Linear Static and Dynamic Finite Element Analysis*; Courier Corporation: Chelmsford, MA, USA, 2012.

geosciences

Article

Models for Considering the Thermo-Hydro-Mechanical-Chemo Effects on Soil–Water Characteristic Curves

Yao Li [1], Roberto Alves [1,2], Sai Vanapalli [1,*] and Gilson Gitirana, Jr. [2]

[1] Department of Civil Engineering, University of Ottawa, Ottawa, ON K1N 6N5, Canada; yli725@uottawa.ca (Y.L.); ralve026@uottawa.ca (R.A.)
[2] School of Civil and Environmental Engineering, Federal University of Goias (UFG), Goiânia 74690-900, GO, Brazil; gilsongitirana@ufg.br
* Correspondence: sai.vanapalli@uottawa.ca; Tel.: +1-613-562-5800 (ext. 6638)

Abstract: The soil–water characteristic curve (SWCC) is widely used as a tool in geotechnical, geo-environmental, hydrology, and soil science fields for predicting and interpreting hydro-mechanical behaviors of unsaturated soils. Several previous studies focused on investigating the influence of initial water content, stress history, temperature, and salt content on the SWCC behavior. However, there is still limited understanding to be gained from the literature on how we can systematically incorporate the influence of complex thermo-hydro-mechanical-chemo (THMC) effects into interpreting and predicting the behavior of unsaturated soils. To address that knowledge gap, in this study, the coupled influence of temperature, initial stress state, initial density, soil structure, and chemical solution effects was modeled using established SWCC equations from the literature. The methodology for incorporating the coupled effects of these influential factors is presented herein. Furthermore, we evaluated the SWCC models proposed in this study, enabling us to provide a comprehensive discussion of their strengths and limitations, using the published SWCC data from the literature. The developments outlined in this paper contribute toward facilitating a rigorous approach for analyzing the THMC behaviors of unsaturated soils.

Keywords: soil–water characteristic curve; unsaturated soils; thermo-hydro-mechanical-chemo behavior; coupled effects

Citation: Li, Y.; Alves, R.; Vanapalli, S.; Gitirana, G., Jr. Models for Considering the Thermo-Hydro-Mechanical-Chemo Effects on Soil–Water Characteristic Curves. *Geosciences* **2024**, *14*, 38. https://doi.org/10.3390/geosciences14020038

Academic Editors: Jesus Martinez-Frias and Mohamed Shahin

Received: 17 December 2023
Revised: 14 January 2024
Accepted: 22 January 2024
Published: 31 January 2024

1. Introduction

The soil–water characteristic curve (SWCC) is defined as the relationship between the amount of water stored in the soil and soil suction [1], as shown in Figure 1. The water content may be represented using different variables, such as the volumetric water content, the gravimetric water content, the degree of saturation, and the effective degree of saturation. Soil suction can be represented in terms of matric, osmotic, or total suction. A generalized view of the water retention properties of the soil also considers the effects of other stress state variables, contributing to net total stresses. The SWCC is widely used in various fields related to geosciences, including hydrology, soil science, and geotechnical engineering, as a tool for interpreting and predicting properties of unsaturated soils [2–9].

Figure 1 indicates that the SWCC is closely related to the pore size distribution (PoSD), which is proportional to the first derivative of the SWCC. The PoSD primarily offers information regarding capillary water retention. However, there are several studies in the literature suggesting that other factors (e.g., soil temperature, initial stress state, soil structure, drying–wetting cycles, and soil–water chemistry) influence the SWCC and its multiple water retention mechanisms [10–16]. During the last three decades, there has been significant interest in understanding the influence of temperature and salt solution effects on SWCC behavior [17–22].

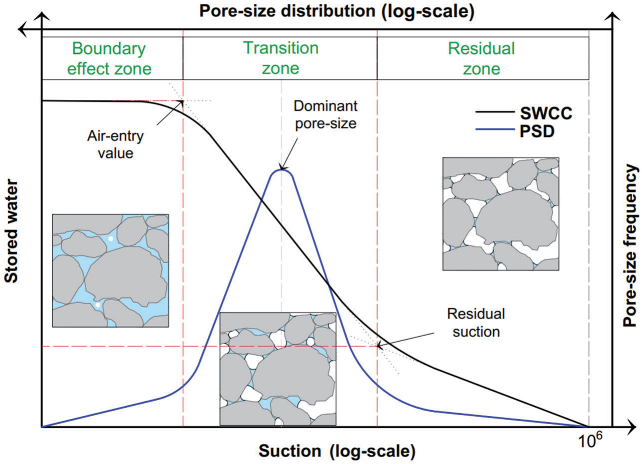

Figure 1. Typical soil–water characteristics and pore size distribution curves.

Reliable determination of the SWCC along with the hydraulic and mechanical properties of soil is required for rational design of geo-infrastructure constructed with or within unsaturated soils, ensuring its safety over the entire service life [23–29]. With this goal in mind, there is an urgent need to systematically investigate SWCCs by considering the coupled influence of physic-chemo properties, allowing for a more complete interpretation of the complex nature of unsaturated soils [30–33].

In this study, several key factors, including initial water content, initial stress state, temperature, and salt solution, were investigated within a unified framework of analysis of the SWCC. Two methods—one based on the variation in soil (matric) suction and the other considering the variation in PoSD—are highlighted herein. Furthermore, this article presents a framework that is strongly related to continuum mechanics principles, which can be used for numerical modeling of the complex thermal-hydro-mechanical-chemo (THMC) behaviors of unsaturated soils, using the SWCC as a tool.

2. Models' Development

The water content stored in soil pores with radius r can be calculated [25] via a widely used mathematical relationship shown in Equation (1).

$$\theta(r) = \int_{r_{min}}^{r} f(r)dr \tag{1}$$

where θ is the volumetric water content, r is the pore radius, $f(r)$ is a function of pore size distribution, and r_{min} is the minimum pore radius.

The capillary law shown in Equation (2a) is widely used in the literature to relate the soil (matric) suction with the surface tension T_s, contact angle θ_s, and soil pore radius r (i.e., $\psi = f\ (T_s, \theta_s, r)$).

$$\psi = \frac{2T_s\cos\theta}{r} \tag{2a}$$

$$\theta(\psi) = \int_{\psi_{max}}^{\psi} f\left(\frac{2T_s\cos\theta}{\psi}\right) d\left(\frac{2T_s\cos\theta}{\psi}\right) = \int_{\psi}^{\psi_{max}} f\left(\frac{2T_s\cos\theta}{\psi}\right) \frac{2T_s\cos\theta}{\psi^2} d\psi \tag{2b}$$

where ψ_{max} is the maximum soil matric suction. Through Equations (1) and (2a), Equation (2b) can be simply found, which builds the links between water content and soil suction.

Several SWCC models are outlined in the literature based on the PoSD functions. Among these SWCC models, the equations proposed by Brooks and Corey (BC model [34]), van Genuchten (VG model [35]), and Fredlund and Xing (FX model [36]), shown in Equations (3)–(5), are well-known.

$$\frac{\theta_{lw}-\theta_{res}}{\theta_{sat}-\theta_{res}}=\begin{cases}1,\ \psi\leq\psi_{AEV}\\ \frac{1}{(\psi/\psi_{AEV})^{\lambda_{bc}}},\psi>\psi_{AEV}\end{cases} \tag{3}$$

$$g(\psi)=\frac{m_{vg}n_{vg}a_{vg}\left(a_{vg}\psi\right)^{n_{vg}-1}}{\left[1+\left(a_{vg}\psi\right)^{n_{vg}}\right]^{m_{vg}+1}} \tag{4a}$$

$$\frac{\theta_{lw}-\theta_{res}}{\theta_{sat}-\theta_{res}}=\frac{1}{\left[1+\left(a_{vg}\psi\right)^{n_{vg}}\right]^{m_{vg}}} \tag{4b}$$

$$\frac{\theta_{lw}}{\theta_{sat}}=c(\psi)\frac{1}{\left[\ln\left(\exp(1)+\left(\psi/a_{fx}\right)^{n_{fx}}\right)\right]^{m_{fx}}} \tag{5a}$$

$$c(\psi)=\left[1-\frac{\ln[1+(\psi/\psi_{res})]}{\ln[1+(10^6/\psi_{res})]}\right] \tag{5b}$$

$$f(\psi)=\frac{m_{fx}n_{fx}\left(\psi/a_{fx}\right)^{n_{fx}-1}}{a_{fx}\left[\exp(1)+\left(\psi/a_{fx}\right)^{n_{fx}}\right]\left[\ln\left(\exp(1)+\left(\psi/a_{fx}\right)^{n_{fx}}\right)\right]^{m_{fx}+1}} \tag{5c}$$

where ψ_{AEV} is air-entry value, λ_{bc} is a model parameter for the BC model, a_{vg}, n_{vg}, and m_{vg} are model parameters for the VG model, a_{fx}, n_{fx}, and m_{fx} are model parameters for the FX model, and ψ_{res} is residual soil suction. Equation (4a) is the PoSD function for the VG model (e.g., Equation (4b)). In Equation (5), $c(\psi)$ is a correction function in the FX model [36].

Figure 2 highlights two methods that are used in the present study, based on widely used SWCC models from the literature. One method is proposed from the pore-scale model for variation in soil matric suction, while the other stems from the overall variation in PoSD due to the influence of various factors.

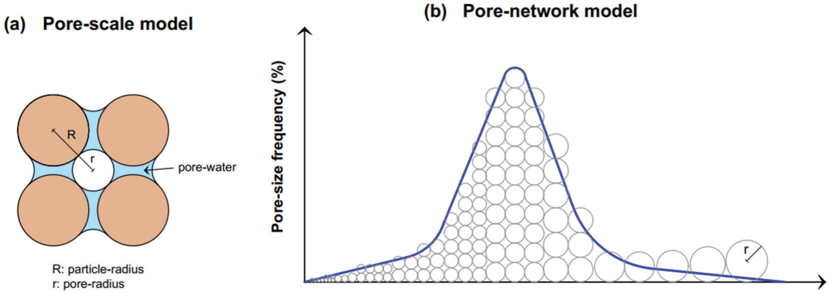

Figure 2. Conceptual models for: (**a**) pore scale; and (**b**) pore networks.

2.1. Basic Methodology for Modeling SWCC Based on the Matric Suction Variation

2.1.1. Basic Framework

In this section, the variation in soil suction due to several influential factors that include temperature, initial water content, initial stress state, and salt concentration is considered via the capillary law (i.e., Equation (2)). The variation in matric suction caused by various influential factors can be written as below.

$$d\psi=d\left(\frac{2T_s\cos\theta}{r}\right)=\frac{\partial\psi}{\partial T}dT+\frac{\partial\psi}{\partial P_{comp}}dP_{comp}+\frac{\partial\psi}{\partial w_i}dw_i+\frac{\partial\psi}{\partial C}dC=\sum\frac{\partial\psi}{\partial\phi_i}d\phi_i \tag{6}$$

where T, P_{comp}, w_i, and c are temperature, initial compaction pressure, initial water content, and salt concentration, respectively, and φ_i refers to an influential factor.

Equation (7) can be obtained by expanding Equation (6), considering the variation in surface tension, contact angle, and pore radius caused by various factors (e.g., temperature, salt concentration [17–22]).

$$d\psi = \frac{2\cos\theta}{r}\left(\frac{\partial T_s}{\partial T}dT + \frac{\partial T_s}{\partial P_{comp}}dP_{comp} + \frac{\partial T_s}{\partial w_i}dw_i + \frac{\partial T_s}{\partial C}dC\right) + \frac{2T_s}{r}[\frac{\partial(\cos\theta)}{\partial T}dT + \frac{\partial(\cos\theta)}{\partial P_{comp}}dP_{comp} + \frac{\partial(\cos\theta)}{\partial w_i}dw_i + \frac{\partial(\cos\theta)}{\partial C}dC] + (2T_s\cos\theta)\left[\frac{\partial\left(\frac{1}{r}\right)}{\partial T}dT + \frac{\partial\left(\frac{1}{r}\right)}{\partial P_{comp}}dP_{comp} + \frac{\partial\left(\frac{1}{r}\right)}{\partial w_i}dw_i + \frac{\partial\left(\frac{1}{r}\right)}{\partial C}dC\right] \tag{7}$$

Equation (7) suggests that temperature affects surface tension, contact angle, and the pore radius. This is a complex model considering the coupled influence of all the discussed parameters. In this study, the variations in surface tension and contact angle are analyzed together by simplifying Equation (7) into Equation (8), as given below.

$$\begin{aligned} d\psi = d\left(\frac{2T_s\cos\theta}{r}\right) &= \frac{1}{r}\left[\frac{\partial(2T_s\cos\theta)}{\partial T}dT + \frac{\partial(2T_s\cos\theta)}{\partial P_{comp}}dP_{comp} + \frac{\partial(2T_s\cos\theta)}{\partial w_i}dw_i + \frac{\partial(2T_s\cos\theta)}{\partial c}dc\right] \\ &\quad + (2T_s\cos\theta)\left[\frac{\partial\left(\frac{1}{r}\right)}{\partial T}dT + \frac{\partial\left(\frac{1}{r}\right)}{\partial P_{comp}}dP_{comp} + \frac{\partial\left(\frac{1}{r}\right)}{\partial w_i}dw_i + \frac{\partial\left(\frac{1}{r}\right)}{\partial c}dc\right] \\ &= \sum\left[\frac{\partial(2T_s\cos\theta)}{\partial\phi_i}d\phi_i + \frac{(2T_s\cos\theta)\partial\left(\frac{1}{r}\right)}{\partial\phi_i}d\phi_i\right] \end{aligned} \tag{8}$$

Equation (8) represents effects related to matric suction in two parts. The first part of the equation relates to the variation in air–water interfacial free energy (e.g., T_s $\cos\theta$), while the second part considers changes that arise in the pore radius. However, not all factors contribute equally to the variation in matric suction. For example, both initial compaction pressure and initial water content in a fine-grained soil may exert minor effects on surface tension and contact angle in comparison with their effects on pore radius.

In this study, temperature and salt concentration are also considered to play a role in the variation in air–water interface energy (e.g., surface tension and contact angle). To achieve this, Equation (8) is further simplified into Equation (9).

$$d\psi = d\left(\frac{2T_s\cos\theta}{r}\right) = \frac{1}{r}\left(\frac{\partial(2T_s\cos\theta)}{\partial T}dT + \frac{\partial(2T_s\cos\theta)}{\partial c}dc\right) + (2T_s\cos\theta)\left[\frac{\partial\left(\frac{1}{r}\right)}{\partial P_{comp}}dP_{comp} + \frac{\partial\left(\frac{1}{r}\right)}{\partial w_i}dw_i\right] \tag{9}$$

2.1.2. Temperature and Salt Solution Effects on Matric Suction

Experimental results published in the literature highlight a rough linear downward trend due to the influence of temperature and soluble salt concentration effects on air–water interface energy. Equations (10) and (11) are suggested to describe this trend, respectively, for temperature and salt solution (concentration).

$$\frac{\partial(2T_s\cos\theta)}{\partial T}dT = -(2T_s\cos\theta)_0\eta_T dT = -(2T_s\cos\theta)_0\eta_T(T - T_0) \tag{10}$$

$$\frac{\partial(2T_s\cos\theta)}{\partial c}dc = -(2T_s\cos\theta)_0\eta_c dc = -(2T_s\cos\theta)_0\eta_c(c - c_0) \tag{11}$$

where $(2T_s\cos\theta)_0$ refers to the constant value in the original state (e.g., the value at T_0 and c_0).

Based on Equations (9)–(11), the following Equation (12) can be obtained.

$$\frac{\psi'}{\psi}=\frac{\psi+\Delta\psi}{\psi}\cong\frac{\psi+\mathrm{d}\psi}{\psi}=1-\eta_T(T-T_0)-\eta_c(c-c_0) \tag{12a}$$

$$\psi=\frac{\psi'}{[1-\eta_T(T-T_0)-\eta_c(c-c_0)]} \tag{12b}$$

2.1.3. Initial Stress and Water Content Effects on Matric Suction

The second part on the right side of Equation (9) is useful for evaluating the influence of the initial stress effect.

$$\frac{\partial\left(\frac{1}{r}\right)}{\partial P_{comp}}dP_{comp}=-\frac{1}{r^2}\frac{\partial(r)}{\partial P_{comp}}dP_{comp}=\frac{1}{r}\left(-\frac{1}{r}\frac{\partial r}{\partial P_{comp}}dP_{comp}\right) \tag{13}$$

The right side of Equation (13) highlights the deformation of soil pores under compression. Equation (13) can model the variation in pore radius under initial compact pressure. However, a direct mathematical relationship between pore radius and compaction pressure is not established. In this regard, two equations—(14) and (15)—might be helpful. Equation (14) builds relationships between volumetric strain and one-dimensional deformation, while Equation (15) proposes a rather simplified link between volumetric strain and compression.

$$\varepsilon_v=-\frac{\Delta e}{1+e}=-\frac{\Delta V_{void}}{V}\cong-\left(\frac{\Delta l_x}{l_x}+\frac{\Delta l_y}{l_y}+\frac{\Delta l_z}{l_z}\right)=-3\frac{\Delta r}{r} \tag{14}$$

$$d\varepsilon_v=k_c\frac{dP_{comp}}{P_{comp}} \tag{15}$$

where ε_v is volumetric strain (contraction is positive), e is the void ratio, V_{void} is the volume of soil void, l_x, l_y, and l_z refer to lengths in the x, y, and z axes, respectively, and k_c is a model parameter.

Equation (16) can be developed based on Equations (14) and (15).

$$\frac{\partial\left(\frac{1}{r}\right)}{\partial P_{comp}}dP_{comp}=\frac{1}{r}\left(-\frac{1}{r}\frac{\partial r}{\partial P_{comp}}dP_{comp}\right)=\frac{1}{r}\left(\frac{1}{3}\frac{d\varepsilon_v}{\partial P_{comp}}dP_{comp}\right)=\frac{1}{r}\left(\frac{k_p}{P_{comp}}dP_{comp}\right) \tag{16}$$

where k_p is a model parameter.

Similar to Equation (12a), the following Equation (17) can be obtained.

$$\frac{\psi'}{\psi}=\frac{\psi+\Delta\psi}{\psi}\cong\frac{\psi+\mathrm{d}\psi}{\psi}=\frac{\psi+(2T_s\cos\theta)\left(\frac{\partial\left(\frac{1}{r}\right)}{\partial P_{comp}}dP_{comp}\right)}{\psi}=\frac{1+k_p\frac{\Delta P_{comp}}{P_{comp}}}{1}=1+k_p(1-P_0/P_{comp}) \tag{17}$$

Equation (18) can be used to model the initial water content effect at wetting optimum.

$$\frac{\partial\left(\frac{1}{r}\right)}{\partial w_i}dw_i=-\frac{1}{r^2}\frac{\partial r}{\partial w_i}dw_i=\frac{1}{r}\left(-\frac{1}{r}\frac{\partial r}{\partial w_i}dw_i\right)=\frac{1}{r}\left(\frac{1}{3}\frac{d\varepsilon_v}{\partial w_i}dw_i\right) \tag{18}$$

The relationships between initial water content and soil matric suction can be evaluated from the BC model (i.e., Equation (19a)). An equation similar to Equation (15) can be found in Equation (19b) for evaluating the effect of volumetric strain on matric suction. Equation (19b) is a simplified model for understanding volume deformation under matric suction.

$$\frac{w_i}{w_0}\cong\left(\frac{\psi_0}{\psi_i}\right)^{\lambda_{bc}} \tag{19a}$$

$$d\varepsilon_v = k_\psi \frac{d\psi_i}{\psi_i} \tag{19b}$$

Based on Equations (19), relationships between initial water content and volumetric deformation can be summarized as Equation (20).

$$dw_i = -\lambda_{bc} w_0 \left(\frac{\psi_0}{\psi_i}\right)^{\lambda_{bc}} \frac{d\psi_i}{\psi_i} = -\frac{\lambda_{bc}}{k_\psi} w_0 \left(\frac{\psi_0}{\psi_i}\right)^{\lambda_{bc}} \left(k_\psi \frac{d\psi_i}{\psi_i}\right) = -\frac{\lambda_{bc}}{k_\psi} w_0 \left(\frac{\psi_0}{\psi_i}\right)^{\lambda_{bc}} d\varepsilon_v = -\frac{\lambda_{bc}}{k_\psi} w_i d\varepsilon_v \tag{20}$$

Based on Equation (20), Equation (18) can be modified and summarized as Equation (21).

$$\frac{\partial\left(\frac{1}{r}\right)}{\partial w_i} dw_i = \frac{1}{r}\left(\frac{1}{3}\frac{d\varepsilon_v}{\partial w_i} dw_i\right) = \frac{1}{r}\left(-\frac{1}{3}\frac{k_\psi}{\lambda_{bc}}\frac{dw_i}{w_i}\right) = \frac{1}{r}\left(-\frac{k_{iw}}{w_i} dw_i\right) \tag{21}$$

Equation (21) can be represented in a form shown in Equation (22).

$$\frac{\psi'}{\psi} = \frac{\psi + \Delta\psi}{\psi} \cong \frac{\psi + \mathrm{d}\psi}{\psi} = \frac{\psi + (2T_s \cos\theta)\left(\frac{\partial\left(\frac{1}{r}\right)}{\partial w_i} dw_i\right)}{\psi} = \frac{1 - \frac{k_{iw}}{w_i}\Delta w_i}{1} = 1 - k_{iw}(1 - w_0/w_i) \tag{22}$$

where k_{iw} is a model parameter, and w_0 is the initial water content at reference state.

Equation (22) is built for modeling the SWCCs of fine-grained soils with initial water contents on the wetting side of the optimum water content. For water contents at dry side of optimum, the initial void ratio decreases (or initial dry density increases) as the initial water content rises. To express the initial water content effect at dry side of optimum, Equation (23) is suggested.

$$\frac{\psi'}{\psi} = \frac{\psi + \Delta\psi}{\psi} = 1 + k_{iw}(1 - w_0/w_i) \tag{23}$$

Equation (24) can be obtained based on Equations (9), (12), (17), (22), and (23). Equation (24a) considers the influence of initial water content in compacted fine-grained soils on wet of optimum conditions. Equation (24b) can be used for fine-grained soils compacted in conditions that are dry of optimum. The variation of soil matric suction can be numerically evaluated by substituting Equation (24) directly into Equation (4b).

$$\psi = \frac{\psi'}{\left[1 - \eta_T(T - T_0) - \eta_c(c - c_0) + k_p\left(1 - P_0/P_{comp}\right) - k_{iw}(1 - w_0/w_i)\right]} \tag{24a}$$

$$\psi = \frac{\psi'}{\left[1 - \eta_T(T - T_0) - \eta_c(c - c_0) + k_p\left(1 - P_0/P_{comp}\right) + k_{iw}(1 - w_0/w_i)\right]} \tag{24b}$$

In some cases, the initial void ratio is used instead of the initial stress state and the initial water content. For the initial stress state and the initial water content at dry optimum of condition, the initial void ratio decreases with the rise of equivalent compaction pressure and the initial water content (e.g., Equation (25b)). Due to the change in soil structure that arises in fine-grained soils because of the higher initial water content in the wet of optimum water content, there will be a rise in initial void ratio that can be attributed to the variation in smaller pores [37]. Equation (25a) can be used for representing such a scenario. Equation (25b) can be used for soils compacted at dry of optimum conditions.

$$\psi = \frac{\psi'}{\left[1 - \eta_T(T - T_0) - \eta_c(c - c_0) - k_p\left(1 - e_0/e_{comp}\right) + k_{iw}(1 - e_0/e_i)\right]} \tag{25a}$$

$$\psi = \frac{\psi'}{\left[1 - \eta_T(T - T_0) - \eta_c(c - c_0) - k_p\left(1 - e_0/e_{comp}\right) - k_{iw}(1 - e_0/e_i)\right]} \tag{25b}$$

where e_0 is the initial void ratio at reference state, and e_{comp} and e_i refer to the initial void ratios at corresponding initial stress state and initial water content, respectively.

The effects of various factors that include temperature, salt solution, initial stress state, and initial water content on SWCCs are highlighted in Figures 3–6, respectively, which were numerically modeled using Equation (25) by substituting that into Equation (4b).

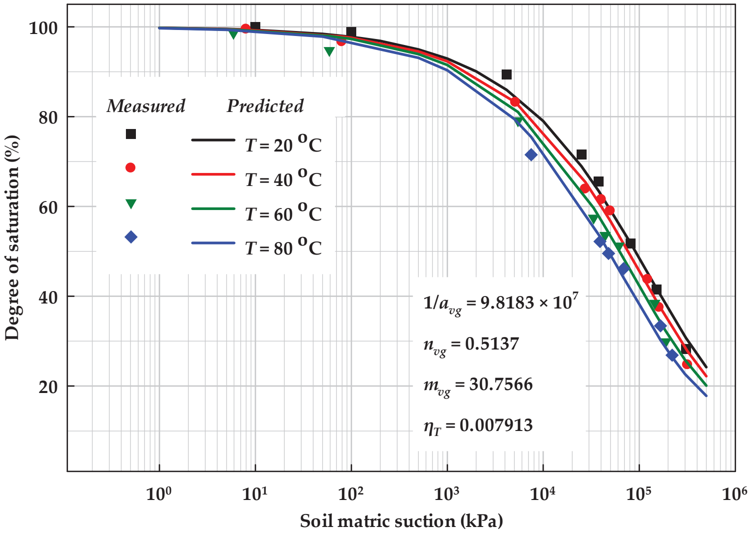

Figure 3. Temperature effects on the soil–water characteristic curve (based on data from [22]).

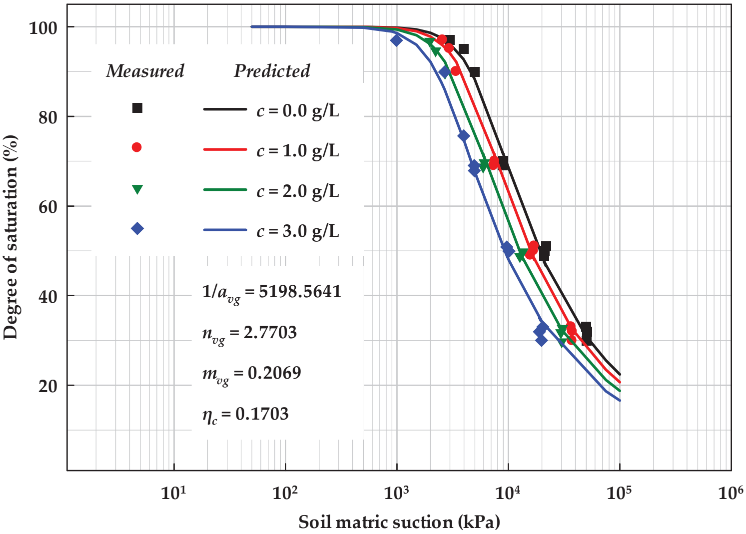

Figure 4. Salt solution effects on the soil–water characteristic curve (based on data from [21]).

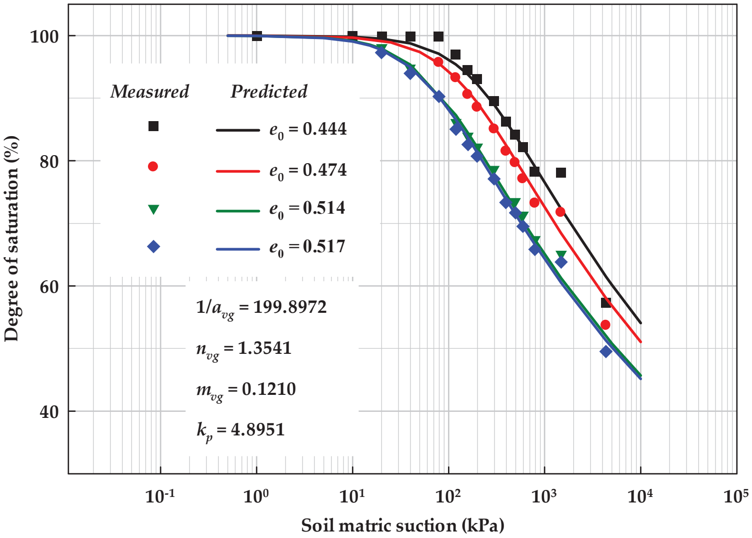

Figure 5. Initial stress state effects on the soil-water characteristic curve (based on data from [3]).

2.1.4. Coupling Effects on Soil Matric Suction

Based on Equation (25), these factors affect each other in a coupled manner. Another feasible approach can be evaluated using Equation (26) by neglecting high-order terms.

$$\begin{aligned} d\psi = d\left(\frac{2T_s\cos\theta}{r}\right) &= \frac{\partial\psi}{\partial\phi_i}(\phi_i-\phi_0) + \frac{\partial\psi}{\partial\phi_j}(\phi_j-\phi_0) + \frac{\partial^2\psi}{2\partial\phi_i\partial\phi_i}(\phi_i-\phi_0)^2 + \frac{\partial^2\psi}{2\partial\phi_j\partial\phi_j}(\phi_j-\phi_0)^2 \\ &+ \frac{\partial^2\psi}{\partial\phi_i\partial\phi_j}(\phi_i-\phi_0)(\phi_j-\phi_0) \cong \frac{\partial\psi}{\partial\phi_i}(\phi_i-\phi_0) + \frac{\partial\psi}{\partial\phi_j}(\phi_j-\phi_0) + \frac{\partial^2\psi}{\partial\phi_i\partial\phi_j}(\phi_i-\phi_0)(\phi_j-\phi_0) \end{aligned} \tag{26}$$

where ϕ_i and ϕ_j represent two distinct influential factors.

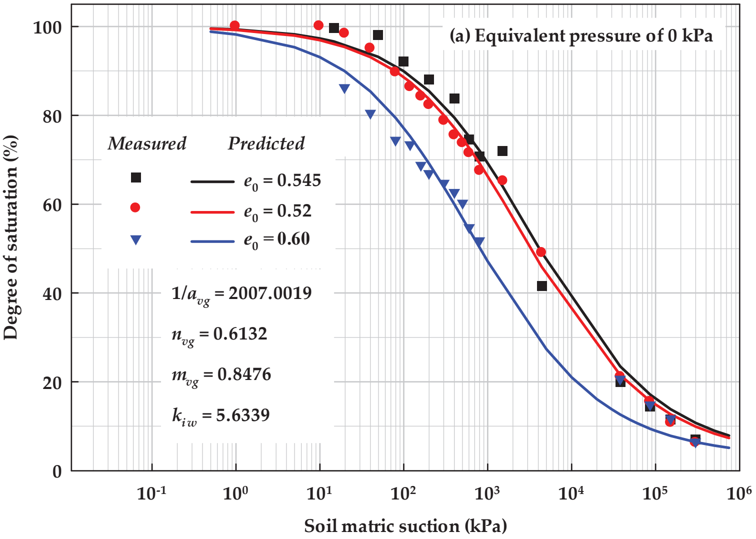

Figure 6. *Cont.*

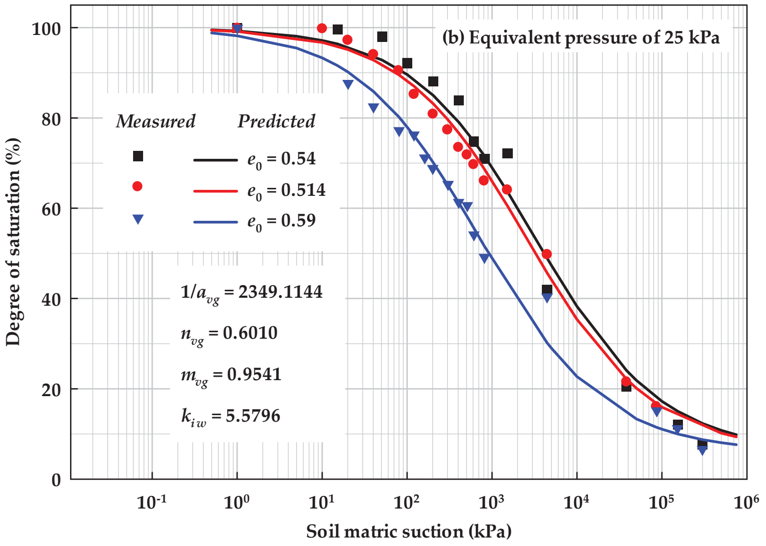

Figure 6. Initial water content effects on the soil–water characteristic curve at equivalent pressure of (**a**) 0 kPa and (**b**) 25 kPa (based on the data from [3]).

For the pore air–water interfacial energy part (e.g., $2T_s\cos\theta$), the coefficient on the right side of Equation (26) can be treated as a constant for simplicity. The high-order term for the variation of pore radius can be modeled using the relationship below.

$$\frac{\partial^2\left(\frac{2T_s\cos\theta}{r}\right)}{\partial\phi_i\partial\phi_j}d\phi_i d\phi_j = 2T_s\cos\theta\frac{2}{r^3}\frac{\partial^2 r}{\partial\phi_i\partial\phi_j}d\phi_i d\phi_j = \frac{2T_s\cos\theta}{r}\frac{2}{r^2}\frac{\partial^2 r}{\partial\phi_i\partial\phi_j}d\phi_i d\phi_j = \frac{2T_s\cos\theta}{r}\frac{2}{r^2}\frac{\partial^2 r}{\partial\phi_i\partial\phi_j}d\phi_i d\phi_j \tag{27}$$

Various SWCC models can be built considering the mutual effects of influential factors using Equation (27). However, due to limited experimental studies in the literature, the framework related to this part of the approach is proposed but not validated.

2.2. Basic Methodology for Representing Pore Size Distribution Variation Using the SWCC Correction Function

In Section 2.1, the variation of soil matric suction due to various influential factors was investigated. As PoSD also has a significant influence on SWCC behavior, this section focuses on the variation in the PoSD induced by factors such as initial water content and initial stress state.

The FX model without a correction function (i.e., Equations (2) and (4)) can also be written in a differential form, as summarized in Equation (28a).

$$\theta(\psi) = \int_{\psi}^{\psi_{max}} f(\psi)d\psi = \int_{\psi}^{\psi_{max}} \frac{m_{fx}n_{fx}\left(\psi/a_{fx}\right)^{n_{fx}-1}}{a_{fx}\left[\exp(1)+\left(\psi/a_{fx}\right)^{n_{fx}}\right]\left[\ln\left(\exp(1)+\left(\psi/a_{fx}\right)^{n_{fx}}\right)\right]^{m_{fx}+1}}d\psi \tag{28a}$$

$$\theta(\psi) = \int_{\psi}^{\psi_{max}} h(\psi)f(\psi)d\psi = \int_{\psi}^{\psi_{max}} h(\psi)\frac{m_{fx}n_{fx}\left(\psi/a_{fx}\right)^{n_{fx}-1}}{a_{fx}\left[\exp(1)+\left(\psi/a_{fx}\right)^{n_{fx}}\right]\left[\ln\left(\exp(1)+\left(\psi/a_{fx}\right)^{n_{fx}}\right)\right]^{m_{fx}+1}}d\psi \tag{28b}$$

$$\begin{cases} h(0) = 0 \\ \int_0^{\psi_{max}} h(\psi) d\psi = 1 \end{cases} \tag{28c}$$

To represent the variation in PoSD, one function *h(ψ)* can be added into PoSD, as shown in Equation (28b). Function *h(ψ)* should satisfy the boundary conditions (i.e., Equation (28c)), which equals zero at saturation, and its integral is one over the entire soil suction. To simplify the integral of the expression in Equation (28b), the following Equation (29) is suggested.

$$\begin{gathered} \theta(\psi) = \int_{\psi}^{\psi_{max}} h(\psi) d\psi \int_{\psi}^{\psi_{max}} f(\psi) d\psi = \\ \int_{\psi}^{\psi_{max}} h(\psi) d\psi \int_{\psi}^{\psi_{max}} \frac{m_{fx} n_{fx} \left(\psi / a_{fx}\right)^{n_{fx}-1}}{a_{fx} \left[\exp(1) + \left(\psi / a_{fx}\right)^{n_{fx}}\right] \left[\ln\left(\exp(1) + \left(\psi / a_{fx}\right)^{n_{fx}}\right)\right]^{m_{fx}+1}} d\psi \end{gathered} \tag{29}$$

Using Equation (29), the method to find function *h(ψ)* can be simplified to model the soil volumetric deformation observed over the soil suction increase (see Figure 7). As soil volume change will clearly result in pore size change, a function to represent soil deformation under variation of matric suction is reasonable.

The following two features should be highlighted: first, the soil deformation in unsaturated soils is predominant within the boundary effect and transition zone, which is typically within several hundred kPa of matric suction [38], as shown in Figure 7. However, some clayey soils may not desaturate as the air-entry value may not be reached within this suction range (i.e., soil is near saturation and correction function is near one). Second, soil pores with varied sizes will be drained at a certain matric suction, typically larger than the air-entry value (i.e., the soil is in an unsaturated state and the correction function plays a role over the entire range of matric suction).

To satisfy the above criteria, two assumptions must be highlighted. The first assumption is the terminal point of volume change under matric suction (e.g., point R_c in Figure 7b). After this point, there can still be some volume change in unsaturated soils. However, the associated volume change due to the influence of this suction is relatively small and hence can be neglected. The second assumption is that at 10^6 kPa, soil will have (almost) zero water content. Both these assumptions are reasonable and are used in the rational explanation of the mechanics of unsaturated soils.

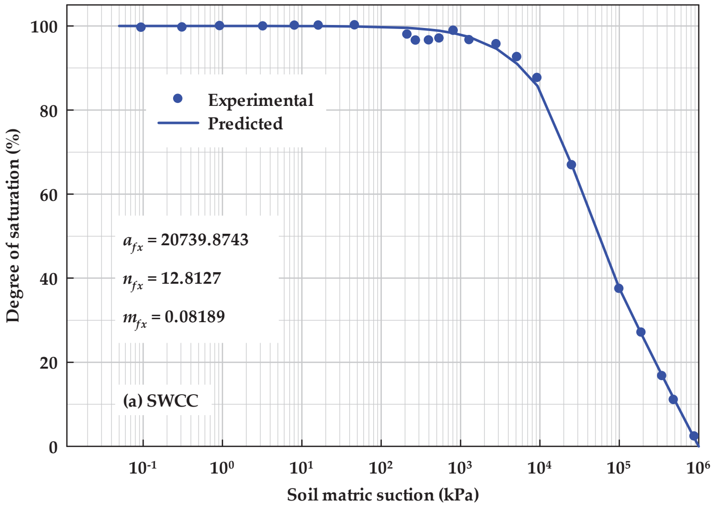

Figure 7. *Cont.*

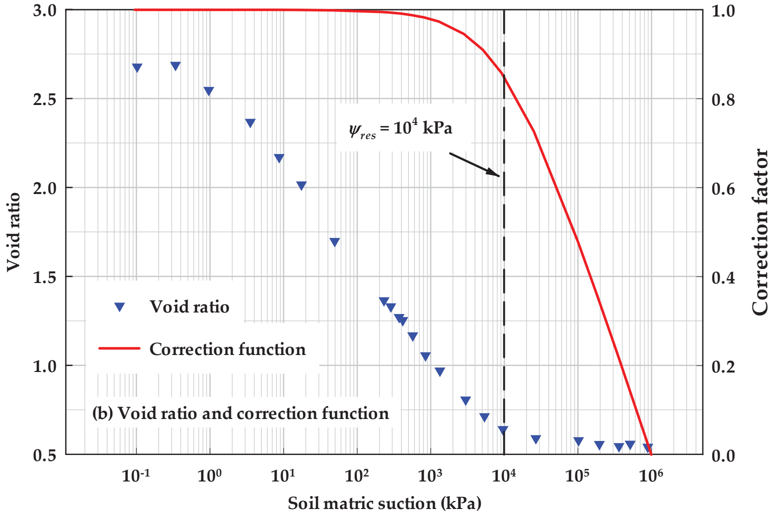

Figure 7. Relationships between soil matric suction and (**a**) degree of saturation; and (**b**) void ratio (based on the data from [12]).

These assumptions or conditions can be introduced into one of the most suitable equations, which is the correction function in Equation (5b). The following Equation (30) is suggested to model THMC (e.g., temperature, salt solution, initial stress state, and initial water content) effects on SWCCs based on the correction function.

$$c(\psi) = \left[1 - \frac{\ln[1 + (\psi/\psi_{res})]}{\ln[1 + (10^6/\psi_{res})]}\right] \tag{30a}$$

$$\psi_{res} = \psi_{res0}\exp\left(-\eta_T(T - T_0) - \eta_c(c - c_0) - k_p\left(e_{comp} - e_0\right) - k_{iw}(e_i - e_0)\right) \tag{30b}$$

$$\psi_{res} = \psi_{res0}\exp(k_{iw}(e_i - e_0)), \text{ for wetting optimum} \tag{30c}$$

where exp () is the exponential function.

It should be noted that residual suction ψ_{res} in Equation (30a) is regarded as a model parameter to obtain the best model performance. Equation (30b) is a general equation for predicting SWCC under temperatures, salt solutions, initial stress states, and initial water contents at dry of optimum side. Equation (30c) is suggested for predicting SWCC for both the wet of optimum side from optimum and dry of optimum sides. More information related to this method is available in [37]. The model results for THMC (e.g., temperature, salt solution, initial stress state, and initial water content) effects are highlighted in Figures 8–11, respectively.

The correction function Equation (30a) can also be used to predict the main wetting curve from the main drying curve. Based on previous studies from the literature, the following Equation (31) is suggested.

$$\frac{\theta_{lw} - \theta_{res}}{\theta_{sat} - \theta_{res}} = c(\psi)\cdot\frac{1}{\left\{\ln\left[\exp(1) + \left(\psi/a_{fx}\right)^{n_{fx}}\right]\right\}^{m_{fx}}} \tag{31a}$$

$$c(\psi) = \left[1 - \frac{\ln[1 + (\psi - P_b)/\psi_{res}]}{\ln[1 + (P_a - P_b)/\psi_{res}]}\right], 0 \leq c(\psi) \leq 1 \tag{31b}$$

where P_a is a model parameter, and P_b is regarded as the merging point between the main wetting and drying curves (see Figure 12).

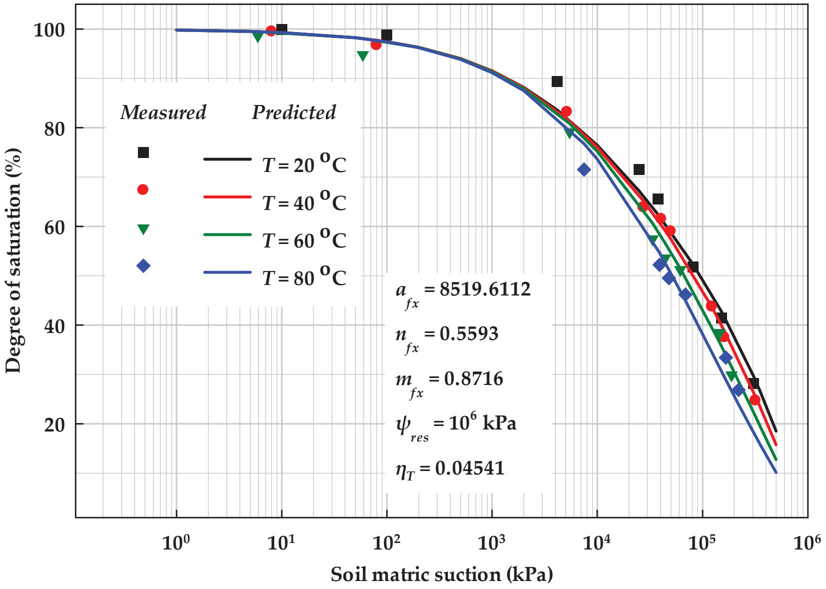

Figure 8. Temperature effects on the soil–water characteristic curve based on the variation of residual suction (based on the data from [22]).

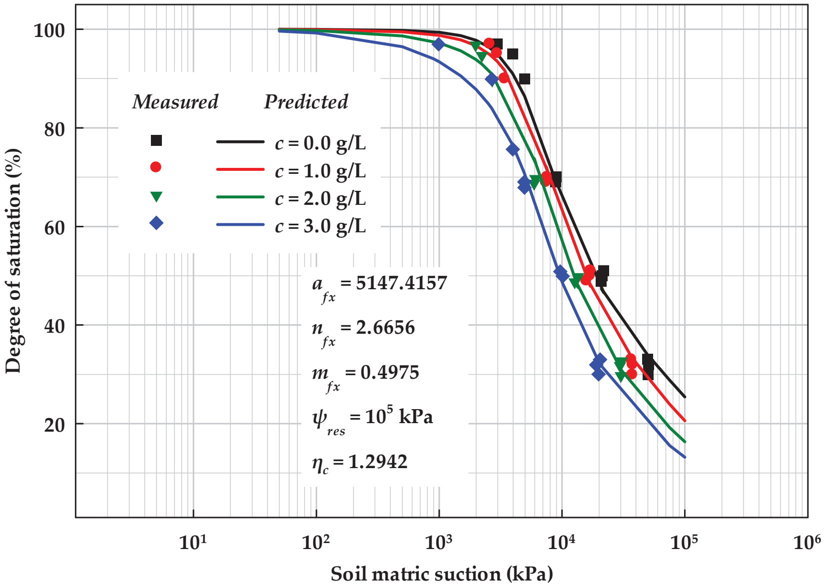

Figure 9. Salt solution effects on the soil–water characteristic curve based on the variation of residual suction (based on the data from [21]).

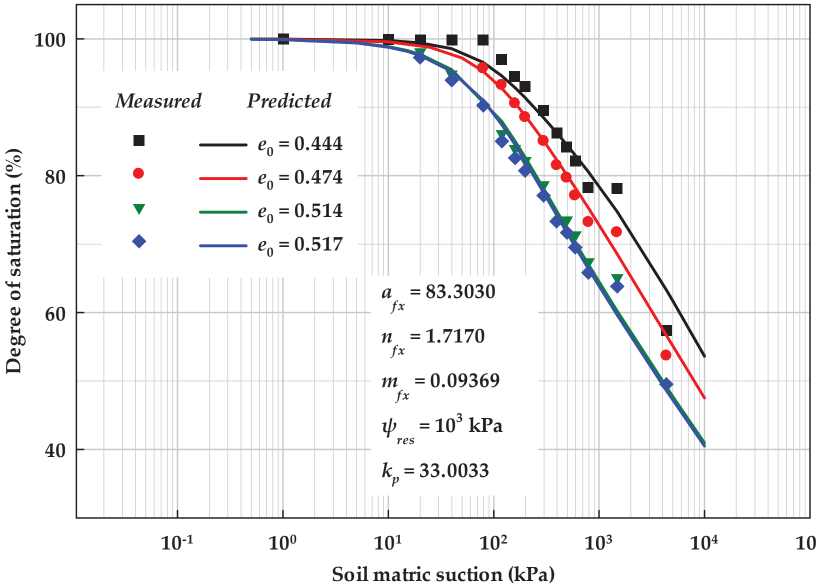

Figure 10. Initial stress state effects on the soil-water characteristic curve based on the variation of residual suction (based on the data from [3]).

The residual water content in Equation (31a) is highlighted, and the correction function in Equation (31b) should always be between zero and one. The prediction results for the main wetting curve from the main drying curve are presented in Figure 12.

Based on Equations (5c), (29), and (31), the models for drying scanning curves can be written as follows in Equation (32).

$$\frac{\theta - \theta_r}{\theta_0 - \theta_r} = c(\psi)\cdot\left(1 - \frac{\int_{\psi}^{\psi_0} f(\psi)d\psi}{\int_{\psi_r}^{\psi_0} f(\psi)d\psi}\right) \tag{32a}$$

$$c(\psi) = \left[1 - \frac{\ln[1 + (\psi - \psi_0)/\psi_{res}]}{\ln[1 + (P_a - \psi_0)/\psi_{res}]}\right], 0 \le c(\psi) \le 1 \tag{32b}$$

Similarly, for wetting scanning curves, the models can be written as follows in Equation (33) based on the FX model.

$$\frac{\theta - \theta_0}{\theta_s - \theta_0} = c(\psi)\cdot\frac{\int_{\psi_0}^{\psi} f(\psi)d\psi}{\int_{\psi_0}^{0} f(\psi)d\psi} \tag{33a}$$

$$c(\psi) = \left[1 - \frac{\ln[1 + (\psi - P_b)/\psi_{res}]}{\ln[1 + (P_a - P_b)/\psi_{res}]}\right], 0 \le c(\psi) \le 1 \tag{33b}$$

where ψ_0 and θ_0 refer to the start points of scanning curves. θ_r and θ_s in Equations (32a) and (33a), respectively, refer to the volumetric water at the merging point (slightly different from the original values).

Based on Equations (32) and (33) for drying and wetting scanning curves, respectively, the model performance is highlighted in Figure 13. θ_r and θ_s in Equations (32) and (33) equal 10.18% and 30.16%, respectively. In the two equations, P_a is regarded as a fitting parameter, while parameter P_b is regarded as the soil suction value at the merging point (i.e., 1.1 kPa in this case).

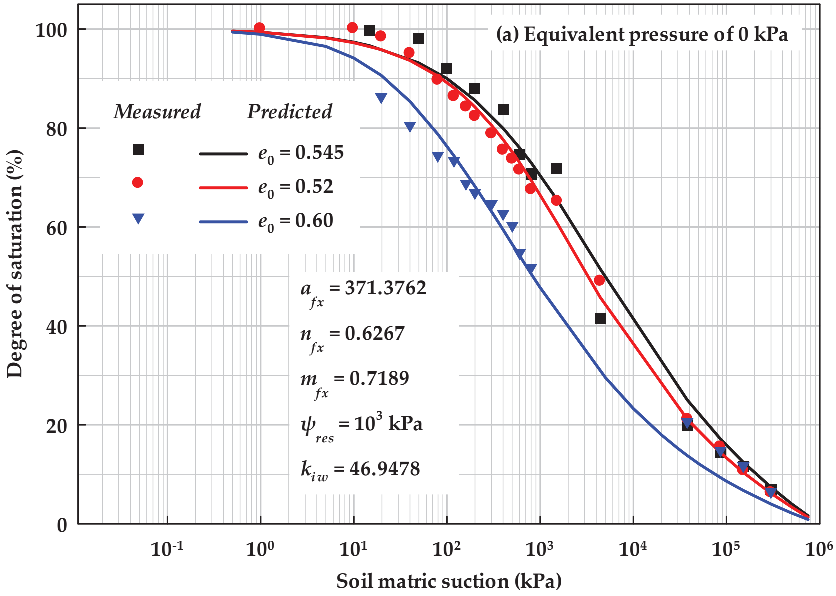

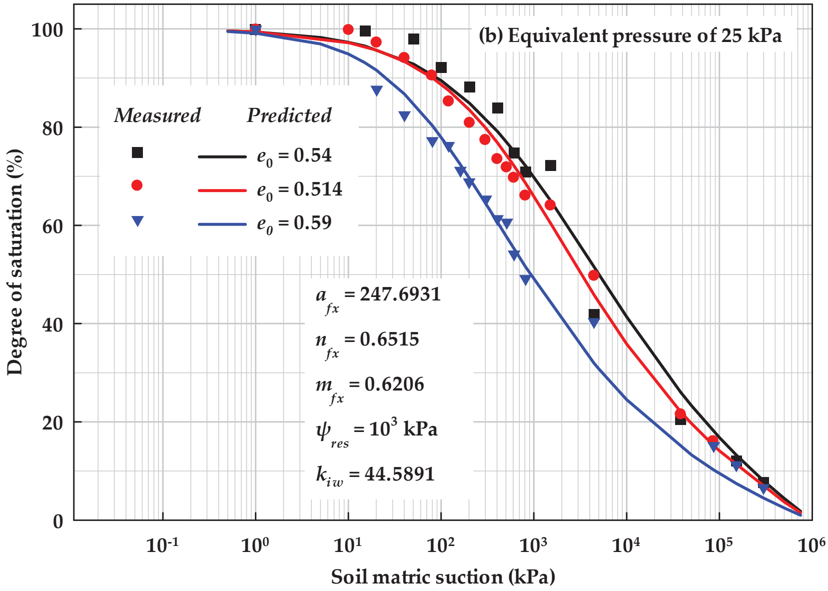

Figure 11. Initial water content effects on soil–water characteristic curve at equivalent pressure of (**a**) 0 kPa and (**b**) 25 kPa, based on the variation of residual suction (based on the data modified from [3]).

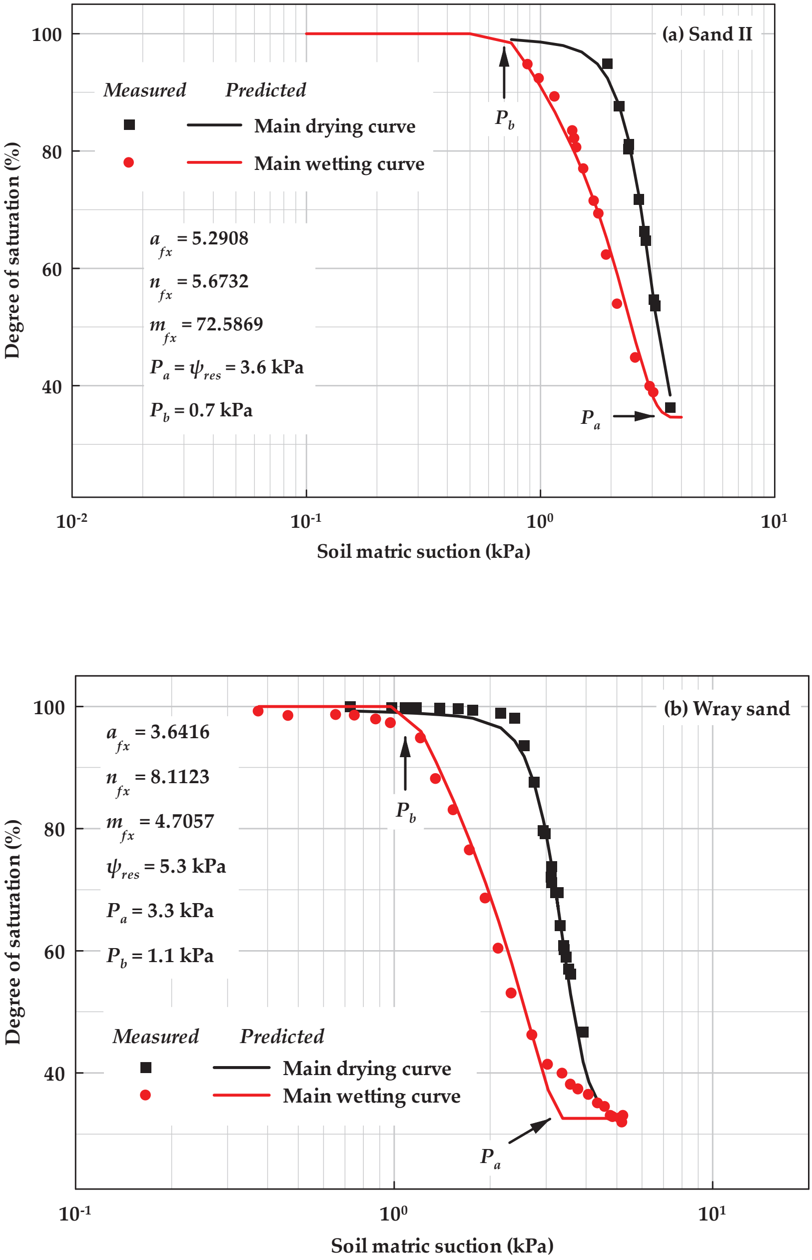

Figure 12. Prediction of main wetting curves from main drying curves based on SWCC correction function for (**a**) Sand II and (**b**) Wray sand (based on the data from [10,23]).

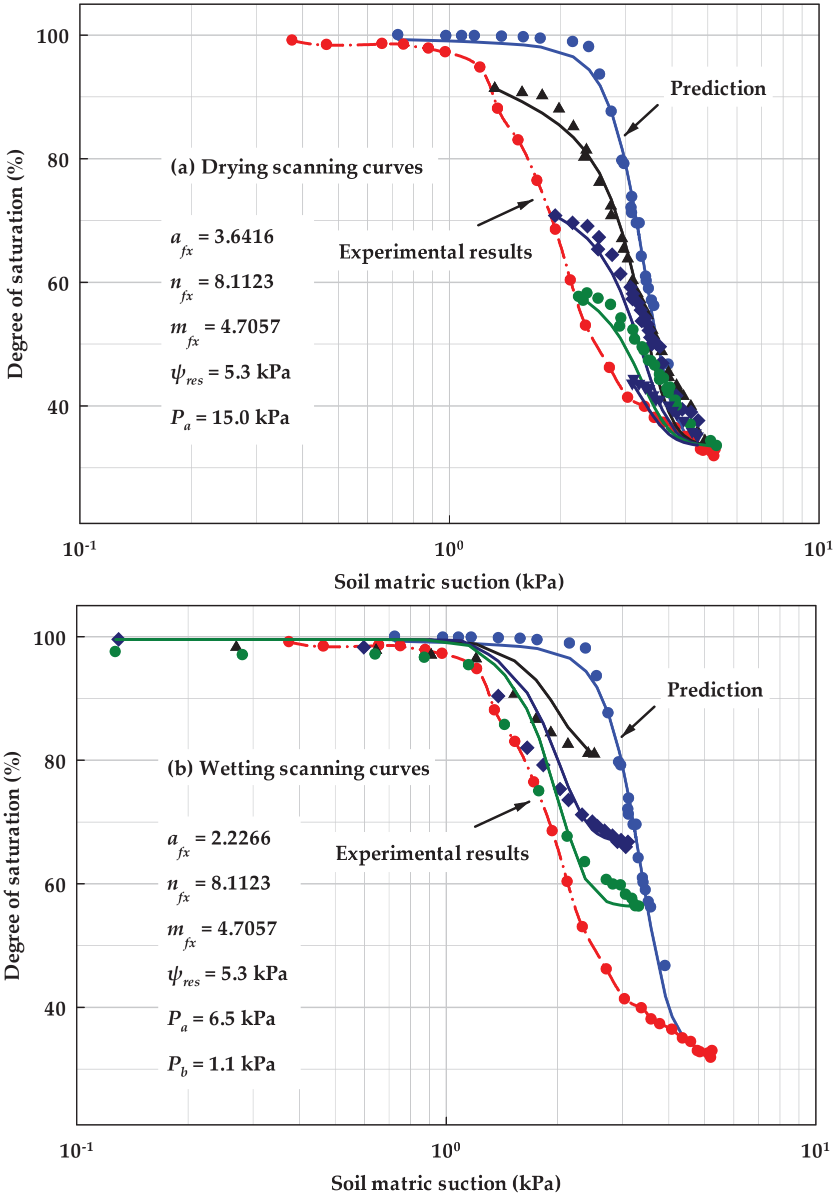

Figure 13. Prediction of (**a**) drying and (**b**) wetting scanning curves based on SWCC correction function (based on the data from [10]).

By repeatedly using Equations (5c), (32), and (33), the cyclic wetting and drying behaviors of SWCCs can be readily modeled. The modeling results are highlighted in Figure 14, while experimental results from the literature [39] are offered for comparison. One point should be noted: in Figure 14b, the value of parameter a_{fx} for the main wetting curve (i.e., parameter a_{wet}) differs from that for the main drying curve.

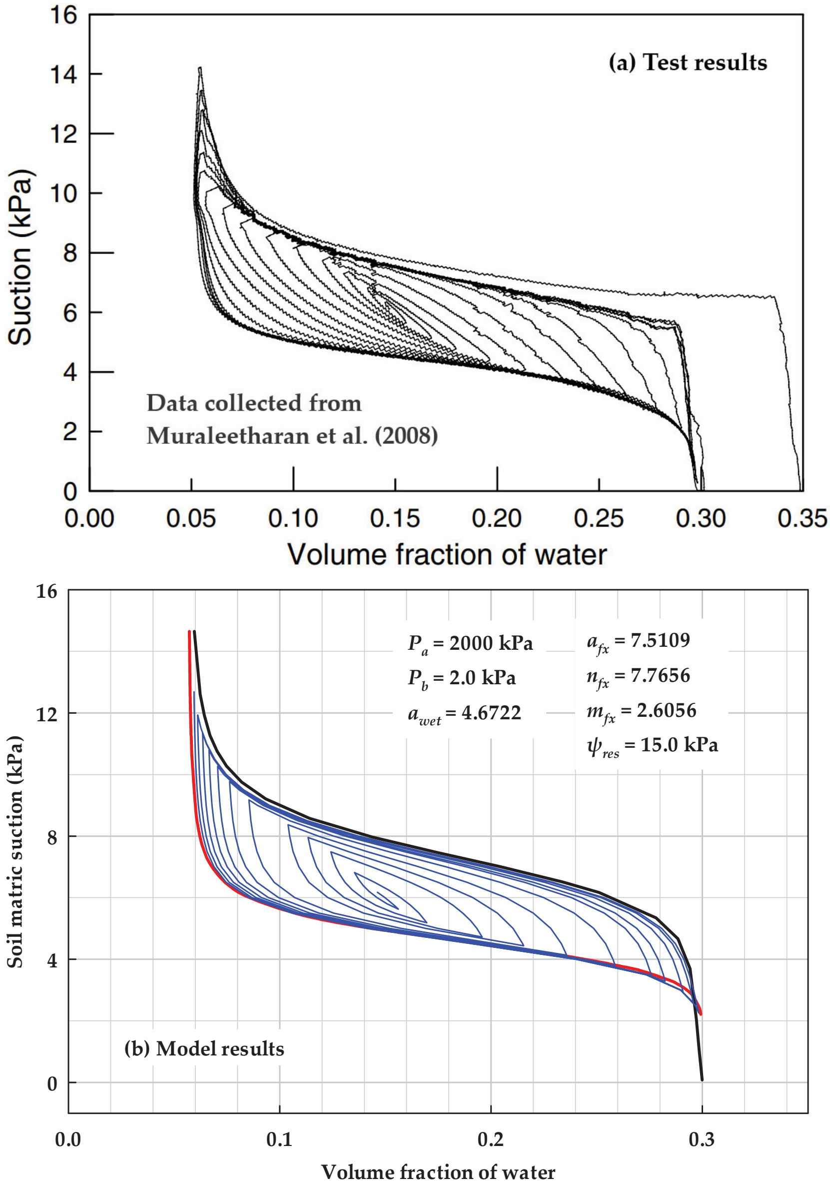

Figure 14. (**a**) Measured and (**b**) predicted drying and wetting cycles of SWCCs based on correction function in the FX model (based on the data from [39]).

3. Model Results and Discussion

Figure 2 highlights the two methods applied to model SWCCs in this study. These two methods are prevailing and can function well to predict the variation in SWCCs under THMC (i.e., temperature, salt solution, initial stress state, and initial water content) effects, as highlighted in the figures. However, these are not the only methods for modeling SWCCs.

Figures 3 and 8 highlight SWCC model prediction results when using these two distinct methods, shown in comparison with experimental data [22]. It should be noted that temperature affects pore sizes and air–water interfacial energy in combination, but in this study, these effects were separately modeled. Systematic research on temperature effects is, therefore, necessary.

Figures 4 and 9 present SWCC prediction model results for salt solution effects, based on experiments presented in the literature [21]. Note that, in this study, only variation in matric suction was modeled, and the influence of osmotic suction was not considered. As shown by the van't Hoff equation for osmotic pressure, osmotic suction should be treated as a constant under a certain solution concentration. However, due to electrical double layers around clayey particles, the ion concentration may not be constant in free water of unsaturated soils.

Figures 5 and 10 present the initial stress state effects on SWCCs based on the experimental results in the literature [3]. Here, the initial void ratio is adopted instead of the initial compact pressure, as the void ratio is a smaller value and will increase the flexibility of the proposed models.

Figures 6 and 11 further highlight the prediction results of the initial water content effects on SWCCs, as determined using experimental results from the literature [3]. In Figures 10 and 11, the residual soil suction is regarded as a model parameter. Note that its value might not represent the exact amount of soil residual suction. The associated variation in PoSD is highlighted based on Equations (30), while the physical meanings of the parameter are omitted.

Figure 7 demonstrates the reason to treat the residual soil suction as a model parameter. Experimental data were gathered from [12]. As highlighted in the figure, a relatively smaller residual suction value can also be used to predict SWCC effectively. This perhaps owes to the flexibility of SWCC equations. Another reason, as discussed in the previous section, may be a feature of SWCC, whereby the correction function is highlighted in a high soil suction range (e.g., larger than 10^5 kPa) while the residual value (10^4 kPa in Figure 7b) might be more related to the turning point in the correction function before the soil suction limit (e.g., 10^6 kPa). The gap between the roles of the correction function and the residual suction inside the correction function reserves space for modeling SWCCs flexibly.

The model results for predicting the main wetting curves from the main drying curves are highlighted in Figure 12. Experimental results were gathered from [23] and [10], respectively. Red dash lines (as well as red and blue circles) in Figure 12 are the experimental results. Our method was consistent with that in a previous study [37], though the role of the correction function was particularly highlighted in the present model (see Equation (31)). The prediction results obtained using the correction function, shown in Figures 8–12, are based on the concept of pore size distribution (or the correction function in SWCC models). The success of predicting THMC (i.e., temperature, salt solution, initial stress state, and initial water content) effects and hysteretic effects on SWCCs (i.e., Equations (30) and (31)) reveals that the suggested unified model is promising for considering the variation of the correction function in SWCC equations.

Figures 13 and 14 highlight the model results for hysteretic behaviors of SWCCs. Solid lines and dots are prediction and experimental results, respectively for Figures 3–13 and Figure 14b. A distinct parameter a_{fx} value for the main wetting curve (i.e., parameter a_{wet}) was used to simplify calibration procedures. All the scanning curves in the figures were predicted using Equations (32) and (33), i.e., the correction function in the FX model.

4. Conclusions

In this article, two methods that address the variation in soil matric suction and pore size distribution (PoSD), respectively, have been highlighted for modeling THMC (e.g., temperature, salt solution, initial stress state, and initial water content) effects on SWCCs using well-known SWCC equations and correction functions, respectively.

The model results of both methods provide close comparisons with experimental results from the literature. The role of the correction function on modeling THMC effects and hysteretic behaviors on SWCCs was of particular interest in this study.

The unified attempts on modeling SWCCs under various factors, based on correction functions of SWCC equations could allow us to gain a comprehensive understanding on both THMC and hysteretic effects on SWCC behaviors of unsaturated soils.

Furthermore, additional studies are needed on the coupling THMC effects on SWCCs, both in experimental and numerical senses. The salt solution effects on total soil suction also require further study, along with the variation in the dissolved salt content under soil suction.

Author Contributions: Conceptualization, Y.L. and S.V.; methodology, Y.L.; validation Y.L., R.A., S.V. and G.G.J.; formal analysis, Y.L., R.A., S.V. and G.G.J.; writing—original draft preparation, Y.L. and R.A.; writing—review and editing, Y.L., R.A., S.V. and G.G.J.; visualization, Y.L., R.A., S.V. and G.G.J.; supervision, S.V.; project administration, S.V. All authors have read and agreed to the published version of the manuscript.

Funding: The first author gratefully acknowledges and extends his appreciation to the China Scholarship Council and University of Ottawa, Canada for jointly funding for his Ph.D. research program. The second author thanks the Coordenação de Aperfeiçoamento de Pessoal de Nível Superior—Brasil (CAPES)—Finance Code 001. The third author is thankful for the Discover Grant (5808-2019) support from Natural Science and Engineering Research Council of Canada.

Data Availability Statement: Data are available upon reasonable request.

Acknowledgments: The authors sincerely thank the reviewers for their constructive criticism, which has significantly contributed to improving this paper.

Conflicts of Interest: The authors declare no conflicts of interest.

References

1. Fredlund, D.; Rahardjo, H. *Soil Mechanics for Unsaturated Soils*, 1st ed.; John Wiley & Sons: New York, NY, USA, 1993.
2. Mualem, Y. A new model for predicting the hydraulic conductivity of unsaturated porous media. *Water Resour. Res.* **1976**, *12*, 513–522. [CrossRef]
3. Vanapalli, S.K.; Fredlund, D.G.; Pufahl, D.E. The influence of soil structure and stress history on the soil-water characteristics of a compacted till. *Géotechnique* **1999**, *49*, 143–159. [CrossRef]
4. Tuller, M.; Or, D. Water films and scaling of soil characteristic curves at low water contents. *Water Resour. Res.* **2005**, *41*, W09403. [CrossRef]
5. Hoyos, L.R.; Suescún-Florez, E.A.; Puppala, A.J. Stiffness of intermediate unsaturated soil from simultaneous suction-controlled resonant column and bender element testing. *Eng. Geol.* **2015**, *188*, 10–28. [CrossRef]
6. Zhou, A.N.; Huang, R.Q.; Sheng, D.C. Capillary water retention curve and shear strength of unsaturated soils. *Can. Geotech. J.* **2016**, *53*, 974–987. [CrossRef]
7. Van Looy, K.; Bouma, J.; Herbst, M.; Koestel, J.; Minasny, B.; Mishra, U.; Montzka, C.; Nemes, A.; Pachepsky, Y.A.; Padarian, J.; et al. Pedotransfer functions in earth system science: Challenges and perspectives. *Rev. Geophys.* **2017**, *55*, 1199–1256. [CrossRef]
8. Zhai, Q.; Rahardjo, H.; Satyanaga, A.; Dai, G.L.; Du, Y.J. Estimation of the wetting scanning curves for sandy soils. *Eng. Geol.* **2020**, *272*, 105635. [CrossRef]
9. Chin, K.B.; Leong, E.C.; Rahardjo, H. A simplified method to estimate the soil water characteristic curve. *Can. Geotech. J.* **2010**, *47*, 1382–1400. [CrossRef]
10. Gillham, R.W.; Klute, A.; Heermann, D.F. Hydraulic properties of a porous medium: Measurement and empirical representation. *Soil Sci. Soc. Am. J.* **1976**, *40*, 203–207. [CrossRef]
11. Gallipoli, D.; Wheeler, S.J.; Karstunen, M. Modelling the variation of degree of saturation in a deformable unsaturated soil. *Géotechnique* **2003**, *53*, 105–112. [CrossRef]
12. Mbonimpa, M.; Aubertin, M.; Maqsoud, A.; Bussière, B. Predictive model for the water retention curve of deformable clayey soils. *J. Geotech. Geoenviron. Eng.* **2006**, *132*, 1121–1132. [CrossRef]
13. Fredlund, D.G.; Sheng, D.C.; Zhao, J.D. Estimation of soil suction from the soil-water characteristic curve. *Can. Geotech. J.* **2011**, *48*, 186–198. [CrossRef]
14. Hu, R.; Chen, Y.F.; Liu, H.H.; Zhou, C.B. A water retention curve and unsaturated hydraulic conductivity model for deformable soils: Consideration of the change in pore-size distribution. *Géotechnique* **2013**, *63*, 1389–1405. [CrossRef]
15. Alves, R.D.; Gitirana, G.F.N., Jr.; Vanapalli, S.K. Advances in the modeling of the soil-water characteristic curve using pore-scale analysis. *Comp. Geotech.* **2020**, *127*, 103766. [CrossRef]
16. Wan, R.; Pouragha, M.; Eghbalian, M.; Duriez, J.; Wong, T. A probabilistic approach for computing water retention of particulate systems from statistics of grain size and tessellated pore network. *Int. J. Numer. Anal. Methods Geomech.* **2019**, *43*, 956–973. [CrossRef]

17. Grant, S.A.; Salehzadeh, A. Calculation of temperature effects on wetting coefficients of porous solids and their capillary pressure functions. *Water Resour. Res.* **1996**, *32*, 261–270. [CrossRef]
18. Romero, E.; Gens, A.; Lloret, A. Temperature effects on the hydraulic behaviour of an unsaturated clay. *Geotech. Geol. Eng.* **2001**, *19*, 311–332. [CrossRef]
19. Tang, A.M.; Cui, Y.J.; Barnel, N. Thermo-mechanical behaviour of a compacted swelling clay. *Géotechnique* **2008**, *58*, 45–54. [CrossRef]
20. Uchaipichat, A.; Khalili, N. Experimental investigation of thermo-hydro-mechanical behaviour of an unsaturated silt. *Géotechnique* **2009**, *59*, 339–353. [CrossRef]
21. Ravi, K.; Rao, S.M. Influence of infiltration of sodium chloride solutions on SWCC of compacted bentonite–sand specimens. *Geotech. Geol. Eng.* **2013**, *31*, 1291–1303. [CrossRef]
22. Wan, M.; Ye, W.M.; Chen, Y.G.; Cui, Y.J.; Wang, J. Influence of temperature on the water retention properties of compacted GMZ01 bentonite. *Environ. Earth Sci.* **2015**, *73*, 4053–4061. [CrossRef]
23. Poulovassilis, A. Hysteresis of pore water in granular porous bodies. *Soil Sci.* **1970**, *109*, 5–12. [CrossRef]
24. Arya, L.M.; Paris, J.F. A physicoempirical model to predict the soil moisture characteristic from particle-size distribution and bulk density data. *Soil Sci. Soc. Am. J.* **1981**, *45*, 1023–1030. [CrossRef]
25. Fredlund, D.G.; Xing, A.; Huang, S. Predicting the permeability function for unsaturated soils using the soil-water characteristic curve. *Can. Geotech. J.* **1994**, *31*, 533–546. [CrossRef]
26. Vanapalli, S.K.; Fredlund, D.G.; Pufahl, D.E.; Clifton, A.W. Model for the prediction of shear strength with respect to soil suction. *Can. Geotech. J.* **1996**, *33*, 379–392. [CrossRef]
27. Lu, N.; Likos, W.J. Suction stress characteristic curve for unsaturated soil. *J. Geotech. Geoenviron. Eng.* **2006**, *132*, 131–142. [CrossRef]
28. Miao, L.; Jing, F.; Houston, S.L. Soil-water characteristic curve of remolded expansive soils. In *Unsaturated Soils*; American Society of Civil Engineers: Carefree, AZ, USA, 2006; pp. 997–1004.
29. Hou, X.K.; Vanapalli, S.K.; Li, T.L. Water flow in unsaturated soils subjected to multiple infiltration events. *Can. Geotech. J.* **2020**, *57*, 366–376. [CrossRef]
30. Li, Y.; Vanapalli, S.K. Correction functions for soil-water characteristics curves extending the principles of thermodynamics. *Can. Geotech. J.* **2023**. accepted. [CrossRef]
31. Li, X.; Li, X.K. A soil freezing-thawing model based on thermodynamics. *Cold Reg. Sci. Technol.* **2023**, *211*, 103867. [CrossRef]
32. Li, X.; Zheng, S.F.; Wang, M.; Liu, A.Q. The prediction of the soil freezing characteristic curve using the soil water characteristic curve. *Cold Reg. Sci. Technol.* **2023**, *212*, 103880. [CrossRef]
33. Li, X.K.; Li, X.; Liu, J.K. A dynamic soil freezing characteristic curve model for frozen soil. *J. Rock Mech. Geotech. Eng.* **2023**. accepted. [CrossRef]
34. Brooks, R.H.; Corey, A.T. *Hydraulic Properties of Porous Media (Hydrology Paper No. 3)*; Colorado State University: Fort Collins, CO, USA, 1964.
35. van Genuchten, M.T. A closed-form equation for predicting the hydraulic conductivity of unsaturated soils. *Soil Sci. Soc. Am. J.* **1980**, *44*, 892–898. [CrossRef]
36. Fredlund, D.G.; Xing, A. Equations for the soil-water characteristic curve. *Can. Geotech. J.* **1994**, *31*, 521–532. [CrossRef]
37. Li, Y.; Vanapalli, S.K. Models for predicting the soil-water characteristic curves for coarse and fine-grained soils. *J. Hydro.* **2022**, *612 Pt C*, 128248. [CrossRef]
38. Leong, E.C.; Rahardjo, H. Review of soil-water characteristic curve equations. *J. Geotech. Geoenviron. Eng.* **1997**, *123*, 1106–1117. [CrossRef]
39. Muraleetharan, K.K.; Liu, C.Y.; Wei, C.F.; Kibbey, T.C.G.; Chen, L.X. An elastoplastic framework for coupling hydraulic and mechanical behavior of unsaturated soils. *Int. J. Plast.* **2009**, *25*, 473–490. [CrossRef]

geosciences

Article

Stress-Based Model for Interpreting Shear Wave Velocity from Seismic Cone Penetration Tests in Unsaturated Soil

Tareq Abuawad *, Gerald A. Miller and Kanthasamy K. Muraleetharan

School of Civil Engineering and Environmental Science, University of Oklahoma, Norman, OK 73019, USA
* Correspondence: tabuawad@ou.edu

Abstract: Shear wave velocity is an important parameter for estimating soil properties used in analyzing the dynamic response of soil to seismic loading. This paper focuses on developing a model for predicting shear wave velocity in unsaturated soils. The model was developed primarily for the interpretation of seismic cone penetration tests (SCPTs) in unsaturated soil to account for seasonal variations in moisture conditions. In practice, SCPTs typically occur over a period of days without the option of choosing a wet or dry period. The question becomes, if tests are conducted during a dry period, how can shear wave velocity corresponding to a wetter period be predicted, or vice versa? Answering this question was the primary motivation of this work. The work involved field testing with the seismic cone penetrometer during wet and dry periods and a focused study at three sites involving comparison between field and laboratory testing for shear wave velocity. The model presented in this paper is built upon the significant work of many other researchers with reference to new experimental data obtained by the authors. It is demonstrated that a stress-based model incorporating matric suction can provide reasonable predictions of shear wave velocity and provides a method to interpret the impact of changing moisture content on shear wave velocities determined with SCPTs.

Keywords: unsaturated soils; shear wave velocity; seismic cone penetration test; shear modulus; effective stress; suction; bender elements

Citation: Abuawad, T.; Miller, G.A.; Muraleetharan, K.K. Stress-Based Model for Interpreting Shear Wave Velocity from Seismic Cone Penetration Tests in Unsaturated Soil. *Geosciences* **2024**, *14*, 227. https://doi.org/10.3390/geosciences14090227

Academic Editor: Enrico Priolo

Received: 1 June 2024
Revised: 14 August 2024
Accepted: 18 August 2024
Published: 24 August 2024

1. Introduction

Shear wave velocity is an important parameter for estimating soil properties used in analyzing the dynamic response of soil to seismic loading. There is a vast number of publications addressing shear wave velocity measurement, interpretation, and modeling in soil. However, this paper focuses on developing a model for predicting shear wave velocity in unsaturated soils. This model was developed primarily for the interpretation of seismic cone penetration tests (SCPTs) in unsaturated soil to account for seasonal variations in moisture conditions. In practice, SCPTs typically occur over a period of days without the option of choosing a wet or dry period. The question becomes, if tests are conducted during a dry period, how can shear wave velocity corresponding to a wetter period be predicted, or vice versa? Answering this question was the primary motivation of this work.

The model presented in this paper to address this question was built upon the significant work of many other researchers with reference to new experimental data obtained by the authors. Specifically, mathematical models representing the relationships between net normal stress, matric suction and shear wave velocity were investigated. The experimental work involved conducting SCPTs at several different test sites at different times of the year, representing wet and dry soil conditions. Each time SCPTs were conducted at a test site, companion samples were obtained for laboratory testing to determine basic soil properties, water content, and suction. At three test sites, the testing program involved SCPTs and companion sampling to obtain thin-walled tube samples. For these three sites, additional laboratory testing included shear wave velocity measurements using bender elements on samples at the field moisture contents. In addition, the tube samples were subjected to wetting and drying, and additional shear wave velocity measurements were obtained with the corresponding determinations of moisture content and suction. Based on the field and laboratory testing data, it was demonstrated that a stress-based model incorporating matric suction can provide reasonable predictions of shear wave velocity and provides a method to interpret the impact of changing moisture content on shear wave velocities determined with SCPTs.

2. Background

2.1. Shear Wave Velocity in Soil

Derivation of the three-dimensional equations of motion for an isotropic linear elastic material can be used to develop the governing equations for irrotational or dilational waves, and distortional waves of rotation with respect to the three principal directional axes. The former represents a primary or *p*-wave, while the latter, which is the focus of this paper, represents a shear or *s*-wave. Equation (1) represents the wave equation with respect to rotation about one axis; similar equations can be developed for the other two principal directions [1].

$$\frac{\partial^2 \Omega_x}{\partial t^2} = \frac{G}{\rho} \nabla^2 \Omega_x \tag{1}$$

Ω_x represents the rotation about the x-axis, and t is time. The ratio of shear modulus G to density ρ has units of velocity squared, and shear wave velocity, V_s, is defined by Equation (2):

$$V_s = \sqrt{\frac{G}{\rho}} \tag{2}$$

Shear wave velocity, V_s, represents a fundamental material property that describes the speed at which a wave travels in a medium. It can be measured using various techniques in the lab and field and such measurements are used to determine the shear modulus, G. Since the strains induced during the wave propagation are very small, G determined from shear wave velocity measurements is referred to as the small strain shear modulus, G_{max}. G_{max} is an important parameter used in ground response analysis.

According to Equation (2), shear wave velocity increases as shear modulus increases and density decreases. In soil, the density and shear modulus are related since the shear modulus represents the shear stiffness of the soil skeleton. For the same soil and given effective stress, an increase in density would increase the shear modulus. Thus, to some degree, the decrease in vs. due to increasing density is offset by an increase in shear modulus that results from increasing density. However, typically, for a given effective stress, changes in shear modulus due to changes in density are not proportional, and hence, shear wave velocity tends to increase with increasing density. The interdependency of G_{max} and ρ in Equation (2) can be investigated using Equation (3), which is an empirical equation applicable to a broad range of soil types [2].

$$G_{max} = A(1+e)^{-3} \sigma \prime^{n} \tag{3}$$

In Equation (3), G_{max} is in MPa, A and n are material parameters depending on soil type, e is void ratio, and σ' is effective confining stress in kPa. Equation (4) represents Equation (3), except with dry density, ρ_d, replacing void ratio as the variable of interest.

$$G_{max} = A\left(\frac{G_s \rho_w}{\rho_d}\right)^{-3} \sigma \prime^{n} \tag{4}$$

In Equation (4), additional parameters include G_s, the specific gravity of soil solids, and ρ_w, density of water. Substituting Equation (4) into Equation (2), one can estimate shear wave velocity and the influence of ρ_d and G_{max} using Equation (5). Note that for dry sand, $\rho = \rho_d$.

$$V_s = \sqrt{\frac{A\left(\frac{G_s\rho_w}{\rho_d}\right)^{-3}\sigma'^n}{\rho}} \tag{5}$$

Using values typical for clays and sands [2] for A (30) and n (0.5), and a range of dry density representing loose (soft) to dense (stiff) soils, values of vs. in Figure 1 were determined. It was assumed that $\rho = \rho_d$ in the calculations, which would be appropriate for dry sand. The baselines in Figure 1 represent vs. for ρ_d = 1400 kg/m^3, G_s = 2.65, and σ' = 10 and 1000 kPa. Equation (4) gives G_{max} = 14 MPa and G_{max} = 140 MPa for σ' = 10 kPa and σ' = 1000 kPa, respectively, for the baseline conditions. The bold solid line shows the combined effect of increasing ρ_d and corresponding increasing G_{max}, based on Equation (5). The other two lines show the influence of only increasing ρ_d with G_{max} constant at the baseline value or increasing G_{max} with ρ_d constant at the baseline value. As indicated, at constant confining stress, the change in shear modulus due to increasing density has a dominant influence on shear wave velocity, resulting in a significant net increase in vs. with increasing density. Increasing the effective confining stress significantly increases the baseline V_s, but the influence of density and shear modulus relative to the baseline remains the same, as shown in Figure 1. The effect of confining stress is more clearly seen in Figure 2 for different dry densities and the corresponding shear modulus. As expected, based on Equation (5), there is a nonlinear relationship between vs. and confining stress.

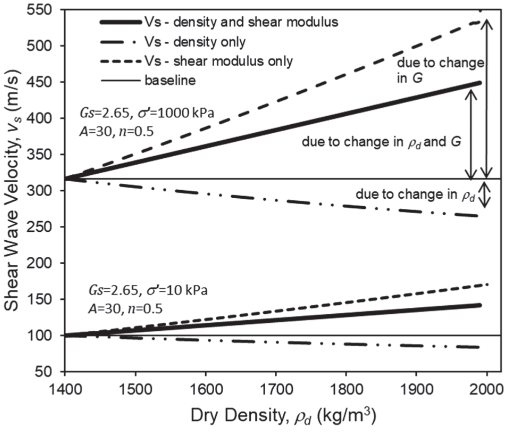

Figure 1. Shear wave velocity versus dry density for a typical soil calculated using the empirical relationship in Equation (5) based on the work of Bui et al. [2].

In recent decades, researchers have focused on understanding the behavior of unsaturated soils and effects of varying saturation on soil properties. In the field, unsaturated soils can make up a substantial part of the upper layers of the soil profile, which are affected by seasonal weather and climate changes that cause wetting and drying. Understanding the behavior of shear wave velocity in unsaturated soils is particularly important because of its use in determining seismic site class and G_{max} for earthquake ground response analysis [1]. While some published research has greatly improved our understanding of the influence of variable saturation on shear wave velocity, the authors have been systematically investigating this topic with the aim of providing a deeper understanding of seasonal effects on shear wave velocity measurements obtained with a seismic cone penetration test (SCPT). Through this research, and building on the work of others, a preliminary framework for predicting changes in shear wave velocity, determined with the SCPT, due to seasonal variations in moisture content was developed. This methodology is built around a stress-based model for unsaturated soils.

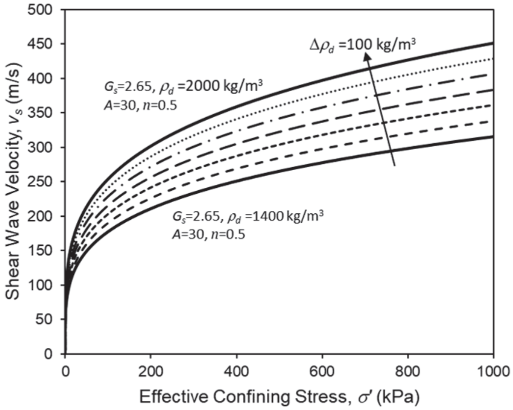

Figure 2. Shear wave velocity versus effective confining stress for a typical soil calculated using the empirical relationship in Equation (5) based on the work of Bui et al. [2]. The curves in the figure represent different densities between 1400 and 2000 kg/m^3.

2.2. Previous Studies of vs. and G_{max} in Unsaturated Soils

As soil changes from a saturated or dry condition to an unsaturated condition, the interparticle stresses change. As the water content of the soil decreases, the capillary pressure or matric suction in the soil increases, resulting in changes in stiffness and shear strength of the soil. The variation of the soil water content with respect to suction is presented graphically as the soil water characteristic curve (SWCC). The SWCC is not a unique relationship between soil suction and water content, as it is different for drying and wetting paths, and the path depends on the initial state of the soil prior to drying or wetting. The path dependency of the SWCC for wetting and drying is an example of hysteretic behavior [3].

Some studies have examined the effect of changing the soil moisture content on shear wave velocity (e.g., [4–8]). The results of this work have shown that as soil saturation increases, shear wave velocity decreases, with the highest shear wave velocity near the dry condition and the lowest near the saturated condition. Other researchers have examined the effect of hysteresis on shear wave velocity (e.g., [8–10]). Measurements of shear wave velocity were taken along the wetting and drying path for various soil types, and the results showed that shear wave velocity is higher along the drying path when compared to that along the wetting path.

The effects of suction and confining stress on shear wave velocity have been investigated (e.g., [5,11–13]) using suction-controlled testing. The tests were done by saturating the soil specimens and controlling the matric suction to measure the shear wave velocity along the drying paths. Additionally, the shear wave velocity was measured at various confining stresses during testing. The results have shown that shear wave velocity was directly proportional to suction; as suction increased, shear wave velocity increased. Additionally, the results have shown that an increase in the confining stress leads to an increase in shear wave velocity.

Some researchers have examined the influence of hysteresis on the small strain shear modulus, G_{max} (e.g., [8,9]), which is directly related to shear wave velocity, as shown in Equation (2). Khosravi and McCartney [9] investigated the effect of hysteresis on low-plasticity soils. The results have shown that along the wetting and drying paths, the shear modulus varies due to hysteresis. Dong and Lu [8] examined the effect of varying saturation on the shear modulus and found that there is a strong relationship between the shear modulus and suction stress.

The work described in this paper builds on the significant body of literature described above. This paper describes a part of a comprehensive study aimed at developing a rational approach to interpreting shear wave velocity measurements from seismic cone penetration tests (SCPTs) conducted in unsaturated soils prone to seasonally variable moisture conditions. The study involved conducting SCPTs at several sites during wet and dry periods with companion test borings to determine corresponding moisture content and suction profiles. In addition, laboratory testing of natural clayey soils from three sites was conducted to compare shear wave velocity determined with SCPTs and in the lab with bender elements. The results from the field and laboratory work are presented in this paper to demonstrate the use of a stress-based model for interpretation of shear wave velocity in unsaturated soil obtained with SCPTs.

3. Experimental Methodology

3.1. SCPTs in Unsaturated Soil

Seismic cone testing was conducted at nine different sites at two different times representing wet and dry weather periods. During each visit, a minimum of three SCPT soundings were conducted, from which average cone parameters were determined. The cone was equipped with two dual-axis geophones for detecting shear waves generated at the ground surface. The arrival time for reference waves and distance of wave travel at each test depth were used to determine the average shear wave velocity for layers between the test depths in general accordance with ASTM Standard D7400/D7400M-19 Standard Test Methods for Downhole Seismic Testing [14]. Soil profiles and average shear wave velocity determinations from SCPTs at three of the test sites are summarized in Figure 3. Of the nine sites, these three demonstrated the greatest impact of varying moisture content on shear wave velocity. As shown in the figures, gravimetric water content (w_n), total suction (ψ) measured with a chilled mirror hygrometer, and shear wave velocity (V_s) were strongly correlated, with vs. increasing as the soil dried and suction increased.

As mentioned previously, the question to answer is: if tests are conducted during a dry period, how can shear wave velocity corresponding to a wetter period be predicted, or vice versa? To begin, simple empirical correlations between water content or suction and shear wave velocity seemed like a reasonable first step. For example, in Figure 4, the data from the three sites shown in Figure 3 are summarized, with only results from cohesive soil shown.

There is considerable scatter in the data shown in Figure 4, which is typical for field testing in variable soil profiles. The trends in the water content–shear wave velocity data are relatively stronger than shown for the suction–shear wave velocity data. Ideally, vs. would be plotted against matric suction since it is the component of total suction that influences mechanical behavior the most. Total suction measurements are significantly influenced by soil type and chemistry of the pore water, which likely explains the lack of stronger trends in this plot. It is known that salt contents in natural soils can significantly influence the total suction measurement, and therefore total suction is not always a good surrogate for matric suction when salt is present (e.g., [15]). In spite of the scatter, trends in Figure 4 show the strong dependence of shear wave velocity on water content at each site.

Because of the inherent variability in field measurements, a systematic laboratory study was conducted to study the relationship between shear wave velocity, moisture content, and suction, as well as other parameters of interest.

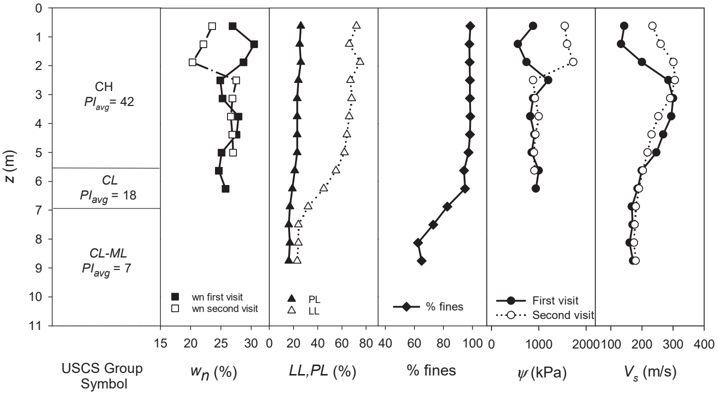

(**a**) Site Wa

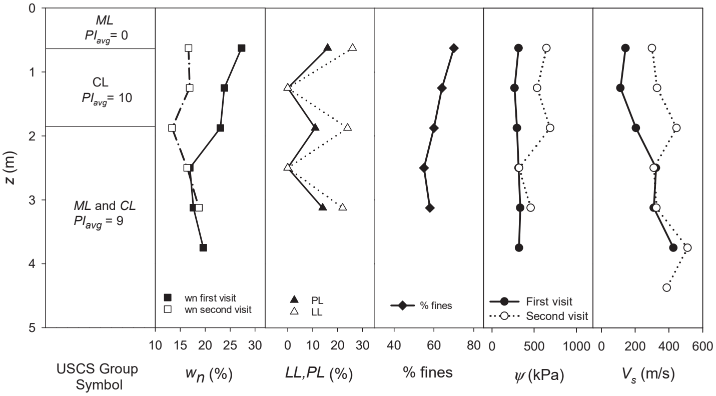

(**b**) Site We

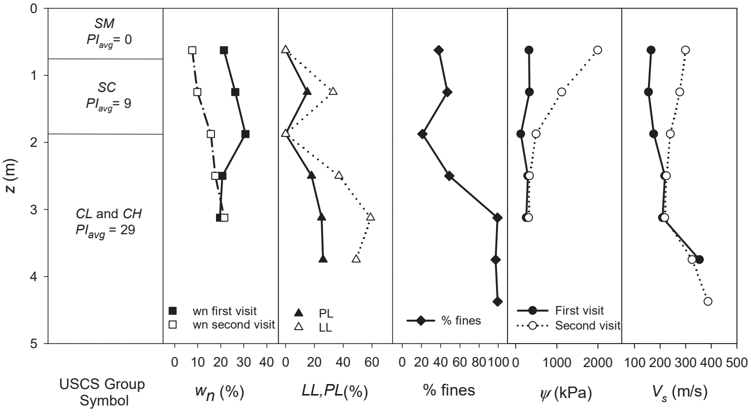

(**c**) Site F

Figure 3. Soil profiles and shear wave velocities determined from the SCPT at three test sites in Oklahoma during wet (first visit) and dry (second visit) periods. From top to bottom the sites are: (**a**) Wa, (**b**) We, and (**c**) F. Unless noted otherwise, solid symbols indicate data from the first visit and open symbols indicate data from the second visit.

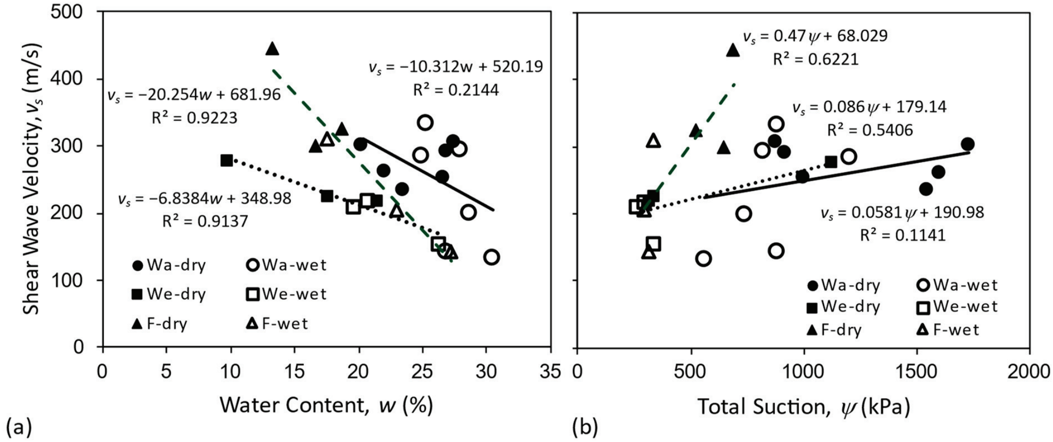

Figure 4. Shear wave velocity from the SCPT plotted against (**a**) water content and (**b**) total suction for cohesive soils at three test sites in Oklahoma during wet and dry periods.

3.2. SCPT and Laboratory Testing of Shear Wave Velocity in Unsaturated Soil

To better understand the variation in shear wave velocity with changing moisture conditions, an in-depth study was conducted at three test sites, different from those presented previously, and designated Site 10, 11, and 12. At each site, shear wave velocity measurements were obtained from the SCPT in the unsaturated profile, and Shelby tube samples were obtained from discrete depths in this zone on the same day. Shelby tube samples were subjected to shear wave velocity measurements in the laboratory at the natural water content under confining stresses simulating the in situ condition. Additionally, these samples were wetted and dried, and additional shear wave velocity measurements were obtained for wet and dry conditions.

In the laboratory, controlled wetting/drying was conducted in a vapor equilibrium chamber by placing the samples on a porous plate above a saltwater solution. Two different chambers were used, one containing a salt solution corresponding to high suction (6.6 MPa) for drying, and one corresponding to low suction (0.23 MPa) for wetting. After drying or wetting, the samples were removed, weighed, and subjected to shear wave velocity measurements using bender elements. Small specimens were extracted to make water content and total suction measurements corresponding to each shear wave velocity test. Total suction measurements were made using a chilled mirror hygrometer.

For shear wave velocity testing, test specimens were enclosed in a rubber membrane sealed to the bottom and top platens containing the bender elements within a triaxial testing chamber. The specimens were subjected to confining air pressure equal to the estimated in situ vertical total stress. Bender element testing was conducted using a function generator to produce a sine wave pulse. Based on previous studies [16–18], the frequency and amplitude of the generated signal were set at 4 kHz and 20 Vpp, respectively. A four-channel oscilloscope and analog to digital reader with a maximum sampling rate of 1 GSa/s was used to display and collect the shear wave signals from the bender element pairs. The start-to-start time domain interpretation mentioned in ASTM D8295 Standard Test Method for Determination of Shear Wave Velocity and Initial Shear Modulus in Soil Specimens using Bender Elements [14] was used to determine shear wave velocity [16,19].

The results of field and lab testing at the natural water content are shown in Figure 5 for each test site, along with basic index properties and USCS group symbols. As shown in each graph, with one exception, the shear wave velocities determined by SCPT were practically the same as those determined using bender element testing on discrete specimens. This indicates that vs. determinations were robust and reliable from both the lab and the field methods used. Based on this observation, it stands to reason that changing the specimen water contents under laboratory conditions and measuring vs. should provide a reasonable surrogate for SCPT-determined values of vs. under similar water contents. As mentioned above, the one exception where field and lab vs. measurements differed significantly was at a depth of 1 m (Figure 5b). This difference is attributed to the fact that lab measurements represent discrete layers having a thickness equal to that of the test sample, whereas the SCPT determinations involve averaging over larger layer thicknesses. If soil conditions vary considerably between SCPT depths, then lack of agreement between lab and field vs. values can occur since the lab measurement represents a sublayer from the larger layer over which the SCPT vs. value is determined. Furthermore, SCPT measurements are more susceptible to the influence of varying moisture contents in the near surface soils, which can be large in the upper 1 m.

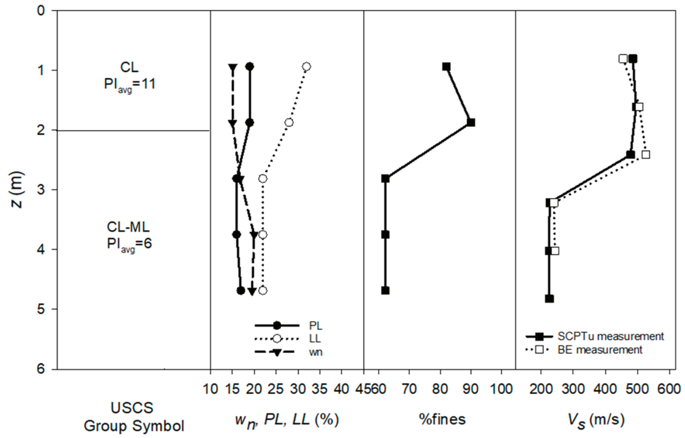

(**a**) Site 10

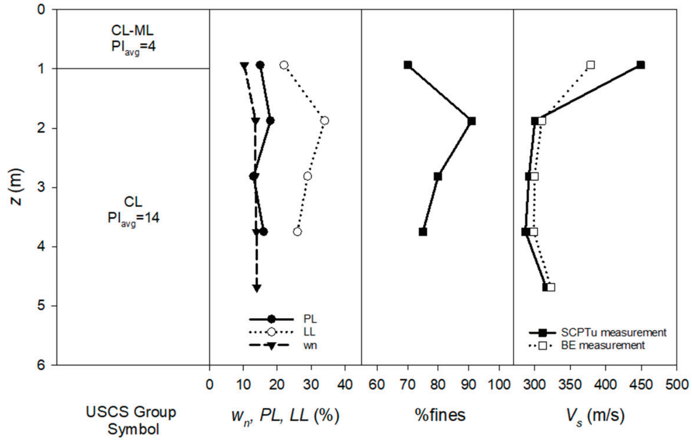

(**b**) Site 11

Figure 5. *Cont.*

(**c**) Site 12

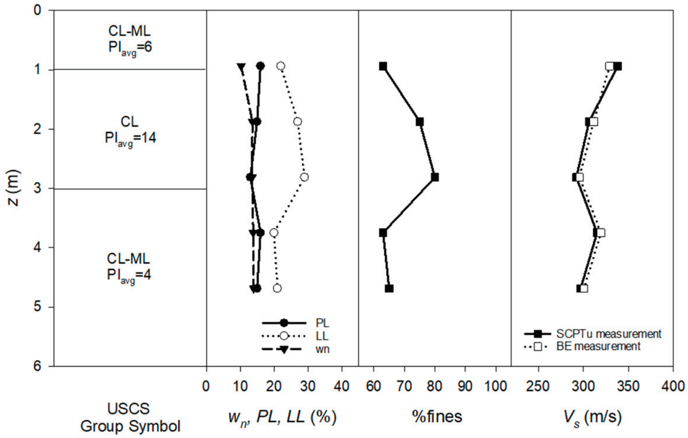

Figure 5. Soil properties and shear wave velocities determined in the field using SCPT and in the lab using bender elements on specimens under confining stresses simulating in situ conditions. From top to bottom, test sites are designated: (**a**) 10, (**b**) 11, and (**c**) 12.

In Figure 6, vs. values under dry and wet conditions determined in the laboratory are presented for each test site. As shown in Figure 6, there are substantial differences in vs. for dry and wet conditions, and it is noted that at the time of the SCPT, the in situ condition was closer to the wet condition. The challenge in using vs. values from the SCPT is estimating how the vs. will change as moisture conditions change in the unsaturated soil. This is particularly important for determining seismic site class when dryer conditions prevail at the time of SCPTs. Additionally, for modeling ground motion and response of overlying structures to earthquakes, both dry and wet conditions may be of interest depending on the natural frequency of the overlying structures.

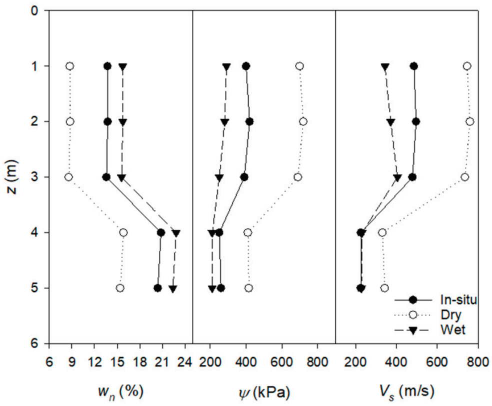

(**a**) Site 10

Figure 6. *Cont.*

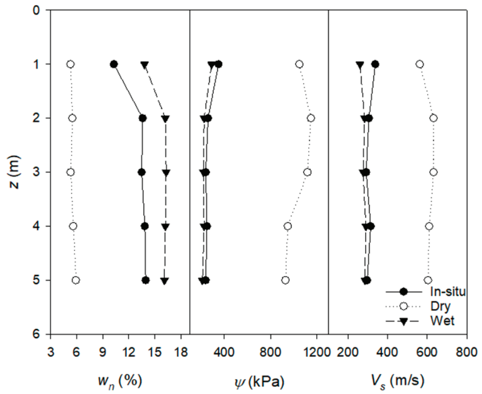

(**b**) Site 11

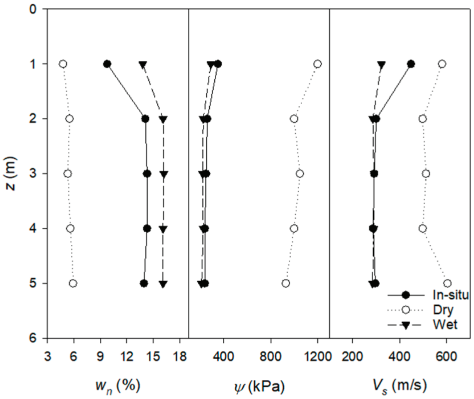

(**c**) Site 12

Figure 6. Water content, total suction, and shear wave velocities determined in the lab using bender elements on specimens at in situ, wet, and dry conditions. From top to bottom, tests sites are designated: (**a**) 10, (**b**) 11 and (**c**) 12.

3.3. Stress-Based Model for Shear Wave Velocity

As a first step in developing a stress-based model for interpreting vs. measurements from the SCPT, the data presented in Figure 6 for the three test sites were summarized in graphs depicting shear wave velocity in relationship to natural water content and measured total suction in Figure 7. Figure 7a depicts the data from all depths, while Figure 7b,c show the data separated based on the predominant soil types at these sites: lean clay (CL) and silty lean clay (CL-ML).

As expected, the relationships shown in Figure 7 are similar to those for other test sites shown in Figure 4, except the relationships were statistically stronger, owing to the much more controlled nature of the testing during wetting and drying in the laboratory. Coefficients of determination for the trend lines in Figure 7 show strong correlations between V_s, w, and ψ. When separated by soil type, the correlations got stronger for the CL soils and slightly weaker for the CL-ML soils. These empirical relationships can be useful for predicting changes in shear wave velocity due to changes in moisture content. However, they also demonstrate the importance of the stress state, since matric suction is a significant component of effective stress in unsaturated soil, particularly in the upper soil profile where net normal stresses are lower.

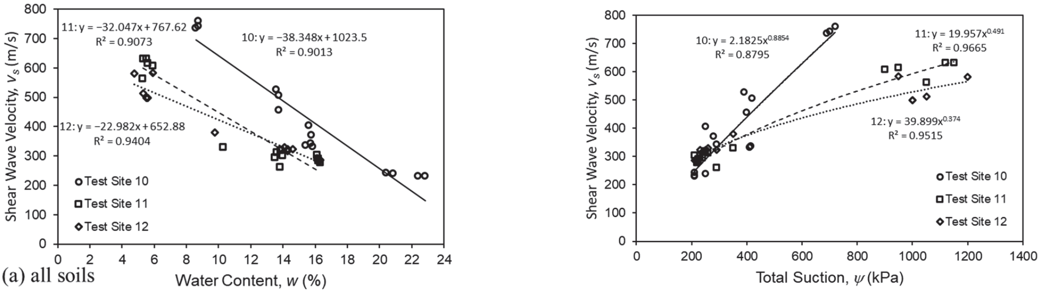

(a) all soils

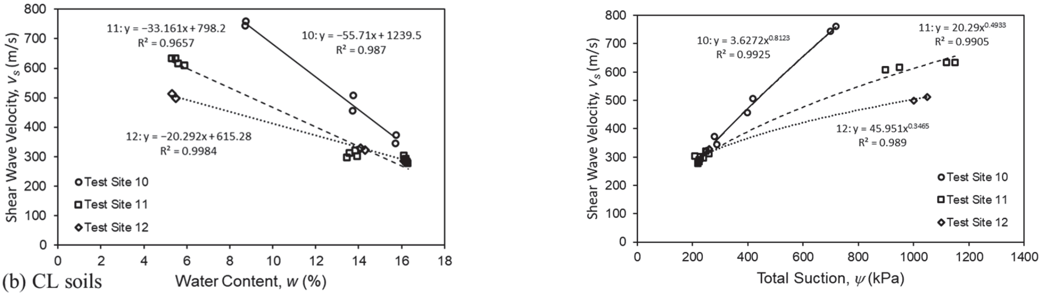

(b) CL soils

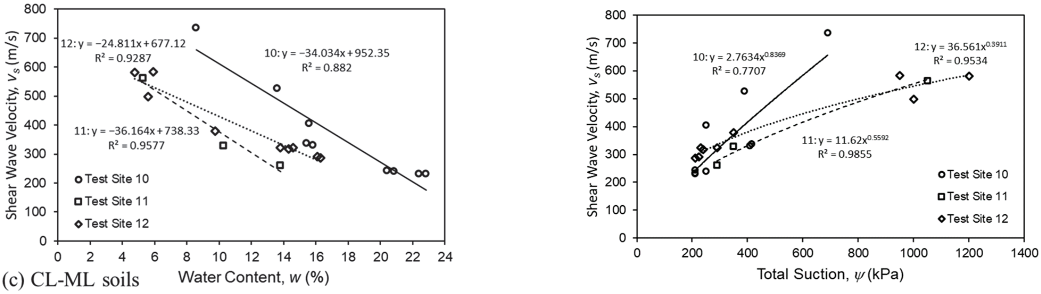

(c) CL-ML soils

Figure 7. Water content and total suction versus shear wave velocities determined in the lab using bender elements on specimens at in situ, wet, and dry conditions. (**a**) All soils, (**b**) CL soils, (**c**) CL-ML soils.

As shown in Figure 7, Sites 11 and 12 exhibited similar relationships between w, ψ, and V_s, while Site 10 exhibited significantly higher vs. for a given w and ψ, except at lower values of suction; around 200 kPa, the three trend lines converge. As total suction got closer to 200 kPa, matric suction was likely approaching zero, and total suction equaled the osmotic suction. Since matric suction largely controls mechanical behavior, this would explain why vs. was similar for all soils as total suction approached 200 kPa. The SWCC for these sites helps explain this behavior. Figure 8 shows the measured water contents versus total suction and estimated matric suction for each site, for all soils (Figure 8a) and separated by soil type (Figure 8b,c). Figure 8 indicates that Sites 11 and 12 had similar soil–water characteristic behavior, while Site 10 was substantially different. For a given water content, Site 10 had higher matric suction compared to that of Sites 11 and 12, except at higher water contents where matric suction approached zero. This helps explain the higher shear wave velocities observed at Site 10 for total suctions greater than 200 kPa.

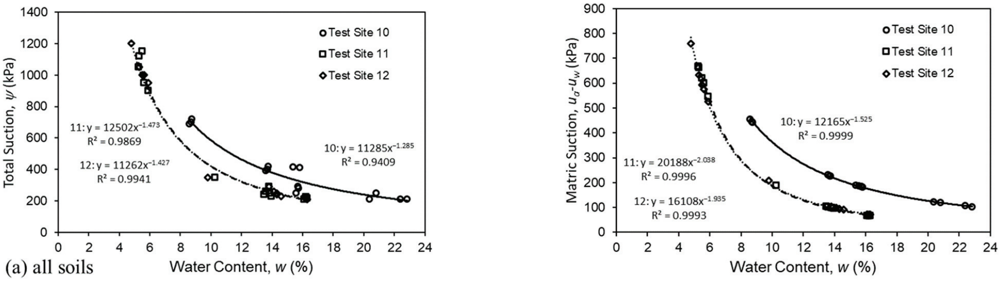

(a) all soils

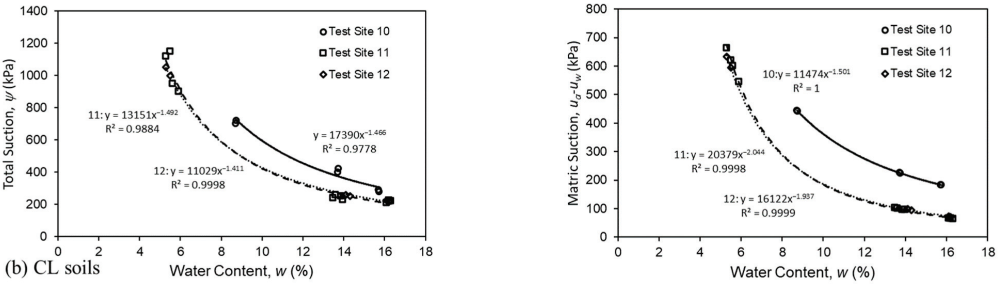

(b) CL soils

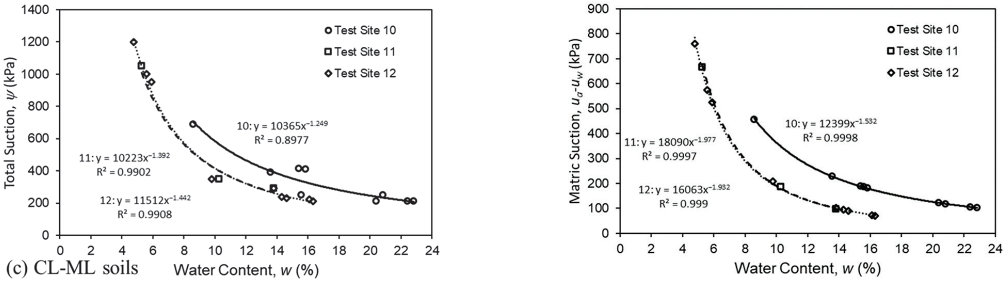

(c) CL-ML soils

Figure 8. Water content versus total suction (**left**) and estimated matric suction (**right**) from specimens at in situ, wet, and dry conditions. (**a**) All soils, (**b**) CL soils, (**c**) CL-ML soils.

Previous researchers have proposed models for saturated and unsaturated soil relating shear wave velocity to effective stress. A general power relationship between shear wave velocity and effective stress was proposed by Santamarina et al. [20], shown in Equation (6).

$$V_s = A\left(\frac{\sigma'_o}{1\ \text{kPa}}\right)^{\beta} \tag{6}$$

where A and β are experimentally determined fitting parameters. This form is similar to that in Equation (5), and thus parameters A and β would encompass the influence of density and other material properties.

Extending this model to unsaturated soils, Sawangsuriya et al. [21] proposed Equation (7), which includes the Bishop effective stress defined by Equation (8).

$$V_s = A[(\sigma - u_a) + \chi(u_a - u_w)]^{\beta} \tag{7}$$

$$\sigma' = (\sigma - u_a) + \chi(u_a - u_w) \tag{8}$$

where A and β are fitting parameters, and χ is the effective stress parameter.

Bishop's [22] proposed parameter χ could be equal to the degree of saturation S. Although this assumption is acceptable in some cases, it does not accurately describe the soil behavior near dry conditions and for fine-grained soils [23]. The challenge of defining the effective stress parameter χ has been addressed by many researchers. Multiple definitions have been proposed for the effective stress parameter χ [23–29].

The suction stress (σ^s) concept was proposed by Lu and Likos [23] to describe the contributions of various interparticle forces to effective stress, as given by Equation (9). Lu et al. [6,28] and Oh et al. [29,30] have demonstrated the implementation of this concept through their studies. Lu et al. [28] have demonstrated that suction stress can be defined as the product of effective degree of saturation, θ_e, and matric suction (Equation (10)). Thus, effective stress takes the form of Equation (11). This essentially results in an equation of similar form to Bishop's equation, with $\chi = \theta_e$, and the resulting expression for shear wave velocity is given by Equation (12).

$$\sigma' = (\sigma - u_a) - \sigma^s \tag{9}$$

$$\sigma_s = -(u_a - u_w)\theta_e \tag{10}$$

$$\sigma' = (\sigma - u_a) + (u_a - u_w)\theta_e \tag{11}$$

$$V_s = A[(\sigma - u_a) + \theta_e(u_a - u_w)]^\beta \tag{12}$$

For unsaturated soil, the relationship between shear wave velocity and stress state can thus be represented by an equation of form similar to those shown in Equations (6), (7), and (12). The difficulty in using Equations (7) and (12) for interpreting SCPT-determined values of vs. lies in the determination of the degree of saturation or effective degree of saturation. This would require at a minimum, thin-walled tube sampling in layers of interest. Even with companion samples corresponding to one water content profile, it is difficult to determine changes in degree of saturation because of volume changes that accompany the drying or wetting of clayey soils. Another approach would be to treat the net normal stress and matric suction independently, such as in Equation (13), where A_1, A_2, β_1, and β_2 represent fitting parameters associated with net normal stress and matric suction.

$$V_s = A_1[(\sigma - u_a)]^{\beta_1} + A_2[(u_a - u_w)]^{\beta_2} \tag{13}$$

In this study, however, the variation in net normal stress over the depths of interest was relatively small and did not have an appreciable influence on V_s, as indicated in Figure 9 for the CL soils. The CL-ML soils showed similar behavior. Net normal stress was simply estimated as the total vertical stress at the test depths, assuming that pore air pressure was zero.

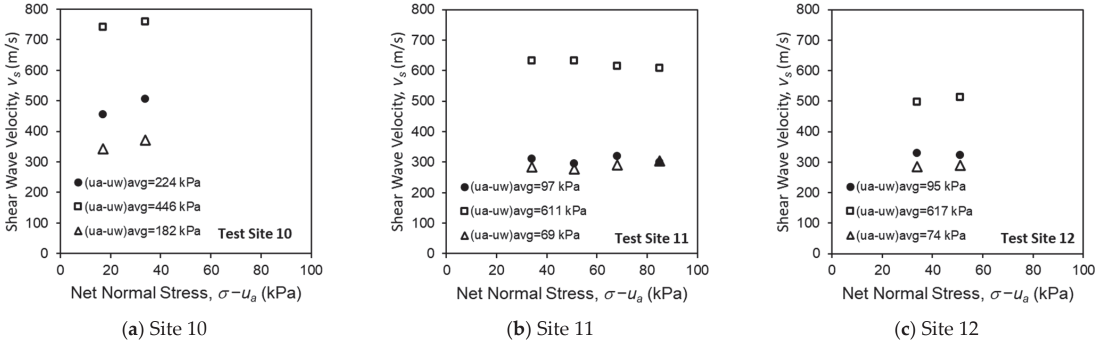

(**a**) Site 10 (**b**) Site 11 (**c**) Site 12

Figure 9. Net normal stress versus shear wave velocity for CL soils at test sites (**a**) 10, (**b**) 11, and (**c**) 12.

Given the strong relationship between suction and shear wave velocity, for this paper, a simplified expression was adopted, as given by Equation (14). This essentially equals Equations (7) or (12) with χ or θ_e, respectively, equal to one.

$$V_s = A[(\sigma - u_a) + (u_a - u_w)]^{\beta} \tag{14}$$

Intuitively, compared to Equation (14), Equations (7) or (12) seem more correct in that, through the degree of saturation, they can capture the nonlinearity associated with the variation in the solid–water interfacial area caused by changing water content. However, parameters A and β can accommodate this nonlinearity. Further, from a practical perspective, as discussed previously, Equation (14) is more easily applied to the interpretation of SCPT vs. measurements, where information to accurately predict existing or future degrees of saturation is lacking. As discussed below, to utilize Equation (14), one would need to estimate the matric suction for the soil and moisture conditions of interest.

Equation (14) is represented by the power relationship parameters shown in Figure 10 for CL and CL-ML soils. As indicated by coefficients of determination in Figure 10, the power relationship is a reasonable model for the relationship between shear wave velocity and stress state variables. It is important to note that in the preceding analysis, it was assumed that the soils representing CL and CL-ML were the same at each test depth. While the soils are geologically similar, they do vary with respect to their index properties. In spite of the natural variations with depth at each test site, the observed relationships were relatively strong. In a similar manner, Equation (14) was applied to the SCPT vs. results shown in Figure 4. Figure 11 indicates that incorporating net normal stress resulted in a slight improvement in statistical strength of the fitted power curves as compared to that with suction alone. The results of this analysis suggest that the use of Equation (14) provided a reasonable means of predicting the influence of changing moisture conditions on vs. determined with the SCPT.

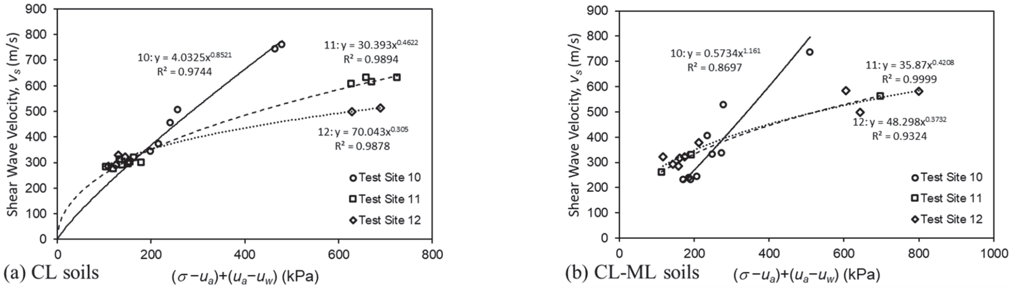

(a) CL soils (b) CL-ML soils

Figure 10. Net normal stress plus matric suction versus shear wave velocity for (**a**) CL soils and (**b**) CL-ML soils.

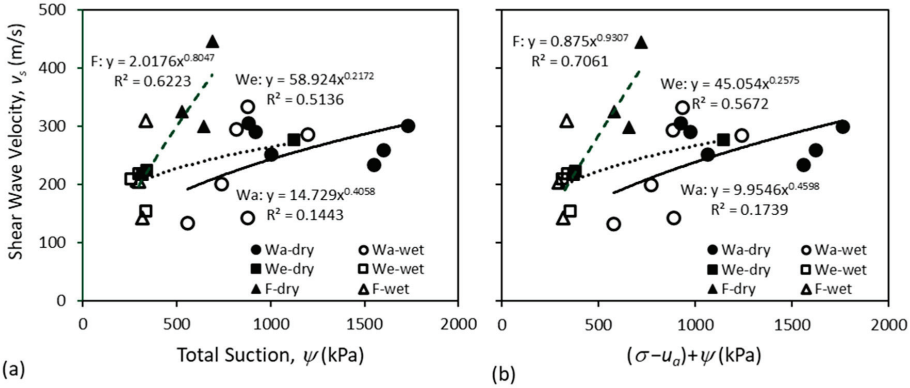

Figure 11. (**a**) Total suction and (**b**) net normal stress plus total suction (**right**) versus shear wave velocity for results from SCPTs shown in Figure 4.

4. Discussion

From a practical perspective, applying the model represented by Equation (14) requires, at a minimum, companion sampling from which soil type, water content, and soil suction can be determined or estimated. There are various levels of sophistication that can be used to determine matric suction, from use of simple empirical correlations for the SWCC (e.g., [31]) to indirect and direct methods of measurement of total, matric, and osmotic suction. Once the water contents and associated matric suctions of interest are determined, the estimates of the *A* and *β* parameters are needed to predict how vs. will vary with changing suction. It is possible that in a natural soil profile, the water content will vary with depth on a given testing date. If the soil profile is geologically similar with depth, then in such cases, site-specific plots, such as those in Figures 10 and 11, may provide a means to estimate *A* and *β*. This would be ideal, since such an approach provides site-specific values of *A* and *β*. Alternatively, *A* and *β* may be estimated using empirical correlations based on physical and index properties for different soil types. For example, Table 1 presents the soil classification, plasticity index (*PI*), percent of fines (*f*), and *A* and *β* for the sites and soil types included in this paper. While the data are relatively limited, there does appear to be a relationship between the index properties and parameters *A* and *β* for the CL soils as shown in Figure 12. In Figure 12, the product of *PI* and *f* is used to represent the index properties of the soil. This parameter was found by Zapata et al. [31] to work well for correlations to determine fitting parameters for the SWCC.

Table 1. Index properties and parameters *A* and *β* for test soils.

Soil	USCS	*PI*	*f* (%)	*fPI*	*A*	*β*
Site 10	CL	11	86	9.5	4.03	0.85
Site 11	CL	14	82	11.5	30.39	0.46
Site 12	CL	14	77.5	10.9	70.04	0.31
We	CL	23.7	65.1	15.4	45.05	0.26
F	CL	10.3	62.7	6.5	0.88	0.93
Site 10	CL-ML	6.5	63	4.1	0.57	1.16
Site 11	CL-ML	4	70	2.8	35.87	0.42
Site 12	CL-ML	5	63	3.2	48.30	0.37
Wa	CH	44.5	98.3	43.7	9.95	0.46

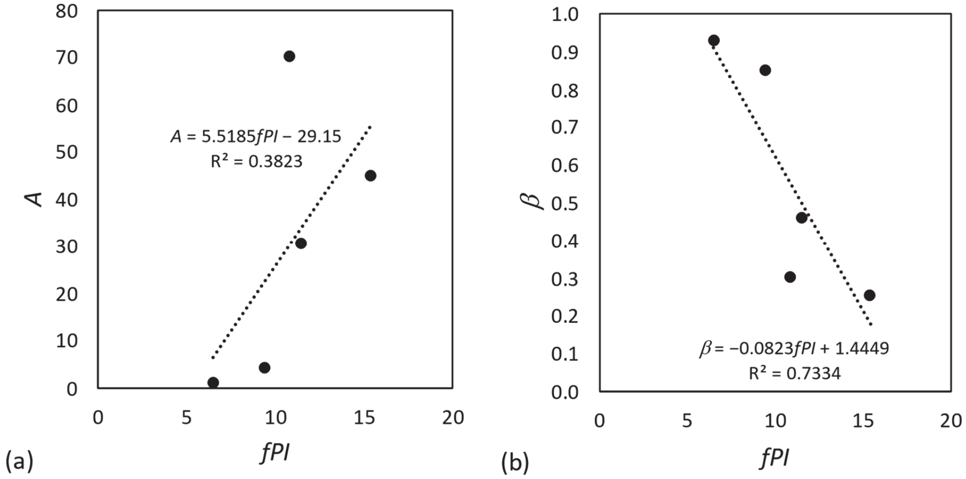

Figure 12. (**a**) Parameter A and (**b**) parameter β versus the product of percent of fines (f) and plasticity index (PI) for CL soils listed in Table 1.

As more field data, such as that presented in this paper, are accumulated, it will be possible to provide typical ranges of A and β for various soil types having various physical and index properties. However, it is expected that datasets used for such correlations will exhibit considerable scatter because shear wave velocity depends on other factors such as void ratio, structure, and stress history, whose influence is not captured by index properties obtained from disturbed samples.

The method presented above based on Equation (14) provides a rational way of predicting how shear wave velocity will change with changes in suction due to changing moisture content. However, there are limitations to the proposed approach as discussed. Natural site variability can cause large scatter in site-specific relationships between shear wave velocity and stress state parameters of interest. Furthermore, attempts to develop correlations between the power model parameters and index properties is expected to exhibit considerable scatter because of natural soil variations and dependence of shear wave velocity on other factors such as void ratio, soil structure, and stress history, for example. What is needed to further this work is additional laboratory and field studies on multiple soil types in which all important parameters of interest are carefully controlled or measured. In the meantime, caution should be exercised in using the method outlined in this paper and site-specific data should be used to the extent possible in determining the model parameters.

5. Conclusions

In this study, shear wave velocity was determined in the field with SCPTs and in the laboratory using the bender element method under wetting and drying conditions on Shelby tube samples obtained from SCPT sites. The following conclusions are based on the analysis of the test results:

1. Shear wave velocity (V_s) determined with the SCPT was strongly dependent on the moisture content and suction in the soil at the time of testing.
2. At three test sites, shear wave velocities determined with the SCPTs were nearly identical to values determined in the laboratory with bender elements under similar stress conditions on thin-walled tube samples obtained on the same day as SCPTs. This suggests that shear wave velocity measurements in the field and laboratory are robust and reliable.

3. Soil water content and suction are strongly correlated with V_s. These relationships can be used to predict changes in vs. resulting from seasonal changes in moisture conditions.
4. A stress-based power model incorporating net normal stress and suction provides a reasonable framework for estimating how shear wave velocity determined with SCPTs may change due to changing moisture conditions. This is important when considering that moisture conditions at the time of SCPTs may not represent future conditions of interest.

Author Contributions: Conceptualization, G.A.M. and T.A.; methodology, T.A., G.A.M. and K.K.M.; software, T.A. and G.A.M.; validation, T.A. and G.A.M.; formal analysis, T.A. and G.A.M.; investigation, T.A.; resources, T.A. and G.A.M.; data curation, T.A. and G.A.M.; writing—original draft preparation, T.A. and G.A.M.; writing— T.A., G.A.M. and K.K.M.; visualization, T.A. and G.A.M.; supervision, G.A.M. and K.K.M.; project administration, G.A.M. and T.A.; funding acquisition, G.A.M. All authors have read and agreed to the published version of the manuscript.

Funding: This research was funded by the Oklahoma Department of Transportation (ODOT) via the Federal Highway Administration (FHWA) grant number ODOT SPR Item Number 2308.

Data Availability Statement: The raw data supporting the conclusions of this article will be made available by the authors on request.

Conflicts of Interest: The authors declare no conflict of interest.

References

1. Kramer, S.L. *Geotechnical Earthquake Engineering*; Prentice Hall: Upper Saddle River, NJ, USA, 1996; 653p.
2. Bui, M.T.; Clayton, C.R.I.; Priest, J.A. The universal void ratio function for small strain shear modulus. *Int. Conf. Recent Adv. Geotech. Earthq. Eng. Soil Dyn.* **2010**, *29*. Available online: https://scholarsmine.mst.edu/icrageesd/05icrageesd/session01/29 (accessed on 17 August 2024).
3. Miller, G.A.; Khoury, C.N.; Muraleetharan, K.K.; Liu, C.; Kibbey, T.C.G. Effects of soil skeleton deformations on hysteretic soil water characteristic curves: Experiments and simulations. *Water Resour. Res.* **2008**, *44*. [CrossRef]
4. Cho, G.C.; Santamarina, J.C. Unsaturated particulate materials—Particle-level studies. *J. Geotech. Geoenviron. Eng.* **2001**, *127*, 84–96. [CrossRef]
5. Yang, S.R.; Lin, H.D.; Kung JH, S.; Liao, J.Y. Shear wave velocity and suction of unsaturated soil using bender element and filter paper method. *J. GeoEngineering* **2008**, *3*, 67–74.
6. Lu, Z.; Sabatier, J.M. Effects of soil water potential and moisture content on sound speed. *Soil Sci. Soc. Am. J.* **2009**, *73*, 1614–1625. [CrossRef]
7. Asslan, M.; Wuttke, F. Wave velocity change and small-strain stiffness in unsaturated soils: Experimental investigation. In *Unsaturated Soils: Research and Applications*; Springer: Berlin/Heidelberg, Germany, 2012; pp. 355–362.
8. Dong, Y.; Lu, N. Dependencies of shear wave velocity and shear modulus of soil on saturation. *J. Eng. Mech.* **2016**, *142*, 04016083. [CrossRef]
9. Khosravi, A.; McCartney, J.S. Impact of hydraulic hysteresis on the small-strain shear modulus of low plasticity soils. *J. Geotech. Geoenviron. Eng.* **2012**, *138*, 1326–1333. [CrossRef]
10. Khosravi, A.; Shahbazan, P.; Pak, A. Impact of hydraulic hysteresis on the small strain shear modulus of unsaturated sand. *Soils Found.* **2018**, *58*, 344–354. [CrossRef]
11. Sawangsuriya, A.; Edil, T.B.; Bosscher, P.J. Modulus−suction−moisture relationship for compacted soils. *Can. Geotech. J.* **2008**, *45*, 973–983. [CrossRef]
12. Sawangsuriya, A.; Edil, T.B.; Bosscher, P.J. Modulus-suction moisture relationship for compacted soils in post compaction state. *J. Geotech. Geoenviron. Eng.* **2009**, *135*, 1390–1403. [CrossRef]
13. Whalley, W.; Jenkins, M.; Attenborough, K. The velocity of shear waves in unsaturated soil. *Soil Tillage Res.* **2012**, *125*, 30–37. [CrossRef]
14. ASTM. *Annual Book of ASTM Standard*; American Society for Testing and Materials, ASTM International: West Conshohocken, PA, USA, 2019; Volume 4.08.
15. Wei, Y.; Miller, G.A. Determining Osmotic Suction Using a Chilled Mirror Device. *Geotech. Test. J.* **2019**, *42*, 1457–1474. [CrossRef]
16. Viggiani, G.; Atkinson, J.H. Interpretation of bender element tests. *Geotechnique* **1995**, *45*, 149–154. [CrossRef]
17. Leong, E.C.; Cahyadi, J.; Rahardjo, H. Measuring shear and compression wave velocities of soil using bend-er-extender elements. *Can. Geotech. J.* **2009**, *46*, 792–812. [CrossRef]
18. Lings, M.L.; Greening, P.D. A novel bender/extender element for soil testing. *Géotechnique* **2001**, *51*, 713–717. [CrossRef]

19. Lee, J.-S.; Santamarina, J.C. Bender elements: Performance and signal interpretation. *J. Geotech. Geoenviron. Eng.* **2005**, *131*, 1063–1070. [CrossRef]
20. Santamarina, J.C.; Klein, A.; Fam, M.A. *Soils and Waves, Particulate Materials Behavior, Characterization and Process Monitoring*; Wiley: Hoboken, NJ, USA, 2001.
21. Sawangsuriya, A.; Edil, T.B.; Bosscher, P.J.; Wang, X. Small-strain stiffness behavior of unsaturated compacted subgrade. In *Unsaturated Soils 2006*; American Society of Civil Engineers: Reston, VA, USA, 2006; pp. 1121–1132.
22. Bishop, A.W. The principle of effective stress. *Teknisk Ukeblad Samarbeide Med. Teknikk.* **1959**, *106*, 859–863.
23. Lu, N.; Likos, W.J. Suction stress characteristic curve for unsaturated soils. *J. Geotech. Geoenviron. Eng.* **2006**, *132*, 131–142. [CrossRef]
24. Vanapalli, S.K.; Fredlund, D.G.; Pufahl, D.E.; Clifton, A.W. Model for the prediction of shear strength with respect to soil suction. *Can. Geotech. J.* **1996**, *33*, 379–392. [CrossRef]
25. Öberg, A.L.; Sällfors, G. Determination of shear strength parameters of unsaturated silts and sands based on the water retention curve. *Geotech. Test. J.* **1997**, *20*, 40–48. [CrossRef]
26. Khalili, N.; Khabbaz, M.H. A unique relationship for χ for the determination of the shear strength of unsaturated soils. *Geotechnique* **1998**, *48*, 681–687. [CrossRef]
27. Likos, W.J.; Lu, N. Hysteresis of capillary stress in unsaturated granular soil. *J. Eng. Mech.* **2004**, *130*, 646–655. [CrossRef]
28. Lu, N.; Godt, J.W.; Wu, D.T. A closed-form equation for effective stress in unsaturated soil. *Water Resour. Res.* **2010**, *46*, 1–14. [CrossRef]
29. Oh, S.; Lu, N.; Kim, Y.K.; Lee, S.J.; Lee, S.R. Relationship between the soil-water characteristic curve and the suction stress characteristic curve: Experimental evidence from residual soils. *J. Geotech. Geoenviron. Eng.* **2012**, *138*, 47–57. [CrossRef]
30. Oh, W.T.; Vanapalli, S.K. Semi-empirical model for estimating the small-strain shear modulus of unsaturated non-plastic sandy soils. *Geotech. Geol. Eng.* **2014**, *32*, 259–271. [CrossRef]
31. Zapata, C.E.; Houston, W.N.; Houston, S.L.; Walsh, K.D. Soil–water characteristic curve variability. In *Advances in Unsaturated Geotechnics*; American Society of Civil Engineers: Reston, VA, USA, 2000; pp. 84–124.

geosciences

Article

Impact of Vetiver Plantation on Unsaturated Soil Behavior and Stability of Highway Slope

Fariha Rahman *, Avipriyo Chakraborty, Sadik Khan and Rakesh Salunke

Department of Civil and Environmental Engineering, College of Science, Engineering and Technology (CSET), Jackson State University, Jackson, MS 39217, USA; j00957875@students.jsums.edu (A.C.); sadik.khan@jsums.edu (S.K.); rakesh.salunke@jsums.edu (R.S.)

* Correspondence: fariha.rahman@students.jsums.edu; Tel.: +1-(601)-291-5578

Abstract: Due to cyclic wetting and drying, the hydro-mechanical behavior of unsaturated soil is impacted significantly. In order to assess the soil strength parameters, knowing the unsaturated behavior is important. Soil moisture content is an important parameter that can define the shear strength of the soil. Most of the highway slopes of Mississippi are built on highly expansive clay. During summer, the evaporation of moisture in the soil leads to shrinkage and the formation of desiccation cracks, while during rainfall, the soil swells due to the infiltration of water. In addition to this, the rainwater gets trapped in these cracks and creates perched conditions, leading to the increased moisture content and reduced shear strength of slope soil. The increased precipitation due to climate change is causing failure conditions on many highway slopes of Mississippi. Vetiver, a perennial grass, can be a transformative solution to reduce the highway slope failure challenges of highly plastic clay. The grass has deep and fibrous roots, which provide additional shear strength to the soil. The root can uptake a significant amount of water from the soil, keeping the moisture balance of the slope. The objective of the current study is to assess the changes in moisture contents of a highway slope in Mississippi after the Vetiver plantation. Monitoring equipment, such as rain gauges and moisture sensors, were installed to monitor the rainfall of the area and the moisture content of the soil. The data showed that the moisture content conditions were improved with the aging of the grass. The light detection and ranging (LiDAR) analysis was performed to validate the field data obtained from different sensors, and it was found that there was no significant slope movement after the Vetiver plantation. The study proves the performance of the Vetiver grass in improving the unsaturated soil behavior and stability of highway slopes built on highly expansive clay.

Keywords: highly expansive clay; slope failure; vetiver grass; slope stability

Citation: Rahman, F.; Chakraborty, A.; Khan, S.; Salunke, R. Impact of Vetiver Plantation on Unsaturated Soil Behavior and Stability of Highway Slope. *Geosciences* **2024**, *14*, 123. https://doi.org/10.3390/geosciences14050123

Academic Editors: Jesus Martinez-Frias, Hongyuan Liu, Dunja Perić and Laureano R. Hoyos

Received: 15 December 2023
Revised: 16 April 2024
Accepted: 25 April 2024
Published: 1 May 2024

1. Introduction

The behavior of expansive soil highly relies on the changes in soil moisture contents. There is a buildup and breakdown within soil molecules when they are subjected to repeated wetting and drying due to the continuous increase in unstable aggregates [1]. The continuous changes in moisture contents lead to volume changes in clay soils. When the soil sample becomes wet, it expands, leading to an increase in volume. Upon drying, the sample reduces its volume, undergoing shrinkage. Clay soils found under natural conditions are subjected to cyclic swelling and shrinkage due to seasonal moisture change. The cyclic wetting and drying of clay soil results in a decreased clay content and reduced plasticity. Khan et al. 2019 found that the number of wet–dry cycles has been shown to increase the void ratio of highly expansive Yazoo clay, leading to a notable decrease in its shear strength, particularly cohesion. After seven wet–dry cycles, cohesion decreased by 77%. This decrease in shear strength affects the stability of the slopes made of Yazoo clay, with the shear strength of the topsoil decreasing from 2.7 to 1.4 with increasing wet–dry cycles. Moreover, when considering the impact of rainfall, specifically in two periods with varying intensities, the factor of safety decreased significantly. For instance, with rainfall of 126.2 mm (2 h) and 271.7 mm over three days, the factor of safety decreased from 1.7 to 1.2 and from 1.68 to 1.02, respectively, when factoring in three, five, and seven wet–dry cycles in the topsoil. This reduction in safety factor is attributed to the combined effects of decreased shear strength due to wet–dry cycles and saturation caused by prolonged rainfall [2]. This reduction is primarily due to particle aggregation during drying, leading to a decrease in the surface area available for interaction with water, including a decrease in the liquid limit. Therefore, particle aggregation reduces the surface area for interaction with water, ultimately lowering clay content and plasticity. After each repeated wetting and drying cycle, the soil exhibits signs of fatigue [3].

In arid or semi-arid areas, expansive soils are subjected to periodic wetting and drying, and as a result, ground movement is a common occurrence in those regions [4]. The majority of the highway slopes in the southern region of the United States, including Mississippi, Texas, Louisiana, and Alabama, are built on highly expansive clay soil. Slopes in this region are vulnerable to failure due to the high plasticity and abrupt volume change in slope soil [5]. During summer, desiccation cracks are formed due to reduced moisture content and shrinkage. In the rainy season, rainwater permeates the soil layer through these cracks. Through repeated wetting and drying cycles, the infiltrated rainwater establishes a perched condition within the slope, elevating the moisture content and reducing the soil's matric suction [6,7]. The clay mineralogy of the soil influences the physical and engineering characteristics of fine-grained soil, including factors such as liquid limit, compressibility, and shear strength [8]. Typically, clay soils are characterized by three primary minerals: illite (mica), kaolinite (Kaolin), and montmorillonite (smectite), alongside other mineral varieties. The extent of swelling potential differs among soils, contingent upon their mineralogical compositions. Specifically, soils rich in montmorillonite minerals may undergo swelling, facilitated by the formation of a diffuse double layer and flocculation. Montmorillonite possesses a notably greater surface area, drawing in a substantial amount of water, and is classified as a high-plasticity clay. The double layer of water surrounding montmorillonite is thickest among clays [9]. The Yazoo clay found in Mississippi comprises 28% smectite, with montmorillonite being a specific type of smectite. This high smectite content is responsible for the rapid shrink–swell characteristics observed in this soil type. In numerous areas, such as those near the metropolitan Jackson region, the highway slopes are built at a steeper gradient (approximately 3H:1V). Consequently, the Mississippi Department of Transportation (MDOT) cannot adopt the conventional design approach of broadening the highway slopes to ratios ranging from 5H:1V to 6H:1V. That is why highway slopes constructed on Yazoo clay are at risk of failure triggered by rainfall [10–13]. A moderate to steep slope built on high-plasticity clay is prone to experiencing softening phenomena within the active zone of the slope (approximately the upper 12 to 15 feet) during seasonal wet–dry cycles. Typically, when constructing highway embankments, the soil's shear strength is assigned based on its Peak Strength value determined through laboratory testing. In the USA, the cost related to damage caused by expansive soil exceeds 9 billion USD annually [14]. As per the American Society of Civil Engineers, expansive soils are responsible for causing damage in 25% of homes [15].

Global temperature rise has been a critical issue related to climate change. The rise in surface temperature results from the increasing emission of greenhouse gases like carbon dioxide (CO_2), methane (CH_4), nitrous oxide (N_2O), and others. NOAA has identified 2023 as the hottest year on record according to its global temperature dataset, which spans back to 1850. There is a one-in-three probability that 2024 will be warmer than 2023 and a 99% probability that 2024 will be among the top five warmest years on record. Due to the impact of climate change, the precipitation pattern in the whole USA has changed drastically. While some states got drier, most of the states have seen more precipitation [16,17]. The average rainfall amounts in different states have shifted significantly. From Figure 1, it is obvious that the precipitation in south-western regions has increased significantly.

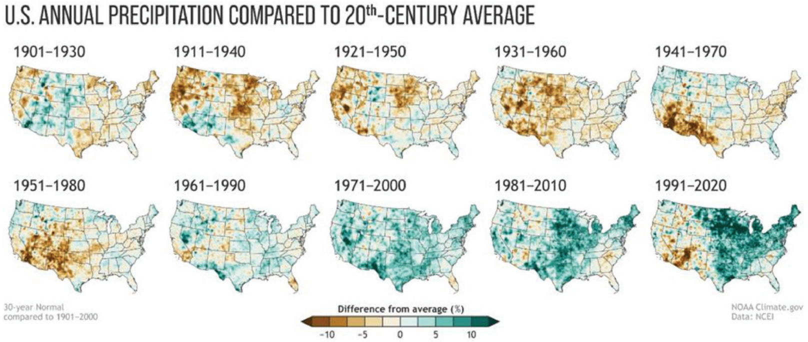

Figure 1. Normal annual U.S. precipitation as a percentage of the 20th-century average [16].

The US Environmental Protection Agency (EPA) emphasized alterations in precipitation patterns due to climate change in the contiguous US, citing a 10–20% shift in precipitation for the mid-western and southeast regions. Analyzing temperature and rainfall trends in selected southern states, projections indicate a rise in temperature followed by increased evaporation. With a 7% rise in the water retention capacity of air per 1 °C warming, this contributes to heightened precipitation during specific weather events such as thunderstorms, extratropical rain, snowstorms, or tropical cyclones [18]. The impact of climate change resulted in an increased frequency of extreme events. Over the last five decades, there has been a 20% rise in the occurrence of exceptionally heavy precipitation in the southeastern plains [19]. In August 2022, Mississippi witnessed six extreme events surpassing the local threshold, meeting the criteria of '1-in-1000-year' rainfall events according to the National Weather Service classification. Within a mere three-hour timeframe on a single day, specific areas in Mississippi encountered rainfall exceeding 8 inches [20]. A study conducted by NASA has revealed that climate change is leading to heightened fluctuations in precipitation patterns. These variations are marked by prolonged dry spells followed by intense storms, which deposit significant rainfall over brief periods. This increase in rainfall affects both slow-moving and fast-moving landslides, demonstrating that heavy precipitation serves as a common trigger for landslides of varying speeds. That is why rainfall-induced slope failure is very common in southern states of the USA, where expansive clay soil is prevalent. The rainwater infiltrates into the slope soil and reduces the matric suction of the slope [21]. The decrease in the matric suction reduces the soil shear strength and leads to a shallow slope failure [22]. In recent years, Mississippi has seen a tremendous increase in rainfall, and creeping slope failure has become a common phenomenon (Figure 2), which causes significant financial loss.

Various mechanical methods have been implemented for stabilizing embankment slope failures, each with its unique characteristics and advantages. One approach involves using tire bales, which are blocks of compressed scrap tires held together by galvanized or steel tie wires [23]. Another effective method utilizes geosynthetics, such as geogrids, geotextiles, or geofoams, known for their flexibility and long-term performance in significantly increasing soil strength. It is important to note that the long-term behavior of geosynthetic materials relies on exposure to various degradation mechanisms [24]. Soil nails represent another technique for reinforcing the soil mass by transferring the tensile and shear resistance to the sliding soil. Retaining structures play a crucial role in slope stabilization by enhancing resisting forces, particularly shear stress, and various types like precast concrete panel walls, cast-in-place concrete gravity and cantilever walls, crib walls, gabion walls, MSE walls, tieback walls, rock walls, and 'H-pile' and leggings are employed in highway slope repair initiatives. However, one limitation of retaining structures lies in the necessity for proper engineering design, as their effectiveness depends on adequate design considerations [25]. Recycled Plastic Pins (RPPs) offer a cost-effective solution for slope stabilization, utilizing recycled plastics and waste materials like polymers, sawdust, and fly ash [26]. Piles contribute to slope stability by providing passive resistance against soil lateral forces [27]. In some cases, slope rebuilding involves replacing the failed soil mass and reshaping the slope to its pre-failure state. However, the effectiveness of this method varies depending on the soil type; while compaction generally improves the physical properties of cohesionless soils, it may not necessarily enhance the properties of cohesive soils like clay [28]. The majority of the current mechanical approaches to slope repair involve substantial fieldwork or financial investments. Bioengineering with plants is a technique that employs vegetation to fortify soil on slopes, bolstering shear strength and ultimately improving slope stability [29]. In various biotechnical methods, the rooting systems of plants offer better reinforcement and drainage properties compared to the earthwork involved in mechanical approaches like slope repair, retaining walls, and sheet piles. Additionally, the biotechnical approach tends to lower both construction and maintenance costs [30].

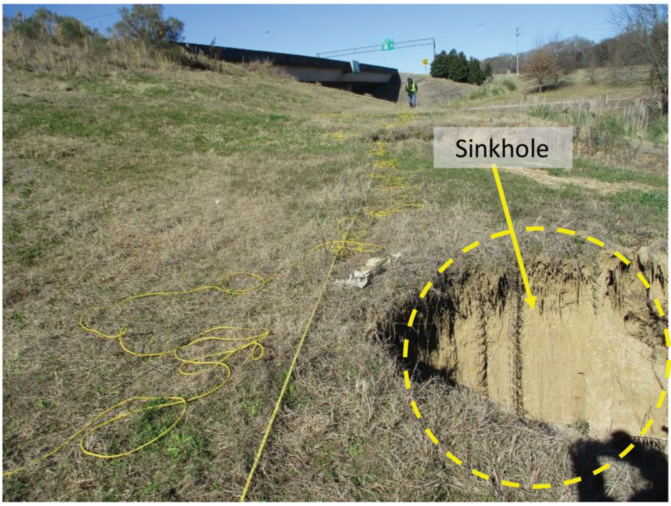

Figure 2. Sinkhole developed in a slope near Metro Centre, Mississippi, in I220N.

Vetiver grass, a perennial grass, has shown much potential in reducing landslides and slope failure. The fast-growing plant can sustain various soil types, a broad pH range (3.3–12.5), temperatures spanning from −15 °C to 55 °C, and high concentrations of micropollutants. The fibrous root can reach up to 3–4 m within the first year of plantation. It also exhibits resilience to extreme climate variations, fires, and pests without causing adverse effects on the soil [31–33]. Thriving in environments challenging for many other plants, this species can be cultivated extensively in marginal lands with minimal maintenance and significantly reduced irrigation needs. The 'Sunshine' vetiver genotype has been acknowledged by the United States Department of Agriculture (USDA) Natural Resources Conservation Service (NRCS) as a non-invasive and sterile variant, making it well-suited for cultivation in the United States [34]. Vetiver grass stabilizes the soil by anchoring it with its thick roots, facilitating water drainage from the soil through evapotranspiration and reducing moisture content. The combined effect of the dense and expansive root network resembles the behavior of soil nails commonly employed in civil engineering projects [35]. The root system substantially enhances the soil's shear strength with increased slope stability by up to 30% [36].

Studies were carried out on analysis concerning the stability of slopes with and without roots. An investigation of the effect that root suction has on the tensile strength of vetiver roots was carried out [9]. Bio-inspired stabilization on levee slopes has been investigated in expansive clay slopes [37,38]. Ng et al., 2020 found that plant growth and spacing had an effect on the hydrological changes that occurred in the soil [39]. Patil et al., 2021 carried out a transient seepage-coupled slope stability analysis under an extreme precipitation event and demonstrated that the slight increase in FOS that was brought about by matric suction induced by root water uptake (RWU) could play a significant role in maintaining the slope's stability during extreme storm events, particularly in situations where the FOS of the bare slope is close to one [40]. In another study, Patil et al., 2022 found that matric suction created within shallow depths as a result of root water uptake (RWU) contributes to the provision of a buffer that prevents slope failure during lower-precipitation occurrences, though this stabilization effect is no longer present during precipitation that lasts for a prolonged time [41]. However, the impact study of sunshine Vetiver on unsaturated soil properties in high plasticity expansive clay is still limited. In addition to this, there is no study on how Vetiver impacts the unsaturated soil property of a high plasticity expansive soil slope.

In order to detect potential hotspots for slope failure and the performance of the slope, continuous slope monitoring is necessary. Different sensor systems are implemented to track various soil parameters like moisture content, pore water pressure, temperature, rainfall, and others. By translating the sensor data, it enables the authority to predict any landslide risk. However, site accessibility, the installation of sensors with boring, data storage, and collection remain some of the main challenges of this sensor system. Light detection and ranging (LiDAR) is a well-known and accepted remote sensing method. A wide range of applications including volume estimation, the 3D modeling of rockfall geometry, the extraction of structural and geometric details of landslides using terrestrial laser scanning (TLS) data, and the refinement of LiDAR for the automated assessment of structural irregularities have been deployed with this technology [42].

The current study assesses the performance of Vetiver grass planted on a highway slope in terms of reducing moisture content and repairing slope failure. One highway slope in Jackson, Mississippi, was planted with Vetiver, and field instruments to track the precipitation and soil moisture content were installed. The moisture content data showed significant improvement after theVetiver plantation. A LiDAR survey was conducted to compare the slope movement trend. The analysis shows that there was no significant movement in the slope after the stabilization with Vetiver.

2. Materials and Methods

2.1. Site Selection and Plantation

The slope near Terry Road along Interstate I-20 Interchange in Jackson, Mississippi, was selected for the study. The slope soil type is Yazoo clay, characterized as a highly expansive soil with a weathered upper zone overlaying unweathered clays. Weathered Yazoo clay typically exhibits a plasticity index exceeding 50%, attributed to a liquid limit ranging from 70% to 100% and a plastic limit of 20% to 30%. Previous observations [5] indicated signs of slope movement at 1.5 m depth. A section of the slope near the existing bridge experienced a shallow rainfall-induced landslide, which was repaired using H-piles. A study conducted on the impact of rainfall on the slope's shear strength found that the slope soil exhibited an increased void ratio with an increase in the number of wet–dry cycles. Stability analysis conducted on the representative slope observed a reduced factor of safety due to rainfall events [2]. The slope has a height of 4.572 m and a slope ratio ranging from 3.5H:1V to 4H:1V. The movement of the section without the H-pile was monitored using an inclinometer for one year starting from January 2019. The inclinometer data indicated a movement of up to 1.6 inches at the slope surface for the year 2019 [5]. For reinforcement, a 15.25 m wide section of the slope was chosen, and the 'Sunshine' Vetiver grass genotype (Chrysopogon zizanioides or Vetiveria zizanioides) was planted at a spacing of 0.6–0.9 around an area of 65 m^2 (Figure 3). The plantation was done at the section where there were no H-piles installed. Due to the tropical character of the grass, planting was conducted to guarantee adequate precipitation, which promotes grass growth. The plantation was done in a staggered way. As the Vetiver root is fibrous enough to spread inside the slope soil, the spacing of 30.48 cm (1 ft) was taken considering the ease of the manual plantation process. It is suggested to plant the Vetiver at the beginning of the rainy season to have sufficient irrigation [43]. Considering this, the plantation was conducted in July 2020 when there was a lot of rainfall in Mississippi. The grass was allowed to grow naturally, and no modifications were made to the surrounding vegetation during the planting process.

(**a**) (**b**)

Figure 3. (**a**) Location of the study site; (**b**) Vetiver grass planted on the slope.

2.2. Site Instrumentation and Data Collection

A micro weather station was set up on the study slope to monitor field weather conditions. This installation included the integration of various industrial-grade sensors, such as the GS-1 moisture sensors to measure moisture sensors, the ECRN-50 tipping-bucket rain gauge to track the precipitation, the RT-1 to measure air temperature, and the EM50 data logger (Figure 4). Variations in moisture contents were observed in the planted section up to the depth of Vetiver growth of 300 cm using sensors, with calibrated sensors positioned at depths of 15.24 cm (6 inches) and 45.72 cm (18 inches). The depths were considered to track the slope soil water content, which may induce shallow slope failure. A 3.5 mm stereo audio extension cable is utilized to link each sensor with the data recorders to continuously capture and record in situ measurements. Following the completion of the installation process, the data recorders were programmed to gather information from the soil temperature, rain gauge, moisture sensor, water potential probe, and air temperature sensors hourly. Changes in moisture content and pore water pressure were monitored using these sensors and water probes within the planted section, with sensors placed at depths of 15.24 cm and 45.72 cm. All the sensors were linked to automatic data loggers programmed to collect data at hourly intervals. The data collected from the moisture sensor installed at 45.72 cm were utilized for this study.

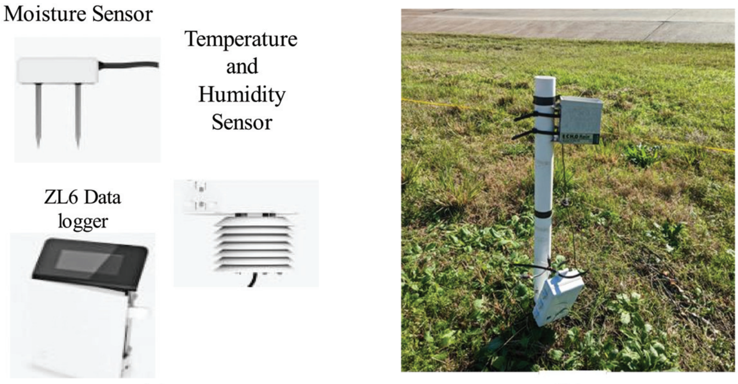

(**a**) (**b**)

Figure 4. (**a**) Different sensors installed at the site; (**b**) rain gauge to track precipitation of the area.

2.3. LiDAR Survey

The attractiveness of LiDAR instruments comes from their high spatial and temporal resolution of measurements, the capability to observe the atmosphere under ambient conditions, and the potential to cover the height range from ground level to over 100 km altitude [44]. Conducting recurring LiDAR point cloud surveys at a consistent location over time aids in monitoring subtle changes within geotechnical assets and mapping potential risks [45]. This current study applied 3D laser scanning with the terrestrial LiDAR equipment Trimble X7. Dense point cloud data were captured from the slope, and topographical surfaces were generated using the dense point cloud data, followed by the extraction of bare ground. Temporally spaced surface profiles for both the failed and undamaged sections of the slopes were created for comparative analysis (Figure 5).

Figure 5. LiDAR survey conducted on the site.

3. Results

3.1. Moisture Content

As part of the process of carrying out the analysis, the information about the moisture content of the slope for the years 2020–21 and 2021–22 was meticulously analyzed. The moisture content of the slope soil was initially higher (about 0.5 m^3/m^3) (Figure 6a), which may indicate that there is a perched water zone at shallower depth. The moisture content started to decrease in August of 2021, which was more than a year after the plantation was formed.

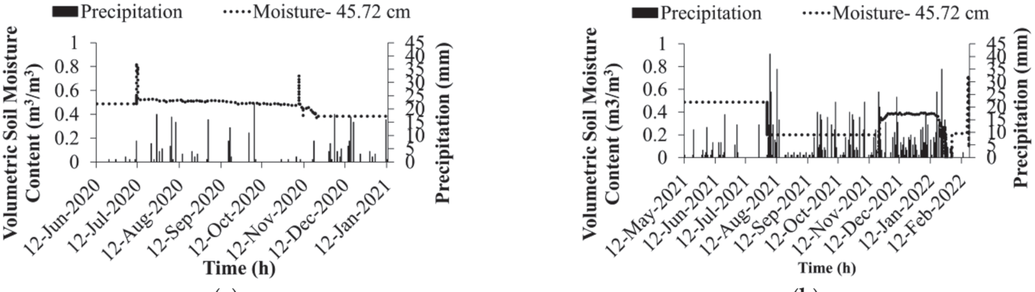

(**a**) (**b**)

Figure 6. Moisture content variations in the slope soil with precipitation. (**a**) June 2020 to January 2021; (**b**) May 2021 to February 2022.

In 2020, which was the year that the plantation was carried out, the initial high volumetric moisture content can imply that Vetiver roots were not sufficiently grown to absorb water initially. As the roots started growing in the latter part of the year after August 2021, the water content stayed mostly constant throughout this period. As Vetiver roots can grow to full length up to 3 m after a one-year period, the results imply that the root uptake of the reduced water content reduces the volumetric water content of the soil. The deep root and long leaves of Vetiver allowed a better evaporation rate. There were several events of extreme precipitation during the study period. However, the lower hydraulic conductivity of expansive soil resulted in a delay in the peak in moisture content.

3.2. LiDAR Survey Result

In this study, the Trimble X7 terrestrial LiDAR equipment was utilized to carry out 3D laser scanning. Dense point cloud data were collected for the site and with the collected data, topographical surfaces were constructed. The LiDAR scanner was set up at five different stations on the slope for surveying and point cloud data were gathered while the scanner was in operation. In addition, ten spherical targets were placed around the slope at a height of four feet above the ground to facilitate the registration of the point cloud data that were collected from each station. To compare the temporally spaced point clouds and identify any changes that may have taken place, the point clouds were georeferenced and stacked, respectively. The slope surface profiles for each season were retrieved from the same locations on both point clouds to compare the changes that occurred in the slope during each season.

After field data collection, surface data from each season were superimposed, and alignments were established along the slope. Following this, surface profiles were created by utilizing the alignments along the Vetiver sections C-C′, D-D′, and E-E′ (Figure 7). This process involved superimposing the surfaces to compare the changes over different seasons, and the alignments along the specific sections allowed for the generation of detailed surface profiles in relation to the Vetiver planting areas.

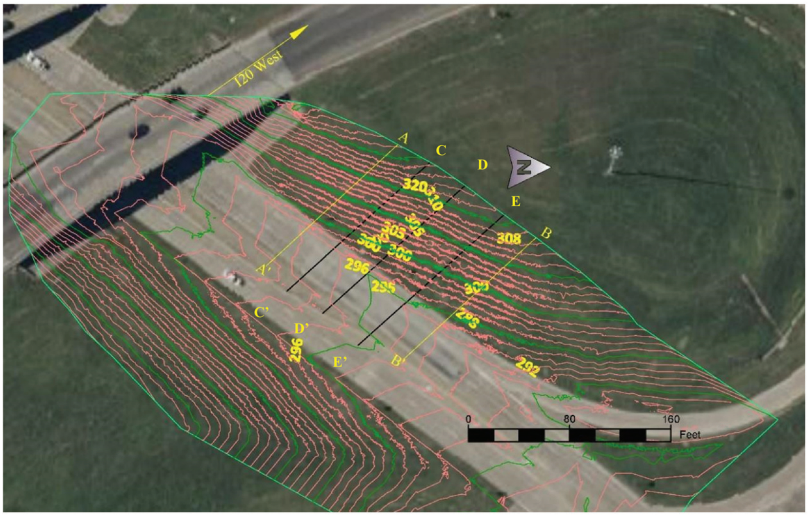

Figure 7. LiDAR surface topography.

Three sectional profiles were created for summer 2021, Spring 2022, and Fall 2022 (Figure 8).

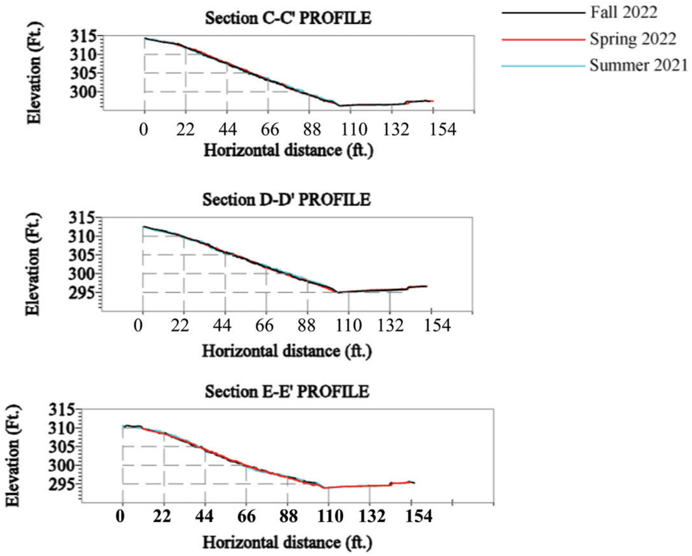

Figure 8. LiDAR surface profiles for (**a**) section C-C′, (**b**) section D-D′, and (**c**) section E-E′.

After the analysis, the profiles obtained for summer 2021, Spring 2022, and Fall 2022 from the cloud point data were superimposed. There were no significant changes in the slope section with seasonal changes. The profiles from the three sections indicate that there was no slope movement after the plantation of the Vetiver. The Vetiver root helped to lower the moisture content of the slope soil, which increased the shear strength eventually. The increased shear strength prevented any substantial movement along the slope soil.

4. Discussion

The constant moisture content along the slope soil in 2020 shows the existence of a perched water zone within the slope. The decrease in water content proves the improvement of soil quality after the Vetiver grass grew deeper into the soil. This illustrates the performance of Vetiver in providing slope stability. This was further evaluated through the LiDAR data analysis and surface profile generated from the point clouds. There was no significant change in the soil sectional profile in summer 2021, spring 2022, and fall 2022. It indicates that there was no significant slope movement during this period. The previous repair to the slope where no vetiver exists is still working as intended (Figure 9).

However, in light of recent actions against climate change, the importance of nature-based solutions has been acknowledged significantly. Although the H-piles provided safety against slope movement, the manufacture and installation of H-piles or other similar techniques cost a huge amount of financial investment. On the other hand, Vetiver grass requires very few days to be planted on a highway slope. A single slip of Vetiver only costs USD 2–3 only. If planted in dry seasons, it is recommended to water the plants every 10 days before the plants get matured. There is no need to fertilize when the plant hedges have been established. So, it can be said that Vetiver system needs very little financial costs for operation and maintenance. The deep and fibrous root system can absorb a huge amount of carbon from the atmosphere [46]. Therefore, Vetiver grass provides a comprehensive solution for slope repair that is a cost-effective, climate-adaptive, and nature-based solution.

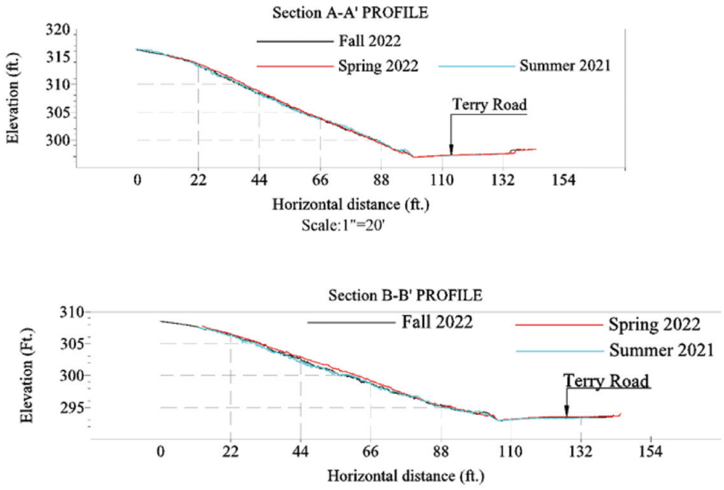

Figure 9. LiDAR surface profiles for the (**up**) repaired section A-A′, and (**down**) control section B-B.

5. Conclusions

The current study evaluates the performance of Vetiver grass in reducing soil moisture content and preventing slope movement. Highway slopes built on highly expansive clay soil are prone to rainfall-induced failure. Climate change has altered the global temperature and, as a result, the precipitation pattern. Increased rainfall and extreme events have affected the infrastructural health and are causing significant financial loss. One highway slope built on highly expansive Yazoo clay located in Jackson, Mississippi, was selected for the study. The slope previously showed a trend of movement. Field instrumentations to track the moisture content, pore water pressure, and precipitation were installed at the site. Rainfall and moisture content data were collected continuously. A LiDAR survey was conducted in each season to monitor if there was any slope movement. Constant moisture content along the slope soil proves the presence of a perched water zone during the first year of the plantation. However, the moisture content reduced in the second year when the Vetiver grew deeper into the soil. The result from the LiDAR survey also proves the performance of Vetiver in preventing slope movement. There was no significant change in the slope sectional profile between summer 2021 and fall 2022. Vetiver grass demonstrates a significant potential in addressing slope failure, particularly in the southern regions of the USA, such as Mississippi. It offers a cost-effective, climate-adaptive, and sustainable solution for enhancing slope stability. As a nature-based approach, it proactively addresses and mitigates slope failure incidents.

Author Contributions: Conceptualization, F.R. and S.K.; methodology, F.R. and S.K.; validation, F.R., A.C. and S.K.; formal analysis, F.R., A.C. and R.S.; data collection and analysis, F.R., A.C. and R.S.; writing—original draft preparation, F.R.; writing—review and editing, F.R and S.K.; supervision, S.K.; project administration, S.K.; funding acquisition, S.K. All authors have read and agreed to the published version of the manuscript.

Funding: This research was funded by the National Science Foundation, CMMI Award No 2046054.

Data Availability Statement: The data that support the findings of this study are available from the corresponding author upon reasonable request.

Acknowledgments: The authors appreciate the Mississippi Department of Transportation (MDOT) for facilitating the site accessibility required for the study.

Conflicts of Interest: The authors declare no conflicts of interest. The funders had no role in the design of the study; in the collection, analyses, or interpretation of data; in the writing of the manuscript; or in the decision to publish the results.

References

1. Allam, M.M.; Sridharan, A. Effect of Wetting and Drying on Shear Strength. *J. Geotech. Eng. Div.* **1981**, *107*, 421–438. [CrossRef]
2. Khan, S.; Ivoke, J.; Nobahar, M. Coupled effect of wet-dry cycles and rainfall on highway slope made of yazoo clay. *Geosciences* **2019**, *9*, 341. [CrossRef]
3. Al-Homoud, A.S.; Basma, A.A.; Husein Malkawi, A.I.; Al Bashabsheh, M.A. Cyclic Swelling Behavior of Clays. *J. Geotech. Eng.* **1995**, *121*, 562–565. [CrossRef]
4. Rao, K.S.; Rao, S.M.; Gangadhara, S. Swelling behavior of a desiccated clay. *Geotech. Test. J.* **2000**, *23*, 193–198. Available online: https://trid.trb.org/view/656646 (accessed on 12 December 2023). [CrossRef]
5. Khan, S.; Amini, F.; Nobahar, M. *Performance Evaluation of Highway Slopes on Yazoo Clay*; Mississippi Department of Transportation: Jackson, MS, USA, 2020.
6. Spears, A.; Khan, M.S.; Whalin, R.W.; Alzeghoul, O.E.; Chakraborty, A. Bio-Inspired Stabilization of a Test Levee Slope Using Vetiver Grass on Highly Plastic Clay. In *Proceedings of the Geo-Congress 2023*; American Society of Civil Engineers: Los Angeles, CA, USA, 2023; pp. 96–105. [CrossRef]
7. Nobahar, M.; Salunke, R.; Alzeghoul, O.E.; Khan, M.S.; Amini, F. Mapping of Slope Failures on Highway Embankments using Electrical Resistivity Imaging (ERI), Unmanned Aerial Vehicle (UAV), and Finite Element Method (FEM) Numerical Modeling for Forensic Analysis. *Transp. Geotech.* **2023**, *40*, 100949. [CrossRef]
8. Prakash, K.; Sridharan, A. Free Swell Ratio and Clay Mineralogy of Fine-Grained Soils. *Geotech. Test. J.* **2004**, *27*, 10860. [CrossRef]
9. Mahannopkul, K.; Jotisankasa, A. Influence of root suction on tensile strength of Chrysopogon zizanioides roots and its implication on bioslope stabilization. *J. Mt. Sci.* **2019**, *16*, 275–284. [CrossRef]
10. Taylor, A.C. Mineralogy and Engineering Properties of The Yazoo Clay Formation, Jackson Group, Central Mississippi. Master's Thesis, Mississippi State University, Mississippi State, MS, USA, 2005.
11. Kim, J.; Jeong, S.; Park, S.; Sharma, J. Influence of rainfall-induced wetting on the stability of slopes in weathered soils. *Eng. Geol.* **2004**, *75*, 251–262. [CrossRef]
12. Khan, S.; Amini, F.; Salunke, R.; Nobahar, M. *Development of Advanced Landslide Investigation Protocol Using Geophysical Methods for Mississippi*; Mississippi Department of Transportation: Jackson, MSA, USA, 2023.
13. Li, J.; Cameron, D.A.; Ren, G. Case study and back analysis of a residential building damaged by expansive soils. *Comput. Geotech.* **2014**, *56*, 89–99. [CrossRef]
14. Amakye, S.Y.; Abbey, S.J.; Booth, C.A.; Mahamadu, A.-M. Enhancing the Engineering Properties of Subgrade Materials Using Processed Waste: A Review. *Geotechnics* **2021**, *1*, 307–329. [CrossRef]
15. Jones, L.D.; Jefferson, I. Expansive Soil. In *Institution of Civil Engineers Manuals Series*; ICE Publishing: London, UK, 2012.
16. NASA Earth Observatory Climate Changes in the United States. Available online: https://earthobservatory.nasa.gov/images/83624/climate-changes-in-the-united-states (accessed on 13 December 2023).
17. NOAA The new, U.S. Climate Normals Are Here. What Do They Tell Us about Climate Change? | National Oceanic and Atmospheric Administration. Available online: https://www.noaa.gov/news/new-us-climate-normals-are-here-what-do-they-tell-us-about-climate-change (accessed on 13 December 2023).
18. Trenberth, K. Changes in precipitation with climate change. *Clim. Res.* **2011**, *47*, 123–138. [CrossRef]
19. Karl, T.R.; Melillo, J.M.; Oeterson, T.C. *Global Climate Change Impacts in the United States*; Cambridge University Press: Cambridge, UK, 2009.
20. Sistek, S. 6 Rare "1000-Year" Rain Events within a Month? Climate Change May Force NOAA to Update Criteria. Available online: https://www.foxweather.com/extreme-weather/5-rare-1000-year-rain-events-within-a-month-climate-change-may-force-noaa-to-update-criteria (accessed on 25 July 2023).
21. Khan, M.S.; Nobahar, M.; Ivoke, J.; Amini, F. Rainfall Induced Shallow Slope Failure over Yazoo Clay in Mississippi. In *PanAm Unsaturated Soils*; ASCE: Austin, Texas, USA, 2018; pp. 153–162. [CrossRef]
22. Tohari, A.; Nishigaki, M.; Komatsu, M. Laboratory Rainfall-Induced Slope Failure with Moisture Content Measurement. *J. Geotech. Geoenviron. Eng.* **2007**, *133*, 575–587. [CrossRef]
23. Nabaei, M. Evaluation of Best Practices for implementation of Slope repair Methods in Texas. Master's Thesis, University of Texas, Arlington, TX, USA, 2019.
24. Nelson, M.; Saftner, D.; Carranza-Torres, C. Slope Stabilization for Local Government Engineers in Minnesota. In *Congress on Technical Advancement*; ASCE: Austin, Texas, USA, 2017; pp. 127–138. [CrossRef]
25. Collin, J.G.; Loehr, J.E.; Hung, C.J. *Slope Maintenance and Slide Restoration Reference Manual for NHI 132081 Course 2008*; National Highway Institute: Washington, DC, USA, 2008.
26. Chen, C.-W.; Salim, H.; Bowders, J.J.; Loehr, J.E.; Owen, J. Creep Behavior of Recycled Plastic Lumber in Slope Stabilization Applications. *J. Mater. Civ. Eng.* **2007**, *19*, 130–138. [CrossRef]
27. Wei, W.B.; Cheng, Y.M. Strength reduction analysis for slope reinforced with one row of piles. *Comput. Geotech.* **2009**, *36*, 1176–1185. [CrossRef]

28. Abramson, L.W.; Lee, T.S.; Sharma, S.; Boyce, G.M. *Slope Stability and Stabilization Methods*, 2nd ed.; John Wiley & Sons, Inc.: New York, NY, USA, 2002.
29. Gray, D.H.; Sotir, R.B. *Biotechnical and Soil Bioengineering Slope Stabilization: A Practical Guide for Erosion Control*; John Wiley & Sons, Inc.: New York, NY, USA, 1996.
30. *Martin Donat Bioengineering Techniques for Streambank Restoration*; Watershed Restoration Program, Ministry of Environment, Lands and Parks and Ministry of Forests, Umweltakademie: Stockhofstr, Austria, 1995.
31. Crocamo, A.; Di Bernardino, S.; Di Giovanni, R.; Fabbricino, M.; Martins-Dias, S. An integrated approach to energy production and nutrient recovery through anaerobic digestion of Vetiveria zizanoides. *Biomass Bioenergy* **2015**, *81*, 288–293. [CrossRef]
32. Mickovski, S.B.; van Beek, L.P.H. Root morphology and effects on soil reinforcement and slope stability of young vetiver (Vetiveria zizanioides) plants grown in semi-arid climate. *Plant Soil* **2009**, *324*, 43–56. [CrossRef]
33. Nirola, R.; Megharaj, M.; Aryal, R.; Naidu, R. Screening of metal uptake by plant colonizers growing on abandoned copper mine in Kapunda, South Australia. *Int. J. Phytoremediation* **2016**, *18*, 399–405. [CrossRef]
34. Samir, S.; Khan, M.S. Water Balance Final Cover Using Vetiver Grass in Texas. *Geo-Congress* **2023**, *2023*, 182–192. [CrossRef]
35. Hengchaovanich, D. Vetiver system for slope stabilization. In Proceedings of the 3rd International Vetiver Conference, Guangzhou, China, 6–9 October 2003; pp. 301–309.
36. Mohammad, S.N.; Masoud, N.; Mohammad Sadik, K.; Alzeghoul, O.; Henry Kini, C. Vetiver Grass Performance on a Distressed Highway Slope of High-Plastic Clay under Excessive Rainfall. *Geo-Congress* **2022**, *2022*, 268–278. [CrossRef]
37. Khan, S.; Whalin, R.W.; Spears, A.; Chakraborty, A. Bio-Inspired Stabilization of Levee Slope on Expansive Yazoo Clay at the Maritime and Multimodal Transportation Infrastructure in Mississippi. 2023. Available online: https://rosap.ntl.bts.gov/view/dot/73004 (accessed on 15 December 2023).
38. Rahman, F.; Chakraborty, A.; Khan, S. A Transformative Approach to Stabilize Highway Slope Using Vetiver Grass. In Proceedings of the ASCE Inspire 2023; American Society of Civil Engineers: Arlington, VA, USA, 2023; pp. 537–545.
39. Ng, C.W.W.; Ni, J.J.; Leung, A.K. Effects of plant growth and spacing on soil hydrological changes: A field study. *Géotechnique* **2020**, *70*, 867–881. [CrossRef]
40. Patil, U.D.; Shelton, A.J.; Catahay, M.; Kim, Y.S.; Congress, S.S.C. Role of vegetation in improving the stability of a tropical hill slope in Guam. *Environ. Geotech.* **2022**, *9*, 562–581. [CrossRef]
41. Patil, U.D.; Shelton Iii, A.J.; Aquino, E. Bioengineering Solution to Prevent Rainfall-Induced Slope Failures in Tropical Soil. *Land* **2021**, *10*, 299. [CrossRef]
42. Hu, H.; Fernandez-Steeger, T.M.; Dong, M.; Azzam, R. Numerical modeling of LiDAR-based geological model for landslide analysis. *Autom. Constr.* **2012**, *24*, 184–193. [CrossRef]
43. Truong, P.; Van, T.P.; Pinners, E. *The Vetiver System for Slope Stabilization*, 1st ed.; The Vetiver Network International: Washington, DC, USA, 2008.
44. Wandinger, U. Introduction to LiDAR. In *Lidar: Range-Resolved Optical Remote Sensing of the Atmosphere*; Weitkamp, C., Ed.; Springer Series in Optical Sciences; Springer: New York, NY, USA, 2005; pp. 1–18, ISBN 978-0-387-25101-1.
45. Hata, A.; Wolf, D. Road marking detection using LIDAR reflective intensity data and its application to vehicle localization. In Proceedings of the 17th International IEEE Conference on Intelligent Transportation Systems (ITSC), Qingdao, China, 8–11 October 2014; pp. 584–589.
46. Singh, M.; Guleria, N.; Prakasa Rao, E.V.; Goswami, P. Efficient C sequestration and benefits of medicinal vetiver cropping in tropical regions. *Agron. Sustain. Dev.* **2014**, *34*, 603–607. [CrossRef]

geosciences

MDPI

Article

Exploring the Influence of Climate Change on Earthen Embankments with Expansive Soil

Debayan Ghosh [1], Aritra Banerjee [1,*], Anand J. Puppala [2] and Prince Kumar [2]

[1] Department of Civil and Environmental Engineering, South Dakota State University, Brookings, SD 57007, USA; debayan.ghosh@jacks.sdstate.edu
[2] Zachry Department of Civil and Environmental Engineering, Texas A&M University, College Station, TX 77843, USA; anandp@tamu.edu (A.J.P.); prince.kumar@tamu.edu (P.K.)
* Correspondence: aritra.banerjee@sdstate.edu; Tel.: +1-605-688-4918

Abstract: Climate change is known to cause alterations in weather patterns and disturb the natural equilibrium. Changes in climatic conditions lead to increased environmental stress on embankments, which can result in slope failures. Due to wetting–drying cycles, expansive clayey soil often swells and shrinks, and matric suction is a major factor that controls the behavior. Increased temperature accelerates soil evaporation and drying, which can cause desiccation cracks, while precipitation can rapidly reduce soil shear strength. Desiccated slopes on embankments built with such soils can cause surficial slope failures after intense precipitation. This study used slope stability analysis to quantify how climate-change-induced extreme weather affects embankments. Historic extreme climatic events were used as a baseline to estimate future extremes. CMIP6 provided historical and future climatic data for the study area. An embankment was numerically modeled to evaluate the effect on slope stability due to the precipitation change induced by climate change. Coupled hydro-mechanical finite element analyses used a two-dimensional transient unsaturated seepage model and a limit equilibrium slope stability model. The study found that extreme climatic interactions like precipitation and temperature due to climate change may reduce embankment slope safety. The reduction in the stability of the embankment due to increased precipitation resulting from different greenhouse gas emission scenarios was investigated. The use of unsaturated soil strength and variation of permeability with suction, along with the phase transition of these earthen embankments from near-dry to near-saturated, shows how unsaturated soil mechanics and the hydro-mechanical model can identify climate change issues on critical geotechnical infrastructure.

Keywords: climate change; slope stability; unsaturated soil mechanics; shared socioeconomic pathways; transient seepage; extreme precipitation

Citation: Ghosh, D.; Banerjee, A.; Puppala, A.J.; Kumar, P. Exploring the Influence of Climate Change on Earthen Embankments with Expansive Soil. *Geosciences* **2024**, *14*, 37. https://doi.org/10.3390/geosciences14020037

Academic Editors: Mohamed Shahin and Jesus Martinez-Frias

Received: 16 December 2023
Revised: 26 January 2024
Accepted: 27 January 2024
Published: 30 January 2024

1. Introduction

Embankments and levees are critical infrastructures that are often impacted by storms and hurricanes. Earthen embankments are used primarily as a means of transportation networks and flood defenses. These act as lifelines for mankind as transportation facilities and river training structures and are often the last form of defense against flooding. The failure of such structures due to extreme climatic events can cause societal and economic disruption [1]. Recently, a levee failed on the Pajaro River in central California that had experienced prolonged periods of drought followed by incessant precipitation. This resulted in mass evacuations and flooding, which highlights the need to study the effects of climate change on critical civil infrastructure [2]. Several factors such as surface erosion, softening of the soil, tensile cracking, soil desiccation, and seismicity can contribute to the failure of a slope [3]. Researchers have illustrated that, for soil slopes, the behavior of the deeper layers is governed by the changing water table, while the surface layers are governed by atmospheric conditions [4]. Climate change can cause a negative effect or even a calamitous effect on the stability of the slope as the slopes are continuously exposed to extreme climatic conditions [5]. It was illustrated that the critical parameters for slope stability are the hydraulic properties, including permeability and water retention, which are highly influenced by environmental factors [5].

Expansive soils are prevalent in arid and semiarid regions worldwide, including Australia, Canada, China, India, South Africa, and the United States. These soils generally display a moderate to high ability to be molded, a low to moderate level of strength, and a high tendency to swell and shrink in volume [6,7]. The weathering by-products of limestone material and alluvial deposits in the North Central Texas region result in moderate- to high-plasticity clayey soils. In this region, the montmorillonite-rich Eagle Ford Shale clay from the upper Cretaceous period is expansive in nature [8]. To mitigate the adverse effects of these soils, different rehabilitation strategies have been employed in the region [9–17]. Untreated forms of expansive soils typically undergo high swell–shrink characteristics with a variation in the moisture regime. Desiccation cracking occurs within the plastic fill materials as a result of repeated drying and wetting cycles [18]. The most important deformation phenomenon of unsaturated soils, and especially expansive soils, is swelling or shrinking [19]. The engineering properties of collapsible, residual, compacted, and expansive soils, which are usually in an unsaturated state, can be better understood by considering the impact of matric suction [20]. Expansive soils have high values of swelling and compression indices and are subject to frequent changes in matric suction ($u_a - u_w$), which causes additional volume changes. A structure constructed on expansive soil is subject to heave or settlement depending on moisture suction fluctuations [20]. Hence, it is crucial to consider the influence of matric suction when evaluating slope stability.

Desiccation cracks develop when the soil can no longer withstand the tensile stresses caused by shrinkage [21]. During precipitation, water infiltrates the soil through these cracks. Infiltration elevates the pore water pressure, leading to a subsequent decrease in the shear strength of the soil, which causes failure to occur [22,23]. After prolonged exposure to environmental factors like the wetting–drying cycle, fully softened shear strength eventually develops in clays [24]. Surficial failures may occur abruptly and without warning. At times, they may be accompanied by fissures or other indications of impending failures. A slope demonstrates greater strength in the dry season due to the soil being in an unsaturated state with negative pore water pressure and higher values of matric suction. This can also lead to an overestimation of the factor of safety [25]. Numerous slopes at the desiccated state fail when subjected to intense rainfall due to a decrease in matric suction and an increase in pore water pressures. The impact of climate change may increase the severity and frequency of these issues, which may be modeled by incorporating the climate prediction models in the slope stability analysis. The soil–water characteristic curve establishes the relationship between the volumetric water content of the soil and the matric suction, which, in turn, determines the failure mechanism. The phenomenon is influenced by the flux boundary conditions, specifically rainfall infiltration, evaporation, and evapotranspiration at the interface between the soil and the atmosphere [26]. The increased rainfall can cause failure in earthen structures [27,28]. In addition to the intensity of rainfall, other factors such as the characteristics of rainfall, previous precipitation, soil properties, and topography also play a role in the failure of a slope [29]. This issue becomes amplified when we consider the distress in expansive soils caused by drought-like conditions [17,30,31]. Any drought-like condition followed by intense precipitation can cause severe damage to earthen structures, which are anticipated to be negatively impacted by climate change [31–33]. Figure 1 shows the interaction between climatic conditions and expansive slope and the subsequent formation of desiccation cracks due to shrinkage–swelling, which ultimately leads to surficial failure. Climate change may also affect agricultural productivity through higher soil erosion, which may occur due to higher-intensity storms, floods, and the exposure of deeper layers due to the formation of desiccation cracks in expansive soils during prolonged periods of drought. Therefore, there is an urgent need to study the behavior of embankments when subjected to stresses caused by climate change.

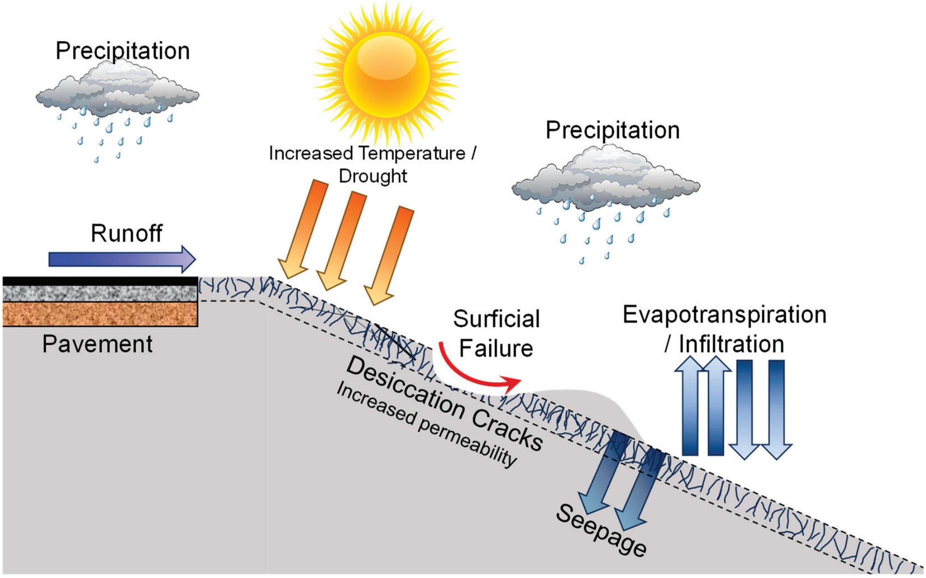

Figure 1. Schematic of climatic interactions with slope and surficial failure.

Incorporating Climate Change Data in Geotechnical Engineering

The advancement in climate and geotechnical modeling has enabled the measurement of the effects of climate change on geotechnical infrastructures. Assessing the impact of climate change on the stability of slopes and embankments involves analyzing three intricate processes: (a) forecasting more detailed future climate data, (b) calculating pore water pressures (PWPs) in slopes caused by changes in variables due to climate conditions, and (c) estimating the factor of the safety of slopes based on the calculated PWPs. Coupled hydro-mechanical finite element analysis can be used for the slope stability analysis of expansive clay embankments. Researchers have used this method to consider the characteristics of expansive clay and the presence of desiccation cracks and found an increase in the saturated coefficient of permeability for the surface layer [34–36].

There are several climate models available to predict future climate scenarios. The CMIP6 (Coupled Model Intercomparison Project Phase 6) presents new global climate model data assessed in the AR6 of the IPCC (Intergovernmental Panel on Climate Change). CMIP6 utilizes shared socioeconomic pathways (SSPs) to simulate different socioeconomic scenarios that may be affected by urbanization, population growth, changes in gross domestic product in different nations, and greenhouse gas (GHG) emissions [37]. The CMIP6 models reveal an approximately 6 °C temperature increase and an increase of 10–30% precipitation over the US under the high emission scenario of SSP5–8.5 by the end of the century, which is considered the extreme scenario [38]. The consideration of the increased intensity and frequency of extreme precipitation due to climate change is an important aspect of the design of future infrastructure as well as the stability analysis of existing infrastructure [2,39]. Robinson et al. (2017) conducted a study to examine how future excessive precipitation will affect landslides in a region close to Seattle, Washington, in the United States [40]. The CMIP5 climate dataset was utilized to generate a collection of current and future intensity–duration–frequency (IDF) curves. Though the analysis focused on a specific emission scenario and intensity duration, the findings of their research suggest that the projected climate conditions in the future may have detrimental consequences for future landslides. Additionally, relying solely on historical climate data in design could result in underestimating the potential risks involved [40]. Researchers have examined the impact of climate change on the stability of embankments [41]. The investigators measured the impact of predicted long-term and extreme precipitation events on the potential instability of sandy and silty highway embankments in southern Ontario, Canada. To conduct their analysis, the researchers employed a two-dimensional (2D) transient variably saturated seepage finite element model to examine pore water pressures. Additionally, they utilized a 2D limit equilibrium slope stability model to assess the stability of the model [41]. The work was conducted using the CMIP5 climate dataset, and the climate data were changed with the introduced shared socioeconomic pathways in CMIP6.

The impact of increased mean precipitation and extreme precipitation events due to climate change on the slope stability of an expansive clay embankment in North Central Texas is presented in this study. To consider the effect of climate change, four general circulation models (GCMs) were considered and compared with the climate normals from the National Oceanic and Atmospheric Administration's National Center for Environmental Information (NOAA NCEI) database. Historical and future precipitation data for 30 years of the location were considered in the study for the climate ensemble. A combination of finite-element-based software, SEEP/W from Geostudio version 2023.1.1, and limit-equilibrium-approach-based software, SLOPE/W from Geostudio version 2023.1.1, was used to quantify the stability of the slope in terms of the factor of safety. The FOS of the embankment slope under baseline and future precipitation was analyzed and compared. The impact of fissures and cracks was assessed by utilizing the soil water characteristic curve (SWCC) and hydraulic conductivity function, which incorporates an elevated saturated coefficient of permeability to accurately simulate the surface layer conditions in the in-situ condition. The study presents a framework to effectively quantify the effect of increased precipitation due to climate change on the existing embankment infrastructure. This study also presents a pioneering study of climatic impact on the short-term failure of embankments of expansive soils using the CMIP6 climate dataset, as most of the assessment of the impact of climate change on existing infrastructure was conducted using the previous CMIP5 dataset.

2. Climate Data

2.1. Historical Climate Dataset

Baseline climate (BC) is considered the datum for the climate change impact assessment for this study. The historical precipitation was used to establish the climate model prediction suitable for the location. The 30 years of precipitation data between 1981 and 2010 were considered in the study as the baseline precipitation. The baseline data for the comparison with four General Circulation Models (GCMs) were collected from the NASA Earth Exchange Global Daily Downscaled Projections (NEX–GDDP) data repository. The observed climate normal data were collected from the NOAA NCEI database for the nearest meteorological station of the study location. The rainfall and mean air temperature data with the daily temporal resolution are shown in Figure 2. The comparison of the average daily rainfall for each month with the observed climate normals was conducted as shown in Table 1. Root-mean-square error (RMSE) is a metric used to evaluate the precision of predicted values in relation to the true value. Regression analysis is a statistical technique used to effectively summarize observed data. The coefficient of determination, also known as the R^2 value, quantifies the degree of correlation between two variables [42]. From Table 1, it could be interpreted that some of the GCMs are better suited for the parameters used for comparison. Though the R^2 value of the data from GFDL ESM4 is not the lowest, it has the lowest root-mean-square error (RMSE) and low average annual precipitation error, whereas the CESM2 dataset has a very high percentage of annual precipitation error. Chai and Draxler (2014) demonstrated the use of RMSE for the comparison of climate models [43]. In this study, the data from the Geophysical Fluid Dynamics Laboratory (GFDL), USA, were selected to predict the future climate data. From the climate data, it can be observed that the average annual precipitation was 903.8 mm for over 30 years.

Daily precipitation of 40 mm or higher is considered a heavy precipitation event in this study. As shown in Figure 2, over 30 years, there were 48 days with 40 mm or more daily precipitation. In September 1999, 74.6 mm of precipitation per day was the highest amount ever recorded in the period.

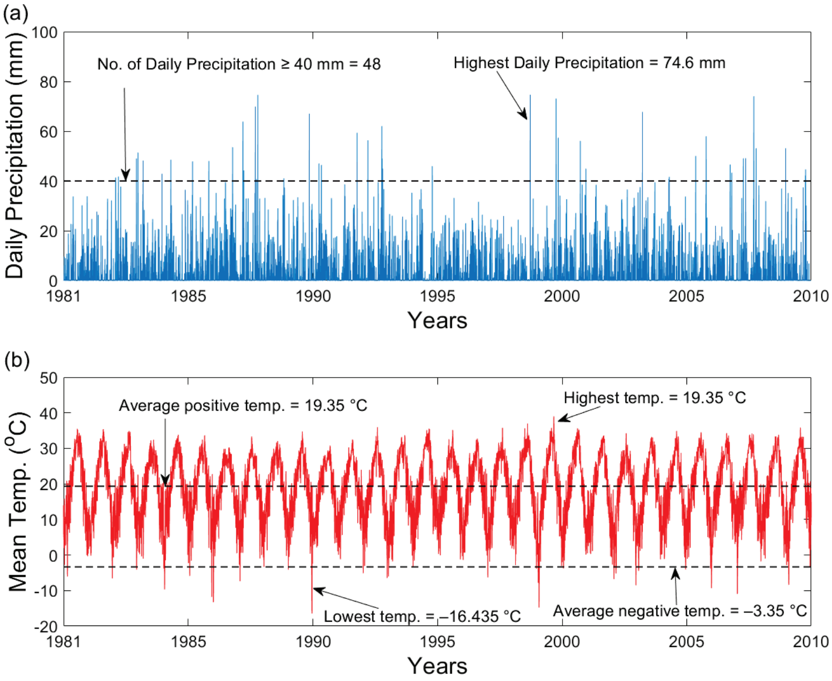

Figure 2. Baseline climatic conditions between 1981 and 2010: (**a**) daily precipitation, (**b**) daily mean temperature.

Table 1. Comparison of different GCMs in relation to baseline climate.

GCM	Modeling Center	RMSE (mm) *	R^2	Percentage Error (Annual)
CESM2	National Center for Atmospheric Research, USA	14.81	0.83	15.26
ACCESS CM2	Australian Community Climate and Earth System Simulator, Australia	13.51	0.73	9.21
GFDL ESM4	Geophysical Fluid Dynamics Laboratory (GFDL), USA	12.68	0.77	8.50
CanESM5	Canadian Centre for Climate Modelling and Analysis, Canada	13.63	0.64	7.69

* RMSE—root-mean-square error.

2.2. Future Climate Dataset

The future climate (FC) data for the site in Texas were collected from the NASA NEX–GDDP [44]. Considering the inherent constraints of climate change models, it is crucial to implement bias adjustment when applying them at the local level. These models, which work at large scales, often fail to accurately capture local climatic variations, leading to systematic inaccuracies or biases. Improving model accuracy by aligning model outputs with observed local climate data through bias correction is essential for making well-informed decisions. Nevertheless, the implementation of this method necessitates prudence in order to prevent the introduction of additional errors. Although bias correction enhances the accuracy of local climate model estimates, it is unable to entirely eradicate all forms of uncertainty [45]. Downscaling techniques are utilized to tackle the low spatial resolution data obtained from Global Climate Models. The NEX GDDP dataset includes downscaled, bias-corrected climate scenarios from the General Circulation Models (GCMs) in 0.25° × 0.25° resolution [45]. The data from the GFDL ESM4 model were collected for SSP2–4.5 and SSP5–8.5 over 2031–2060 and 2071–2100. The 2031–2060 and 2071–2100 years represent the mid-century and end of the century, respectively. The daily precipitation data for these SSPs and periods are shown in Figure 3.

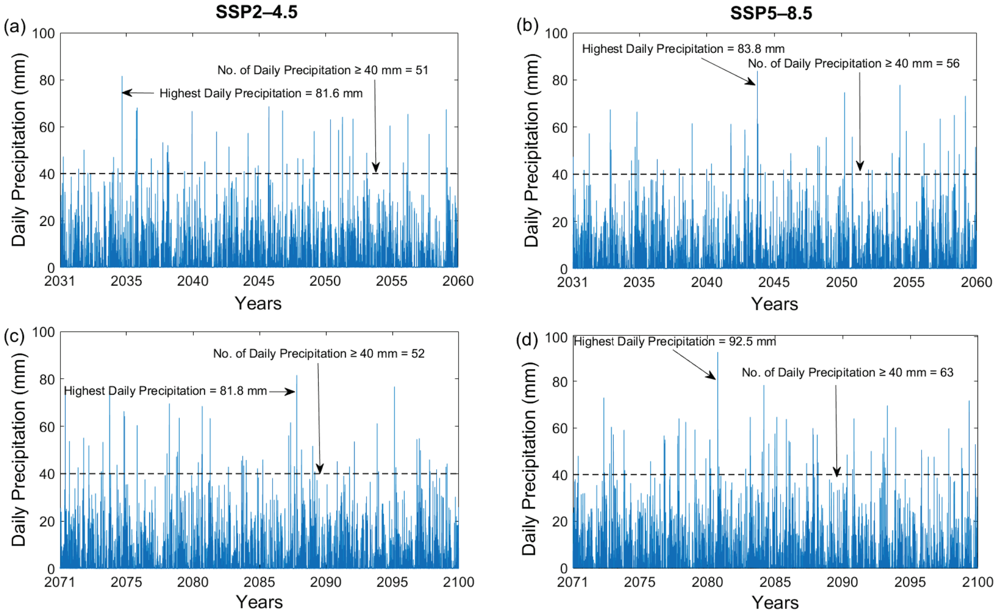

Figure 3. Modeled future daily precipitation from GFDL ESM4 dataset: (**a**) SSP2–4.5 2031–2060, (**b**) SSP5–8.5 2031–2060, (**c**) SSP2–4.5 2071–2100, and (**d**) SSP5–8.5 2071–2100.

As discussed earlier, SSPs are a collection of scenarios created to illustrate possible future changes in human society. SSPs play a crucial role in predicting future levels of greenhouse gas emissions and their effects on climate change. The SSP2 scenario is considered to have moderate challenges to mitigation and adaptation. Environmental systems will undergo degradation, although with some improvements, and there will be an overall decrease in the intensity of resource and energy utilization in SSP2 [46]. The SSP5–8.5 scenario predicts that there will be high levels of greenhouse gas emissions and insufficient efforts to mitigate climate change. SSP5–8.5 may lead to a global temperature increase of 4–6 °C above pre-industrial levels by the end of the century. The scenario also predicts a peak radiative forcing of 8.5 W/m^2 before a subsequent decrease [47]. It can be observed from Figure 3a,c that, for SSP2–4.5, the number of extreme precipitation events does not increase significantly with time.

2.3. Extreme Events

For most of the climate data repository, the data are often limited to daily resolution, but the intensity of precipitation can fluctuate from minutes to hours. The precipitation data resolution for NEX GDDP was daily. The historical extreme precipitation events were compared to the DDF curves to address the effects of the temporal resolution of precipitation and more plausible resolutions were chosen. An intensity–duration–frequency curve was converted to a DDF curve for a selected period [41]. The DDF curve for the embankment location is shown in Figure 4 and was obtained from the National Oceanic and Atmospheric Administration (NOAA) Atlas 14. As the 30-year climatic ensemble is considered for the study, the return period of the extreme precipitation for the highest rainfall is considered to be 30 years and the duration of the event is estimated using the DDF curve.

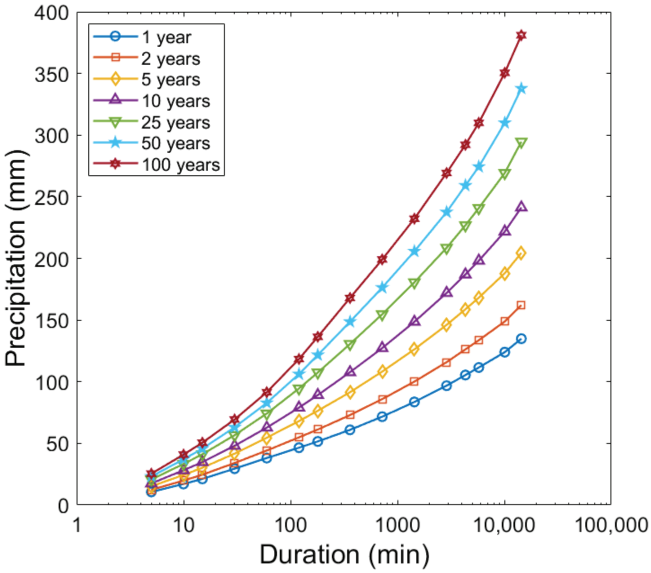

Figure 4. Depth–duration–frequency curves for the site.

3. Numerical Modeling and Analysis

3.1. Soil Properties

Most of the soil data was obtained from various experiments and studies conducted by the authors and their research groups. The SWCC data of the soil are presented in Figure 5. The SWCC was determined using the filter paper method and a chilled mirror hygrometer. The closed-form solution proposed by the Fredlund–Xing (FX) (1994) model was used as shown below to fit the experimental data into the SWCC curve [48]. The hydraulic conductivity and volumetric water content in unsaturated soils are dependent on matric suction. The air entry value (AEV) is the critical suction at which soil starts to lose moisture with increasing desaturation. AEV is dependent on the pore spaces and pore structure within the soil. The AEV of this soil at its maximum dry density was determined to be 10 kPa. The saturated volumetric water content and residual volumetric water content were computed to be 0.441 and 0.08, respectively. The unsaturated hydraulic conductivity of the soil was determined based on experimental studies conducted on a modified suction-controlled permeability setup. The soil sample was maintained at a specific suction state, while the hydraulic conductivity was measured after equilibration. The steps were repeated for different suction levels, and the HCF of the soil used in this study is shown in Figure 6. Table 2 shows the soil properties used in the study. For compacted core soil, shear strength parameters were measured using a direct shear test, and a torsional ring shear test was used for the strength parameters of the surface layer.

$$\theta_w = C(\psi)\theta_s \left[\frac{1}{ln\{e + (\frac{\psi}{a})^n\}} \right]^m \tag{1}$$

where θ_w, θ_s, and θ_r are natural, saturated, and residual volumetric water content, respectively, ψ is matric suction, and a, n, and m are the curve fitting parameters. The hydraulic conductivity function from the data in Figure 6 was fitted using the van Genuchten (1980) model, as shown below [49].

$$K(h) = K_s S_e^l [1 - (1 - S_e^{l/m})^m]^2 \tag{2}$$

where K_s is saturated hydraulic conductivity, l is the pore conductivity parameter, S_e is effective saturation, and m represents the curve fitting parameter. Some of the material properties for this study were collected from experiments conducted in several studies [18,25,50].

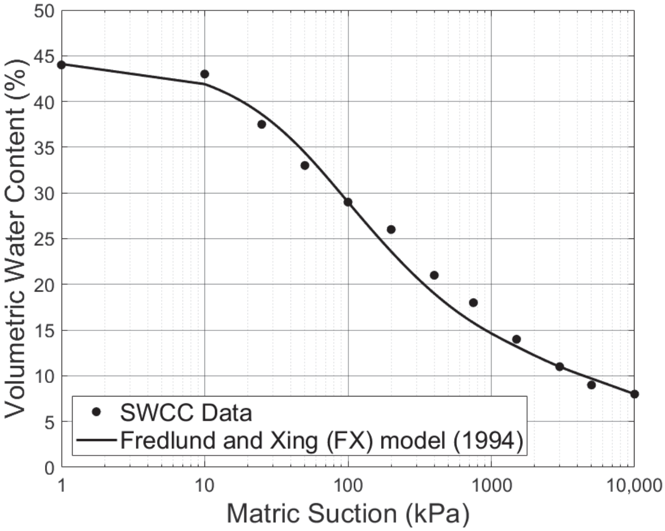

Figure 5. Soil–water characteristics curve of the soil plotted using Fredlund and Xing (1994) model [48].

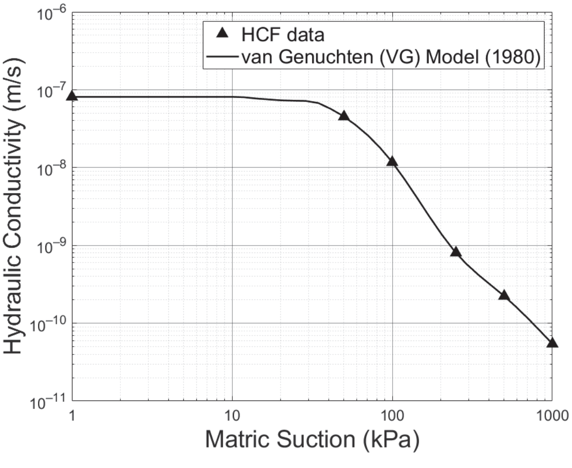

Figure 6. Hydraulic conductivity function of soil plotted using van Genuchten (1980) model [49].

Table 2. Soil properties used in the study.

Region	Soil Property	Value
Compacted fill/Surface layer	Dry unit weight (kN/m^3)	16.5
Compacted fill soil	Saturated Coefficient of Permeability, k_s (m/s)	8.1×10^{-8}
	Cohesion, c (kPa)	38
	Angle of internal friction, φ (°)	17
Surface layer (desiccated soil)	Saturated Coefficient of Permeability, k_s (m/s)	8×10^{-5}
	Cohesion, c (kPa)	0
	Angle of internal friction, φ (°)	27

3.2. Geometry of the Section

In this study, the steepest part of an embankment of expansive soil was considered for analysis. The cross-section of the slope with a steepness of 2.5 H:1 V is shown in Figure 7. The embankment has two parts: compacted fill soil and surface layer. The surface layer thickness of the slope is 1.1 m (3.6 ft). The slope has a height of 8.54 m (28 ft), and the ground water table is situated at 8 m on the right side and 4 m on the left side above the base of the embankment. A mesh convergence study was conducted on the embankment section with a non-fissured surface layer to obtain an optimum mesh size suitable for the study. The change in the factor of safety (FOS) with mesh size was considered. Based on the mesh convergence study, a mesh size of 0.8 m was considered for the analysis. The mesh structure of the embankment is illustrated in Figure 7. For better modeling of the fissured surface layer and estimation of flow through the surface layer, the surface layer of 1.1 m is modeled with four layers of finer mesh. The finite element analysis (FEA) model is scaled up in both the horizontal and vertical dimensions to prevent the influence of boundary conditions. The bottom boundary is considered to be rigid with no permissible movement in either direction, while the two lateral boundaries are free to move only vertically. The desiccated layer is considered for the 3 m wide shoulder provided at the top of the embankment.

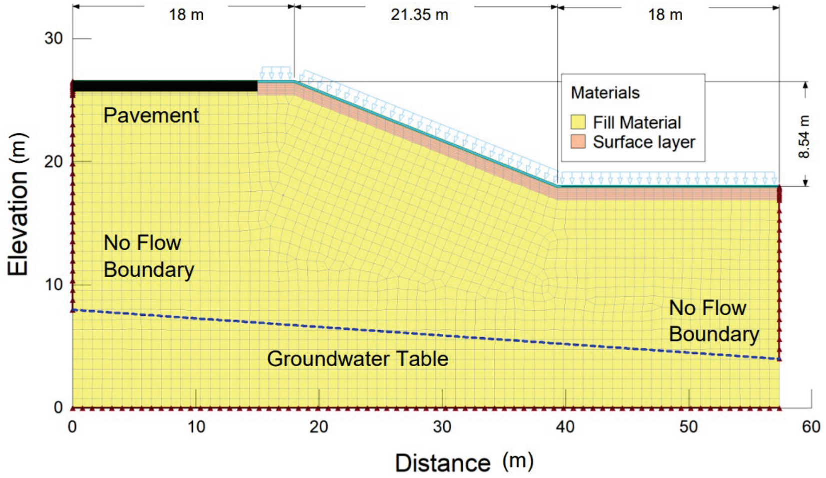

Figure 7. Profile and mesh structure of the embankment.

3.3. Numerical Modeling of Unsaturated Soil and Hydro-Geotechnical Behavior

A finite element transient variably saturated seepage analysis was performed using SEEP/W software to model the temporal and spatial distribution of pore water pressures within the embankments. The soil material model was considered to be in a saturated or unsaturated state to account for all types of soil characteristics. The flow through the soil in both saturated and unsaturated conditions was simulated in Geo-slope GeoStudio SEEP/W 2023.1.1 using Darcy's law. In unsaturated conditions, the changing hydraulic conductivity with matric suction or degree of saturation was considered by using the HCF curve from Figure 6. The partial differential equation that governs the calculation of flux for 2D transient flow is shown below:

$$\frac{\partial}{\partial x}\left(k_x \frac{\partial H}{\partial x}\right) + \frac{\partial}{\partial x}\left(k_y \frac{\partial H}{\partial y}\right) + Q = m_w \gamma_w \frac{\partial H}{\partial t} \tag{3}$$

where H is the total hydraulic head, k_x and k_y are the coefficient of permeability in the x (horizontal) and y (vertical) direction, respectively, Q is the boundary flux, and m_w is the storage curve slope.

In SEEP/W, Richard's (1931) equation was employed to accurately estimate the effect of unsaturated flow. The equation for 2D flow through pores can be written as follows [51]:

$$K\frac{\partial \theta}{\partial t} = \frac{\partial}{\partial x_i}\left[K\left(K_{ij}^{A} \frac{\partial h}{\partial x_i} + K_{iz}^{A}\right)\right] - S \tag{4}$$

where h is the pressure head in the soil, θ is the volumetric water content, S represents the sink term, x_i are the coordinates, K_{ij}^{A} is the anisotropy tensor, and K is the hydraulic conductivity function.

The boundary conditions are illustrated in Figure 7. The flux boundary was used to simulate the rainfall intensity and duration and applied on the slope. The top portion of the slope is impermeable considering the presence of the pavement. No flow boundaries were considered on either the right or left side above the groundwater table, and the base of the profile was considered the no-flow boundary. The flux boundary for the precipitation was considered to be in a non-ponding condition; this prevented the accumulation of rainfall on the slope of the embankment.

At each time step of 0.5 h, SEEP/W simulated the seepage conditions, and that pore water pressure was used for the limit-equilibrium-based software, SLOPE/W 2023.1.1 analysis, which uses the Morgenstern–Price (1965) method to determine the factor of safety (FOS) of the slope [52]. The seepage conditions were imported from SEEP/W using a similar grid technique. The unsaturated shear strength was determined using the GeoStudio SLOPE/W program, which utilizes the extended Mohr–Coulomb failure model. This model provides two methods to incorporate the influence of matric suction on the shear strength of soil. The unsaturated shear strength is determined using two independent stress variables: the net normal stress and the matric suction. The method proposed by Vanapalli et al. (1996) was used to consider the unsaturated shear strength [53]. This method can be expressed as:

$$\tau = c' + (\sigma_n - u_a)\, tan\ \varphi' + (u_a - u_w)\left[\left(\frac{\theta_w - \theta_r}{\theta_s - \theta_r}\right) tan\ \varphi'\right] \tag{5}$$

where τ represents the unsaturated shear strength, c' is the effective cohesion, σ_n represents the total stress, φ' is the effective angle of internal friction, $(\sigma_n - u_a)$ is the net normal stress, and $(u_a - u_w)$ is the matric suction. The strength due to suction was incorporated into the limit equilibrium (LE) method employed by SLOPE/W. The factor of safety from the coupled hydro-geotechnical model obtained through the integration of the FE and LE methods was used as the indicator of the stability of the slope.

4. Results and Discussion

The impact of the changing climate on the embankment was evaluated with a variation of FOS from slope stability analysis conducted by coupled hydro-geotechnical modeling. Precipitation, among all other climatic parameters, has the most short-term destabilizing effect. As the embankment was built with expansive soil, due to swelling–shrinkage properties, desiccation cracks were found to occur. From the field data collected from the literature, the depth of the desiccated layer was 1.1 m. Considering the extreme events and the effect of drought, the coefficient of permeability was considered to be significantly higher by magnitude, as shown in Table 2. Due to rainfall infiltration, the desiccated zone parallel to the slope became saturated. For all cases, the slope was considered to have a desiccated surface.

The FOS results from SLOPE/W for the embankment for historical precipitation are shown in Figure 8. Figures 9 and 10 illustrate FOS with pore water pressure distribution for SSP2 and SSP5, respectively. The reduction in FOS can be seen for FC scenarios compared to the historical climate. Due to the increased precipitation intensity and coefficient of permeability of the surface layer, the FOS decreased further for extreme events. The FOS continuously decreased with the increasing intensity of precipitation, which was due to the reduction in the matric suction. In the "middle of the road" scenario, SSP2, the maximum rainfall intensity and the number of extreme precipitations does not increase significantly from the middle of the century to the end of the century. Thus, the change in FOS for the scenario with time is much less. However, for the higher gas emission scenario, SSP5–8.5, the decrease is significant at the end of the century as the number of extreme precipitation events and maximum daily precipitation both increase, which also increases the duration of future design storms significantly. The reduction in FOS for SSP5–8.5 compared to the historical climate from Figures 8 and 10 was found to be 19.5%. Figure 8 also shows the variation in PWP in the surface layer of the slope for historical precipitation. The higher PWP in the desiccated layer can be observed for extreme precipitation events. From the pore water pressure distributions for extreme events, the accumulation of percolated water between the desiccated layer and the non-desiccated layer can be observed. The intense precipitation and the difference between the coefficient of permeability may be the reason behind this accumulation. From Figures 8–10, it can be observed that with an increase in the intensity of precipitation and duration of the event, the accumulation increased. This may have facilitated the continued surficial failure.

The effect of climate change was estimated using transient seepage and slope stability analysis. The factor of safety of the slope was determined for each step with an interval of 30 min for a 24 h precipitation event. The degradation of FOS with time is shown in Figure 11. The reduction in the matric suction of the soil due to rainfall could have been attributed to the reduction in the stability of the slope.

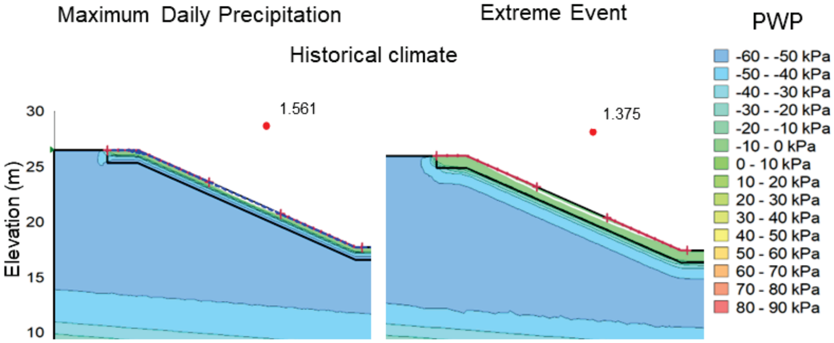

Figure 8. FOS with PWP distribution at the end of the precipitation event for the different scenarios for historical data.

It can be observed that, initially, the FOS was more than 3.5 and the value was stable for the initial hours for every scenario. With time, rainwater permeated further inside the embankment and reduced the matric suction, which eventually decreased the unsaturated shear strength. The intense rainfall generated the high pore water pressure early in the surface layer. The infiltration of rainfall in the desiccated layer caused the rapid degradation of FOS with time, mostly after 12 h of rainfall. The accumulation of water between the two layers discussed earlier could be the reason behind this rapid degradation of the stability of the slope.

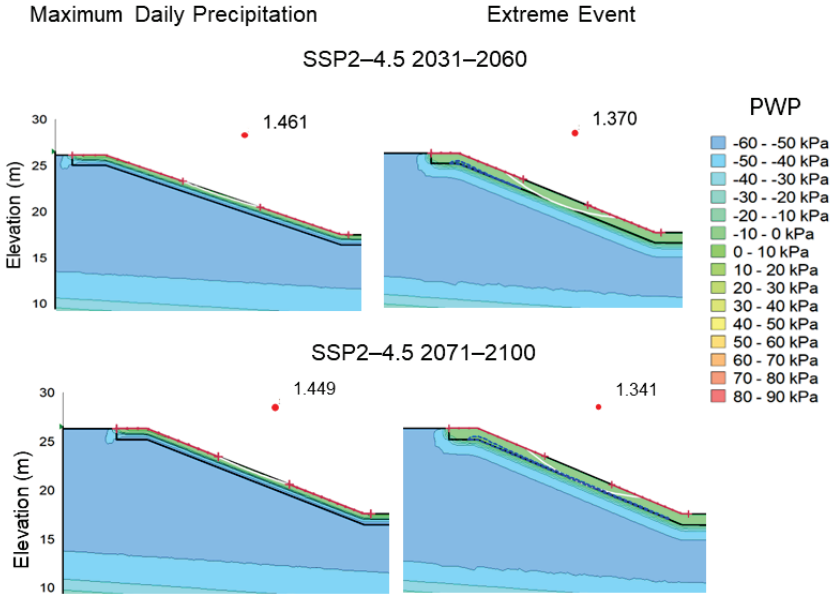

Figure 9. FOS with PWP distribution at the end of the precipitation event for the different scenarios in the future for SSP2–4.5.

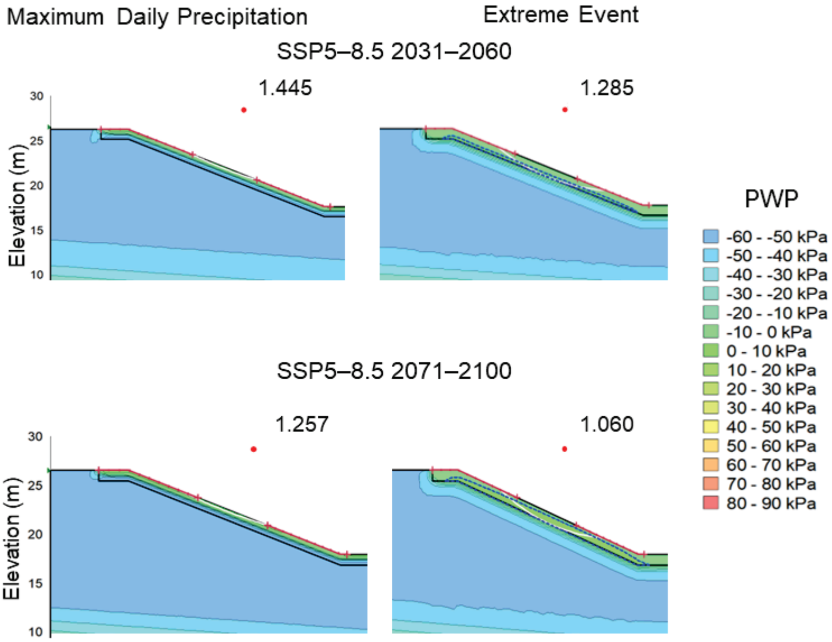

Figure 10. FOS with PWP distribution at the end of the precipitation event for the different scenarios in the future for SSP5–8.5.

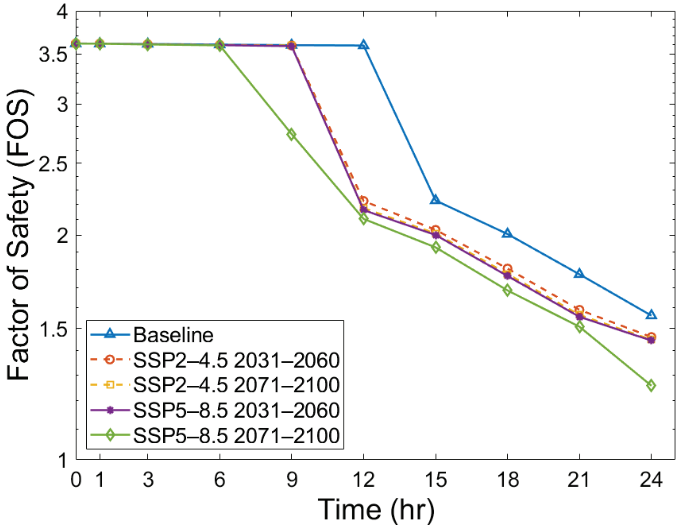

Figure 11. Change in FOS with temporal variations for 24 h precipitation for the baseline and future climate.

5. Conclusions

In this study, the impact of changing climate on the stability of earth embankments built with expansive soil in North Central Texas was numerically analyzed. The main focus of the study was to investigate the effect of the change in precipitation imparted due to climate change and the formation of desiccated layers due to the swell–shrink characteristics of the soil. The important observations of the study are as follows:

- Slopes built with expansive soil tend to form desiccation cracks due to swelling and shrinkage with climatic interactions. In the study, the stability of the slope was found to be reduced due to the formation of the desiccated surface layer.
- A 23% increase in the maximum daily precipitation and a 31.25% increase in the number of extreme precipitation events for SSP5 at the end of the century compared to historical precipitation between 1981 and 2010 was observed. In the future, the intensity of precipitation is predicted to be higher, with shorter intervals between the occurrence of extreme precipitation events.
- The stability analysis of the slope was conducted for two different SSPs: one with moderate greenhouse gas emissions and the other one with extreme GHG emissions with no emission control. The stability of the slope was predicted to be dependent on the greenhouse gas emission scenarios as it directly impacts the number of extreme precipitation events and the amount of daily precipitation.
- For both scenarios, two 30-year periods from the middle and end of the century were considered. With progress in the future, the FOS of the slope was predicted to be lower, and this reduction was significant for the extreme GHG emission scenario. The possibility of surficial failure was predicted to increase significantly for extreme events.

The influence of SSP5, which is an extreme scenario, on the precipitation intensity may be significant enough to induce the surficial surface of slopes with a desiccated top layer for other earthen embankments as well. Additional studies need to be conducted to understand the impact of other parameters such as temperature and solar radiation for different scenarios of climate change to quantify the potential impact of climate change on the resilience of earthen structures in different regions. Subsequently, sustainable measures need to be investigated and implemented to mitigate such issues by the end of the century. The incorporation of thermal and environmental stresses caused by climate change should be considered in the design of new structures, as such change is expected to have a negative impact on earthen infrastructures like dams, levees, and pavements throughout their lifespan.

Author Contributions: Conceptualization, A.B., P.K. and D.G.; methodology, D.G., P.K. and A.B.; software, D.G. and P.K.; formal analysis, D.G.; resources, A.B. and A.J.P.; data curation, D.G.; writing—original draft preparation, D.G.; writing—review and editing, D.G., A.B. and A.J.P.; visualization, D.G. and A.B.; supervision, A.B. and A.J.P.; project administration, A.B.; funding acquisition, A.B. All authors have read and agreed to the published version of the manuscript.

Funding: This research was funded by the US Department of Transportation—University Transportation Consortium (UTC)—Mountain-Plains Consortium (MPC), grant number MPC-687.

Data Availability Statement: All of the relevant data and models used in the study have been provided in the form of figures and tables in the submitted article. The data are also available upon reasonable request.

Acknowledgments: The authors gratefully acknowledge the US Department of Transportation—University Transportation Consortium (UTC)—Mountain-Plains Consortium (MPC), who funded this study. Any findings, conclusions, or recommendations expressed in this study are those of the authors and do not necessarily reflect the views of the funding agency.

Conflicts of Interest: The authors declare no conflict of interest.

References

1. Vardon, P.J. Climatic Influence on Geotechnical Infrastructure: A Review. *Environ. Geotech.* **2015**, *2*, 166–174. [CrossRef]
2. National Research Council. *Abrupt Impacts of Climate Change*; National Academies Press: Washington, DC, USA, 2013; ISBN 978-0-309-28773-9. [CrossRef]
3. Leshchinsky, B.; Vahedifard, F.; Koo, H.B.; Kim, S.H. Yumokjeong Landslide: An Investigation of Progressive Failure of a Hillslope Using the Finite Element Method. *Landslides* **2015**, *12*, 997–1005. [CrossRef]
4. Alonso, E.E.; Gens, A.; Delahaye, C.H. Influence of Rainfall on the Deformation and Stability of a Slope in Overconsolidated Clays: A Case Study. *Hydrogeol. J.* **2003**, *11*, 174–192. [CrossRef]
5. Fredlund, D.G.; Rahardjo, H.; Fredlund, M.D. *Unsaturated Soil Mechanics in Engineering Practice*; John Wiley & Sons, Inc.: Hoboken, NJ, USA, 2012; ISBN 9781118280492.
6. Sherwood, P.T. Effect of Sulfates on Cement- and Lime-Stabilized Soils. *Highw. Res. Board* **1962**, *41*, 98–107.
7. Alonso, E.E.; Romero, E.; Hoffmann, C.; García-Escudero, E. Expansive Bentonite-Sand Mixtures in Cyclic Controlled-Suction Drying and Wetting. *Eng. Geol.* **2005**, *81*, 213–226. [CrossRef]
8. Puppala, A.J.; Punthutaecha, K.; Vanapalli, S.K. Soil-Water Characteristic Curves of Stabilized Expansive Soils. *J. Geotech. Geoenviron. Eng.* **2006**, *132*, 736–751. [CrossRef]
9. He, S.; Yu, X.; Banerjee, A.; Puppala, A.J. Expansive Soil Treatment with Liquid Ionic Soil Stabilizer. *Transp. Res. Rec. J. Transp. Res. Board* **2018**, *2672*, 185–194. [CrossRef]
10. Talluri, N.; Puppala, A.J.; Congress, S.S.C.; Banerjee, A. Experimental Studies and Modeling of High-Sulfate Soil Stabilization. *J. Geotech. Geoenviron. Eng.* **2020**, *146*, 5. [CrossRef]
11. George, A.M.; Banerjee, A.; Puppala, A.J.; Saladhi, M. Performance Evaluation of Geocell-Reinforced Reclaimed Asphalt Pavement (RAP) Bases in Flexible Pavements. *Int. J. Pavement Eng.* **2021**, *22*, 181–191. [CrossRef]
12. Puppala, A.J.; Banerjee, A.; Congress, S.S.C. Geosynthetics in Geo-Infrastructure Applications. In *Durability of Composite Systems*; Reifsnider, K., Ed.; Woodhead Publishing: Sawston, UK, 2020; ISBN 9780128182604. [CrossRef]
13. Khan, M.A.; Biswas, N.; Banerjee, A.; Puppala, A.J. Field Performance of Geocell Reinforced Recycled Asphalt Pavement Base Layer. *Transp. Res. Rec. J. Transp. Res. Board* **2020**, *2674*, 69–80. [CrossRef]
14. Das, J.T.; Banerjee, A.; Puppala, A.J.; Chakraborty, S. Sustainability and Resilience in Pavement Infrastructure: A Unified Assessment Framework. *Environ. Geotech.* **2022**, *9*, 360–372. [CrossRef]
15. Caballero, S.; Acharya, R.; Banerjee, A.; Bheemasetti, T.V.; Puppala, A.; Patil, U. Sustainable Slope Stabilization Using Biopolymer-Reinforced Soil. *Geo-Chicago* **2016**, *2016*, 116–126. [CrossRef]
16. Samuel, R.; Puppala, A.J.; Banerjee, A.; Huang, O.; Radovic, M.; Chakraborty, S. Improvement of Strength and Volume-Change Properties of Expansive Clays with Geopolymer Treatment. *Transp. Res. Rec. J. Transp. Res. Board* **2021**, *2675*, 308–320. [CrossRef]
17. Biswas, N.; Puppala, A.J.; Khan, M.A.; Congress, S.S.C.; Banerjee, A.; Chakraborty, S. Evaluating the Performance of Wicking Geotextile in Providing Drainage for Flexible Pavements Built over Expansive Soils. *Transp. Res. Rec. J. Transp. Res. Board* **2021**, *2675*, 208–221. [CrossRef]
18. Acharya, R.; Pedarla, A.; Bheemasetti, T.V.; Puppala, A.J. Assessment of Guar Gum Biopolymer Treatment Toward Mitigation of Desiccation Cracking on Slopes Built with Expansive Soils. *Transp. Res. Rec. J. Transp. Res. Board* **2017**, *2657*, 78–88. [CrossRef]

19. Banerjee, A. Response of Unsaturated Soils under Monotonic and Dynamic Loading over Moderate Suction States. Ph.D. Thesis, Department of Civil and Environmental Engineering, University of Texas at Arlington, Arlington, TX, USA, 2017.
20. Fredlund, D.G. The 1999 R.M. Hardy Lecture: The Implementation of Unsaturated Soil Mechanics into Geotechnical Engineering. *Can. Geotech. J.* **2000**, *37*, 963–986. [CrossRef]
21. Fredlund, D.G. The Stress State for Expansive Soils. In Proceedings of the 6th International Conference on Expansive Soils, Keynote Address, New Delhi, India, 1–4 December 1987; pp. 1–9.
22. Cho, S.E.; Lee, S.R. Evaluation of Surficial Stability for Homogeneous Slopes Considering Rainfall Characteristics. *J. Geotech. Geoenviron. Eng.* **2002**, *128*, 756–763. [CrossRef]
23. Rahardjo, H.; Lim, T.T.; Chang, M.F.; Fredlund, D.G. Shear Strength Characteristics of a Residual Soil with Suction. *Can. Geotech. J.* **1995**, *32*, 60–77. [CrossRef]
24. Saleh, A.A.; Wright, S.G. *Shear Strength Correlations and Remedial Measure Guidelines for Long-Term Stability of Slopes Constructed of Highly Plastic Clay Soils*; FHWA/TX-98/1435-2F; Texas Department of Transportation: Austin, TX, USA, 1997.
25. McCleskey, L.K.; Puppala, J.A.; Dronamraju, S.V.; Perrin, L. Remedial Measures Planned to Prevent Surficial Failures. *Proc. GeoEdmonton* **2008**, *8*, 21–24.
26. Rahardjo, H.; Ong, T.H.; Rezaur, R.B.; Leong, E.C. Factors Controlling Instability of Homogeneous Soil Slopes under Rainfall. *J. Geotech. Geoenviron. Eng.* **2007**, *133*, 1532–1543. [CrossRef]
27. Vahedifard, F.; Jasim, F.H.; Tracy, F.T.; Abdollahi, M.; Alborzi, A.; AghaKouchak, A. Levee Fragility Behavior under Projected Future Flooding in a Warming Climate. *J. Geotech. Geoenviron. Eng.* **2020**, *146*, 04020139. [CrossRef]
28. Robinson, J.D.; Vahedifard, F. Weakening Mechanisms Imposed on California's Levees under Multiyear Extreme Drought. *Clim. Chang.* **2016**, *137*, 1–14. [CrossRef]
29. Church, M.; Miles, M.J. Meteorological Antecedents to Debris Flow in Southwestern British Columbia; Some Case Studies. In *Reviews in Engineering Geology, Vol. VII—Debris Flows/Avalanches: Process, Recognition, and Mitigation*; Costa, J.E., Wieczorek, G.F., Eds.; Reviews in Engineering Geology; Geological Society of America: Boulder, CO, USA, 1987; Volume 7, pp. 63–80. ISBN 0-8137-4107-6.
30. Banerjee, A.; Puppala, A.J.; Hoyos, L.R.; Likos, W.J.; Patil, U.D. Resilient Modulus of Expansive Soils at High Suction Using Vapor Pressure Control. *Geotech. Test. J.* **2020**, *43*, 3. [CrossRef]
31. Banerjee, A.; Puppala, A.J.; Congress, S.S.C.; Chakraborty, S.; Pedarla, A. Recent Advancements in Predicting the Behavior of Unsaturated and Expansive Soils. In *Lecture Notes in Civil Engineering*; Patel, S., Ed.; Springer: Singapore, 2021; Volume 140, pp. 1–21.
32. Banerjee, A.; Puppala, A.J.; Congress, S.S.C.; Chakraborty, S.; Likos, W.J.; Hoyos, L.R. Variation of Resilient Modulus of Subgrade Soils over a Wide Range of Suction States. *J. Geotech. Geoenviron. Eng.* **2020**, *146*, 9. [CrossRef]
33. Kumar, P.; Banerjee, A.; Chandra, S.S.; Puppala, A.J. Effect of Future Extreme Precipitation on Expansive Soil Embankments. In Proceedings of the IFCEE 2021, Reston, VA, USA, 6 May 2021; American Society of Civil Engineers: Reston, VA, USA; pp. 255–266. [CrossRef]
34. Qi, S.C.; Vanapalli, S.K. Numerical Study on Expansive Soil Slope Stability Considering the Cracks and Coupling Effects. In *Unsaturated Soil Mechanics—From Theory to Practice, Proceedings of the 6th Asia-Pacific Conference on Unsaturated Soils, Guilin, China, 23–26 October 2015*; CRC Press: London, UK, 2015; pp. 621–628. [CrossRef]
35. Yang, R.; Xiao, P.; Qi, S. Analysis of Slope Stability in Unsaturated Expansive Soil: A Case Study. *Front. Earth Sci.* **2019**, *7*, 292. [CrossRef]
36. Qi, S.; Vanapalli, S. Stability Analysis of an Expansive Clay Slope: A Case Study of Infiltration-Induced Shallow Failure of an Embankment in Regina, Canada. *Int. J. Geohazards Environ.* **2015**, *1*, 7–19. [CrossRef]
37. O'Neill, B.C.; Lamarque, J.; Lawrence, D. Developing Climate Model Comparisons. *Eos Trans. Am. Geophys. Union* **2014**, *95*, 462. [CrossRef]
38. Almazroui, M.; Islam, M.N.; Saeed, F.; Saeed, S.; Ismail, M.; Ehsan, M.A.; Diallo, I.; O'Brien, E.; Ashfaq, M.; Martínez-Castro, D.; et al. Projected Changes in Temperature and Precipitation Over the United States, Central America, and the Caribbean in CMIP6 GCMs. *Earth Syst. Environ.* **2021**, *5*, 1–24. [CrossRef]
39. Committee on Adaptation to a Changing Climate. *Adapting Infrastructure and Civil Engineering Practice to a Changing Climate*; Olsen, J.R., Ed.; American Society of Civil Engineers: Reston, VA, USA, 2015; ISBN 9780784479193.
40. Robinson, J.D.; Vahedifard, F.; AghaKouchak, A. Rainfall-Triggered Slope Instabilities under a Changing Climate: Comparative Study Using Historical and Projected Precipitation Extremes. *Can. Geotech. J.* **2017**, *54*, 117–127. [CrossRef]
41. Pk, S.; Bashir, R.; Beddoe, R. Effect of Climate Change on Earthen Embankments in Southern Ontario, Canada. *Environ. Geotech.* **2019**, *8*, 148–169. [CrossRef]
42. Weisberg, S. *Applied Linear Regression*, 3rd ed.; John Wiley & Sons, Inc.: Hoboken, NJ, USA, 2005.
43. Chai, T.; Draxler, R.R. Root Mean Square Error (RMSE) or Mean Absolute Error (MAE)?—Arguments against Avoiding RMSE in the Literature. *Geosci. Model Dev.* **2014**, *7*, 1247–1250. [CrossRef]
44. Thrasher, B.; Wang, W.; Michaelis, A.; Melton, F.; Lee, T.; Nemani, R. NASA Global Daily Downscaled Projections, CMIP6. *Sci. Data* **2022**, *9*, 262. [CrossRef] [PubMed]
45. Giorgi, F.; Gao, X.-J. Regional Earth System Modeling: Review and Future Directions. *Atmos. Ocean. Sci. Lett.* **2018**, *11*, 189–197. [CrossRef]

46. *IPCC Climate Change 2021—The Physical Science Basis*; Cambridge University Press: Cambridge, UK; New York, NY, USA, 2021; ISBN 9781009157896.
47. Richter, I.; Tokinaga, H. An Overview of the Performance of CMIP6 Models in the Tropical Atlantic: Mean State, Variability, and Remote Impacts. *Clim. Dyn.* **2020**, *55*, 2579–2601. [CrossRef]
48. Fredlund, D.G.; Xing, A. Equations for the Soil-Water Characteristic Curve. *Can. Geotech. J.* **1994**, *31*, 521–532. [CrossRef]
49. van Genuchten, M.T. A Closed-Form Equation for Predicting the Hydraulic Conductivity of Unsaturated Soils1. *Soil Sci. Soc. Am. J.* **1980**, *44*, 892. [CrossRef]
50. Dronamraju, V.S. Studies on Field Stabilization Methods to Prevent Surficial Slope Failures of Earthfill Dams. Ph.D. Thesis, Department of Civil and Environmental Engineering, The University of Texas at Arlington, Arlington, TX, USA, 2008.
51. Richards, L.A. Capillary Conduction of Liquids through Porous Mediums. *Physics* **1931**, *1*, 318–333. [CrossRef]
52. Morgenstern, N.R.; Price, V.E. The Analysis of the Stability of General Slip Surfaces. *Géotechnique* **1965**, *15*, 79–93. [CrossRef]
53. Vanapalli, S.K.; Fredlund, D.G.; Pufahl, D.E.; Clifton, A.W. Model for the Prediction of Shear Strength with Respect to Soil Suction. *Can. Geotech. J.* **1996**, *33*, 2. [CrossRef]

geosciences

Article

A Multiphysics Simulation of the Effects of Wicking Geotextile on Mitigating Frost Heave under Cold Region Pavement

Yusheng Jiang [1], Zaid Alajlan [1], Claudia Zapata [2] and Xiong Yu [1,*]

[1] Department of Civil and Environmental Engineering, Case Western Reserve University, 2104 Adelbert Road, Bingham 203C, Cleveland, OH 44106, USA; zzs4@case.edu (Z.A.)
[2] School of Sustainable Engineering and the Built Environment, Ira A. Fulton Schools of Engineering, Arizona State University, Tempe, AZ 85042, USA; czapata@asu.edu
* Correspondence: xxy21@case.edu

Abstract: Geotextile offers numerous benefits in improving pavement performance, including drainage, barrier functionality, filtration, and reinforcement. Wicking geotextile, a novel variant in this category, possesses the intrinsic ability to drain water autonomously from soils. This paper details the development and application of a comprehensive multiphysics model that simulates the performance of wicking geotextile within a pavement system under freezing climates. The model considers the inputs of various environmental dynamics, including the impact of meteorological factors, groundwater levels, ground heat, and drainage on the pavement system. The model was firstly validated using field data from a long-term pavement performance (LTPP) road section in the cold region. It was subsequently applied to assess the impacts of wicking geotextile if it was installed on the road section. The model simulated the coupled temporal and spatial variations in soil moisture content and temperature. The simulation results demonstrated that wicking geotextile would create a suction zone around its installation location to draw water from surrounding soils, therefore reducing the overall unfrozen water content in the pavement. The results also showed that the installation of wicking geotextile would delay the initiation of frost heave and reduce its magnitude in cold region pavement.

Keywords: wicking geotextile; multiphysics modeling; frost heave mitigation; cold region; pavement

Citation: Jiang, Y.; Alajlan, Z.; Zapata, C.; Yu, X. A Multiphysics Simulation of the Effects of Wicking Geotextile on Mitigating Frost Heave under Cold Region Pavement. *Geosciences* **2024**, *14*, 34. https://doi.org/10.3390/geosciences14020034

Academic Editors: Meng Lu and Jesus Martinez-Frias

Received: 8 December 2023
Revised: 19 January 2024
Accepted: 23 January 2024
Published: 28 January 2024

1. Introduction

The base and subgrade materials under pavement usually exhibit varied water content. The variation of moisture content may lead to adverse conditions such as shrinkage, heave, settlement, and fissure on pavement [1–3]. In addition, excessive water in pavement layers can result in a range of pavement distresses, including reduced strength and stiffness of geomaterials, soil particle erosion, freeze-thaw cycles, and durability cracking in concrete [4]. Wicking geotextile, a recent advancement in geosynthetic materials, offers a promising solution to these challenges in pavement structures [5]. Unlike traditional geotextiles, which primarily serve separation, filtration, and reinforcement purposes but offer limited efficacy in water drainage during unsaturated conditions, wicking geotextiles, composed of hydrophilic and hygroscopic nylon fiber yarns, exhibit the capability to laterally drain water in both saturated and unsaturated states [6–8]. The unique microstructure of wicking geotextile, marked by deep grooves with small openings, facilitates a higher capillary force and water transportation efficiency [8,9].

In practical engineering applications, geotextiles are typically installed within or at the base course bottom, extending to road slope surfaces [10]. The extended geotextile ends are exposed to the air to facilitate water evaporation, enhancing the driving force for drainage. In the cross-plane direction, the geotextile impedes upward movement of capillary water, protecting the overlying base course. In the in-plane direction, wicking geotextile absorbs both free and capillary water from surrounding soils and laterally transports it to the extended end [11]. Laboratory tests have affirmed the superior drainage capabilities of wicking geotextiles in reducing soil water content [12–15]. Field tests have also validated the effectiveness of wicking geotextile in mitigating issues associated with water pumping [16], expansive soil [5], and frost heave [8].

The detrimental effects of soil freeze-thaw cycles on pavement, a complex multiphysics process of water transfer and phase transition, are pronounced in cold regions and contribute significantly to pavement damages [11,17–19]. Under freezing temperature, frost heave occurs in soil due to the growth of ice lens and volume expansion of water turning into ice [20], resulting in cracks and uneven surfaces. The subsequent thawing of ice causes local water enrichment, leading to localized soil strength reduction [21,22]. In addition, the ice lens melting can contribute to soil porosity increments with loose structure, therefore giving rise to pavement distresses by thaw settlement [23]. Effective drainage in cold regions is crucial to mitigate the adverse effects of freeze-thaw cycles on soil. Given the moisture control capabilities, wicking geotextile has shown great potential in enhancing pavement performance in these regions, as evidenced in field applications and site monitoring [24,25]. However, the intricacies of the coupled water variation process in pavement influenced by wicking geotextile remain relatively unexplored.

Numerical modeling serves as an effective tool for evaluating the interacted variations of moisture, heat, and stress-strain in unfrozen and frozen soils. While several models have been proposed to investigate these coupled processes, classifiable into thermal-hydro [26–30] models and thermal-hydro-mechanical [31–34] models, research integrating wicking geotextile within multiphysics models remains scarce [10]. This study introduces an advanced coupling model that assimilates various environmental dynamics, including meteorological, geothermal, and hydrological factors, and incorporates wicking geotextile to assess its impact on pavement under diverse environmental conditions. The highly non-linear partial differential equations of the model are solved using COMSOL5.5 (finite element solver). Initially, the model is validated with field data for a pavement case analysis without wicking geotextile. Subsequently, the wicking geotextile is incorporated into the same pavement case to simulate its effects on the frozen soil beneath the pavement.

2. Theoretical Background

The soil temperature and water content variation response to different environmental factors (e.g., ambient temperature, precipitation, solar radiation, etc.) are highly coupled processes in either frozen or unfrozen unsaturated soils. Following energy and mass conservation principles, two partial differential equations (PDE) govern the proposed model and form the theoretical basis of it, from where the water transport and thermal transfer in soil is described.

The transfer of heat in soil is evaluated by Fourier's equation:

$$\mathrm{C_a}\frac{\partial \mathrm{T}}{\partial \mathrm{t}} = \nabla(\lambda\nabla\mathrm{T}) \tag{1}$$

where $\mathrm{C_a}$ represents the apparent volumetric heat capacity in $\mathrm{J/(m^3{\cdot}K)}$, T represents the temperature in K, t represents time, and λ represents thermal conductivity in W(m·K). In Equation (1), $\mathrm{C_a}$ and λ are phases-ratio dependent. To reduce computation nonlinearity, the apparent heat capacity $\mathrm{C_a}$ [35] is taken in the model to consider the energy absorption and release during phase transition by:

$$C_a = C_s\theta_s + C_w\theta_w + C_i\theta_i + C_v(n - \theta_w - \theta_i) - L_f\rho_i\frac{d\theta_i}{dT} \tag{2}$$

where subscripts i, s, w, and v denote ice, soil solid, unfrozen water, and air phase separately; θ is volumetric content of different phases; C is heat capacity of different phases in $\mathrm{J/(m^3{\cdot}K)}$; $\mathrm{L_f}$ is latent heat in J/kg; and ρ_i represents density of ice in $\mathrm{kg/m^3}$. λ is evaluated by

Equation (3) considering the impact of solid soil, liquid moisture, ice, and air on heat transport [28,36,37]:

$$\lambda = \lambda_s^{\theta_s} \lambda_w^{\theta_w} \lambda_i^{\theta_i} \lambda_a^{\theta_a} \tag{3}$$

where the subscripts have same meanings as those of heat capacity in Equation (2).

The mass migration in the partially saturated porous media is evaluated by a modified Richards' equation:

$$\frac{\partial \theta_w}{\partial t} + \frac{\rho_i}{\rho_w}\frac{\partial \theta_i}{\partial t} = \nabla(K_{Lh}\nabla h + K_{Lh} i + K_{LT}\nabla T) \tag{4}$$

where ρ_w denotes the water density in kg/m^3, K_{Lh} and K_{LT} are the hydraulic conductivity related to pore pressure and temperature gradient in m/s, h denotes the matric suction in m (water pressure unit), and i denotes the unit vector along gravity direction.

The soil-water characteristics curve (SWCC) by Van Genuchten [38] is utilized to describe the relationship between unfrozen water content and suction for either unfrozen or frozen soil [39,40]. The hydraulic conductivity in Equation (4) is calculated through Van Genuchten's equations as suggested by [28]:

$$S_e = \frac{\theta - \theta_r}{\theta_s - \theta_r} = \left(1 + |\alpha h|^n\right)^{-m} \tag{5}$$

$$K_{Lh} = K_s S_e^l \left[1 - \left(1 - S_e^{\frac{1}{m}}\right)^m\right] \tag{6}$$

$$K_{LT} = K_{Lh}\left(\frac{hG_{wT}}{\gamma_0}\frac{d\gamma}{dT}\right) \tag{7}$$

$$K_{fLh} = 10^{-\Omega Q} K_{Lh} \tag{8}$$

where S_e represents the effective saturation, θ_r and θ_s denote the residual and saturated water content in percentage, α, m, n, and l are material-specified constants specific to the material as determined by the SWCC, K_s is the saturated hydraulic conductivity measured in m/s, γ signifies the surface tension of soil water in gs^2 varying with temperature and calculated as $\gamma = 75.6 - 0.145\mathrm{T} - 2.38 \times 10^{-4} T^2$ (T is in degC), K_{fLh} refers to the hydraulic conductivity linked to the pore pressure head in frozen soil in m/s accounting for the obstructive effect of ice on moisture movement, Ω is an impedance factor contingent on the type of material, and Q represents the ratio of θ_i to $\theta_i + \theta_s - \theta_r$. Equation (4) determines the volumetric ice content using empirical formulas [41,42]:

$$B(T) = \frac{\theta_i}{\theta_w} = \begin{cases} \frac{\rho_w}{\rho_i}\left(\left|\frac{T}{T_f}\right|^b - 1\right) & (T < T_f) \\ 0 & (T \geq T_f) \end{cases} \tag{9}$$

$$\theta_i = B(T) * \theta_w \tag{10}$$

where B represents the ratio of volumetric ice content to unfrozen water content, T denotes the temperature measured in K, T_f stands for the freezing point in K, and b signifies empirical coefficients related to the soil type with specified values of 0.56 for clay, 0.47 for silt, and 0.61 for sand and gravel.

The proposed model integrates various environmental effects. For the thermal aspect, it considers effects including solar short-wave radiation, upward longwave radiation, air temperature, wind speed, relative humidity, and ground heat flux, which are factored in using Neumann boundary conditions. In the hydraulic domain, the model incorporates the effects of precipitation, evaporation on geotextile, and changes in groundwater elevation, which are addressed through either Neumann or Dirichlet boundary conditions. The absorption of shortwave solar radiation on the structure surface can be described by [43]:

$$q_s = (1 - albedo) * S \tag{11}$$

where q_s denotes the short-wave absorption of the solar radiation, the albedo refers to the solar reflectivity, and S represents the solar radiation in $\mathrm{W/m^2}$. The total long-wave radiation, which encompasses both outgoing radiation and counter-radiation, is evaluated by the Stefan–Boltzmann law [44]:

$$q_l = \epsilon \sigma T_s^4 - \epsilon_a \sigma T_{sky}^4 \tag{12}$$

$$T_{sky} = \left(0.754 + 0.0044 T_{dp}\right)^{0.25} * T_{amb} \tag{13}$$

$$T_{dp} = T_{amb} - \frac{100 - RH}{5} \tag{14}$$

where total q_l represents the long-wave radiation, ϵ signifies the emission coefficient, and ϵ_a denotes the absorption coefficient of pavement. For simplicity in analysis, it is assumed that $\epsilon = \epsilon_a$. The Stefan-Boltzmann constant, σ, is equal to $5.68 * 10^{-8}\ W * m^{-2} * K^{-4}$, T_s is the pavement surface temperature measured in K, T_{sky} is the effective ambient temperature above the structure in K, T_{dp} represents the dewpoint temperature in K at which air becomes saturated when cooled, and RH is relative humidity in percentage. T_{amb} is the ambient air temperature in K. Additionally, as mentioned in Equation (13), the effect of the ambient air temperature, along with wind speed, is also revealed in the convective heat flux on structure surface via Newton's law of cooling [45]:

$$n \cdot (\lambda \nabla T) = h_c (T_{amb} - T) \tag{15}$$

$$\begin{cases} h_c = 5.6 + 4 * v_{wind}\ for\ v_{wind} \leq 5\ \mathrm{m/s} \\ h_c = 7.2 + 4 * v_{wind}^{0.78}\ for\ v_{wind} > 5\ \mathrm{m/s} \end{cases} \tag{16}$$

where n represents the normal unit vector perpendicular to the boundary surface, λ_c denotes the thermal conductivity in W/(m·K), T indicates the temperature at boundaries in K, and h_c is the convection heat transfer coefficient in W/(m^2·K). The ground heat flux is calculated by:

$$q_g = n \cdot \lambda_{botom} \nabla T_{bottom} \tag{17}$$

where λ_{botom} and ∇T_{bottom} are the thermal conductivity in W/(m·K) and temperature gradient in K/m of the material right at bottom boundary, respectively.

In the hydraulic field, Horton's empirical equation [46] is used to evaluate the infiltration capacity as well as infiltration rate via Neumann boundary condition. The GWT is usually located at the interface where the positive and negative pore water pressure is separated with zero water pressure on. Hence, Dirichlet boundary condition is added on the bottom boundary to represent the effect of the equivalent GWT change. The drainage effects of wicking geotextile can be simulated via assigning either Neumann boundary [10] or Dirichlet boundary [7], depending on the geometry assumptions and solving stability. In current studies, a Dirichlet boundary condition is utilized to simulate the evaporation effect on the extended geotextile end.

3. Model Validation

To validate the model, a case analysis is performed for the LTPP section 46-0804. The site measured subgrade gradation, water content, and temperature data, all of which indicated that the soil below the section is frost susceptible. In addition, the SMP database has well-documented site-measured time series data of climate, temperature, and moisture content of this section, hence its selection for the case analysis. The case study first verifies the proposed model for the pavement without geotextile, then it simulates the installation of geotextile in the same pavement system to study the effect of the wicking geotextile. The filed data are collected from SMP database. The geometry of the pavement is shown in Figure 1, which includes a three-layer structure in a two-dimensional form. The detailed layer information is summarized in Table 1.

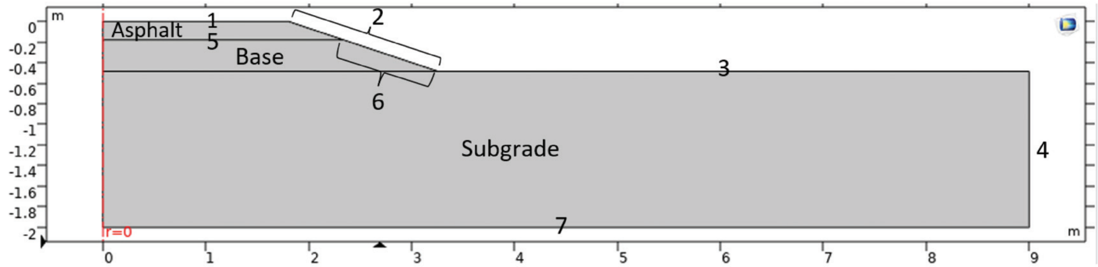

Figure 1. Geometry of the three-layer pavement system without geotextile.

Table 1. Layer information.

Layer #	Material	Thickness (m)
3	Asphalt concrete: hot mixed, hot laid AC, dense graded	0.180
2	Unbound (granular) base: crushed stone	0.305
1	Subgrade (untreated): fine-grained soils: silty clay	1.515

The analysis includes boundary conditions for various environmental factors, assessing the impacts of air temperature, solar short-wave radiation, precipitation, wind velocity, relative humidity, geothermal temperature gradient, and groundwater table elevation. To model the energy transfer between the atmosphere and the pavement surface, the upper three boundaries (boundaries one to three, as shown in Figure 1) are subjected to fluxes from short-wave radiation, long-wave radiation, and air convection. The temperature gradient at the lower boundary is calculated using temperature measurements taken near a depth of two meters, as shown in Figure 2c. This measurement facilitates the calculation of time-varying geothermal flux. The geothermal influence is incorporated by applying a Neumann boundary condition at boundary seven using this flux. Considering the low rainfall intensity and relative high soil permeability, the infiltration capacity is presumed to always exceed rainfall intensity, implying that water flux due to precipitation is the same as the rainfall intensity in the analyzed case. This precipitation flux is applied to boundaries three, five, and six. The GWT effects are simulated by assigning pressure head (Dirichlet boundary) to boundary seven. The right boundary (boundary four in Figure 1) is assumed to be both thermally and hydraulically insulated.

For the model verification case, a 220-day analysis was conducted starting from 1 September 2000 and ending 15 March 2001. The temporal variation of air temperature, precipitation, solar short-wave radiation, wind speed, and relative humidity are shown in Figure 2.

Table 2 presents the simulation's needed parameters, including the parameters of geotextile, pavement surface material, and soil layers. These parameters are found or calculated using site measured data from the LTPP database and literature [7,34,47]. The SWCC and hydraulic conductivity variation with suction of base, subgrade, and wicking geotextile are presented in Figure 3 with data from [7].

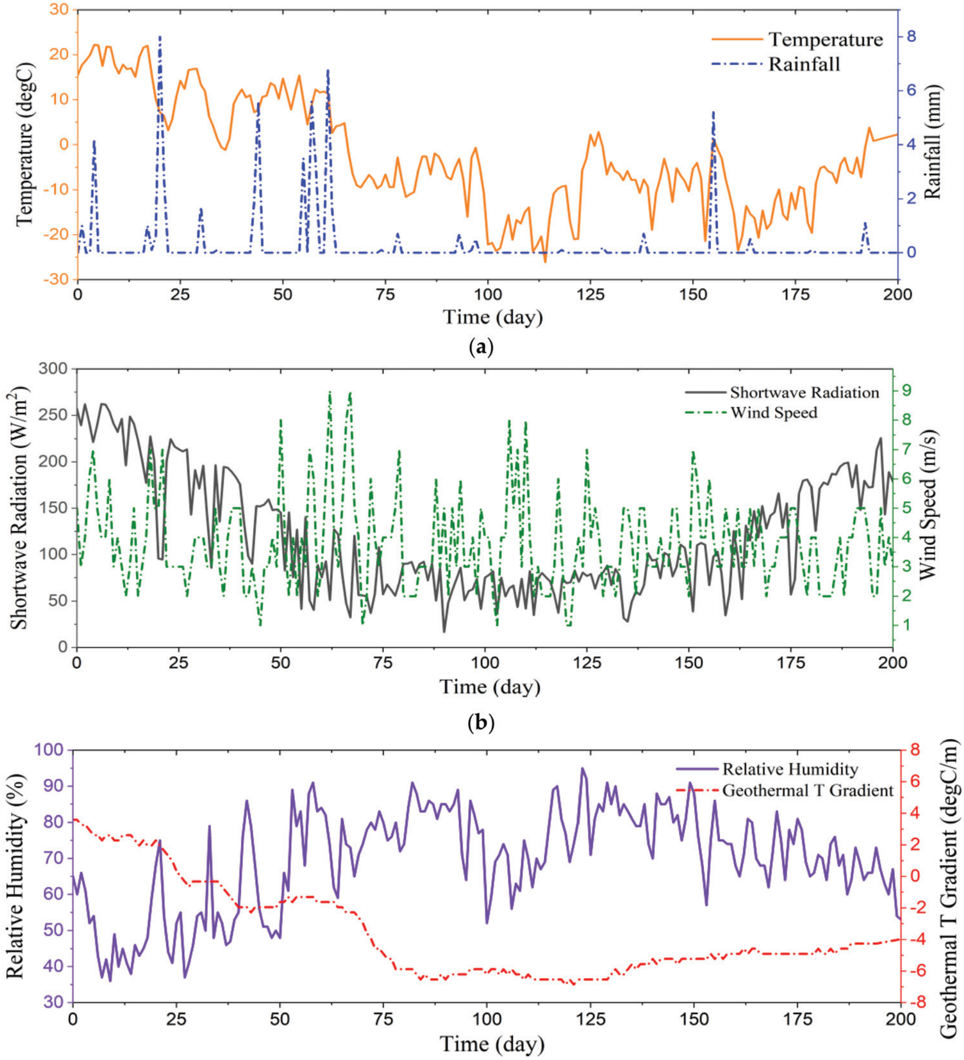

(a)

(b)

(c)

Figure 2. Temporal changes in climatic and environmental factors from 1 September 2000 to 15 March 2001: (**a**) air temperature and precipitation, (**b**) solar short-wave radiation and wind velocity, and (**c**) relative humidity and temperature gradient related to geothermal heat.

Table 2. Constant parameters of calculation example.

Symbol	Value (Unit)	Description
C_i	1.9×10^6 [J/(m^3*K)]	Volumetric heat capacity of ice
C_n	2.0×10^6 [J/(m^3*K)]	Volumetric heat capacity of solid
C_v	1.2×10^3 [J/(m^3*K)]	Volumetric heat capacity of air
C_w	4.2×10^6 [J/(m^3*K)]	Volumetric heat capacity of liquid
C_{pp}	2.3×10^6 [J/(m^3*K)]	Heat capacity of pavement surface layer
λ_p	1.1 [W/(m*K)]	Heat conductivity of pavement surface layer
L_f	3.3×10^5 [J/kg]	Freezing latent heat

Table 2. *Cont.*

Symbol	Value (Unit)	Description
L_0	3.3×10^8 [J/m^3]	Volumetric freezing latent heat
γ_0	71.9 [g/s^2]	Surface tension of soil water at 25° Celsius
ρ_i	931 [kg/m^3]	Density of ice
ρ_n	2700 [kg/m^3]	Density of soil mass
ρ_w	1000 [kg/m^3]	Density of water
g	9.8 [m/s^2]	Acceleration due to gravity
K_{s1}	1.3×10^{-3} [m/s]	Saturated hydraulic conductivity of base
K_{s2}	1.1×10^{-7} [m/s]	Saturated hydraulic conductivity of subgrade
K_{sw}	0.001 [m/s]	Saturated hydraulic conductivity of geotextile
θ_{s1}	0.36	Saturated volumetric moisture content of base
θ_{s2}	0.50	Saturated volumetric moisture content of subgrade
θ_{sw}	0.33	Saturated volumetric moisture content of geotextile
θ_{r1}	0.075	Residual volumetric moisture content of base
θ_{r2}	0.01	Residual volumetric moisture content of subgrade
θ_{rw}	0.04	Residual volumetric moisture content of geotextile
ϵ_a	0.95	Absorption coefficient on pavement surface
ϵ	0.95	Emission coefficient on pavement surface
albedo	0.22	Solar reflectivity

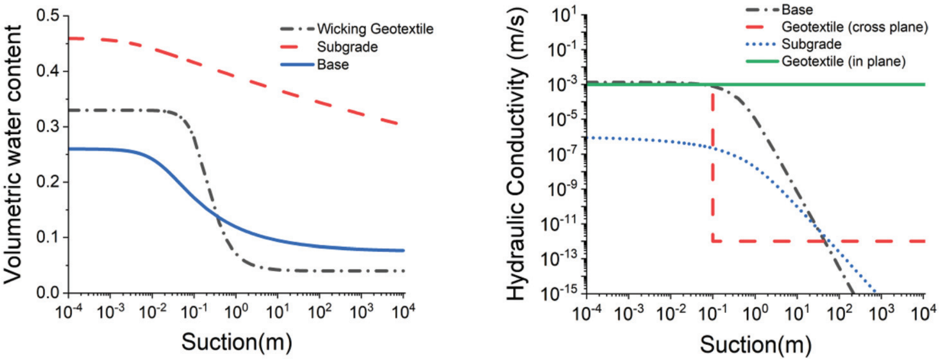

(**a**) (**b**)

Figure 3. (**a**) SWCC of base, subgrade, and wicking geotextile, (**b**) hydraulic conductivity vs. suction of base, subgrade, and wicking geotextile.

The temperature, water content, and frost depth variation with depth and time are calculated by the proposed model. The results are compared with site-monitored data as shown in Figures 4–6, which shows closely matched values. This validates the model's performance to simulate the thermal and hydraulic filed response of soil to environmental dynamics for the analyzed case. More detailed information about model validations can be found in [19].

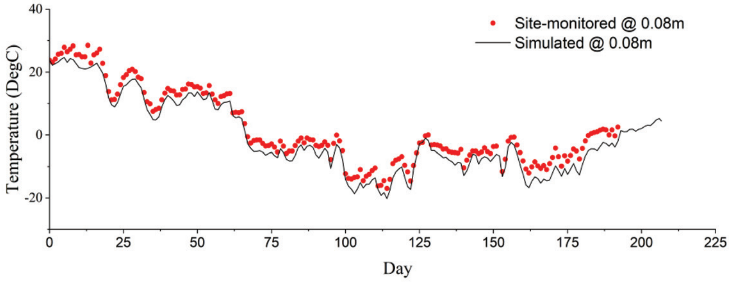

(**a**)

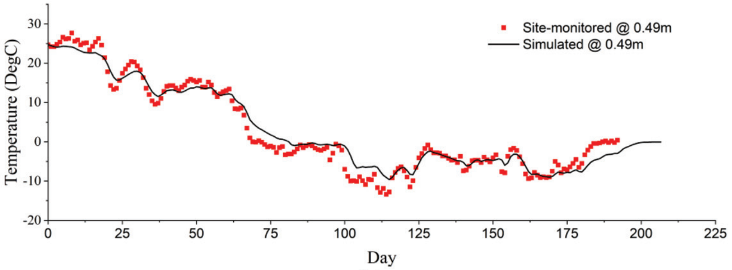

(**b**)

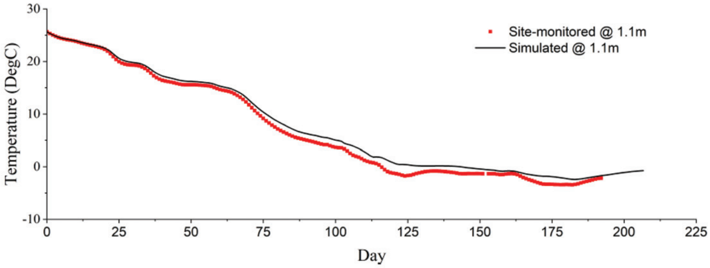

(**c**)

Figure 4. Comparison of simulated and actual temperatures over time: (**a**) at a depth of 0.08 m in asphalt layer, (**b**) at a depth of 0.49 m in base layer, and (**c**) at a depth of 1.1 m in subgrade layer (along the axis of symmetry of the pavement).

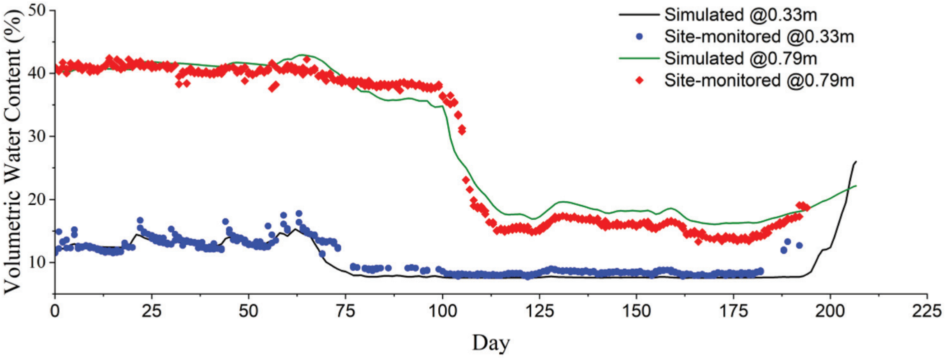

Figure 5. Comparison of simulated and actual temperatures over time at depth of 0.33 m in base layer and 0.79 m in subgrade layer (along the axis of symmetry of the pavement).

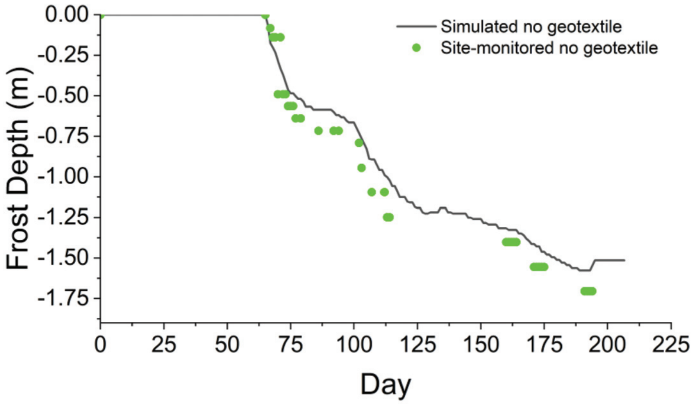

Figure 6. Simulated and site-measured frost depth (below pavement slope top) vs. time.

4. The Effects of Wicking Geotextile on Frost Heave Mitigation

Based on the verified case, a model with wicking geotextile is then simulated. Identified boundary conditions, layer parameters, and model settings are simulated as the validation case study is utilized. In this model, the geotextile is simplified as a domain layer that is three centimeters thick, as shown in Figure 7. A 6.6 m length geotextile is assumed to be buried at a depth −1.5 m from the pavement surface and on the interface between the base and the subgrade layer. Referring to [7], to simulate the drainage effect of the evaporation on the wicking geotextile end, a constant pressure head of 200 kPa boundary is added on the right end of the geotextile layer (a Dirichlet line boundary). Figure 8 shows the simulated suction and water flow direction comparison between pavement with and without geotextile, where results of time at the start of simulation (first day) and after a rainfall event (twenty-fifth day) are presented. The black arrows in Figure 8 point out the direction of water flow. As shown in Figure 8, the wicking geotextile can influence the suction distribution apparently. Figure 8b,d show obvious higher suction in zones along the geotextile, reflecting the pumping effects. The arrow direction indicates the water in surrounding soils are absorbed and flow toward the wicking geotextile. The zoomed-in figure displays the simulated unfrozen water migration direction inside of the geotextile, where the unfrozen water transport horizontally and drained out to the right side.

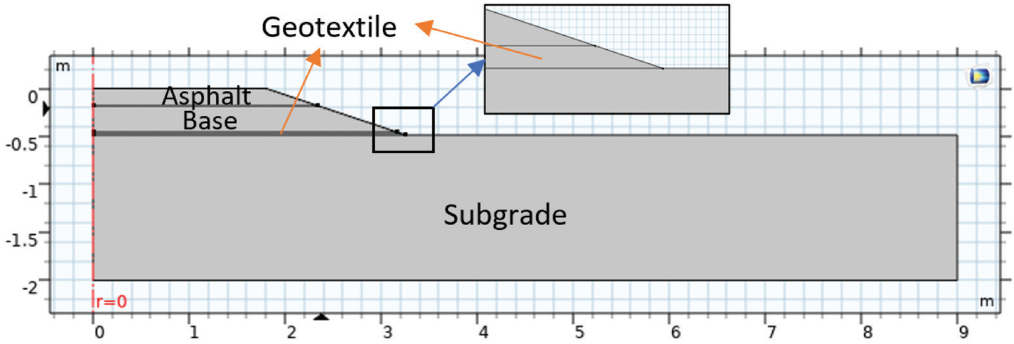

Figure 7. Geometry of the three-layer pavement system with geotextile.

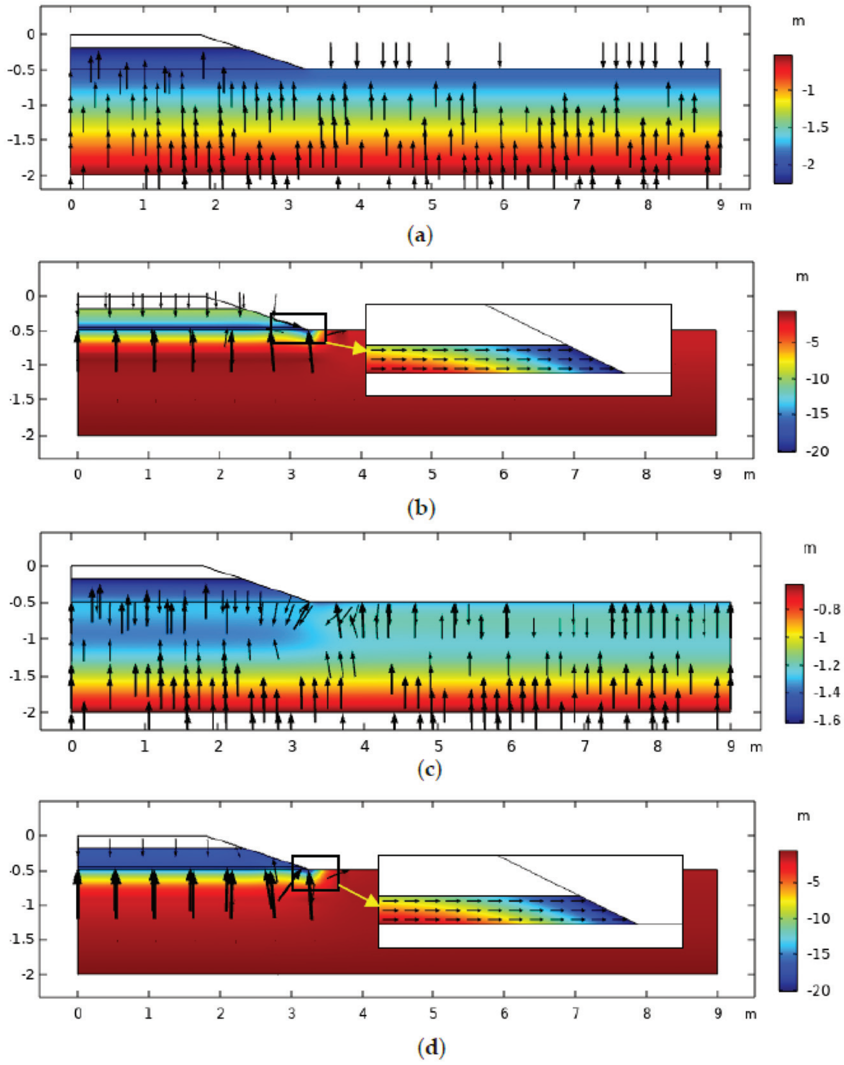

Figure 8. Simulated suction (pressure in m water) distribution and water flow direction on: (**a**) first day without geotextile, (**b**) first day with geotextile, (**c**) twentieth day without geotextile, and (**d**) twentieth day with geotextile.

Figure 9 shows the moisture content variation comparison between the pavement with and without geotextile. According to results of Figure 9, the wicking geotextile effectively decreases water content from the start of the simulation at both 0.33 m depth and 0.79 m depth. The obvious drop of water content around the 70th day at 0.33 m and the 100th day at 0.79 m are induced by water freezing. Note that Figures 5 and 9 merely present unfrozen water content and the TDR sensor only recorded unfrozen water content in the LTPP database. The expanded volumetric content is defined as the total volumetric water content (summation of volumetric unfrozen water content and ice content) during freezing minus the porosity of the soil. Assuming the frost heave occurred when the total volumetric water content exceeds the porosity, frost heave can be evaluated by integration of the expanded volumetric content along vertical direction. Based on the model-simulated volumetric unfrozen and frozen water content, the frost heave along the pavement center line is estimated and compared in Figure 10. As indicated in Figure 10, the geotextile delays the time of frost heave initiation and mitigates the magnitude of frost heave with time.

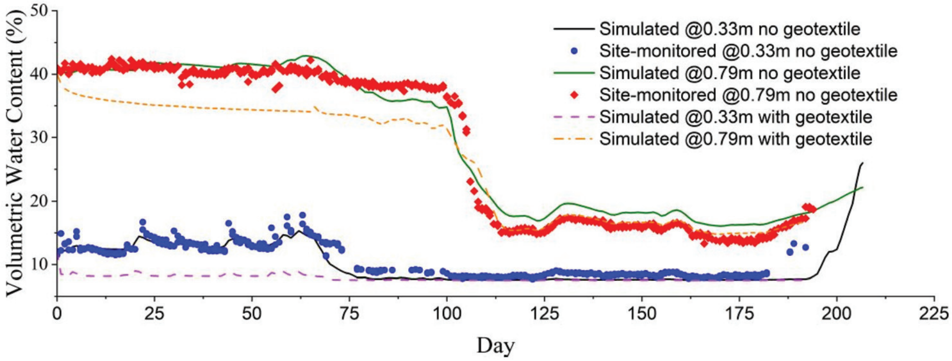

Figure 9. Water content vs. time at 0.33 m and 0.97 m depth, with and without geotextile.

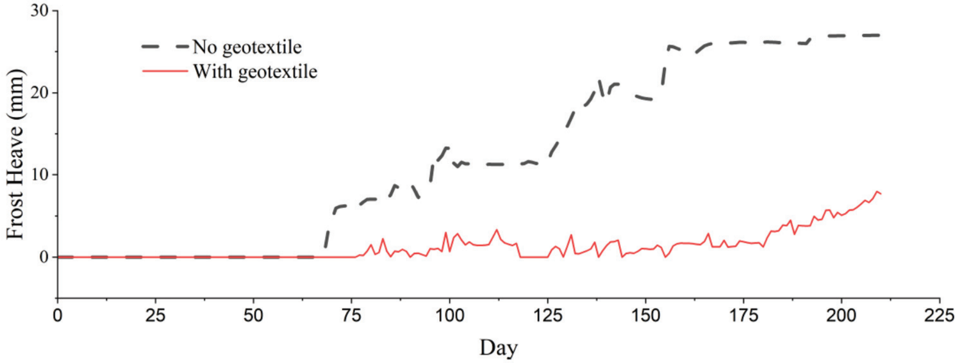

Figure 10. Frost heave (along pavement axis of symmetry) without geotextile installation and with geotextile installation.

According to the simulated results, it is interesting to note that geotextile has inappreciable effect on frost depth. Figure 11 shows the freezing conditions on the 80th day. It classifies the pavement into a frozen zone (with red color) and an unfrozen zone (with blue color) based on the freezing temperature of pore soil water. As seen in Figure 11, the wicking geotextile has barely any impact on frost depth distribution in pavement and ground. Although the wicking geotextile removes the soil water from the subgrade (Figure 9) and decreases the heat capacity, the induced larger volumetric air content decreases the soil thermal conductivity at the same time. As a result, the ground freezing speed does not change greatly, and frost depth is not significantly influenced. This conclusion can also be supported by Figure 12, which displays the frost depth vs. time, with and without geotextile.

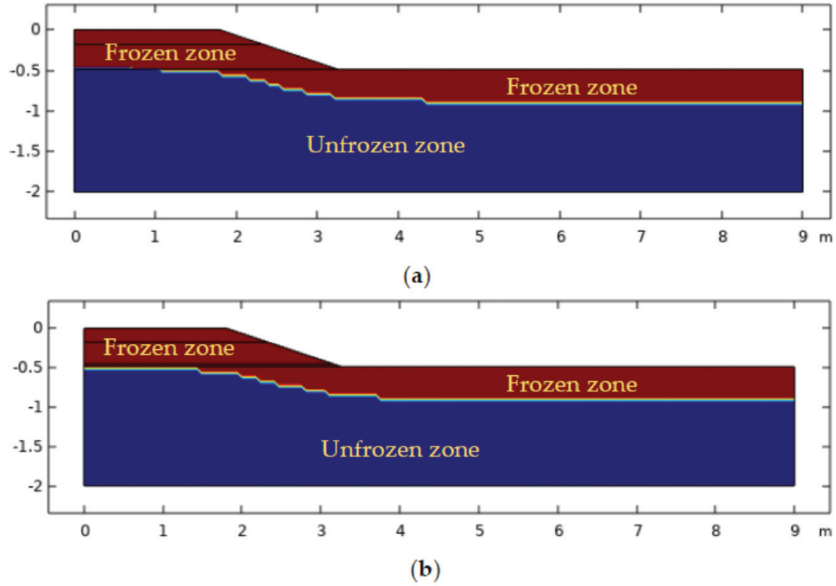

Figure 11. Frost depth spatial distribution comparison between (**a**) without geotextile installation and (**b**) with geotextile installation on the 80th day in simulation.

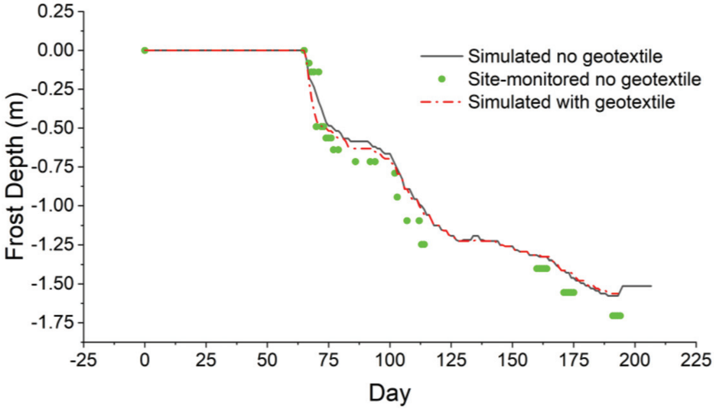

Figure 12. Frost depth (below pavement slope top) vs. time, with and without geotextile.

The simulated temperature variations over time, both with and without the geotextile, are compared at various depths of each pavement layer. As depicted in Figure 13, the simulations reveal that the wicking geotextile exerts a negligible influence on temperature fluctuations over time. This observation aligns with the findings presented in Figures 11 and 12. A marginal decrease in temperature was noted between the 62nd and the 112nd days in the presence of the geotextile. This slight temperature reduction is likely attributable to the diminished release of latent heat, which is a consequence of water drainage facilitated by the geotextile.

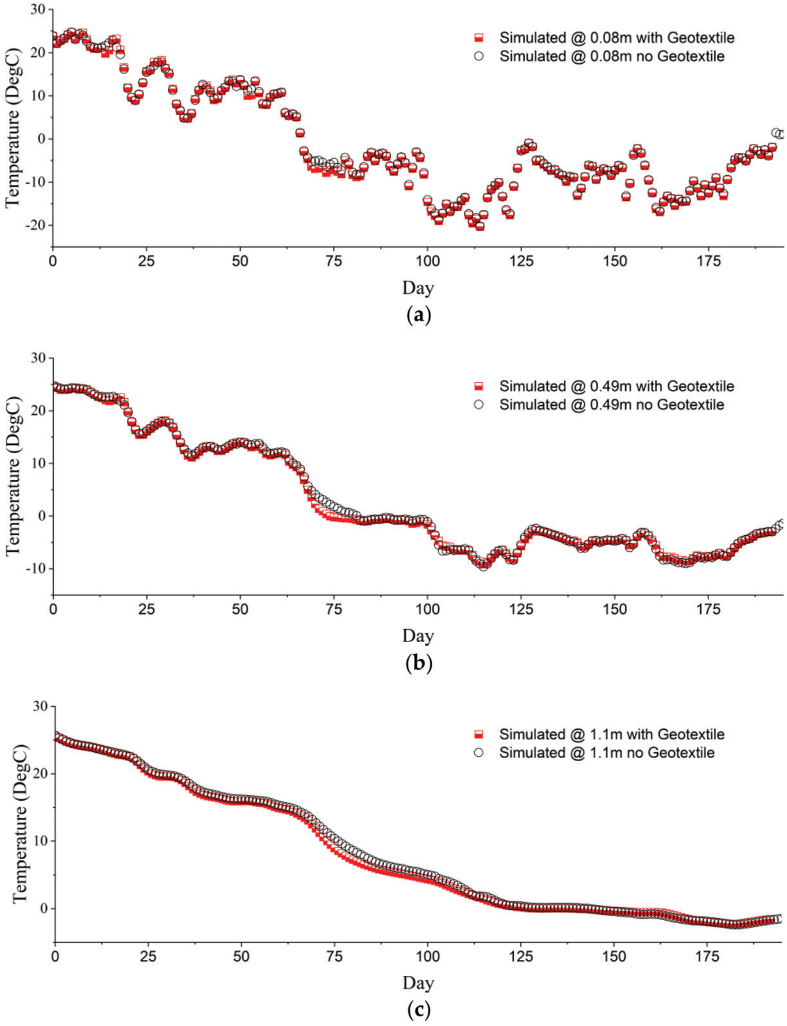

Figure 13. Simulated temperatures vs. time: (**a**) at 0.08 m in asphalt layer, (**b**) at 0.49 m in base layer, and (**c**) at 1.1 m in subgrade layer (along pavement axis of symmetry).

5. Conclusions

An advanced coupled model was developed to analyze pavements subjected to freezing climates. The model captures the coupled thermo-hydro processes within unsaturated frozen soils under pavement structure, and also accounts for environmental factors, including short-wave radiation, upward longwave radiation, air temperature, wind speed, relative humidity, ground heat flux, precipitation, ground water table (GWT), and evaporation. The accuracy of the model is validated by comparing the simulated temperature and moisture profiles with field data collected on the LTTP road section. The results confirmed its accuracy to provide comprehensive simulations of pavement structural responses to cold region climate considering unsaturated frozen soils.

The validated model was further applied to analyze the effects of wicking geotextile. The simulation results revealed that the wicking geotextile facilitated water absorption and drainage, and consequently changed water content (or suction) distributions in the surrounding soils. In addition, the simulation results indicate that wicking geotextile delayed the onset of frost heave as well as reduced the magnitude of frost heave. While wicking geotextile reduces the liquid water contents and hence reduces the overall heat capacity, the simulation does not show apparent change of frost depth in the pavement. This might be due to the lower thermal conductivity induced by the replacement of water with air in the soil. Overall, the various effects of wicking geotextile on cold region pavements are simulated under various environmental dynamics using the comprehensive numerical model. This model provides a tool to temporally and spatially quantify the thermal-hydraulic processes induced by the wicking geotextile. The results of the simulations can serve as the bases for a more thorough and constructive guide for construction practices.

Author Contributions: Conceptualization, Y.J. and Z.A.; methodology, Y.J., Z.A., C.Z. and X.Y.; formal analysis, Y.J.; literature review, Z.A. and Y.J.; data acquisition, Y.J.; writing—original draft preparation, Y.J., Z.A. and X.Y.; writing—review and editing, Y.J., Z.A., C.Z. and X.Y. All authors have read and agreed to the published version of the manuscript.

Funding: This research was partially supported by the National Science Foundation (1638320) and National Cooperative Highway Research Program (01-59). This work is based in part of research funded by the National Academies of Science, Engineering, and Medicine Transportation Research Board's (TRB) National Cooperative Highway Research Program (NCHRP) Project 01-59. The opinions, conclusions, and interpretations are those of the authors and not necessarily of NCHRP.

Data Availability Statement: The LTPP pavement data are available free of charge from the LTPP database. The simulation data are contained within the article and are free to use.

Conflicts of Interest: The authors declare no conflicts of interest.

References

1. Mukhopadhyay, A.; Ye, D.; Zollinger, D. *Moisture-Related Cracking Effects on Hydrating Concrete Pavement*; Texas Transportation Institute, Texas A & M University System: College State, TX, USA, 2006; Volume 7.
2. Puppala, A.J.; Manosuthkij, T.; Nazarian, S.; Hoyos, L.R. Threshold Moisture Content and Matric Suction Potentials in Expansive Clays Prior to Initiation of Cracking in Pavements. *Can. Geotech. J.* **2011**, *48*, 519–531. [CrossRef]
3. Dong, S.; Jiang, Y.; Yu, X. A Novel Random Finite Element Model for Holistically Modeling of the Frost Effects on Soils and Cold Region Pavements. *J. Infrastruct. Preserv. Resil.* **2022**, *3*, 16. [CrossRef]
4. Liu, H.; Han, J.; Al-Naddaf, M.; Parsons, R.L.; Kakrasul, J.I. Field Monitoring of Wicking Geotextile to Reduce Soil Moisture under a Concrete Pavement Subjected to Precipitations and Temperature Variations. *Geotext. Geomembr.* **2022**, *50*, 1004–1019. [CrossRef]
5. Biswas, N.; Puppala, A.J.; Khan, M.A.; Congress, S.S.C.; Banerjee, A.; Chakraborty, S. Evaluating the Performance of Wicking Geotextile in Providing Drainage for Flexible Pavements Built over Expansive Soils. *Transp. Res. Rec.* **2021**, *2675*, 208–221. [CrossRef]
6. Guo, J.; Han, J.; Zhang, X.; Li, Z. Experimental Evaluation of Wicking Geotextile-Stabilized Aggregate Bases over Subgrade under Rainfall Simulation and Cyclic Loading. *Geotext. Geomembr.* **2021**, *49*, 1550–1564. [CrossRef]
7. Lin, C.; Zhang, X.; Galinmoghadam, J.; Guo, Y. Working Mechanism of a New Wicking Geotextile in Roadway Applications: A Numerical Study. *Geotext. Geomembr.* **2022**, *50*, 323–336. [CrossRef]
8. Zornberg, J.G.; Azevedo, M.; Sikkema, M.; Odgers, B. Geosynthetics with Enhanced Lateral Drainage Capabilities in Roadway Systems. *Transp. Geotech.* **2017**, *12*, 85–100. [CrossRef]
9. Lin, C.; Galinmoghadam, J.; Han, J.; Liu, J.; Zhang, X. Quantifying and Incorporating the Benefits of Wicking Geotextile into Pavement Design. *J. Transp. Eng. Part B Pavements* **2021**, *147*, 04021044. [CrossRef]
10. Wu, Y.; Ishikawa, T.; Maruyama, K.; Ueno, C.; Yasuoka, T.; Okuda, S. Modeling Wicking Fabric Inhibition Effect on Frost Heave. *Appl. Sci.* **2022**, *12*, 4357. [CrossRef]
11. Wu, Y. Effect Verification of Wicking Fabric on Inhibition to Frost Heave at Cold Region Pavement. Ph.D. Thesis, Hokkaido University Sapporo, Sapporo, Japan, 2022.
12. Guo, J.; Wang, F.; Zhang, X.; Han, J. Quantifying Water Removal Rate of a Wicking Geotextile under Controlled Temperature and Relative Humidity. *J. Mater. Civ. Eng.* **2017**, *29*, 04016181. [CrossRef]
13. Wang, F.; Han, J.; Zhang, X.; Guo, J. Laboratory Tests to Evaluate Effectiveness of Wicking Geotextile in Soil Moisture Reduction. *Geotext. Geomembr.* **2017**, *45*, 8–13. [CrossRef]
14. Lin, C.; Zhang, X. Laboratory Drainage Performance of a New Geotextile with Wicking Fabric. *J. Mater. Civ. Eng.* **2018**, *30*, 04018293. [CrossRef]
15. Zaman, M.W.; Han, J.; Zhang, X. Evaluating Wettability of Geotextiles with Contact Angles. *Geotext. Geomembr.* **2022**, *50*, 825–833. [CrossRef]

16. Zhang, X.; Galinmoghadam, J. *Performance of Wicking Geotextile on Mitigating Water Pumping Issue on I-44 Highway*; Department of Transportation, Construction and Materials Division: Kansas City, MI, USA, 2020.
17. Ud Din, I.M.; Mir, M.S.; Farooq, M.A. Effect of Freeze-Thaw Cycles on the Properties of Asphalt Pavements in Cold Regions: A Review. *Transp. Res. Procedia* **2020**, *48*, 3634–3641. [CrossRef]
18. Qiao, Y.; Dawson, A.R.; Parry, T.; Flintsch, G.; Wang, W. Flexible Pavements and Climate Change: A Comprehensive Review and Implicatio. *Sustainability* **2020**, *12*, 1057. [CrossRef]
19. Jiang, Y.; Yu, X. Holistic Multiphysics Simulation of the Climatic Responses of Cold Region Pavements. *J. Infrastruct. Preserv. Resil.* **2023**, *4*, 24. [CrossRef]
20. Krantz, W.B. A Generalized Secondary Frost. *SIAM J. Appl. Math.* **1994**, *54*, 1650–1675.
21. Zhan, Y.; Lu, Z.; Yao, H.; Xian, S. A Coupled Thermo-Hydromechanical Model of Soil Slope in Seasonally Frozen Regions under Freeze-Thaw Action. *Adv. Civ. Eng.* **2018**, *2018*, 7219826. [CrossRef]
22. Subramanian, S.S. Numerical Modelling and Geomechanical Analyses of Soil Slope Stability Evaluation in Seasonal Cold Regions. Ph.D. Thesis, Hokkaido University Sapporo, Sapporo, Japan, 2017; pp. 1–117.
23. Simonsen, E.; Isacsson, U. Thaw Weakening of Pavement Structures in Cold Regions. *Cold Reg. Sci. Technol.* **1999**, *29*, 135–151. [CrossRef]
24. Zhang, X.; Presler, W.; Li, L.; Jones, D.; Odgers, B. Use of Wicking Fabric to Help Prevent Frost Boils in Alaskan Pavements. *J. Mater. Civ. Eng.* **2014**, *26*, 728–740. [CrossRef]
25. Lin, C.; Presler, W.; Zhang, X.; Jones, D.; Odgers, B. Long-Term Performance of Wicking Fabric in Alaskan Pavements. *J. Perform. Constr. Facil.* **2017**, *31*, D4016005. [CrossRef]
26. Noborio, K.; McInnes, K.J.; Heilman, J.L. Two-Dimensional Model for Water, Heat, and Solute Transport in Furrow-Irrigated Soil: II. Field Evaluation. *Soil Sci. Soc. Am. J.* **1996**, *60*, 1010–1021. [CrossRef]
27. Konrad, J.M. Sixteenth Canadian Geotechnical Colloquium: Frost Heave in Soils: Concepts and Engineering. *Can. Geotech. J.* **1994**, *31*, 223–245. [CrossRef]
28. Hansson, K.; Šimůnek, J.; Mizoguchi, M.; Lundin, L.; Genuchten, M.T. Water Flow and Heat Transport in Frozen Soil: Numerical Solution and Freeze–Thaw Applications. *Vadose Zo. J.* **2004**, *3*, 693–704. [CrossRef]
29. Liu, X.; Rees, S.J.; Spitler, J.D. Modeling Snow Melting on Heated Pavement Surfaces. Part I: Model Development. *Appl. Therm. Eng.* **2007**, *27*, 1115–1124. [CrossRef]
30. Wang, C.; Ma, Z. Mathematical Model and Numerical Simulation of Hydrothermal Coupling for Unsaturated Soil Subgrade in the Seasonal Frozen Zone. *IOP Conf. Ser. Earth Environ. Sci.* **2021**, *719*, 032042. [CrossRef]
31. Li, N.; Chen, B.; Chen, F.; Xu, X. The Coupled Heat-Moisture-Mechanic Model of the Frozen Soil. *Cold Reg. Sci. Technol.* **2000**, *31*, 199–205. [CrossRef]
32. Coussy, O.; Monteiro, P. Unsaturated Poroelasticity for Crystallization in Pores. *Comput. Geotech.* **2007**, *34*, 279–290. [CrossRef]
33. Sweidan, A.H.; Niggemann, K.; Heider, Y.; Ziegler, M.; Markert, B. Experimental Study and Numerical Modeling of the Thermo-Hydro-Mechanical Processes in Soil Freezing with Different Frost Penetration Directions. *Acta Geotech.* **2022**, *17*, 231–255. [CrossRef]
34. Dong, S.; Jiang, Y.; Yu, X. Analyses of the Impacts of Climate Change and Forest Fire on Cold Region Slopes Stability by Random Finite Element Method. *Landslides* **2021**, *18*, 2531–2545. [CrossRef]
35. Anderson, D.M.; Tice, A.R.; McKim, H.L. Unfrozen Water and the Apparent Specific Heat Capacity of Frozen Soils. In *Second International Conference on Permafrost, Yakutsk, USSR*; North American Contribution; Wiley Online Library: Hoboken, NJ, USA, 1973; pp. 289–295.
36. Cass, A.; Campbell, G.S.; Jones, T.L. *Hydraulic and Thermal Properties of Soil Samples from the Buried Waste Test Facility*; United States Department of Energy, Pacific Northwest Lab: Washington, DC, USA, 1981; p. 23.
37. McInnes, K.J. Thermal Conductivities of Soils from Dryland Wheat Regions of Eastern Washington. MS Thesis, Washington State University, Washington, DC, USA, 1981.
38. van Genuchten, M.T. A Closed-Form Equation for Predicting the Hydraulic Conductivity of Unsaturated Soils. *Soil Sci. Soc. Am. J.* **1980**, *44*, 892–898. [CrossRef]
39. Koopmans, R.W.R.; Miller, R.D. Soil Freezing and Soil Water Characteristic Curves. *Soil Sci. Soc. Am. J.* **1966**, *30*, 680–685. [CrossRef]
40. Spaans, M. Monte Carlo Models of the Physical and Chemical Properties of Inhomogeneous Interstellar Clouds. *Astron. Astrophys.* **1996**, *307*, 271–287.
41. Deng, Q.; Liu, X.; Zeng, C.; He, X.; Chen, F.; Zhang, S. A Freezing-Thawing Damage Characterization Method for Highway Subgrade in Seasonally Frozen Regions Based on Thermal-Hydraulic-Mechanical Coupling Model. *Sensors* **2021**, *21*, 6251. [CrossRef]
42. Tang, T.; Shen, Y.; Liu, X.; Zhang, Z.; Xu, J.; Zhang, Z. The Effect of Horizontal Freezing on the Characteristics of Water Migration and Matric Suction in Unsaturated Silt. *Eng. Geol.* **2021**, *288*, 106166. [CrossRef]
43. Alavi, M.Z.; Pouranian, M.R.; Hajj, E.Y. Prediction of Asphalt Pavement Temperature Profile with Finite Control Volume Method. *Transp. Res. Rec.* **2014**, *2456*, 96–106. [CrossRef]
44. Huang, K.; Zollinger, D.G.; Shi, X.; Sun, P. A Developed Method of Analyzing Temperature and Moisture Profiles in Rigid Pavement Slabs. *Constr. Build. Mater.* **2017**, *151*, 782–788. [CrossRef]

45. Schlangen, E. *Online Help/Manual Module HEAT of FEMMASSE, 1990–2000*; Femmasse B.V.: Sittard, The Netherlands, 2000.
46. Morbidelli, R.; Corradini, C.; Saltalippi, C.; Flammini, A.; Dari, J.; Govindaraju, R.S. Rainfall Infiltration Modeling: A Review. *Water* **2018**, *10*, 1873. [CrossRef]
47. Liu, Z.; Yu, X. Coupled Thermo-Hydro-Mechanical Model for Porous Materials under Frost Action: Theory and Implementation. *Acta Geotech.* **2011**, *6*, 51–65. [CrossRef]

geosciences

MDPI

Article

Seismic Response of Pile Foundations in Clayey Soil Deposits Considering Soil Suction Changes Caused by Soil–Atmospheric Interactions

Ali Shojaeian *, Tommy Bounds , Kanthasamy K. Muraleetharan and Gerald Miller

School of Civil Engineering and Environmental Science, University of Oklahoma, Norman, OK 73019, USA; tbounds@ou.edu (T.B.); muralee@ou.edu (K.K.M.); gamiller@ou.edu (G.M.)
* Correspondence: a.shojaeian@ou.edu

Abstract: Extreme variations in weather patterns have become increasingly common across the Southern Great Plains of the United States. The soil layer in the active zone above the groundwater table is often subjected to moisture variations due to seasonal weather changes that will influence the behavior of soils, including their strength and stiffness parameters. Designing a pile foundation in seismic-prone areas without considering the moisture changes in soil interacting with piles may adversely impact the seismic performance of the piles. The main aim of this study is to investigate the role of soil moisture conditions and suction caused by soil–atmospheric interactions on the dynamic behavior of the pile foundations interacting with clayey soils. This study uses a stand-alone finite element computer code called DYPAC (Dynamic Piles Analysis Code) developed using the Beams on Nonlinear Winkler Foundation (BNWF) approach. The influence of soil suction is incorporated into the p-y curves and free-field soil displacements using site response analyses by employing the concept of apparent cohesion. To perform nonlinear site response analyses, DEEPSOIL software V6.1 is utilized. The variation in soil suction with depth along the pile is considered using unsaturated seepage analysis performed by employing the commercial software PLAXIS LE Groundwater for three different clayey soils with plasticity ranging from low to medium to high. The analyses were performed using actual past daily recorded weather data for a testbed that experienced significant back-to-back flash droughts in 2022. This study found that extreme weather events like flash droughts can significantly affect the soil suction and seismic performance of the piles interacting with the unsaturated clayey soils.

Keywords: soil–structure interaction; seismic response analysis; unsaturated clayey soils

Citation: Shojaeian, A.; Bounds, T.; Muraleetharan, K.K.; Miller, G. Seismic Response of Pile Foundations in Clayey Soil Deposits Considering Soil Suction Changes Caused by Soil–Atmospheric Interactions. *Geosciences* **2024**, *14*, 234. https://doi.org/10.3390/geosciences14090234

Academic Editors: Mohamed Shahin and Dominic E. L. Ong

Received: 25 March 2024
Revised: 1 July 2024
Accepted: 26 August 2024
Published: 29 August 2024

1. Introduction and Background

The main aim of this study is to investigate the role of soil moisture conditions and suction caused by soil–atmospheric interactions on the dynamic behavior of the pile foundations interacting with clayey soils. In this section, the motivation for this work is discussed relative to the occurrence of increasingly extreme weather in the form of flash drought, followed by the impacts of this weather on soil and the behavior of pile foundations. Particular emphasis is placed on lateral load behavior during earthquakes. Finally, the method of analysis used in this study to examine dynamic pile–soil interaction, and the influence of moisture conditions is introduced at the end of this section.

Extreme variations in weather patterns have become increasingly common across the Southern Great Plains of the United States. The frequency, duration, and intensity of these events is projected to increase as we progress into the mid-21st century [1]. One of the many features of these weather patterns is extreme and rapid changes from normal to drought conditions and vice versa. Rapid changes from normal to drought conditions have been termed flash droughts. Flash droughts have become a common phenomenon across the Southern Great Plains. Flash drought was observed in portions of this area for

26 of the 37 years between 1979 and 2016 [2]. More recently, back-to-back flash droughts have been observed. These events are characterized by a series of flash droughts in a short amount of time. The back-to-back flash drought used in this study occurred over five months. There was a small period of rainfall between the flash droughts indicating the end of one drought and the beginning of another. Soil moisture contents in the active zone near the ground surface can change significantly during the wetter and dry periods associated with these flash droughts, which can significantly influence the soil strength and stiffness. The active zone generally extends from 3 to 5 m below the ground surface in Oklahoma, and so changes in soil properties in this zone can have a large impact on the behavior of foundations interacting with these soils.

It is well established that the behavior of foundations is impacted by changes in soil moisture content and soil suction. These impacts are most notable in clayey soils which experience large variations in soil suction and volume change due to changes in soil moisture. Shallow foundations are much more susceptible to the effects of soil volume change that results from variations in soil moisture. As a result, shallow foundations have received much attention with respect to unsaturated soils. Deep foundations, particularly those that are founded in bedrock, are assumed to be isolated from the effects of variations in soil moisture content under axial loads. The lateral loading of deep foundations, however, will depend on soil moisture variations and this dependency has not been very well investigated.

Pile foundations are commonly employed to effectively transmit axial and lateral loads from superstructures to the subsurface in situations where the superstructure loads are substantial and/or there are weak soil layers near the ground surface. Lateral loads are important in the structural analysis and design of pile foundations, which serve as essential support systems for various structures such as tall buildings, bridges, transmission lines, and offshore installations. Earthquakes have resulted in substantial damage to civil engineering structures, often due to insufficient lateral load capacity and excessive deformation of pile foundations that support these structures [3,4]. The moisture content of the soil in the active zone above the groundwater table fluctuates due to seasonal weather or water table changes. The groundwater table level can vary seasonally and spatially, leading to saturated soils transitioning to unsaturated conditions at specific times. A considerable proportion of many pile foundations are embedded in unsaturated soils, and the fluctuations in moisture levels in the surrounding soils can impact the characteristics of the soils, such as their strength and stiffness parameters. Changes in these soil parameters can have a significant impact on the seismic response of pile foundations. Unsaturated soils exhibit distinct dynamic properties when compared to soils that are either fully saturated or completely dry [5,6]. As demonstrated by Hoyos et al. [7], unsaturated soils exhibit greater shear stiffness but lower damping in comparison to both dry and fully saturated soils. In addition, it has been found in other studies that the level of soil saturation significantly influences the settlement of soils caused by seismic activity [8]. Moreover, the seismic response of sites [9,10] and the response of foundations to seismic events [11–13] have also been observed to be affected by the degree of soil saturation. The seismic performance of pile foundations may be negatively affected if the soil moisture changes are not considered in the soil–pile interaction analyses during the design process.

The literature contains many notable studies about the behavior of laterally loaded piles. The primary focus of the majority of these studies pertains to the seismic response of piles in soils that are fully saturated. Insufficient emphasis has been placed on investigating the impact of unsaturated soil conditions on the behavior of laterally loaded piles. Nevertheless, it is widely recognized that the mechanical properties of soil layers near the ground surface, often situated above the groundwater table, exert a significant influence on pile response [14]. Based on the available literature, it appears that limited research has been conducted on the influence of soil suction on the behavior of laterally loaded piles in unsaturated soils. Mokwa et al. [15], in their study, presented a methodology aimed at determining the load versus lateral displacement curves for unsaturated soils.

This approach was developed by analyzing the outcomes of five comprehensive load tests conducted at full scale. In their study, Stacul et al. [16] employed the Modified Kovacs model to develop a hybrid BEM p-y curve methodology for individual piles. This technique effectively replicates the impact of matric suction by elevating the stress state and stiffness of near-surface soil layers. Lalicata et al. [11] conducted centrifuge experiments to investigate the influence of the degree of saturation on the response of laterally loaded piles. Based on their study, a significant enhancement in soil stiffness and ultimate lateral resistance was observed in unsaturated soils.

The main aim of this present study is to investigate the role of moisture conditions and soil suction, as affected by season-to-season weather extremes, on the dynamic behavior of the pile foundations interacting with clayey soils. This study uses a stand-alone finite element computer code called DYPAC (Dynamic Piles Analysis Code) developed using the Beams on Nonlinear Winkler Foundation (BNWF) approach [17]. DYPAC analyzes the seismic response of a single pile in a layer of soil. This computer code models the pile as a beam element and the nonlinear soil behavior as springs and viscous dashpots using a nonlinear p-y element [18]. The influence of soil suction is incorporated into the p-y curves and site response analyses using the concept of apparent cohesion, which is a nonlinear relationship as described by Vanapalli et al. [19]. To perform nonlinear site response analyses, DEEPSOIL software is utilized. The variation in soil suction with depth along the embedded portion of the pile is also considered in the analysis. To incorporate these effects, unsaturated seepage analysis was completed using the commercial software PLAXIS LE Groundwater [20] for three different hypothetical clayey soils with plasticity ranging from low to medium to high. The soil properties selected for analysis encompass the range of clayey soil types across the testbed area. The seepage analyses were performed using actual past daily recorded weather data for this testbed which experienced significant flash droughts in 2022. An illustrative case study is presented to show how a pile foundation's seismic response can be affected in unsaturated clayey soils by changes in moisture conditions caused by soil–atmospheric interactions.

2. Method of Approach

This section begins with a brief introduction to moisture migration analysis. It is followed by the DYPAC modeling description with a discussion of the Winkler model used in DYPAC as a soil–pile interaction analysis method and Hilber–Hughes–Taylor (HHT)-α method as a numerical method to solve the governing equation. This section proceeds with a description of site response analyses and will end with an explanation to clarify how the effects of unsaturated conditions are incorporated into DYPAC modeling to estimate the seismic response of pile foundations in clayey soils subjected to seasonal weather changes. The next section is an illustrative case study to show how a comprehensive study can be conducted using real weather data.

2.1. Moisture Migration Analysis

The effects of back-to-back flash droughts on soil moisture were incorporated in this study using seepage analysis performed with PLAXIS LE Groundwater. PLAXIS LE Groundwater allows the user to import weather data for the study duration which act as the input for the soil–atmospheric interaction analysis. The weather data can include average daily temperatures, wind speed, solar radiation, relative humidity, and daily precipitation. The potential evaporation is estimated by the software according to Penman [21]. The weather loading is then applied in the soil model as a series of time steps. Pertinent information such as soil moisture content, soil suction, moisture flux, and evaporation can be obtained from the software at different times of the analysis.

2.2. DYPAC Modeling

DYPAC is a stand-alone finite element computer code developed using the Beams on Nonlinear Winkler Foundation (BNWF) approach. Winkler [22] developed a simplified method called Beams on Elastic Foundation (BEF) that is commonly used in civil engineering practice today to analyze soil–pile interactions. This approach models the pile as a beam element and the interaction with the soil through an infinite number of discrete spring elements with the interactions described using a p-y curve. Here, "p" denotes lateral soil resistance per unit length of the pile, and "y" denotes the lateral pile displacement. Later, this concept was extended as the BNWF and used discrete nonlinear springs to account for the nonlinearity of soils. DYPAC analyzes the seismic response of a single pile in a layer of soil. This computer code models the pile as a beam element and the nonlinear soil behavior as springs and viscous dashpots using a nonlinear p-y element [18].

It is important to consider factors such as soil yielding, gapping, radiation damping, and soil cave-in and recompression when employing BNWF for seismic problems [23]. The integration of these elements into the nonlinear p-y components poses a notably intricate and demanding challenge, even in cases where the soil system exhibits homogeneity. DYPAC utilizes the Boulanger et al. [18] model for its p-y representation. This model features a nonlinear p-y element comprising elastic, plastic, and gap constituents (Figure 1) interconnected in series. The elastic component simulates the far-field soil motion through a linear spring and a dashpot in parallel, mimicking radiation damping. The plastic component simulates the near-field motion of the soil adjacent to the pile using a nonlinear spring that accounts for stiffness and strength degradation. The gap component simulates the drag force on the pile when it moves within the gap by using a nonlinear drag spring. The transition from the gap to contact is made smooth by a parallel nonlinear closure spring. Free-field soil displacements (soil displacements relative to the base) obtained using a site response analysis are input to the free end of elastic spring/dashpot to solve the nonlinear governing differential equation at every time step using an iterative numerical algorithm. The governing differential equation contains mass, damping, and stiffness of the pile, stiffness due to soil–pile interactions (stiffness from the p-y curves), and the applied base acceleration time history [15]. The y in the p-y curve is the difference between the pile displacement relative to the base and the soil displacement relative to the base. For this study, the input parameters p_{ult} and y_{50} were based upon Matlock's [24] Equations (1)–(3):

$$p_{ult} = c_u b N_p \tag{1}$$

$$N_p = \left(3 + \frac{\gamma' x}{c_u} + \frac{Jx}{b}\right) \leq 9 \tag{2}$$

$$y_{50} = 2.5 b \varepsilon_{50} \tag{3}$$

where b = pile diameter, N_p = lateral bearing capacity factor, γ' = average buoyant unit weight, x = depth, c_u = undrained shear strength, and ε_{50} = strain corresponding to a stress of 50% of the ultimate stress in a laboratory stress–strain curve. ε_{50} was taken as 0.005 for $c_u \geq 96$ kPa based on the typical values proposed in the literature for stiff clay. Also, J was taken as 0.25 according to Matlock's recommendations for stiff clay.

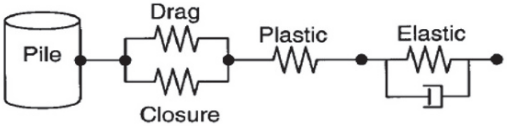

Figure 1. Nonlinear p-y element that includes elastic, plastic, and gap components interconnected in series to simulates the far-field soil motion, near-field soil motion, and drag force on the pile, respectively [18].

In addressing nonlinear dynamic issues, a robust time-stepping approach proves effective in mitigating the spurious effects of high-frequency modes and achieving rapid convergence, thereby enhancing computational efficiency. The Hilber–Hughes–Taylor

(HHT)-α method [25], also known as the α-method, stands out as a widely utilized numerical integration technique in structural dynamics. A precursor to the HHT-α method is the Newmark time integration method. Notably, the HHT-α method exhibits superior accuracy and favorable numerical damping characteristics when compared to the Newmark method. Muraleetharan et al. [26] applied a time integration scheme based on the HHT-α method to address the dynamic behavior of saturated soils governed by nonlinear equations. In this present study, the HHT-α method is combined with the Newton–Raphson method to solve the nonlinear governing equations in DYPAC similar to the approach used by Muraleetharan et al. [26].

Nonlinear site response analyses to obtain free-field soil displacements were conducted using the DEEPSOIL computer code [27]. The curves representing G/G_{max} and damping ratio (%) were established as functions of shear strain (%) for clayey soils using the nonlinear approach proposed by Darendeli [28] and Equation (4). Dickenson [29] introduced an empirical relationship for the shear wave velocity (v_s) in cohesive soils as follows in Equation (5):

$$v_s = \sqrt{\frac{G_{max}}{\rho}} \tag{4}$$

$$v_s = 18(c_u)^{0.475} \tag{5}$$

where v_s is shear wave velocity in m/s, G_{max} is the maximum shear modulus of the soil, ρ is the density of the soil, and c_u is undrained shear strength in kPa. In free-field soil displacement analyses, the impact of suction was considered by adjusting the shear strength and consequently the shear wave velocity for each suction value based on Equation (5). For simplicity, G/G_{max} and damping ratio curves are kept constant across all suction values. Free-field soil displacements were determined for each suction level and subsequently utilized as input for DYPAC analyses.

The influence of soil moisture is incorporated into the p-y curves and site response analyses using a nonlinear relationship that was proposed by Vanapalli et al. [19] as follows in Equation (6):

$$\tau = c' + (\sigma_n - u_a)\tan\phi' + (u_a - u_w)(\tan\phi')\left(\frac{S - S_r}{100 - S_r}\right) \tag{6}$$

where τ is the shear strength of an unsaturated soil, c' denotes the effective cohesion for a saturated soil, ϕ' represents the effective internal friction for a saturated soil, $(\sigma_n - u_a)$ is the net normal stress on the plane of failure, $(u_a - u_w)$ is the matric suction of the soil on the plane of failure, S is the degree of saturation, and S_r is the residual degree of saturation. An approximation of $c_u \approx \tau$ has been used here based on the assumption that τ is reasonably close to the top of the Mohr's circle and c_u is equal to one-half the difference in major and minor net principal stresses [30]. Hence, the values of τ were used for c_u, as a close approximation, in Equations (1) and (2) to calculate the p_{ult} values and were also used in the Dickenson equation (Equation (5)) to assess the shear wave velocities for DEEPSOIL analyses. This implies that changes in matric suction leads to changes in shear strength (c_u), shear wave velocity, and free-field soil displacements. Furthermore, changes in suction results in updates to the p_{ult} in the p-y model. These modifications collectively impact the seismic response of a pile foundation as the moisture conditions in unsaturated soil undergo changes.

3. Illustrative Case Study

An illustrative case study is presented to show how a pile foundation's seismic response can be affected in unsaturated soils by changes in moisture conditions induced by soil–atmospheric interactions. The testbed for this case study is Pittsburg County, Oklahoma. Pittsburg County is in southeast Oklahoma. The site was chosen because it is home to expansive soils and experienced back-to-back flash droughts in 2022. The soils in the testbed are diverse, ranging from moderate to high PI clayey soils to non-plastic silty sands. A wide range of PI and percent of fines (w) were chosen to characterize the soils for this case study (see Table 1). Based on the literature, there are some correlations between effective cohesion/friction angle and the plasticity index of clay. Given the utilization of unsaturated soils, which commonly display overconsolidated characteristics, Equations (7) and (8) have been chosen. These equations are recommended for application in overconsolidated clays. To estimate the effective cohesion Equation (7), which is proposed by Tchakalova [31], is used. For friction angle estimation, Equation (8), proposed by Sorensen [32], is used. Values of effective cohesion and friction angle obtained using these equations are listed in Table 1.

$$c' = 8.476 + 0.776\,PI \tag{7}$$

$$\phi' = 45 - 15\log PI \tag{8}$$

where c′ denotes the effective cohesion for a saturated soil, ϕ' represents the effective internal friction for a saturated soil, and *PI* is the plasticity index of the soil.

Table 1. Characteristic soil properties.

Clay Type	w	PI	wPI	Effective Cohesion (kPa)	Effective Friction Angle (°)
Low-plasticity	0.60	5	3	12	34
Medium-plasticity	0.75	20	15	24	25
High-plasticity	0.90	35	32	35	22

Soil water characteristic curves (SWCCs) were developed for each of the study soils according to the relationship developed by Fredlund and Xing [33]. This relationship requires four fitting parameters that can be estimated based on the soil PI and percent fines according to Zapata [34]. The SWCCs for each of the soils according to these relationships are shown in Figure 2.

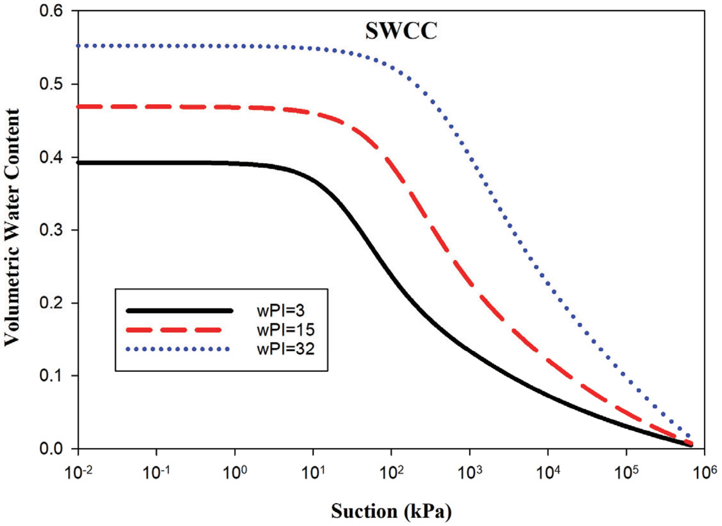

Figure 2. SWCCs for study soils obtained using Fredlund and Xing [33] model.

The base motion event used in this study is a scaled version of a motion recorded during the 1979 El Centro earthquake in California. Figure 3 shows the base motion acceleration time history used in DEEPSOIL analyses and DYPAC modeling.

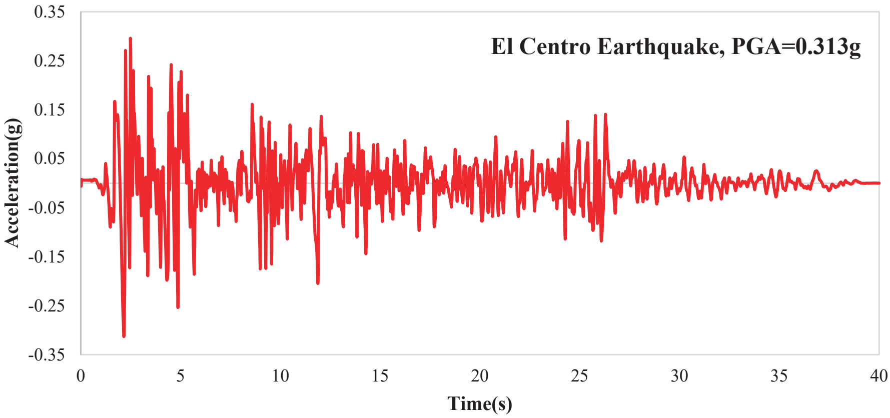

Figure 3. El Centro earthquake acceleration time history used in the current study with a PGA (Peak Ground Acceleration) of 0.313 g.

The testbed experienced back-to-back flash droughts in 2022. The first flash drought peaked in August and the second started in September and drought conditions lasted through October [35]. The variation in flash drought across Oklahoma in 2022 is shown in Figure 4. Pittsburg County is indicated by the white star in the image. It can be observed from the images that the back-to-back flash droughts resulted in exceptional drought conditions for the testbed.

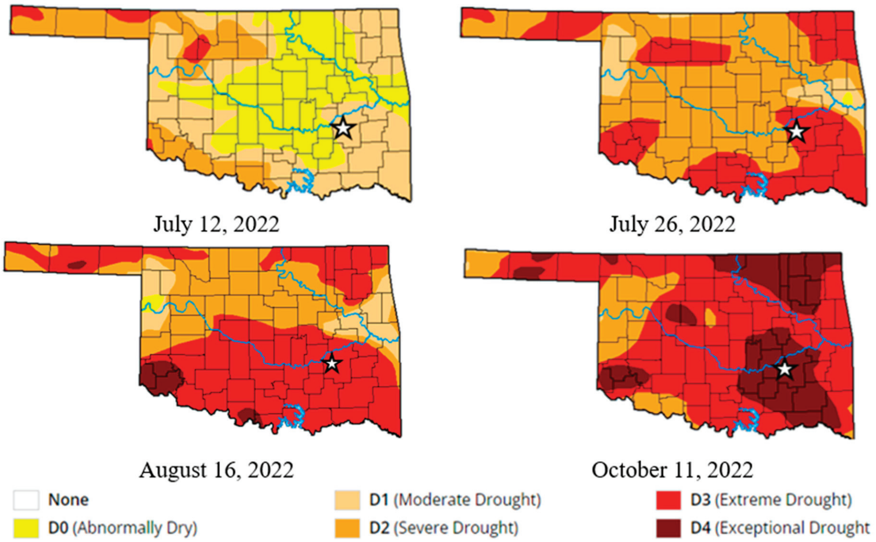

Figure 4. Variation in exceptional drought conditions across Oklahoma in 2022 [35] that shows the back-to-back flash droughts. Testbed indicated by white star.

Seepage analysis for each soil profile was conducted using the finite element software PLAXIS LE Groundwater [20]. PLAXIS LE Groundwater models seepage within the context of continuum mechanics and therefore assumes that soil phases can be described according to continuum mechanics. Furthermore, pore air including water vapor is assumed to behave as an ideal gas, thermodynamic equilibrium between liquid and vapor phases exists at all points in the soil and during all times of the analysis, and atmospheric pressure gradients are negligible. The software estimates the variation in soil moisture conditions as a function of weather input at the soil surface. Weather input for this study included precipitation, relative humidity, radiation, air temperature, and wind speed. The initial pore-water pressure is calculated according to hydrostatic conditions using the following equation:

$$u_w = \gamma_w (h - y) \tag{9}$$

where u_w is the pore-water pressure, γ_w is the unit weight of water, h represents the total water head, and y is the elevation. The phreatic surface occurs when $h = y$, saturated regions occur when $h > y$, and unsaturated regions occur when $h < y$. The initial groundwater table for the soil model was set at a depth of 50 m resulting in an initial maximum soil suction of 490.5 kPa at the surface. The initial moisture profile was identical for each soil profile since the pore-water pressure was initialized independent of soil properties according to Equation (9). The soil moisture profiles quickly deviated from the initial values as a function of soil properties and weather loading on the model.

Daily weather data collected by the Pittsburg County Mesonet station was used in the seepage analysis to capture the impacts of weather variations on soil suction. The Mesonet network is a system of weather stations throughout Oklahoma that are monitored and maintained by the University of Oklahoma and Oklahoma State University [36,37]. The weather data collected at the Pittsburg County Mesonet and used in this study are shown in Figure 5. The potential evaporation as estimated by PLAXIS LE Groundwater during the analysis for this weather data is also included in the figure. The flash droughts can be observed in Figure 5 according to the rainfall data. There is a delay between dry conditions and droughts. The same is true for ending the drought. Rainfall events occurred during August, but the drought persisted during this time.

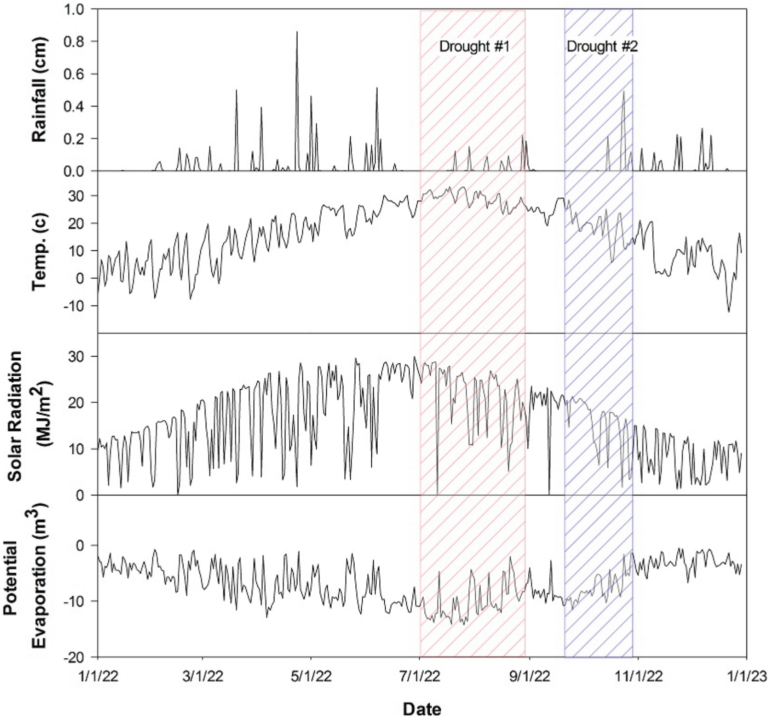

Figure 5. Pittsburg Co. Oklahoma weather data and potential evaporation as estimated by PLAXIS LE Groundwater.

The permeability of unsaturated soils is related to the soil suction according to the SWCC for the soil. The change in permeability with respect to soil suction was estimated by the software according to Fredlund et al. [38]. The seepage analysis was conducted using 1D conditions. The 1D column of soil had a height of 50 m and contained 100 elements with a uniform height of 0.5 m. The suction for the wPI = 3 soil was found to vary erratically for shallow depths (less than 1 m) throughout the analysis. The variation in suction throughout the analysis at a depth of 1.5 m is shown in Figure 6. At this depth, most of the erratic variations in suction are not present. The effects of the first flash drought are shown as the first large increase in suction during July. A series of rain events in August provides some moisture to the soil reducing the suction between the two events. The rain events occurred on 8, 17, 21, 29, and 31 August. The total rainfall from this series of events was 8.3 cm. It should be noted that for events such as these, the suction remains elevated above baseline conditions despite the temporary brake in the drought. The second flash drought begins shortly after these rain events and takes the soils to higher suction levels than the first flash drought. The effects of back-to-back flash droughts are apparent from Figure 6. Without proper time to return to the baseline conditions, the soil will dry out more than it would have otherwise.

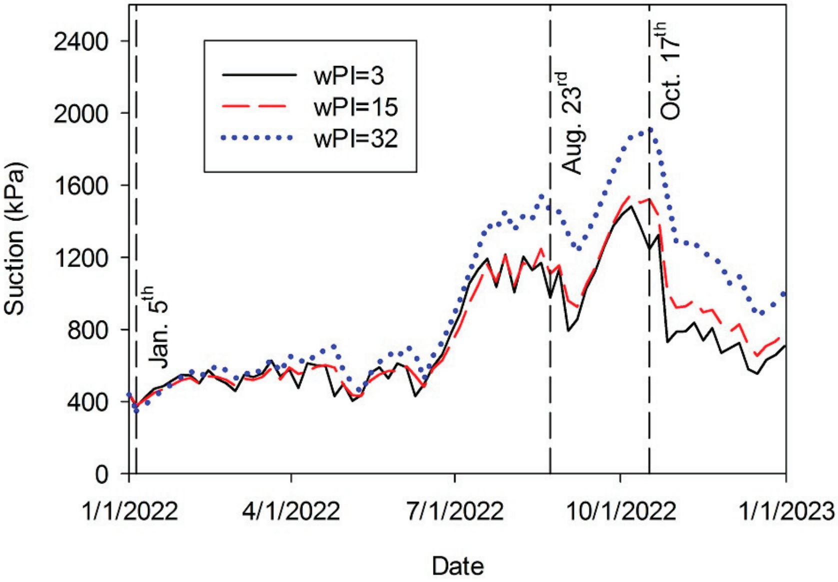

Figure 6. Variation in suction for 1.5 m depth that clearly shows the first and second flash droughts on 23 August and 17 October.

Soil suction profiles for the soil column were obtained on three dates: 5 January, 23 August, and 17 October. The first date represents the soil under initial conditions. The second and third dates occur when the first and second droughts are at their maximum with respect to soil moisture. It should be noted that the second profile occurs after several of the rain events that caused the end of the first drought. However, at this time only 3.7 cm of rain has entered the model. These small rain events set the stage for ending the drought, but the suction remains relatively high in the soil during this time. This can be observed in Figure 6 by the spikes in soil suction proceeding the valley in the profile between the two events. Soil suction profiles for the three study soils on these dates are shown below in Figure 7. As shown in the figure, the variations between different soil types are minimal for the 5 January profile and become pronounced for the 17 October profile. During drought periods, higher values of suction are observed for the higher wPI soils in the top 5 m of the soil profile. Beyond this depth, there is some deviation between the profiles, but the overall trend is consistent between the three profiles.

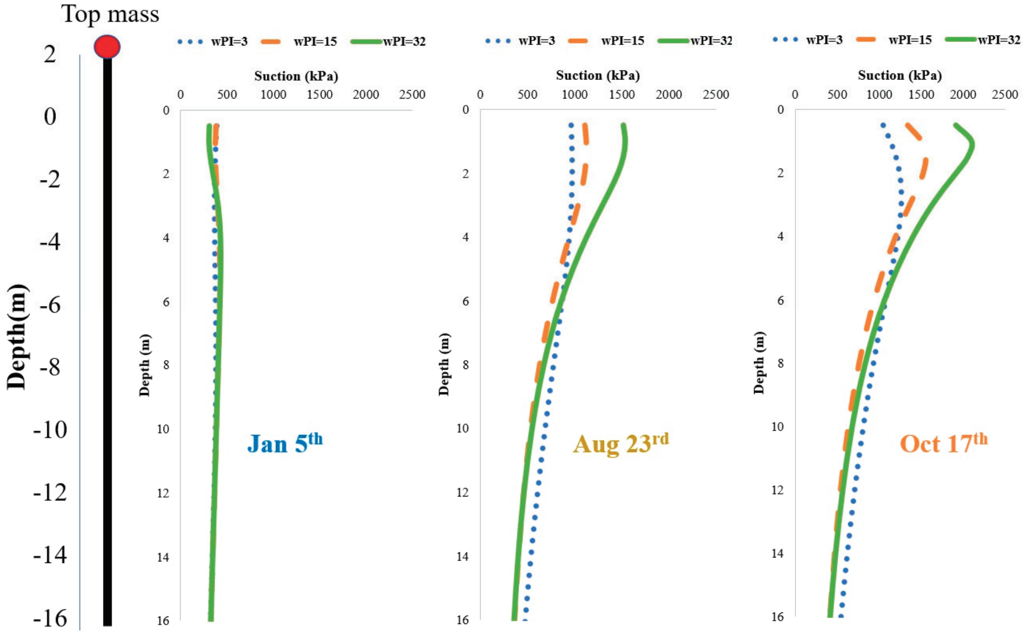

Figure 7. Soil suction profiles for three different clayey soils in various seasons.

As shown in Figure 7, the pile has a length of 18 m and 2 m of the pile was assumed to be above the ground surface. The pile diameter was assumed to be 0.3 m. The analysis also includes a seismic mass of 660 kg on top of the pile.

4. Results and Discussion

The results obtained from the investigation of the role of moisture conditions and soil suction on the seismic response of pile foundations in clayey soils are presented and key findings are discussed in this section. The primary focus is to illustrate the impact of varying moisture content, driven by extreme weather patterns, on free-field soil displacements, p-y curves, and ultimately on the response of pile foundations. The results presented here are derived from simulations using DEEPSOIL and DYPAC, incorporating realistic soil suction profiles obtained by PLAXIS LE as shown in Figure 7. The results of these analyses are presented in Figures 8–15 and observed trends and patterns are systematically discussed. The discussion starts with the site response analyses followed by the effects of moisture variations on the p-y curves, illustrating how changes in soil moisture content influence free-field soil displacements and the lateral soil resistance, respectively. Finally, these findings are integrated to evaluate the seismic response of pile foundations impacted by moisture variations. The results underscore the significance of moisture variations on soil–pile interactions, highlighting the necessity for incorporating these factors in seismic design considerations.

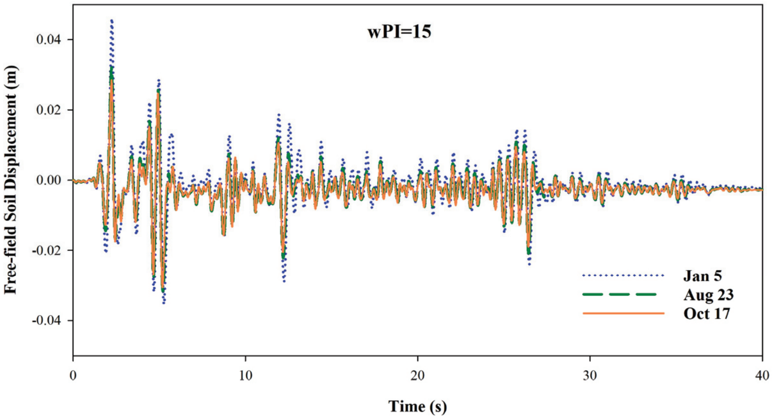

Figure 8. Free-field surface displacement time histories predicted by DEEPSOIL for medium-plasticity clay in different seasons.

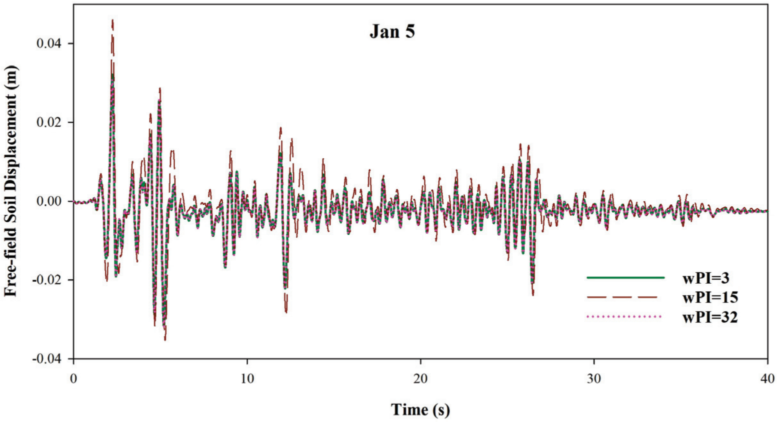

Figure 9. Free-field surface displacement time histories predicted by DEEPSOIL for various clays on Jan 5th.

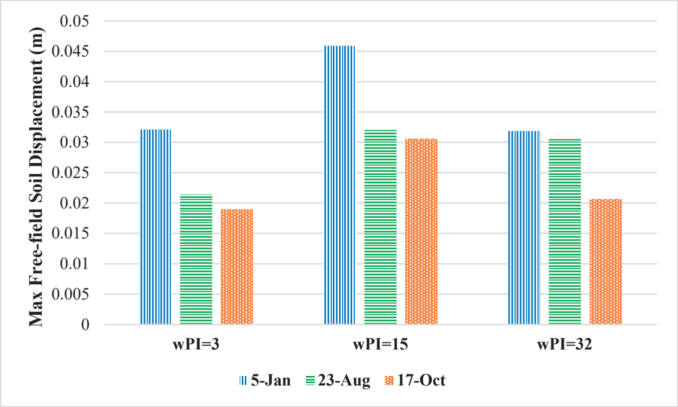

Figure 10. Maximum free-field surface soil displacements in different seasons for different soil types.

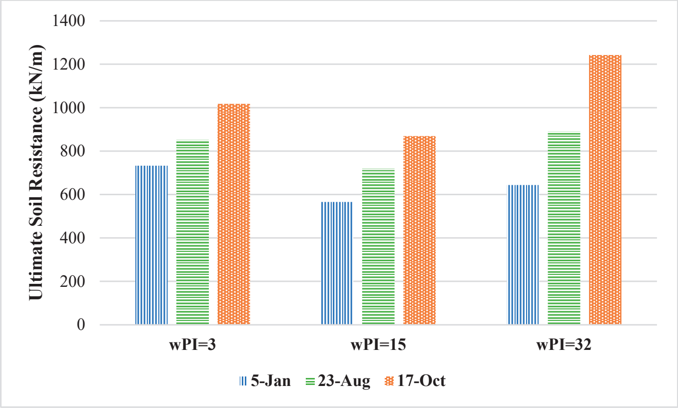

Figure 11. Ultimate soil resistance (p_{ult}) in different seasons and soil types.

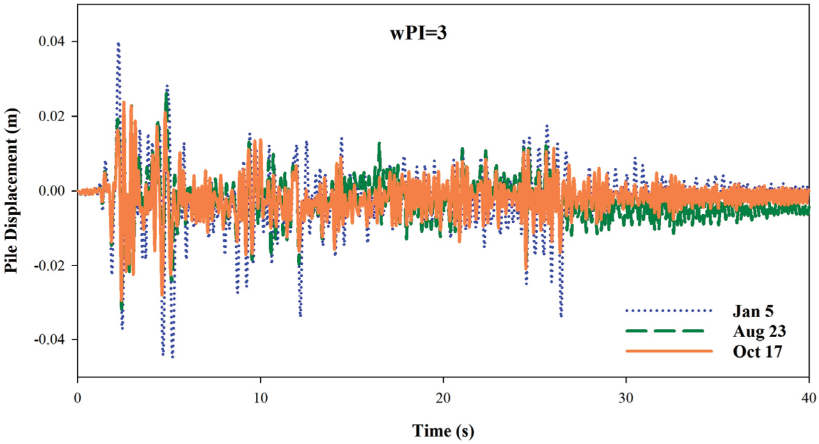

Figure 12. Pile top displacement time history for low-plasticity clay.

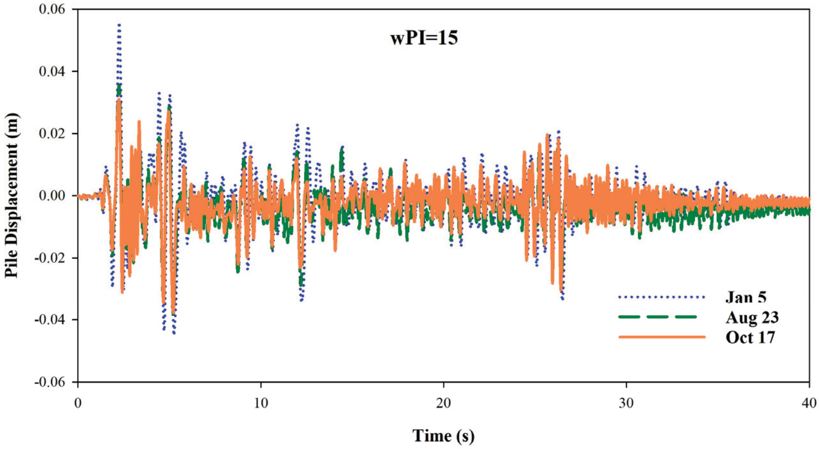

Figure 13. Pile top displacement time history for medium-plasticity clay.

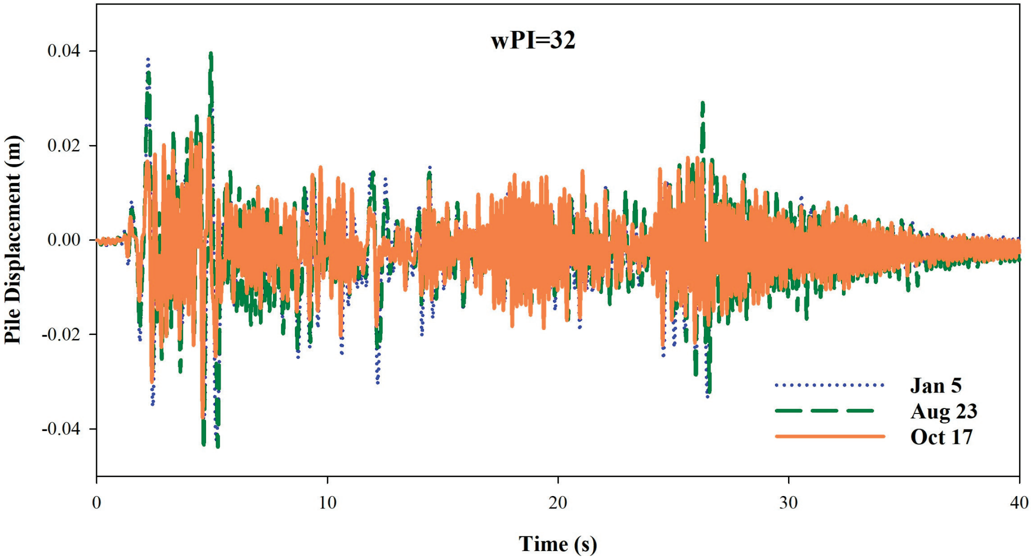

Figure 14. Pile top displacement time history for high-plasticity clay.

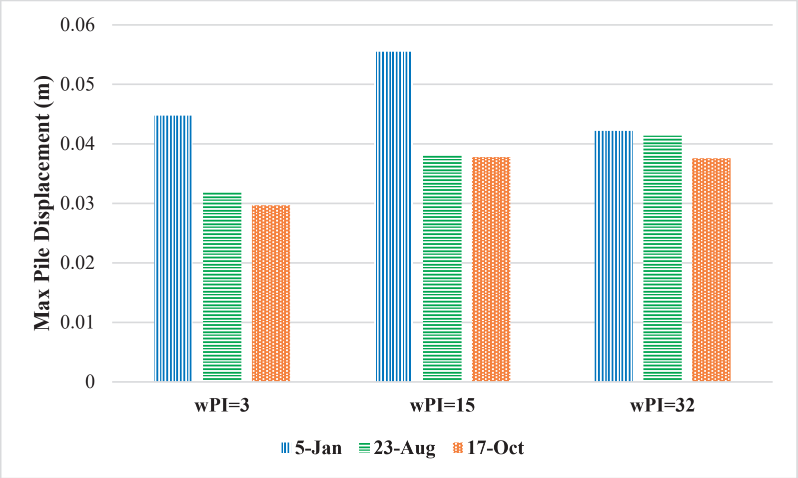

Figure 15. Maximum pile top displacements for various clays in different seasons.

Site response analyses were performed using DEEPSOIL to obtain the free-field soil displacements as input for DYPAC analyses. As shown in Figures 8 and 9, the free-field soil displacements at the node on the ground surface are compared for different suction scenarios based on the weather conditions. These serve as examples of free-field soil displacement analyses conducted to prepare input for DYPAC analyses. Figure 10 compares the maximum free-field surface soil displacement in different seasons for different soil types. As shown, for each soil type, the minimum displacement is associated with 17 October when the maximum drought occurs, which is reasonable because of the high value of soil suction in dry seasons. In all three soil types, the maximum free-field surface soil displacement on 5 January is almost 1.5 times that of 17 October. Soil suction is incorporated into the free-field displacement analysis through modification of the shear wave velocity according to Equation (5). According to Equations (5) and (6), higher suctions will result in larger shear strengths and shear wave velocities. Higher shear wave velocities result in higher shear modulus (Gmax) values and, in general, result in lower displacements at the ground surface.

The influence of soil suction is also incorporated into the p-y curves to consider the effects of seasonal moisture changes in soil–pile interaction. The p-y curves for various weather and soil-type scenarios were evaluated using the Boulanger et al. model [18]. As shown in Figure 11, the ultimate lateral soil resistance increased with the soil suction in the dry period for each soil type. The wPI = 15 soil had lower p_{ult} values for each of the conditions considered, which is counter intuitive. We would expect that the wPI = 3 profile would have the lowest p_{ult} values for the range of conditions. The observed behavior is a function of the moisture migration analysis, the initial parameters, and the relationship used to define c_u. It can be observed from Equations (1)–(3) and (5) that the soil's effective friction angle and suction have a profound influence on the calculation of p_{ult}. For example, the wPI = 3 soil had the highest value of p_{ult} on January 5 despite the suction being very similar for each profile. This soil also has the highest effective friction angle. At the height of the droughts the wPI = 32 soil had the largest value of p_{ult} despite having the lowest effective friction angle. The wPI = 15 soil had an effective friction angle in between the other two soils but had the lowest calculated maximum p_{ult} value on each of the dates. This interesting relationship highlights the complexity of the problem since there are many parameters influencing the behavior of the soil.

Figures 12–14 show pile top displacement obtained by DYPAC for specific low-, medium-, and high-plasticity clays in different seasons, facilitating a comparison of the impact of seasonal weather changes on the seismic response of piles in diverse clayey soils. Figure 15 provides a summary comparison of maximum pile displacements for various scenarios leading to the following findings:

- The most significant pile displacements occurred on 5 January, the wettest period of the year, while the lowest pile displacements occurred on 17 Oct, coinciding with the maximum suction values due to compounded flash droughts. Higher suction values are directly linked to a higher p_{ult} for each soil through Equations (1)–(3) and (6). In lateral pile analysis, p_{ult} serves as the maximum lateral resistance for soil and defines the p-y curve. For a given y50 parameter, a larger p_{ult} will result in smaller pile displacements.
- Seasonal weather changes notably influence pile response in low- and medium-plasticity clay. The disparity between pile responses during the wet period and dry period is negligible for high-plasticity clays. In low- and medium-plasticity clay, pile displacement during the wet period is nearly 1.5 times that during drought.
- The minimum pile displacement in the wet period is associated with piles in high-plasticity clays. However, the pile displacement in low-plasticity clays is the lowest one compared to the medium- and high-plasticity clays in the dry period. This observation can be explained by the relatively high p_{ult} values found for the low-plasticity clay paired with the low free-field motion estimated by DEEPSOIL during the dry period for the low-plasticity clay.
- The most substantial pile displacement occurred in medium-plasticity clay on 5 January, almost twice that of the lowest pile response related to low-plasticity clay on 17 October. This significant variation underscores the influence of seasonal weather changes on the seismic response of pile foundations in low- and medium-plasticity clays. It can highlight the importance of understanding the impact of seasonal weather conditions on the seismic design of pile foundations.

5. Conclusions

It is well established that the behavior of foundations is impacted by changes in soil moisture content and soil suction due to extreme variations in weather patterns that have become increasingly common across the Southern Great Plains of the United States. The main aim of this study was to investigate the role of moisture conditions and soil suction, as affected by season-to-season extreme weather variations, on the dynamic behavior of the pile foundations interacting with clayey soils. This study used a stand-alone finite element computer code called DYPAC (Dynamic Piles Analysis Code) developed using the Beams on Nonlinear Winkler Foundation (BNWF).

Predicted suction values corresponding to different moisture contents were used to determine the p-y curve parameters needed for DYPAC modeling. The free-filed soil displacements were also obtained using the affected soil shear strength and shear wave velocity values based on the moisture migration analyses. The variation in soil suction with depth along the embedded portion of the pile was also considered in the analysis. To incorporate these effects, unsaturated seepage analysis was completed using the commercial software PLAXIS LE Groundwater for three different clayey soils with plasticity ranging from low to medium to high. The seepage analysis used past daily recorded precipitation and other realistic weather data for a testbed that experienced back-to-back flash droughts in 2022.

This study found that soil suction variation due to the changing moisture conditions induced by soil–atmospheric interactions can significantly affect the seismic performance of the piles in unsaturated clayey soils. Results showed that the best seismic performance of the pile with the minimum lateral pile displacement occurred in low-plasticity clays when experiencing back-to-back flash droughts, while the maximum pile displacement occurred in medium-plasticity clays during the wettest period. In medium-plasticity clay, pile displacement during the wet period is nearly twice that in low-plasticity clay during drought. The seasonal variations in pile displacements were minimal for the high-plasticity clays.

Author Contributions: Conceptualization, K.K.M. and G.M.; methodology, K.K.M., T.B. and A.S.; software, A.S. and T.B.; validation, A.S., T.B. and K.K.M.; formal analysis A.S. and T.B.; investigation, A.S. and T.B.; resources, K.K.M. and G.M.; data curation, A.S.; writing—original draft preparation, A.S. and T.B.; writing—review and editing, K.K.M., G.M., T.B. and A.S.; visualization, K.K.M.; supervision, K.K.M., G.M. and T.B.; project administration, K.K.M.; funding acquisition, K.K.M. and G.M. All authors have read and agreed to the published version of the manuscript.

Funding: This research was funded by the U.S. National Science Foundation and the Oklahoma EPSCoR under Grant No. OIA-1946093.

Data Availability Statement: Some or all data, models, or code that support the findings of this study are available from the corresponding author upon reasonable request.

Acknowledgments: This work was supported by the U.S. National Science Foundation and the Oklahoma EPSCoR under Grant No. OIA-1946093. Their support is greatly appreciated. Any opinions, findings, and conclusions or recommendations expressed in this paper are those of the authors and do not necessarily reflect the views of the U.S. National Science Foundation or the Oklahoma EPSCoR.

Conflicts of Interest: The authors declare no conflict of interest.

References

1. Kloesel, K.; Bartush, B.; Banner, J.; Brown, D.P.; Lemery, J.; Lin, L.; Loeffler, C.; Mcmanus, G.; Mullens, E.; Nielsen-Gammon, J.; et al. Southern Great Plains. In *Impacts, Risks, and Adaptation in the United States: Fourth National Climate Assessment*; U.S. Global Research Program: Washington, DC, USA, 2018; Volume 2, pp. 987–1035. [CrossRef]
2. Christian, J.I.; Basara, J.B.; Otkin, J.A.; Hunt, E.D.; Wakefield, R.A.; Flanagan, P.X.; Xiao, X. A methodology for flash drought identification: Application of flash drought frequency across the United States. *J. Hydrometeorol.* **2019**, *20*, 833–846. [CrossRef]
3. Mylonakis, G.; Gazetas, G. Seismic soil-structure interaction: Beneficial or detrimental? *J. Earthq. Eng.* **2000**, *4*, 277–301. [CrossRef]
4. Yang, H.; Wang, H.; Jeremić, B. An energy-based analysis framework for soil structure interaction systems. *Comput. Struct.* **2022**, *265*, 106758. [CrossRef]
5. Le, K.N.; Ghayoomi, M. Cyclic direct simple shear test to measure strain-dependent dynamic properties of unsaturated sand. *Geotech. Test. J.* **2017**, *40*, 381–395. [CrossRef]
6. Zhang, B.; Muraleetharan, K.K.; Liu, C. Liquefaction of unsaturated sands. *Int. J. Geomech.* **2016**, *16*, D4015002. [CrossRef]

7. Hoyos, L.R.; Cruz, J.A.; Puppala, A.J.; Douglas, W.A.; Suescún, E.A. Dynamic shear modulus and damping of compacted silty sand via suction-controlled resonant column testing. In Proceedings of the 18th International Conference on Soil Mechanics and Geotechnical Engineering, Paris, France, 2–6 September 2013; pp. 1125–1128.
8. Yee, E.; Duku, P.M.; Stewart, J.P. Cyclic volumetric strain behavior of sands with fines of low plasticity. *J. Geotech. Geoenviron. Eng.* **2014**, *140*, 04013042. [CrossRef]
9. Mirshekari, M.; Ghayoomi, M. Centrifuge tests to assess seismic site response of partially saturated sand layers. *Soil Dyn. Earthquake Eng.* **2017**, *94*, 254–265. [CrossRef]
10. Zhang, B.; Muraleetharan, K.K. Liquefaction of level ground unsaturated sand deposits using a validated fully coupled analysis procedure. *Int. J. Geomech.* **2018**, *18*, 04018118. [CrossRef]
11. Lalicata, L.M.; Desideri, A.; Casini, F.; Thorel, L. Experimental observation on a laterally loaded pile in unsaturated silty soil. *Can. Geotech. J.* **2018**, *56*, 1545–1556. [CrossRef]
12. Borghei, A.; Ghayoomi, M.; Turner, M. Centrifuge tests to evaluate seismic settlement of shallow foundations on unsaturated silty sand. In *Geo-Congress 2020*; American Society of Civil Engineers: Reston, VA, USA, 2020; pp. 198–207.
13. Shojaeian, A.; Sivakumaran, S.; Muraleetharan, K.K. Seismic behavior of pile foundations in unsaturated soils. In *E3S Web of Conferences*; EDP Sciences: Les Ulis, France, 2023; Volume 382.
14. Borghei, A.; Ghayoomi, M.; Turner, M. Effects of groundwater level on seismic response of soil–foundation systems. *J. Geotech. Geoenviron. Eng.* **2020**, *146*, 04020110. [CrossRef]
15. Mokwa, R.L.; Duncan, J.M.; Helmers, M.J. Development of py curves for partly saturated silts and clays. In *New Technological and Design Developments in Deep Foundations*; American Society of Civil Engineers: Reston, VA, USA, 2000; pp. 224–239.
16. Stacul, S.; Squeglia, N.; Morelli, F. Laterally loaded single pile response considering the influence of suction and nonlinear behaviour of reinforced concrete sections. *Appl. Sci.* **2017**, *7*, 1310. [CrossRef]
17. Sivakumaran, S. Development of a Verified Non-Linear Winkler Model for the Seismic Analysis of Piles in Improved Ground. Master's Thesis, University of Oklahoma, Norman, OK, USA, 2019.
18. Boulanger, R.W.; Curras, C.J.; Kutter, B.L.; Wilson, D.W.; Abghari, A. Seismic soil-pile-structure interaction experiments and analyses. *J. Geotech. Geoenviron. Eng.* **1999**, *125*, 750–759. [CrossRef]
19. Vanapalli, S.K.; Fredlund, D.G.; Pufahl, D.E.; Clifton, A.W. Model for the prediction of shear strength with respect to soil suction. *Can. Geotech. J.* **1996**, *33*, 379–392. [CrossRef]
20. Bentley Systems Team. *PLAXIS LE Groundwater*; Bentley: Exton, PA, USA, 2021.
21. Penman, H.L. Natural evaporation from open water, bare soil and grass. *Proc. R. Soc. Lond. Ser. A Math. Phys. Sci.* **1948**, *193*, 120–145.
22. Winkler, E. *Die Lehre vonder Elastizitaf Und Festigkeit*; on Elasticity and Fixity; Czechoslovakia: Prague, Czech Republic, 1867; p. 182.
23. Soltani, H.; Muraleetharan, K.K. Predicting Seismic Response of a Single Pile in Cement-Treated Soft Clay Using a Bouc-Wen Type Model. In *IFCEE 2018*; American Society of Civil Engineers: Reston, VA, USA, 2018; pp. 262–271.
24. Matlock, H. Correlation for design of laterally loaded piles in soft clay. In *Offshore Technology Conference*; OnePetro: Richardson, TX, USA, 1970.
25. Hilber, H.M.; Hughes, T.J.; Taylor, R.L. Improved numerical dissipation for time integration algorithms in structural dynamics. *Earthq. Eng. Struct. Dyn.* **1977**, *5*, 283–292. [CrossRef]
26. Muraleetharan, K.K.; Mish, K.D.; Arulanandan, K. A fully coupled non-linear dynamic analysis procedure and its verification using centrifuge test results. *Int. J. Numer. Anal. Methods Geomech.* **1994**, *18*, 305–325. [CrossRef]
27. Hashash, Y.M.A.; Musgrove, M.I.; Harmon, J.A.; Groholski, D.R.; Phillips, C.A.; Park, D. *DEEPSOIL 6.1, Users Manual*; Board of Trustees of University of Illinois at Urbana-Champaign: Urbana, IL, USA, 2016.
28. Darendeli, M.B. Development of a New Family of Normalized Modulus Reduction and Material Damping Curves. Ph.D. Thesis, The University of Texas at Austin, Austin, TX, USA, 2001.
29. Dickenson, S.E.; Seed, R.B. *Preliminary Report on Correlations of Shear Wave Velocity and Engineering Properties for Soft Soil Deposits in the San Francisco Bay Region*; research report; Department of Civil Engineering, UCB/EERC-94/XX: Berkeley, CA, USA, 1994.
30. Fredlund, D.G.; Rahardjo, H. *Soil Mechanics for Unsaturated Soils*; John Wiley & Sons: Hoboken, NJ, USA, 1993.
31. Tchakalova, B.; Ivanov, P. Correlation between effective cohesion and plasticity index of clay. *Geolodica Balc.* **2021**, *51*, 45–49. [CrossRef]
32. Sorensen, K.K.; Okkels, N. Correlation between drained shear strength and plasticity index of undisturbed overconsolidated clays. In Proceedings of the 18th International Conference on Soil Mechanics and Geotechnical Engineering, Paris, France, 2–6 September 2013; Volume 1, pp. 423–428.
33. Fredlund, D.G.; Xing, A. Equations for the soil-water characteristic curve. *Can. Geotech. J.* **1994**, *31*, 521–532. [CrossRef]
34. Zapata, C. Uncertainty in Soil-Water-Characteristic Curve and Impacts on Unsaturated Shear Strength Predictions. Ph.D. Thesis, Arizona State University, Tempe, AZ, USA, 1999.
35. National Drought Mitigation Center (NDMC); U.S. Department of Agriculture (USDA); National Oceanic and Atmospheric Administration (NOAA). US Drought Monitor. 2022. Available online: https://droughtmonitor.unl.edu/Maps/MapViewer.aspx (accessed on 25 August 2024).

36. McPherson, R.A.; Fiebrich, C.A.; Crawford, K.C.; Kilby, J.R.; Grimsley, D.L.; Martinez, J.E.; Basara, J.B.; Illston, B.G.; Morris, D.A.; Kloesel, K.A.; et al. Statewide monitoring of the mesoscale environment: A technical update on the Oklahoma Mesonet. *J. Atmos. Ocean. Technol.* **2007**, *24*, 301–321. [CrossRef]
37. Brock, F.V.; Crawford, K.C.; Elliott, R.L.; Cuperus, G.W.; Stadler, S.J.; Johnson, H.L.; Eilts, M.D. The Oklahoma Mesonet: A technical overview. *J. Atmos. Ocean. Technol.* **1995**, *12*, 5–19. [CrossRef]
38. Fredlund, D.G.; Xing, A.; Huang, S. Predicting the permeability function for unsaturated soils using the soil-water characteristic curve. *Can. Geotech. J.* **1994**, *31*, 533–546. [CrossRef]

MDPI AG
Grosspeteranlage 5
4052 Basel
Switzerland
Tel.: +41 61 683 77 34

Geosciences Editorial Office
E-mail: geosciences@mdpi.com
www.mdpi.com/journal/geosciences

Academic Open
Access Publishing

mdpi.com

ISBN 978-3-7258-2892-0